

**A Thesis Submitted for the Degree of PhD at the University of Warwick**

**Permanent WRAP URL:**

<http://wrap.warwick.ac.uk/91958>

**Copyright and reuse:**

This thesis is made available online and is protected by original copyright.

Please scroll down to view the document itself.

Please refer to the repository record for this item for information to help you to cite it.

Our policy information is available from the repository home page.

For more information, please contact the WRAP Team at: [wrap@warwick.ac.uk](mailto:wrap@warwick.ac.uk)

*Engineering modelling  
of the progressive retreat  
of cliffs*

---

*A thesis submitted in partial fulfilment of the  
requirements for the degree of Doctor of Philosophy in  
Engineering*

by Voulgari Chrysoula

January 2017

## Table of Contents

List of Tables .....	vi
List of Figures .....	viii
Acknowledgements.....	xvii
Declaration .....	xviii
Abstract .....	xx
Symbols.....	xxii
Abbreviations.....	xxiii
Chapter 1 : Introduction .....	1
1.1. Context and Motivation .....	1
1.2. Aims and Objectives of the thesis .....	5
1.3. Structure of the thesis .....	7
Chapter 2 : Literature review and Theory .....	9
2.1. Causes of slope instability.....	10
2.1.1. Increase of driving forces .....	10
2.1.2. Decrease of resisting forces .....	15
2.2. Methods to study slope stability .....	16
2.3. Review of analytical and numerical methods.....	17
2.3.2. Limit analysis (LA).....	17
2.3.1. Limit equilibrium method (LEM) .....	18
2.3.3. Finite elements method (FEM) .....	20

2.3.4. Discrete element method (DEM) .....	21
2.3.5. Finite limit analysis method (FELA) .....	21
2.3.6. Choice of the analytical method.....	22
2.4. Review of physical modelling studies .....	24
2.4.1. Scaled model tests .....	25
2.4.2. Centrifuge tests .....	27
2.4.3. Choice of small scale tests .....	27
Chapter 3 : Analytical study .....	30
3.1. Limit analysis upper bound method.....	32
3.2. First failure (landslide).....	34
3.2.1. Tension crack.....	37
3.2.2. Seismic action .....	41
3.2.3. Pore pressure.....	43
3.2.4. Calculation of the first failure mechanism .....	45
3.3. Second and successive failures (landslides) .....	46
3.3.1. Weathering simulated by cohesion decrease .....	49
3.3.2. Effect of seismic acceleration .....	50
3.3.3. Work of water during the second failure .....	56
3.3.4. Calculation of the second failure mechanism.....	56
3.4. Geometric approximations .....	57
3.4.1. Slope profile after each failure .....	58
3.4.2. Slope profile after a number of failures .....	60



3.5. Results.....	62
3.5.1. Parametric analysis of slope evolution for various hydrogeological scenarios .....	62
3.5.2. Case study .....	76
3.5. Conclusions .....	84
Chapter 4 : Experimental Methodology .....	87
4.1. Preliminary tests .....	88
4.1.1. Selection and design of (artificial) weakly bonded geomaterial suitable for laboratory weathering .....	89
4.1.2. Microstructure characterisation of the selected material .....	94
4.1.3. Macro scale tests to show the short term debonding process .....	97
4.2. Physical Model.....	101
4.2.1. Dimensional Analysis .....	102
4.2.2. Main test Apparatus .....	106
4.2.3. Slope model .....	107
4.2.4. Rainfall simulation device .....	109
4.2.5. Monitoring System.....	110
4.3. Experimental Procedure.....	114
4.3.1. Camera setting.....	114
4.3.2. Orthogonality between Plane of Interest and Camera .....	115
4.3.3. Camera shake.....	115
4.3.4. Lens Distortion .....	116
4.3.5. Refraction of light .....	118

Chapter 5 : Experimental Study .....	119
5.1. Preliminary one dimensional tests.....	120
5.2. Other verification techniques.....	123
5.3. GeoPIV analysis .....	127
5.4. Experiments and Results .....	130
5.5. Slope behaviour under different rainfall intensities .....	135
5.5.1. First failure .....	137
5.5.2. Second failure .....	149
5.5.3. General observations .....	155
5.6. Effect of flume bottom on the evolution of the slope .....	156
5.7. Stabilising effect of the failed mass .....	160
5.8. Experimental results for inclined slope front .....	166
5.10. Conclusions .....	168
Chapter 6 : Conclusions.....	170
6.1. Analytical model.....	170
6.2. Experimental model .....	172
6.3. Comparison of experimental with analytical results .....	173
6.4. Recommendations for future work.....	176
Appendices.....	178
Appendix A - SOIL MOISTURE SENSORS .....	178
Calibration.....	178
ARDUINO Code for data logging.....	181

Appendix B - ANALYTICAL CALCULATIONS.....	182
Appendix C- MATLAB SCRIPTS.....	187
Successive failures with cracks.....	187
Bibliography.....	204
Online Sources .....	214

## List of Tables

Table 2.1. Catastrophic Landslides of the 20th Century - Worldwide / Source: <a href="http://landslides.usgs.gov/learn/majorls.php">http://landslides.usgs.gov/learn/majorls.php</a> .....	12
Table 2.2. Properties of traditional methods used for geotechnical stability analysis (Sloan, 2013).....	23
Table 3.1. Stability number and crack depth for second 'significant' failure for different starting slope profiles for the second 'significant' failure ..	60
Table 3.2. Values for Associated Crest Retreat, Sliding Area and Crack Depth for Slopes with Initial Inclination $\beta$ and Friction Angle $\phi$ , for slopes with $t=1.0$ , $t=0.5$ , $t=0.2$ and $t=0$ .....	74
Table 3.3. Values for Associated Crest Retreat and Sliding Area with Initial Inclination $\beta$ and Friction Angle $\phi$ , for intact slopes under seismic action or with the existence of water.....	75
Table 3.4. Estimated yield acceleration for four past failure events ...	80
Table 3.5. Results for Associated Stability Number $\gamma H/c$ , Crest Retreat normalized by the initial height of the slope $CR/H$ and Sliding Area normalized by the square initial height of the slope $A/H^2$ for slopes with initial inclination $\beta=40^\circ$ and friction angle $\phi=35^\circ$ , for horizontal seismic acceleration $K_h=0.2$ , $K_h=0.3$ and $K_h=0.4$ .....	83
Table 4.1. List of the 20 specimens tested .....	93
Table 4.2. Geotechnical properties of the materials used in the experiments.....	94

Table 4.3. Porosity values calculated by means of the standard weighting method, mercury intrusion porosimetry MIP, and 2D image analysis .....	97
Table 4.4. The governing parameters of the slope model.....	103
Table 4.5. Dimensional analysis of the physical quantities in model test .....	105
Table 4.6. General characteristics of the slope model (height H=15.00cm).....	107
Table 4.7. Main Technical Features of Probes Used for Monitoring.	111
Table 5.1. Water content during calibration box test.....	121
Table 5.2. Tests characteristics .....	132
Table 5.3. Model and soil characteristics.....	133
Table 0.1. Soil moisture content calibration .....	179

## List of Figures

Figure 1.1. Holbeck Hall landslide, Scarborough, June 1993 / Source: <a href="http://www.bgs.ac.uk">http://www.bgs.ac.uk</a> .....	2
Figure 1.2. Photographs of steep slope in weakly and moderately cemented cliffs in Daly City near San Francisco, California [N37 39.23 W122 29.87] showing the successive retreat of the slope since 2002 .....	4
Figure 1.3. Illustration of the problem and possible approaches .....	5
Figure 2.1. Methods to study slope stability problems reviewed in this chapter .....	16
Figure 3.1. First and second failure mechanisms: Region of soil EBCD slides away rotating around point $P_1$ and then region of soil GIDCB rotates around point $P_2$ . .....	36
Figure 3.2. Mohr-Coulomb failure criteria illustrating the failure mechanisms associated with soil of: (a) full unconfined tensile strength ( $t=1$ ). (b) limited tensile strength ( $t=0.5$ ). (c) zero tensile strength ( $t=0$ ), after (Michalowski, 2013). .....	40
Figure 3.3. Presence of pore pressure in the calculation of the most critical failure mechanism.....	44
Figure 3.4. Crack depth against slope inclination for friction angle $\varphi=30^\circ$ for the first failure and for different kind of crack formation for seismic coefficient $K_h=0$ , $K_h=0.1$ and $K_h=0.2$ (for slope inclinations higher than $72^\circ$ and for the case of tension cut off when $K_h=0.2$ , a translational failure mechanism takes place - no curve).....	46

Figure 3.5. Potential failure mechanisms for the second failure, relative to different mechanisms considered (for different critical heights $h_i$ ).....	48
Figure 3.6. (a) Weathering of granite, after (Kimmance, 1988) , (b) failure loci of cemented sands for different cement contents, after (Wang and Leung, 2008) .....	49
Figure 3.7. Calculation for the rate of the external work for each 'old' landslide .....	55
Figure 3.8. Most critical failure mechanism for the second 'significant' failure for slope with initial slope inclination $\beta=80^\circ$ and friction angle $\varphi=40^\circ$ (tension cut off).....	59
Figure 3.9. Deep seated failure mechanism for a slope with $\beta=70^\circ$ and initial friction angle $\varphi=20^\circ$ .....	62
Figure 3.10. Dimensionless normalized sliding area for inclination $\beta=70^\circ$ and for friction angle $\varphi=40^\circ$ , showing the influence of the tensile crest on the evolution of slopes for different $Kh$ , for 6 successive failures.....	65
Figure 3.11. Critical height ( $\gamma H/c$ ) for six successive failures for slope inclination $\beta=60^\circ$ and $\varphi=20^\circ$ for soil of full unconfined tensile strength ( $t=1$ ), soil of limited tensile strength ( $t=0.5$ and $t=0.2$ ) and soil of zero tensile strength ( $t=0$ ), (a) for $r_u=0.25$ and (b) for $r_u=0.50$ .....	66
Figure 3.12. Dimensionless normalized cohesion versus crest retreat for inclination $\beta=70^\circ$ , (a) step-like relationship obtained for $\varphi = 20^\circ$ , for different tensile strengths for $Kh=0$ , $Kh=0.1$ and $Kh=0.2$ , for 8 successive failures (b) If the first two failures are excluded, the values of critical cohesion and crest retreat lie on straight lines only for intact slopes.....	68
Figure 3.13. Dimensionless normalized cohesion versus crest retreat for inclination $\beta=70^\circ$ , step-like relationship between cohesion and crest retreat	

obtained for  $\phi=20^\circ$ , for intact slopes (dry case) a) slope evolution for various  $K_h$  values and b) slope evolution for various  $r_u$  values for 6 successive failures (static case) ..... 69

Figure 3.14. Critical height ( $\gamma H/c$ ) and dimensionless cliff retreat ( $L/H$ ) as a function of the friction angle represented in the same graph as curves for six successive failures for slope inclinations  $\beta=60^\circ$ ,  $\beta=70^\circ$  and  $\beta=80^\circ$  for the case of intact slope, for soil of full unconfined tensile strength, soil of limited tensile strength and soil of zero tensile strength. Solid black lines are used for the critical height and dashed lines for the dimensionless crest retreat. The corresponding failure number is marked on the curves. .... 71

Figure 3.15. Critical height ( $\gamma H/c$ ) and dimensionless cliff retreat ( $L/H$ ) as a function of the friction angle represented in the same graph as curves for six successive failures for slope inclinations  $\beta=60^\circ$ ,  $\beta=70^\circ$  and  $\beta=80^\circ$  for intact slopes and for seismic scenarios with coefficient  $K_h=0.1$  and  $K_h=0.2$ . Solid black lines are used for the critical height and dashed lines for the dimensionless crest retreat. The corresponding failure number is marked on the curves. .... 72

Figure 3.16. Critical height ( $\gamma H/c$ ) and dimensionless cliff retreat ( $L/H$ ) as a function of the friction angle represented in the same graph as curves for six successive failures for slope inclinations  $\beta=60^\circ$ ,  $\beta=70^\circ$  and  $\beta=80^\circ$  for the case of intact slope and for pore pressure with coefficient  $r_u=0.25$  and  $r_u=0.5$ . Solid black lines are used for the critical height and dashed lines for the dimensionless crest retreat. The corresponding failure number is marked on the curves. .... 73

Figure 3.17. Area of interest for the case study. .... 77



Figure 3.18. a. Elevation profiles for the rock avalanche area before and after the failures, b. group of rock avalanches studied here. The failure surface envelope daylight above the slope toe. ....	78
Figure 3.19. Past failure mechanisms for a simplified slope profile with initial slope inclination $\beta=27^\circ$ .....	81
Figure 3.20. Sliding volumes and areas normalised to the first failure	82
Figure 3.21. Slope evolution during four successive failures under three different earthquake scenarios for slope with initial inclination $\beta=40^\circ$ and friction angle $\phi=35^\circ$ . Solid lines refer to failure mechanisms under horizontal acceleration $K_h=0.2$ , dashed lines to $K_h=0.3$ and dotted to $K_h=0.4$ . ....	84
Figure 4.1. Twenty different specimens tested .....	90
Figure 4.2. a. Small specimen b. glass and powder structured sample preparation (Ciantia et al., 2015a).....	91
Figure 4.3. Specimen under load a. dry b. with water at its base .....	91
Figure 4.4. Small slope models (15.00x8.00x6.00cm) with vertical front .....	94
Figure 4.5. Sieve Analysis - Particle size distribution curve .....	95
Figure 4.6. SEM images of 3D microstructure observations at increasing magnification (where GB stands for Glass beads and CB for calcarenite bonds) .....	96
Figure 4.7. Typical thin-sections obtained at an optical microscope (where GB stands for Glass beads and CB for calcarenite bonds).....	96
Figure 4.8. Porosimetry (blue curve for the cumulative pore volume and red columns for relative pore volume) .....	97

Figure 4.9. a. Dry soil sample after failure during the uniaxial test b. a. Wet soil sample after failure during the uniaxial test c. Stress strain curve at different moisture contents.....	99
Figure 4.10. Comparison of SWCC derived from pressure plate tests and ku-pF and from measurements taken during calibration box tests.....	100
Figure 4.11. Shear box tests for different water contents.....	100
Figure 4.12. Repose angle of dry and saturated sample .....	101
Figure 4.13. Arrangement of the experimental apparatus.....	106
Figure 4.14. Picture during the construction phase and placing the sensors.....	108
Figure 4.15. Transparent plastic drainage rails at the sides of the container.....	109
Figure 4.16. a.M1 - Mini Nozzles, b. GSC1 gravity nozzles .....	110
Figure 4.17. Soil texture after using blue and white paint for some glass beads.....	113
Figure 4.18. Cylinder for the orthogonal set-up.....	115
Figure 4.19. a. Barrel distortion, b. Pincushion Distortion (Hugemann, 2010) .....	117
Figure 4.20. Calibration mesh for the effect of distortion.....	118
Figure 5.1. Calibration box and sample extraction.....	120
Figure 5.2. Gravimetric water content from oven-dry test during the calibration box test.....	122
Figure 5.3. Volumetric water content from sensors readings during the calibration box test.....	123

Figure 5.4. a. Sequence of photographs showing the advancing wet dye front and b. vertical slice of the model during the test showing uniform movement of water also inside the model .....	125
Figure 5.5. Location of the failure vs. rainfall intensity .....	126
Figure 5.6. Time of failure vs. rainfall intensity.....	126
Figure 5.7. Time when water front reaches moisture sensor $m_1$ vs. rainfall intensity .....	127
Figure 5.8. Different patch size used in the analysis.....	129
Figure 5.9. Identified noise during the test.....	130
Figure 5.10. Experimental apparatus a. front view, b. plan view, c. location of soil moisture sensors & tensiometers (all dimensions are in cm)	134
Figure 5.11. a. Vertical crack in the upper part of the slope and b. initiation of failure.....	136
Figure 5.12. Time history of water content during test S90_H15_L35_3 .....	137
Figure 5.13. Soil suction during test S90_H15_L35_3.....	138
Figure 5.14. Accumulated soil element displacements before the onset of the first failure for a point on the slope crest (test: S90_H15_L35_3) .....	139
Figure 5.15. Incremental a. horizontal and b. vertical displacement contours at the initiation of the first failure event (test S90_H15_L35_3).....	141
Figure 5.16. Observed displacement vectors at the initiation of the first failure event for test S90_H15_L35_3.....	142
Figure 5.17. Digital images a. before and b. after the first failure during test S90_H15_L35_3.....	142

Figure 5.18. Digital images a. before and b. after the first failure during test S90_H15_L35_16 .....	143
Figure 5.19. Observed displacement vectors before the first failure event for test S90_H15_L35_16 .....	144
Figure 5.20. Accumulated soil element displacements before the onset of the first failure for a point on the slope crest (test: S90_H15_L35_16) ....	145
Figure 5.21. Crack forming in the slope during test S90_H15_L35_2 .....	146
Figure 5.22. Observed displacement vectors before the first failure event for test S90_H15_L35_2 .....	147
Figure 5.23. Accumulated soil element displacements before the onset of the first failure for a point a. on the slope top and b. at the slope bottom (test: S90_H15_L35_2).....	148
Figure 5.24. Observed displacement vectors during the second failure event for test S90_H15_L35_16 .....	150
Figure 5.25. Digital images showing the evolution of second failure during test S90_H15_L35_16 .....	151
Figure 5.26. Observed displacement vectors during the second failure event for test S90_H15_L35_2 .....	152
Figure 5.27. Digital images showing the slope profile during test S90_H15_L35_2, observation of two slides and then flow occurs in the model .....	153
Figure 5.28. Velocity of sliding masses during test S90_H15_L35_2	154
Figure 5.29. Sliding area of each failure normalised to the area of the first failure .....	156

Figure 5.30. Container bottom made of a. Plexiglas and b. Soil particles layer .....	157
Figure 5.31. Slope profile at t=105min from the initiation of rainfall for $I_r=10\text{mm/h}$ and after the occurrence of one failure for a. Plexiglas bottom (test: S90_H15_L35_6) b. soil particles glued on the bottom of the container (test: S90_H15_L35_18).....	159
Figure 5.32. Slope profile at t=40min from the initiation of rainfall for $I_r=20\text{mm/h}$ and after the occurrence of one failure for a. Plexiglas bottom (test: S90_H15_L35_4) b. soil particles glued on the bottom of the container (test: S90_H15_L35_19).....	160
Figure 5.33. Removal of slumped debris after the occurrence of each failure (test: S90_H15_L35_14) .....	161
Figure 5.34. Initiation of three successive failure when debris is removed from the slope toe (test: S90_H15_L35_14), a. initial state ( $t_0= 0$ min) b. first failure ( $t_1= 16$ min) c. second failure ( $t_2=22$ min) d. third failure ( $t_3= 33\text{min}$ ) .....	163
Figure 5.35. Initiation of successive failure without debris removal (test: S90_H15_L35_16) a. initial state ( $t_0'= 0$ min) b. first failure ( $t_1'= 16$ min) c. second failure ( $t_2'= 25\text{min}$ ) d. at the end of the test ( $t_3'= 45\text{min}$ ) .....	164
Figure 5.36. Slope profile at t=45min from the initiation of rainfall after the occurrence of a. four failures (debris removal) b. two failures (no debris removal) .....	165
Figure 5.37. Construction of inclined slope profile .....	166
Figure 5.38. Local slope failure for initial slope inclination $\beta=60^\circ$ and for rainfall intensity a. $I_r=10\text{mm/h}$ , b. $I_r=16\text{mm/h}$ and c. $I_r=30\text{mm/h}$ .....	167

Figure 5.39. Local slope failure for initial slope inclination $\beta=45^\circ$ and for rainfall intensity a. $I_r=16\text{mm/h}$ and b. $I_r=60\text{mm/h}$ .....	167
--	-----

Figure 6.1. Failure mechanism developed during test S90_H15_L35_3 and failure lines as derived from the analytical model .....	174
--	-----

Figure 0.1. Plot of calibration data and soil specific calibration equation. ....	180
---	-----

The analytical calculations for each successive failure are given below. The areas are shown in Figure 0.2.....	182
---	-----

## Acknowledgements

---

A rewarding part of this thesis is the ability to reminisce and look back over the course of my studies and acknowledge the support, guidance and all the experiences that have been imparted upon me throughout my academic endeavors. As such, this acknowledgment section provides initial opportunity to thank those who have been most influential in encouraging me through my research and also supported me throughout these years.

First and foremost, I would like to thank my family for their understanding, patience, love and support throughout the duration of my studies.

Special thanks to my supervisor Professor Stefano Utili for offering me support and guidance over the course of the project. His encouragement, advice and constructive criticism helped guide me through my studies. His reassurance and patience sustained my desire to succeed, focused my energy and encouraged me to proceed; irrespective of the size of the obstacles placed before me. My gratitude also goes to Professor Riccardo Castellanza, who supported me during this work, especially for the experimental part.

Finally, I am very grateful to my colleagues that made considerable comments and sound suggestions for the content and writing of the thesis and all my friends that made my experience at Warwick as memorable as it was.

## Declaration

---

The present thesis titled 'Engineering modeling of the progressive retreat of slopes' is submitted to the University of Warwick in support of my application for the degree of Doctor of Philosophy.

I declare that the work presented in this thesis was conducted by me under the direct supervision of Professor Stefano Utili. None of the work presented has been previously submitted for any other degree.

Parts of this thesis have been published by the author:

1. Voulgari C., Utili S. (2016). A general analytical solution for the evolution of cliffs accounting for strength degradation, seismic action, formation of tension cracks and seepage. *Engineering Geology*\_(Voulgari and Utili, 2017).
2. Voulgari C., Utili S., Crosta G.B., Dattola G., Hermanns R.L. (2016). A model for earthquake driven slope instabilities and morphologic landscape evolution. *Landslides and Engineered Slopes. Experience, Theory and Practice. Proceedings of the 12th International Symposium on Landslides (Napoli, Italy, 12-19 June 2016)*, pp. 2007-2012.
3. Voulgari C., Utili S. (2016). Experimental modelling of successive slope failures due to heavy rainfall. *Landslides and Engineered Slopes. Experience, Theory and Practice. Proceedings of the 12th International Symposium on Landslides (Napoli, Italy, 12-19 June 2016)*, pp. 2013-2022.



4. Voulgari C., Utili S. (2016). Small scale tests on slope failures on different surfaces. European Geosciences Union General Assembly 2016, Vienna, Austria, number 18359.
5. Voulgari C., Utili S. (2016). Influence of pore pressure on the successive failures of intact slopes. European Geosciences Union General Assembly 2016, Vienna, Austria, number 18358.
6. Voulgari C. (2015). An experimental model for slopes subject to weathering. International Symposium on Geohazards and Geomechanics (Coventry, UK, 10-11 September 2015). IOP Conference Series: Earth and Environmental Science. IOP Publishing, 012047.
7. Voulgari C. (2015). Modelling weathering induced retreat of c- $\phi$  cliffs with limited tensile strength. International Symposium on Geohazards and Geomechanics (Coventry, UK, 10-11 September 2015). IOP Conference Series: Earth and Environmental Science. IOP Publishing, 012048.
8. Voulgari C., Utili S., Castellanza R. (2015). Small scale tests on the progressive retreat of soil slopes. European Geosciences Union General Assembly 2015, Vienna, Austria, number 12283.
9. Voulgari C., Utili S. (2014). Small scale tests on the progressive retreat of soil slopes. Proceedings of the 13th BGA Young Geotechnical Engineers' Symposium (Manchester, UK, 30 June - 2 July 2014), pp.51-52.

# Abstract

---

## **Engineering modelling of the progressive retreat of cliffs**

A thesis submitted for the degree of Doctor of Philosophy

to the University of Warwick

Chrysoula Voulgari

In this thesis, the morphologic evolution of uniform  $c$ ,  $\phi$  slopes subject to successive failures is investigated. The research is conducted in two parts; the analytical part (employing the limit analysis upper bound method) and the experimental (by small scale model tests).

An experimental prototype model to study the influence of water infiltration on the morphologic evolution of natural cliffs subject to progressive retreat is presented. A set of small scale laboratory tests is designed to investigate successive failures. The failure is reached by applying rainfall on the slope through a rainfall simulator device. The moisture content and the suction of the soil during the tests are monitored by soil moisture sensors and tensiometers that are buried inside the slope model. High resolution cameras record the behaviour of the slope model and GeoPIV is used to analyse the frames and obtain the deformations of the slope model during the tests. After a short time of rainfall, vertical cracks appear in the slope model with significant vertical deformations developing. Experimental results indicate that there is a strong connection between moisture content and the occurrence of

a landslide. A prediction model of slope failures can be introduced based on the observed moisture content response of the slope models.

For the analytical part a semi analytical model on the evolution of intact and slopes with fissures is illustrated. A general analytical solution for the assessment of the stability of homogeneous slopes obeying the linear Mohr-Coulomb criterion accounting for strength degradation, seismic action, formation of tension cracks and seepage is presented and a parametric analysis is run to assess the effect of each factor on cliff evolution. The so-called pseudo-static approach and the pore pressure coefficient  $r_u$  are employed. Results for a range of internal shearing resistance angle ( $\phi$ ) values of engineering interest are presented in the form of dimensionless ready-to-use stability charts.

## Symbols

---

$e$	Void ratio
$n$	Porosity
$M$	Richter magnitude scale
$S$	Degree of saturation
$V_a$	Volume of air ( $\text{cm}^3$ )
$V_s$	Volume of soil ( $\text{cm}^3$ )
$V_T$	Volume of soil sample ( $\text{cm}^3$ )
$V_w$	Volume of water (g)
$W_b$	Glass beads (g)
$W_c$	Calcarenite (g)
$w_c$	Gravimetric water content
$w_c$	Gravimetric water content at saturation
$W_s$	Dry weight of soil (g)
$W_T$	Total Weight (g)
$W_T$	Weight of soil sample (g)
$W_w$	Water (g)
$W_w$	Weight of water (g)
$\gamma_b$	Glass beads specific gravity
$\gamma_c$	Calcarenite specific gravity
$\gamma_d$	Dry unit weight ( $\text{kN/m}^3$ )
$\gamma_m$	Mixture specific gravity
$\gamma_{\text{sat}}$	Saturated unit weight
$\gamma_T$	Total unit weight ( $\text{kN/m}^3$ )
$\gamma_w$	Water specific weight ( $\text{kN/m}^3$ )
$\rho_d$	Dry density ( $\text{g/cm}^3$ )
$\rho_{\text{sat}}$	Saturated densiity ( $\text{g/cm}^3$ )
$\rho_T$	Total density ( $\text{g/cm}^3$ )
$\rho_w$	Water density ( $\text{g/cm}^3$ )

## Abbreviations

---

2D	Two-dimensional
3D	Three-dimensional
SEM	Scanning electron microscope analyses
MIP	Mercury intrusion porosimetry
UCT	Uniaxial Compression Test
SWCC	Soil water characteristic curve

## Chapter 1 : Introduction

---

### 1.1. Context and Motivation

Hundreds of lives and properties are lost every year due to slope failures, commonly called landslides. In the last decades, the increasing impacts of landslide hazards on human lives and infrastructure around the world have led to the need of finding cost effective and trustworthy techniques to predict the occurrence and magnitude of landslides. Landslides occur when earth material moves rapidly downhill after failing along a shear zone. They play a key role in landscape evolution, erosion, and sediment transport and they also constitute for a significant natural hazard. Landslides can be triggered by various actions such as rainfall, seismic events, weathering, etc. A good understanding of the underlying triggering mechanisms of slope failures is required to evaluate landslide risk and to optimise slope stabilization and mitigation strategies. The analysis of slope stability problems in geotechnical engineering is of paramount importance. However, despite intensive research, these events continue to result in human and property losses, and environmental degradation every year.

The morphological evolution of cliffs (natural and excavated slopes) is a traditional subject in engineering geology and geomorphology (Carson and Kirkby, 1972, Hutchinson, 1969, Hutchinson, 1970, Hutchinson, 2001, Selby, 1982, Parsons, 2002) which investigates the evolution of the landscape over time. Modelling the progressive retreat of cliffs has recently received considerable attention by the engineering community due to increasing coastal erosive processes caused by climate change and amplified environmental awareness at national and European level (Bray and Hooke, 1997). The insurance industry needs reliable models to predict the amount of cliff retreat over time for residential buildings located in exposed areas, whereas local authorities, stakeholders and decision makers need to know the level of risk faced by the public infrastructure (e.g. coastal roads, pedestrian footpaths, car parks, etc.).



*Figure 1.1. Holbeck Hall landslide, Scarborough, June 1993 / Source:*

<http://www.bgs.ac.uk>

In Figure 1.1, a typical example of cliff retreat due to rainfall and limited tensile strength in United Kingdom is illustrated. In June 1993, the Holbeck Hall Hotel collapsed after a long dry period followed by heavy rainfall. Over a three days period, a rotational landslide including about 1 million tons of glacial till cut back the 60m high cliff by 70m under smaller landslides that occurred, south of Scarborough in North Yorkshire on the North East Coast of England. It flowed across the beach to form a semicircular promontory 200m wide projecting 135m outward from the foot of the cliff. The first signs of movement on the cliff were seen six weeks before the main failure, when cracks developed in the tarmac surface of footpaths running across the cliffs.

In Figure 1.2, an example of cliff retreat due to successive failures is illustrated. A steep slope in weakly and moderately cemented cliffs in Daly City near San Francisco, California can be observed. The slope has suffered a number of successive failures bringing its crest closer to the existing buildings. The assessment of the hazards caused by landslides and the possibility of slope failure are commonly addressed through slope stability analysis, allowing for analytical predictions of the failure conditions in a selected slope.

The evolution of natural slopes over time is ruled by several factors, namely the strength of its component geomaterials and its weakening over time due to weathering processes, the occurrence of seismic events and the hydrogeological conditions, e.g. seepage as well as other atmospheric agents that affect the slopes.



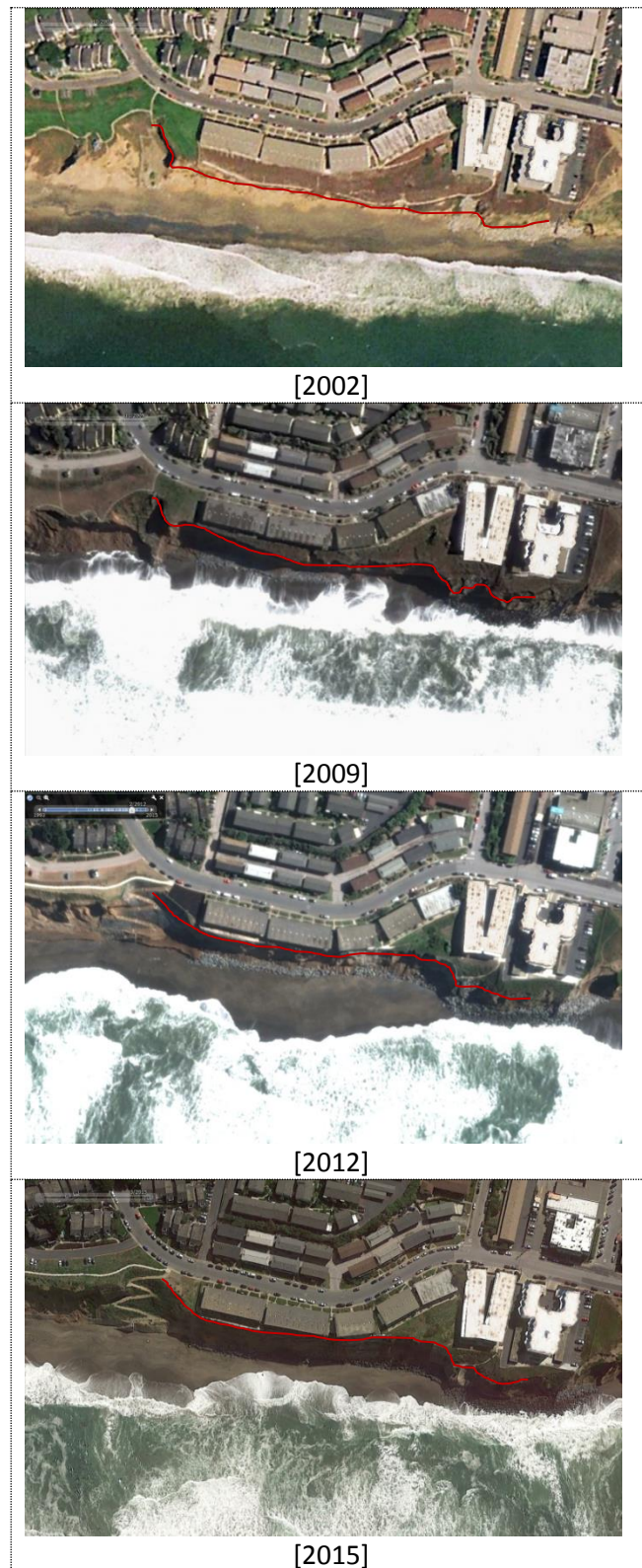


*Figure 1.2. Photographs of steep slope in weakly and moderately cemented cliffs in Daly City near San Francisco, California [N37 39.23 W122 29.87] showing the successive retreat of the slope since 2002*

## 1.2. Aims and Objectives of the thesis

Given all the above it is obvious that it is very complex to study all the parameters that might affect the stability of slopes. This thesis is aimed at investigating and engineering modelling the morphological evolution of natural cliffs subject to progressive retreat induced by various actions.

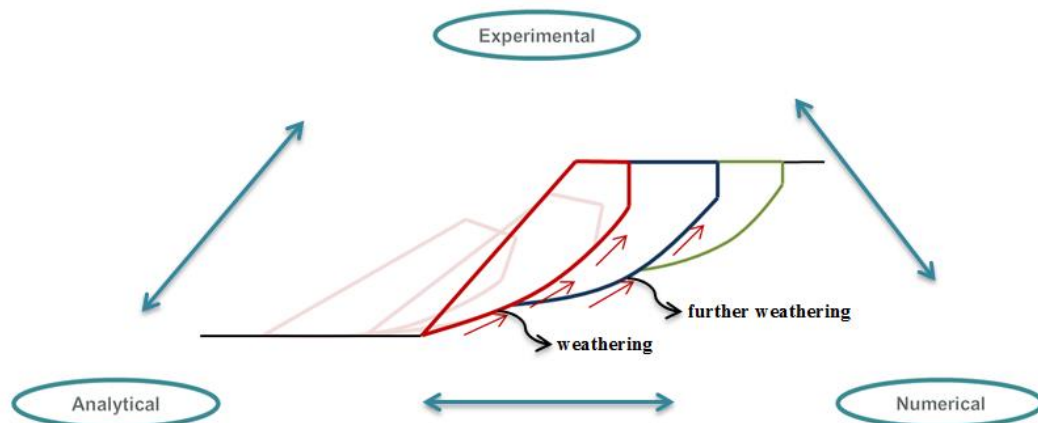


*Figure 1.3. Illustration of the problem and possible approaches*

A slope can become unstable when the gravity forces that act on a mass of soil overcome the available shear stress within the mass and along its base. The result will be movement of the mass of soil down the slope, which in cases of populated areas can have catastrophic consequences. In unpopulated areas the result might be minimal and could lead only to the natural degradation of the slope surface. Figure 1.3 illustrates the possible ways to approach this issue. This thesis is focused on the experimental and analytical methods to approach the problem.

For the analytical part the analysis upper bound method and the pseudo-static approach (Terzaghi, 1950) are used to derive the analytical law

describing the evolution of homogeneous cohesive frictional ( $c$ ,  $\phi$ ) slopes with limited or no tensile strength subject to progressive retreat induced by weathering for static and seismic scenarios and with the presence of water and to provide rigorous upper bounds to the true collapse values. Moreover the use of the  $r_u$  coefficient is adopted to include the influence of the water pore pressure. The work includes the introduction of the effect tension cracks, seismic action and pore water pressure in the pre-existing model for cliff retreat (Utili and Crosta, 2011a) and to extend its validity to wet conditions and to soils of limited tensile resistance and under earthquake loading. The aim is to build a model, which will be capable of predicting the evolution of slopes due to various actions.

Soil strength is characterised by the Mohr-Coulomb failure criterion therefore only three parameters are needed to describe the soil properties (unit weight, internal friction angle and cohesion). The limit analysis upper bound method was applied to determine each discrete landslide event occurring over time for successive destabilization and complete removal of the failed mass after each event. The inclusion of tension crack, the seismic acceleration and the existence of pore water pressure lead to a change of the analytical expression of the energy balance equation. A full set of solutions for the stability of homogeneous slopes for mechanisms including crack formation is presented both by nomograms and tables for different values of slope inclination, cohesion and internal friction angle.

As for the experimental part, this thesis reports on a laboratory apparatus and a set of experiments that were designed and carried out, aiming to investigate the morphologic evolution of natural cliffs made of weakly cemented materials subject to progressive retreat under various causes. A set of small scale laboratory tests is designed and tested in an experimental

prototype apparatus to investigate successive landslides. Small scale slope models are constructed and a rainfall simulation device is placed on top of them; rainfall is then applied to them until successive failures are observed. The moisture content and the suction of the soil during the tests are monitored through soil moisture sensors and tensiometers, buried inside the slope model during the construction phase, while high resolution cameras record the behaviour of the slope model and GeoPIV software is used to analyse the frames and obtain the deformations of the slope model during the tests. After a short time of rainfall, vertical cracks appear in the slope model and significant vertical deformations are developed until a first failure is reached. Subsequently and due to further wetting of the slope material successive failure takes place.

### **1.3. Structure of the thesis**

This thesis comprises of six chapters, with a summary of the main points covered at the beginning of each chapter.

- Chapter 1 is the introductory chapter, illustrating the motivation and the focus of this research as well as the aims, objectives and the structure of this thesis.
- Chapter 2 forms the literature review, presenting different methodologies for slope stability assessment as well as the current knowledge from a number of previous studies on the same field. The reasons why the analytical kinematic approach of limit analysis is adopted and also the small-scale experiments are chosen are justified.
- Chapter 3 is focused on the analytical part of this thesis, explaining the basic concepts of the limit analysis upper bound method adopted in this

study together with the analytical model developed and the parametric analysis that has been carried out.

- In Chapter 4 the preliminary results that led to the design of the final experimental set up and the experimental methodology are described. The experimental procedure is described in detail and the dimensional analysis is presented. Since this project required a novel testing approach, this section follows the development process and is in itself a result of this research.
- Chapter 5 presents the set of experiments that were carried out for this research as well as the main experimental findings and
- Chapter 6 presents the main conclusions from the conducted research for this thesis, the results and the main concluding points are summarised, while recommendations for future research are provided.

This thesis also includes an Appendix section containing:

- Sensors calibrations curves
- Analytical calculations regarding the limit analysis model
- MATLAB scripts

## **Chapter 2 : Literature review and Theory**

---

Landslides occur when earth material moves rapidly downhill after failing along a shear zone and they account for a significant natural hazard. The assessment of these hazards and the possibility of slope failure are commonly addressed through slope stability analysis, allowing for analytical predictions of the failure conditions in a selected slope. A large range of different tools exist today to investigate slope stability and many experimental, analytical and numerical studies have been conducted so far concerning slope stability. In order to study the landslide mechanisms, many different ways of modelling a slope and study the mechanism of slope failure have been implemented. The general aim of these studies is to assess, whether or not, a slope is considered to be stable and also to provide a safe distance from the slope crest behind which structures and other facilities can be safely constructed.

In this chapter, the main factors causing slope instability are examined and the methods to study slope instability have been reviewed. Moreover, some important studies of modelling landslides due to various factors are listed. The reasons for using small scale tests to model successive failures are

illustrated and the choice of the upper bound method of limit analysis as the main research tool in the thesis is also justified.

## **2.1. Causes of slope instability**

Slope failure occurs when gravity and shear stresses exceed the shear strength of the material, leading to the downward movements of slope material. Therefore, causes of slope instability can be divided into the factors that tend to increase the shear stresses applied on the slope and those that tend to decrease the available shear strength of the slope material.

### **2.1.1. Increase of driving forces**

Natural landslides occur on slopes around the world. Ground water pressures and seismic loading are two major factors contributing to slope instability. A quick look in Table 2.1, illustrating the most catastrophic landslides of the 20<sup>th</sup> century can prove that rainfall and earthquake movement are the two most common triggering factors for these large slope failures, resulting in thousands of people being killed and huge infrastructure loss.

Present slope stability is strongly influenced also by high pore pressures which can develop at the base of the soils in the previous top of the weathered rock (Grainger and Harris, 1986). Water infiltration can lead to slope instability by the increase in soil moisture content, leading to a decrease in soil matric suction and then a decrease in the shear strength of the potential failure surface (Rahardjo et al., 1995), while at the same time the soil weight increases due to the ingression of the water. The effect of water has been extensively studied using several different approaches (Michalowski, 1995a, Griffiths and Lu, 2005, Viratjandr and Michalowski, 2006, Oh and Lu, 2015).

Earthquake shaking, on the other hand, can increase shear stresses in soils and thereby reduce the stability of a slope. In addition, earthquake

loading can influence the shape of failure surface, particularly when tension cracks are present. Earthquake-induced landslides are among the most destructive slope movements and there is a large body of literature on limit analysis or other methods applied on landslides triggered by seismic activities (Chang et al., 1984, Ling and Leshchinsky, 1995, Crespellani et al., 1998, Cao and Zaman, 1999, You and Michalowski, 1999, Loukidis et al., 2003, Chen and Liu, 1990, Yang and Chi, 2014). Seismic shaking can directly trigger slope failures and at the same time cause damage within the slope material, predisposing it to successive failures under different triggering factors or earthquakes of smaller magnitude.

Cliff evolution is caused and / or accelerated by several physical agents (Arkin and Michaeli, 1985, de Lange and Moon, 2005, Briaud, 2008, Collins and Sitar, 2010). Key drivers of slope instability are seismic action (Chen and Liu, 1990, Ling and Leshchinsky, 1995, Loukidis et al., 2003, Wasowski et al., 2011, Rathje and Antonakos, 2011, Yang and Chi, 2014, Tsai and Chien, 2016), rainfall and climatic variations (Leroueil, 2001, Frayssines and Hantz, 2006, Take and Bolton, 2011, Conte and Troncone, 2012, Springman et al., 2013), weathering (Yokota and Iwamatsu, 2000, Hachinohe et al., 2000), crack formation (Baker, 1981, Hales and Roering, 2007) and wave action for sea cliffs (Benumof et al., 2000, de Lange and Moon, 2005). In the analytical part of this work all these actions, but the last one, are considered. To account for the presence of water the pore-water pressure,  $u$ , is considered in the analytical model using the coefficient  $r_u$ . Seismic action will be accounted for by employing the so-called pseudo-static approach (Terzaghi, 1950) following the approach presented in (Utili and Abd, 2016).



Table 2.1. Catastrophic Landslides of the 20th Century - Worldwide / Source:

<http://landslides.usgs.gov/learn/majorls.php>

Year	Country (State/Province)	Name & type(s)	Triggering factor	Impact
1911	Tadzhik Rep. (Formerly USSR)	Usoy rock slide	Usoy earthquake M = 7.4	Usoy village destroyed; 54 killed; Murgab River dammed, impounding 65-km long still existing Lake Sarez
1919	Indonesia (Java)	Kalut lahars (Volcanic mudflows)	Eruption of Kalut volcano	5,110 killed; 104 villages destroyed or damaged
1920	China (Ningxia)	Haiyuan landslides	Haiyuan earthquake	100,000 killed; many villages destroyed
1921	Kazakh Rep. (formerly USSR)	Alma-Ata debris flow	Snowmelt	500 killed
1933	China (Sichuan)	Deixi landslides	Deixi earthquake M = 7.5	6,800 killed by landslides; 2,500 drowned when landslide dam failed
1939	Japan (Hyogo)	Mount Rokko slides and mud flows	Heavy rain	505 dead/missing; 130,000 homes destroyed or badly damaged by mass movements and/or floods
1949	Tadzhik Rep. (formerly USSR)	Khait rock slide	Khait earthquake M = 7.5	12,000 - 20,000 killed or missing; 33 villages destroyed
1953	Japan (Wakayama)	Arita River slides and debris/mud flows	Heavy rain	460 dead/missing; 4,772 homes destroyed by mass movements/floods
1953	Japan (Kyoto)	Minamiy-amashiro slides & debris/mud flows	Heavy rain	336 dead/missing; 5,122 homes destroyed or badly damaged by mass movements/floods
1958	Japan (Shizuoka)	Kanogawa slides and mud/debris flows	Heavy rain	1,094 dead/missing; 19,754 homes destroyed or badly damaged by mass movements/floods
1962	Peru (Ancash)	Nevados Huascaran debris avalanche	Not known	4,000-5,000 killed; much of village of Ranrahirca destroyed
1963	Italy (Friuli-venezia-Griulia)	Vaiont Reservoir Rockslide	Not known	2,000 killed; city of Longarone badly damaged; total damages: US\$200 million (1963 \$)

1964	United States (Alaska)	1964 Alaska landslides	Prince William Sound Earthquake M = 9.4	Estimated US\$280 million (1964 \$) damages
1965	China (Yunnan)	Rock slide	Not known	Four villages destroyed and 444 killed
1966	Brazil (Rio de Janeiro)	Rio de Janeiro slides, avalanches, debris/mud flows	Heavy rain	1,000 dead from landslides and floods
1967	Brazil (Serra das Araras)	Serra das Araras slides, avalanches, debris/mud flows	Heavy rain	1,700 dead from landslides and floods
1970	Peru (Ancash)	Nevados Huascaran debris avalanche	Earthquake M = 7.7	18,000 dead; town of Yungay destroyed; Ranrahirca partially destroyed
1974	Peru (Huancaavelica)	Mayunmarca rock slide-debris avalanche	Not known	Mayunmarca village destroyed, 450 killed; failure of 150-m-high landslide dam caused major downstream flooding
1980	United States (Washington)	Mount St. Helens slide-debris avalanche	Eruption of Mount St. Helens	Only 5-10 killed, but major destruction of homes, highways, etc.; major debris flow; deaths low because of evacuation
1983	United States (Utah)	Thistle debris slide	Snowmelt & heavy rain	Major railroad and highways destroyed; Spanish Fork flooding town of Thistle dammed; no deaths
1983	China (Gansu)	Saleshan landslide	Not known	237 dead; four villages buried; two reservoirs filled
1985	Colombia (Tolima)	Nevado del Ruiz debris flows	Eruption of Nevado del Ruiz	Four towns and villages destroyed; flow in valley of Lagunillas River killed more than 20,000 in city of Armero.
1986	Papua, New Guinea (East New Britain)	Bairaman Rock slide-debris avalanche	Bairaman earthquake M = 7.1	Village of Bairaman destroyed by debris flow from breached landslide dam; evacuation prevented casualties; huge effect on local landscape
1987	Ecuador (Napó)	Reventador landslides	Reventador earthquakes M = 6.1 and 6.9	1,000 killed; many kms of trans-Ecuadorian oil pipeline and highway destroyed; total losses: US\$ 1 billion (1987 \$)
1994	Colombia (Cauca)	Paez landslides	Paez	Several villages partially destroyed

			earthquake, M = 6.4	by landslides; 271 dead; 1,700 missing; 158 injured; 12,000 displaced.
1998	Honduras, Guatemala, Nicaragua, Salvador	El Salvador	Hurricane Mitch flooding Landslides debris-flows	Hurricane Mitch Around 10,000 people killed in the flooding and landslides, which occurred throughout the region. Casitas volcano in Nicaragua experienced large debris flows. Impossible to differentiate deaths from landslides from deaths due to flooding.
1999	Venezuela (Vargas)		Vargas tragedy	Heavy rain Caused by a heavy storm that deposited 30,000 people killed.
2004	Indonesia (Sulawesi)	(South Sulawesi)	Mt. Bawakaraeng landslide	Collapse of caldera wall of 32 casualties.
2005	United States (California)	La Conchita	Landslide	Remobilization of a previous landslide deposit 13 houses were destroyed and 23 others severely damaged, 10 confirmed fatalities.
2006	Philippines (Southern Leyte)	Southern Leyte	mudslide	Heavy rain The landslide overwhelmed the village of Guinsaunon resulting in the loss of over 1100 people, including 250 schoolchildren who were attending morning classes at the Guinsaunon School.
2007	Bangladesh (Chittagong)	Chittagong	mudslides	Illegal hillside cutting and monsoon rains Landslides in two days killed at least 123 people in the port city.
2008	Egypt (Cairo)	Cairo	landslide	Not known Rockfall from cliffs, individual boulders up to 70 tonnes, 119 people died in the rockslide.
2009	China (Taiwan)	Shiaolin	landslide	Typhoon 439-600 casualties.
2010	Uganda (Bududa District)	2010 Uganda	Landslide	Heavy rain The slides buried three villages, leaving 83 dead and more than 300 missing.
2013	India (Uttarakhand)	2013 Uttarakhand	floods	Floods More than 5,700 people were "presumed dead".
2014	Afghanistan (Badakhshan Province)	Badakhshan	mudslides	A pair of mudslides The number of deaths varying from 350 to 2,700. Around 300 houses were buried and over 14,000 were affected.
2015	Colombia (Antioquia Department)	2015 Colombian	landslide	Heavy rain At least 78 people were killed by the landslide. An additional 37 people were injured.

### **2.1.2. Decrease of resisting forces**

Apart from the increase of driving forces that are leading to slope instability, there are also factors causing the resisting force of the slope to decrease thus making it prone to failure subject to lower loads. An example of such factors is the presence of cracks. Cracks or fissures are widely present in soil slopes and can cause a significant decrease in their stability (Baker, 1981, Michalowski, 2013, Utili, 2013), as they provide preferential flow channels which increase the soil permeability and decrease the soil strength. Moreover, cracks form a part of the critical slip surface that has no shear strength and when filled with water, an additional driving force is applied on the slope. Cracks can be the result of a variety of phenomena, for instance exceedance of the ground tensile strength (Michalowski, 2013), the occurrence of differential settlements (Vanicek and Vanicek, 2008), desiccation (Konrad and Ayad, 1997, Dyer et al., 2009, Péron et al., 2009) and freezing (Hales and Roering, 2007) and are often found in cohesive soils and rock slopes. They may cause a significant decrease in the stability of a slope both in static (Michalowski, 2013, Utili, 2013, Utili, 2015, Gao et al., 2015) and seismic conditions (Utili and Abd, 2016). For this reason, the existence of cracks in slopes and their influence on its stability has been addressed before by several researchers (Spencer, 1968, Spencer, 1967). In this work, not only the intact slopes but also the stability of slopes with cracks is investigated for slopes with limited or no tensile strength.

Cracks can also be a result of weathering. Weathering is one stage of the rock cycle, which involves the processes that form the earth's surface. Weathering reduces hard rocks into soft rocks which maintain the structure of the intact rocks, but are characterised by higher void ratios and reduced bond strengths, soft rocks are transformed into granular soils generally called

residual soils (Utli, 2004). That is to say, that a common result of weathering processes, is a degradation of the mechanical properties of the material. A number of landslides happen to slopes due to weathering and the result is the progressive retrogression of the slope front and the further degradation within the weathering zone.

In this work cracks are considered in the analytical model and also weathering by assuming a decrease on the cohesion of the material until a failure is reached.

## 2.2. Methods to study slope stability

Different approaches have been developed through the years to give reliable estimations on slope stability problems. Slope stability can be approached through analytical, numerical or experimental techniques, as shown in Figure 2.1.

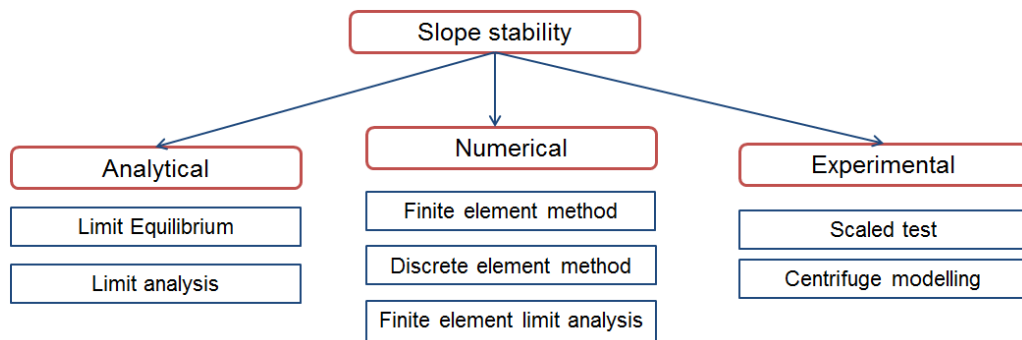


*Figure 2.1. Methods to study slope stability problems reviewed in this chapter*

All these methods are reviewed in this chapter showing that each of them has its own advantages and disadvantages and often they are used in combination to acquire the most reliable results. The most suitable method

should be carefully chosen to study each problem according to its specific needs.

### **2.3. Review of analytical and numerical methods**

In general there are many ways to study slope stability either analytical or numerically. In what follows both the analytical and the numerical methods that have been developed and used in the past years are reviewed.

The analytical methods are:

- Limit equilibrium method (LEM)
- Limit analysis (LA)

While the numerical models are:

- Finite element method (FEM)
- Discrete element method (DEM)
- Finite element limit analysis (FELA)

#### **2.3.2. Limit analysis (LA)**

Limit analysis is based on the limit theorems formulated by (Drucker et al., 1952, Drucker et al., 1950), and assumes that the geotechnical structures under investigation undergo small deformations that they are made of rigid-perfectly plastic materials obeying an associated flow rule (normality rule). Following that, limit analysis can be either an upper bound or a lower bound theorem (Drucker et al., 1952, Chen, 1975).

According to the upper bound theorem, if a set of external loads acts on a failure mechanism and the work done by them in an increment of displacement equals the work done by the internal stresses, the external loads obtained are not lower than the true collapse loads. It is noted that the external loads are not necessarily in equilibrium with the internal stresses and the

mechanism of failure is not necessarily the actual failure mechanism (Yu et al., 1998). The lower bound theorem states if an equilibrium distribution of stress covering the whole body can be found that balances a set of external loads on the stress boundary and is nowhere above the failure criterion of the material, the external loads are not higher than the true collapse loads. It is noted that in the lower bound theorem, the strain and displacements are not considered and that the state of stress is not necessarily the actual state of stress at collapse (Yu et al., 1998). By examining different possible mechanisms, or different admissible states of stress, the best (least) upper bound and the best (highest) lower bound value can be found respectively. Thus, the actual collapse load can be bracketed when upper bound and lower bound values are known. However, most of the time it is not possible to construct statically admissible stress fields needed by the lower bound theorem and the kinematic approach of limit analysis upper bound method is more popular and widely used.

The application of limit analysis has been extended to various factors causing slope instabilities, for example the influence of pore water pressure (Michalowski, 1995a, Michalowski, 1995b, Viratjandr and Michalowski, 2006), seismic action (Michalowski, 2002, Chen et al., 2012, Utili and Abd, 2016) or reinforcement (Michalowski, 1997, Michalowski, 1998, Michalowski, 2008, Abd and Utili, 2016). Some recent studies are available on the stability of slopes with cracks with limit analysis approach (Michalowski, 2013, Utili, 2013) and on the progressive retreat of slopes (Utili and Crosta, 2011a).

### **2.3.1. Limit equilibrium method (LEM)**

Limit equilibrium is the oldest method for performing stability analysis, and was first applied in a geotechnical setting by (Coulomb, 1776), dominating the field of slope stability research. Limit equilibrium methods generally

prescribe the failure mechanism in advance and assume that the stresses along a pre-assumed failure surface are governed by linear (Mohr-Coulomb) relationships between shear strength and the normal stress on the failure surface.

The first stability analyses of slopes were based on limit equilibrium methods (Espinoza et al., 1994), most of which methods are based on the method of slices, a technique that is first reported in (Fellenius, 1927), where the soil mass is discretized into vertical, horizontal or inclined slices., while others on wedge methods. The most used stability analyses of slopes are based on the conventional limit equilibrium methods (Janbu, 1954, Janbu, 1975, Bishop, 1955, Morgenstern and Price, 1965, Spencer, 1967, Sarma, 1979). Most limit equilibrium methods fulfil both moment and force equilibrium, while there are also the 'simplified methods' that fulfil only one. General two-dimensional limit equilibrium formulation was extended by development of a generalized model for three-dimensional analysis (Chen et al., 2003, Fredlund et al., 2011). The application of the method has been employed also to evaluate the stability of slopes under seismic effect by (Sarma, 1975) employing the pseudo-static approach, which is employed also in this research.

However, limit equilibrium analyses present several shortcomings (Duncan, 1996) one of which is the fact that the solution is neither a lower nor an upper bound of the true collapse load. Another major disadvantage is that the failure surface needs to be assumed in advance, with poor choices giving poor estimates of the failure load (Sloan, 2013). Moreover, the weakness with limit equilibrium methods, when it comes to studying slopes with more complicated geometry, e.g. existence of cracks, is that they are not rigorous



methods and are limited in their capacity of analysis, since they usually require the user to assume a crack depth and location in the slope.

### **2.3.3. Finite elements method (FEM)**

The use of numerical methods such as finite element method (Zheng et al., 2005, Potts et al., 2001, Huang and Jia, 2009) and material point method (Yerro et al., 2015) to provide approximate solutions to the slope stability problem is also increased in the latest decades. There are also plenty of numerical studies, using finite element method (Smith and Hobbs, 1974, Duncan, 1996, Griffiths and Lane, 1999) and discrete element method (Utili and Crosta, 2011a, Camones et al., 2013) to analyse slope stability. Many researchers (Cheng et al., 2007, Dawson et al., 2000, Chang and Huang, 2005) have tried to approach slope stability analysis by using the strength reduction technique. Unlike limit equilibrium method, no assumptions need to be made about the location or shape of the failure surface or lateral forces on the sides of the slices and their directions. The critical failure mechanism in a complicated model may assume any shape. The factor of safety in case of slope stability analysis by strength reduction method may be defined as the ratio of the resisting shear strength of the material to the driving shear stress developed along the failure plane.

One of the main disadvantages of FEM in the analysis of slope stability is that results depend on which indicator of slope failure is selected and since there is no universally accepted slope failure indicator users can rely on their experience and intuition to interpret FEM results. Moreover, as in every FEM analysis, mesh density, number of load steps, numerical integration scheme, tolerances used to check convergence of the global equilibrium iterations and the type of element employed in the model (Sloan, 2013) can influence and

change the obtained results. For these reasons, the results obtained from FEM analysis should be used together with some other techniques.

#### **2.3.4. Discrete element method (DEM)**

The Discrete Element Method was firstly used by (Cleary and Campbell, 1993) to simulate granular flows and since then it has been employed (Utili and Crosta, 2011b, Camones et al., 2013, Utili et al., 2015) to study slope stability and more recently also for 3D analyses of the stability of rock slopes (Boon et al., 2014) which has been made possible by computational advances in the DEM contact detection algorithms to deal with polyhedral blocks (Boon et al., 2012, Boon et al., 2013) and new algorithms for rock slicing (Boon et al., 2015). It has also become a complementary research method to laboratory experiments, revealing the fundamental mechanical characteristics of landslides (Staron and Hinch, 2007, Lacaze et al., 2008). However, in cases of rather uniform slopes subject to a few cracks, such a numerical approach is not justified. Numerical methods struggle to deal with the presence of cracks in the slope, because of the discontinuities introduced both in the static and kinematic fields by the presence of cracks.

#### **2.3.5. Finite limit analysis method (FELA)**

The finite element limit analysis (FELA) can be used to compute the upper or lower bound plastic collapse load. The founder of the finite element lower bound analysis is (Lysmer, 1970), while (Sloan, 1988) and (Makrodimopoulos and Martin, 2006) have then extended the theory to include non-linear yield surfaces, including also more efficient optimisation processes.

As for the finite element upper bound analysis, (Bottero et al., 1980, Sloan and Kleeman, 1995, Lyamin and Sloan, 2002) have combined constant

strain elements with kinematically admissible discontinuities in the displacement field, which help to compensate for the low order of the elements themselves. Moreover, second order cone programming is employed by (Makrodimopoulos and Martin, 2007) to increase the efficiency of the optimization process in FELA.

Although with the rise of computer capabilities many complex behaviours and interactions such as existence of cracks or presence of water can be modelled, FELA still faces the same disadvantages (mesh dependency, element types, etc.) as those in traditional FEM.

### **2.3.6. Choice of the analytical method**

As it is obvious from the studies that were described above, there are many different ways of modelling a slope and study the mechanism of a slope's failure due to various factors. Although many researches have modelled slope stability under various conditions (Yu et al., 1998, Fourie, 1996, Le Cossec et al., 2011), the evolution of a slope subject to successive failures and the deformation response of a slope subject to weathering are not yet thoroughly clarified.

Some of the methods (LEM, FEM, LA, FELA) introduced in the previous sections are traditionally adopted in slope stability assessment. As summarized in (Sloan, 2013), the properties of each technique are compared in Table 2.2. It is obvious that no single method can outperform the others and they all have their strong points and drawbacks; to this end, the choice of which method will has to be determined on a case by case basis.

In this thesis, a sequence of slope failures for initially planar slope profiles is systematically explored through an optimization technique. Thousands slope stability analyses have to be executed in order to calculate

the most critical failure mechanisms for intact slopes, slopes with cracks, water presence and under seismic action. This makes the numerical methods less favourable, due to the calculation time that they would require. Moreover, the new profile is always a result of the failure mechanism of the previous landslide which would complicate the numerical model even more. Moreover, regarding the analytical solutions and although the LEM is more widely used, it is known that when it comes to studying slopes with more complicated geometry, it is less efficient (Fredlund, 1984).

*Table 2.2. Properties of traditional methods used for geotechnical stability analysis (Sloan, 2013)*

<b>Property</b>	<b>LEM</b>	<b>Upper Bound LA</b>	<b>Lower Bound LA</b>	<b>FEM</b>
Assumed failure mechanism?	Yes	Yes	-	No
Equilibrium satisfied everywhere?	No (in slices)	-	Yes	No (nodes only)
Flow rule satisfied everywhere?	No	Yes	-	No (integration points only)
Complex loading and boundary conditions possible?	No	Yes	Yes	Yes
Complex soil models possible?	No	No	No	Yes
Coupled analysis possible?	No	No	No	Yes
Error estimate?	No	Yes (with lower bound)	Yes (with upper bound)	No

To this end, the kinematic approach of limit analysis is a suitable candidate as it is more rigorous and simple method and able to cope with some issues, such as the presence of cracks, water pressure and seismic

actions. Moreover, the limit analysis theory has already been used to study the influence of cracks (Utili, 2013, Michalowski, 2013), seismic action (Chang et al., 1984, Utili and Abd, 2016) and presence of water (Michalowski, 1995a, Viratjandr and Michalowski, 2006) on slope stability, but more importantly it has been used to study the evolution of slope subject to successive failures due to weathering (Utili and Crosta, 2011a).

In this thesis a simple semi-analytical model is presented based on the explicit consideration of all discrete failure events (landslides) leading to significant modifications of the morphology of a slope. The model, derived under the framework of limit analysis assuming plane strain conditions, provides a tool for the assessment of whether manufacts and/or infrastructures located on a slope subject to various natural degradation phenomena will be affected by the occurrence of failures. Most of the models developed so far, assume that the normal and shear stresses along the slip surface comply the Mohr-Coulomb yield criterion, which is the most used criterion for slope stability problems in cohesive soils and is also used in this model. The pseudo-static method is employed to investigate the stability of slopes subject to seismic actions and the pore pressure coefficient  $r_u$  to account for the presence of water, while weathering is taken into consideration by assuming that cohesion reduces in time.

## **2.4. Review of physical modelling studies**

Physical modelling plays a fundamental role in the development of the understanding of the triggering mechanisms of landslides and has been used through the years to simulate the behaviour of slopes subject to many factors, in addition it is also performed in order to validate theoretical and empirical hypotheses (Wood, 2003).

Many researchers investigating the triggering mechanism of slope failure have approached the problem through experimental procedures. In each case, different techniques were applied to initiate the failure, while a number of different monitoring devices were used in order to record soil characteristics and the behaviour of the slope during the tests. Many kinds of sensors were also vastly used to record the changes in the characteristics of the soil (moisture content, pore pressure, temperature etc.) and digital cameras to record the displacements and the changes in the slope front. When investigating the influence of rainfall on slope stability, the results of most of these studies suggest that measurements of the changes of moisture content can be a factor to predict the slope's movement, while the initiation of the slopes failure is mainly caused with a decrease of the cohesion of the soil, thus making the cohesion the most critical property of the soil to measure, when it comes to slope stability.

The experimental models simulating slope stability issues can generally be divided in three categories:

- Scaled model tests
- Centrifuge tests

Many of the studies reviewed here are used to validate analytical models or numerical analyses.

#### **2.4.1. Scaled model tests**

Scaled model tests are an efficient method to study slope stability as they can be performed in well controlled conditions and simulate failure initiation factors and failure process. When performing a scaled model test, the model and the prototype should be related by satisfying geometric similarity, for example the scaling factor of length between the prototype and the model

should be chosen and the materials used in the real slope and the slope model can have the same unit weight (Roscoe, 1968). Different geological conditions, soil materials and triggering factors have been considered as variables to test the stability of scaled slope models in the past.

Most of the laboratory experiments require large slope models (Moriwaki et al., 2004, Jia et al., 2009, Iverson et al., 1997, Zhang et al., 2005) to realistically simulate slopes and clarify the triggering factors and failure processes of landslides. The large scale experiments provide insight into failure mechanisms and failure mode and the scale effects that occur because of the differences in stress level between the model slopes and the natural slopes are less when compared to those of smaller scale models. However, the costs involved in the slope model preparation and instrumentation of such scale as well as operational costs are prohibitively high. Field experiments demand continuous monitoring of the characteristics of the slope and soil and need time and are cost intensive; therefore not so many examples can be found in the literature.

Smaller model test is also an important approach, in order to investigate the behaviour of a slope. Despite the limitation of scaled physical models under 1-g conditions, where the stress levels in the models are smaller than in the real slope, leading to different soil properties and loading condition, they are widely being used to give a first approximation of the failure conditions. In the case of rainfall induced slope failures, model test also provides the opportunity to observe the processes of infiltration, the progression of the water front, the deformation of the slope and finally the occurrence of a failure (Wang and Sassa, 2001, Chen et al., 2012, Okura et al., 2002, Huang et al., 2008, Orense, 2004, Tohari et al., 2007, Hu et al., 2005). A vibrating sand box has also been used in the study of (Katz and

Aharonov, 2006) to induce cracks in soils and investigate the instability of heterogeneous slopes.

#### **2.4.2. Centrifuge tests**

Concern over stress level differences has led to the use of centrifuge model tests where the stress conditions can be scaled. The centrifuge modelling technique was proposed by (Bucky, 1931) and has later found applications in the study of the behaviour of geological structures. The principle, when performing centrifuge tests on slope stability and in order to preserve the stress strain behaviour of soil, is to use a reduced-scale model to simulate the full-scale slope with dimensions  $n$  times smaller and under an acceleration  $n$  times the gravity (Taylor, 1995). More information on centrifuge scaling laws can be found in (Wood, 2003, Schofield, 1978).

Although there many limitations in modelling which in many cases are difficult to overcome, centrifuge modelling is widely used especially to validate other analytical and numerical models. Centrifuge modelling has often been used to investigate the behaviour of slopes under certain conditions. There are several centrifuge studies on slope instability subject to rainfall (Take et al., 2004, Wang et al., 2010, Askarinejad et al., 2012, Ling et al., 2009, Xu et al., 2005, Kimura et al., 1991), others have even include the influence of cracks (Zhang et al., 2011, Zhang et al., 2012). The use of the centrifuge technique has also been used to study the performance of geo-synthetic reinforced slopes (Zornberg et al., 1998, Bolton and Pang, 1982).

#### **2.4.3. Choice of small scale tests**

From the short review in this chapter it was shown that all the types of physical modelling have been used in the past by researchers to study different triggering processes on slope stability and also the failure



mechanism. For each case the method should be chosen carefully, based on the problem that needs to be modelled and the available means to carry out the experiments.

Although different aspects of slope instability problems have been modelled through the years, no example exists in the literature for experimental modelling of successive failures. In this work the evolution of a slope due to successive failure is modelled with triggering factor being the infiltration of water.

For this research, slopes of different geometries and under different rainfall intensities had to be tested, resulting in a big number of tests that needed to be carried out. This made the use of the large scale test impossible due to the high cost that it would require. Moreover, the challenges of modelling rainfall (e.g. size of rain drops) and also capturing successive failures in a centrifuge are almost prohibitive. For this reason, the small scale test was chosen to study the evolution of slopes subject to successive failure. The slope models used in this research are rather small (dimensions: 15.00cm height, 12.00cm width and 35.00cm length) making it possible to produce a numerous amount of homogeneous slope models and to install proper instrumentation to observe soil behaviour prior, during and after failure.

Some preliminary tests have been carried out at the Department of Environmental Sciences and Territory of Bicocca University in Milan and a larger experimental apparatus was built in the Geotechnical laboratory in the University of Warwick in Coventry to carry out the main experiments. Scaled slope models were constructed and then by applying different rainfall intensities on the material of the slope, the evolution of the slope subject to successive failures was simulated. The water content and the suction of the soil were recorded through sensors buried inside the slope model and

connected to data loggers and also the behaviour of the slope, the changes of the slope front and the propagation of the material were recorded by high resolution cameras.

## Chapter 3 : Analytical study

---

In this chapter, the development of the semi analytical model on the evolution of intact slopes and slopes with fissures is illustrated. A model for the assessment of the stability of homogeneous slopes obeying the linear Mohr-Coulomb criterion subjected to weathering, presence of cracks, seismic action and water pressure is presented, based on the existing framework on the stability of slopes and slopes with fissures (Chen, 1975, Uti, 2013, Michalowski, 2013) as well as on the model for the static case to study the evolution of initially intact slopes (Uti and Crosta, 2011a).

When cracks are present in the failure mechanisms of a slope they can cause changes in their evolution, compared to the intact case. Crack formation is also an important parameter which can lead to different stability numbers and geometries. In this chapter, a model based on the kinematic approach of limit analysis to predict evolution of slopes with cracks has been proposed. The location and the depth of the crack as well as the most critical failure mechanism for every failure were calculated through an optimisation procedure. Solutions were provided for three different types of problem; determination of the evolution of slopes with pre-existing cracks, slopes with no tensile strength (tension cut-off) where crack forming requires work to open and slopes with soil tensile strength limited to half of that described by the

classical Mohr-Coulomb yield condition for dry slopes and for slopes with presence of water. With this model, it is possible to relate the evolution of natural slopes with the presence of cracks by a sequence of rotational sliding block failures to the degradation of material strength properties. It can be concluded that with the proposed model it is possible, in principle, to predict the evolution by successive failures of any cliff made, knowing the strength degradation over time.

The presence of cracks, the inclusion of the seismic effect and pore pressure lead to a change of the analytical expression of the energy balance equation (the balance between external work and dissipated energy) and as a consequence of the functions whose minimum provides the solutions in terms of failure mechanisms and associated values of soil strength. In this model, the geometry assumed by the slope profile after each landslide event is a function of the previous profile shape. As for the seismic action, the pseudo-static approach is adopted and constant seismic accelerations are applied on the slope, while for the presence of water the  $r_u$  coefficient is used to account for the pore pressure.

This thesis presents a set of analytical solutions that were obtained considering a succession of discrete failure events (landslides) due to strength degradation, seismic action, formation of tension cracks and seepage; that progressively alters the slope morphology over time. A parametric analysis is run to assess the effect of each factor on cliff evolution. Results for a range of  $\phi$  values of engineering interest are presented in the form of dimensionless ready-to-use stability charts for the benefit of practitioners. The strength degradation is assumed to be uniform within the slope and therefore the decrease in cohesion will be considered as homogeneous as well. This assumption is not realistic as the weathering is generally not uniform within the

slope, but has greater effects on the material exposed to the surface, but it offers a rough estimation on the evolution of slope.

### 3.1. Limit analysis upper bound method

In order to develop an analytical solution describing the morphological evolution of natural cliffs with limited tensile strength subject to progressive retreat induced by ground strength degradation, for instance weathering, for static and seismic scenarios and various hydrological conditions, for slopes with uniform cohesion  $c$  and internal friction angle  $\varphi$ , the kinematic approach of limit analysis upper bound method has been adopted. The limit analysis upper bound method (Chen, 1975) and the pseudo-static approach (Terzaghi, 1950) are used to derive the analytical law describing the evolution of homogeneous  $c$ ,  $\varphi$  slopes subject to strength degradation, seismic action, formation of tension cracks and various seepage conditions. Perhaps the greatest limitation of the analytical solution presented resides in assuming the slopes homogeneous. In fact, natural heterogeneity, layering, different material properties of the layers etc. tend to produce geomorphic features unique to each particular slope that are not captured by the solution here presented. On the other hand, such a strong assumption allows for the derivation of a comprehensive analytical solution that can be used to achieve a first rough estimation of the past or future evolution of a slope knowing a limited amount of information and to explore the relative influence on slope evolution of the various physical phenomenon considered in general terms.

As described by (Chen, 1975), an upper-bound solution can be obtained by considering a rotational discontinuity, as shown in Figure 3.1. A fictitious homogeneous slope, with zero pore pressure and constant unit weight  $\gamma$  is presented, with  $H$  and  $\beta$  being the height and the inclination of the

slope respectively. Basic geometrical elements of the slope under study are illustrated in Figure 3.1. For the sake of simplicity, all the calculations presented below refer to the case of a horizontal slope crest,  $\alpha=0$ . However, the solution can be straightforwardly extended to the case of a non-horizontal upper slope; as reported in (Utili, 2013, Utili and Crosta, 2011a).

The ground strength is here characterised by the Mohr-Coulomb failure criterion therefore only three parameters are needed to describe its properties (unit weight, internal friction angle and cohesion). The limit analysis upper bound method was applied to determine each discrete landslide event occurring over time for successive destabilization and complete removal of the failed mass after each event (Utili and Crosta, 2011a). The material accumulated at the slope toe cannot be taken into account in our model since the limit analysis method is not able to give any information about the final geometry of the debris accumulated after each landslide. Therefore, it is assumed that the debris accumulating at the slope toe is removed by atmospheric agents or fluvial or marine erosion or it is simply deposited far from the slope toe, before a new landslide develops. This condition is known in the literature as a strong erosion condition and is typical of weathering-limited processes (Hutchinson, 1975).

The following geometrical relationships will be employed in the derivation of the semi-analytical solution:

$$r_{y1} = r_{x1} \exp[\tan \varphi (y_1 - x_1)] \quad [3.1]$$

$$r_{z1} = r_{x1} \exp[\tan \varphi (z_1 - x_1)] \quad [3.2]$$

$$r_{y2} = r_{x2} \exp[\tan \varphi (y_2 - x_2)] \quad [3.3]$$

$$r_{z2} = r_{x2} \exp[\tan \varphi (z_2 - x_2)] \quad [3.4]$$

$$H = r_x \{ \exp[\tan \varphi(y-x)] \sin y_1 - \sin x_1 \} \quad [3.5]$$

$$L = r_{x1} \left\{ \frac{\sin(x_1 + \beta)}{\sin \beta} - \exp[\tan \varphi(y_1 - x_1)] \frac{\sin(y_1 + \beta)}{\sin \beta} \right\} \quad [3.6]$$

$$L_1 = r_{x1} \cos x_1 - \cos y_1 \exp[\tan \varphi(y_1 - x_1)] \quad [3.7]$$

$$l_1 = r_{x1} \cos x_1 - \cos z_1 \exp[\tan \varphi(z_1 - x_1)] \quad [3.8]$$

$$L_2 = r_{x2} \cos x_2 - \cos y_2 \exp[\tan \varphi(y_2 - x_2)] \quad [3.9]$$

$$l_2 = r_{x2} \cos x_2 - \cos z_2 \exp[\tan \varphi(z_2 - x_2)] \quad [3.10]$$

where  $r_x$ ,  $r_y$  and  $r_z$  are the radii of the spiral at the angles  $x$ ,  $y$  and  $z$  respectively,  $L$ ,  $L_1$ ,  $l_1$ ,  $L_2$ ,  $l_2$  are the horizontal lengths (see Figure 3.1) and  $H$  is the height of the slope.

### 3.2. First failure (landslide)

The majority of analytical solutions that exist on slope stability analyses are based on the assumption that slopes are made of isotropic, homogeneous and continuous material (Chen et al., 1969, Chen, 1975), however, it has been proved that the presence of cracks can substantially reduce slope stability (Utili, 2013, Michalowski, 2013) as they form a part of the failure surface thus reducing slope resistance to failure.

In this part, detailed calculations for the upper-bound limit analysis on the first failure mechanism are illustrated, considering cracks of any possible depth and location, departing from the upper surface of the slope are illustrated, presence of water and seismic action. The weathering of the slope can cause decrease in the cohesion and the friction angle of the slope's material. In what follows, only the case of decreasing cohesion is illustrated.

The failure mechanisms assumed in this analysis are 2D single wedge rigid rotational mechanisms (see Figure 3.1). Concerning the occurrence of the first landslide and according to the failure mechanism assumed above, the region of soil EDCB rotates rigidly around point  $P_1$  with the ground lying on the right of the log-spiral DC and the vertical crack CB remaining at rest. The equation describing the logarithmic spiral line DC written in polar coordinates with reference to the spiral centre is:

$$r = r_0 \exp[\tan \varphi (\theta - \theta_0)]$$

with  $r$  being the distance of a generic point of the spiral to its centre,  $\theta$  the angle formed by  $r$  with a reference axis, and  $\theta_0$  and  $r_0$  identifying the angle and distance of a particular point of the spiral to its centre. (see Figure 3.1).

The upper bound is derived by imposing energy balance for the failing wedge EDCB:

$$\dot{W}_d + \dot{W}_{cf} = \dot{W}_{ext} \quad [3.11]$$

where  $\dot{W}_d$ ,  $\dot{W}_{cf}$  and  $\dot{W}_{ext}$  are the rate of the dissipated energy, of the energy required for a crack to open and of the external work respectively.

Energy is dissipated along the failure line BC, according to the assumed rigid rotational mechanism:

$$\begin{aligned} \dot{W}_{d1} &= \omega \gamma r_{x1}^2 f_{d1}(x_1, y_1, \varphi) \\ &= \left\{ \exp[\tan \varphi (y_1 - x_1)] \sin y_1 - \sin x_1 \right\} \frac{\exp[2 \tan \varphi (y_1 - x_1)] - 1}{2 \tan \varphi} \end{aligned} \quad [3.12]$$

where  $\omega$  is the angular velocity.

The calculations for the first failure mechanisms can be found in (Utili, 2013, Michalowski, 2013). The mechanism is defined by three variables  $x_1$ ,  $z_1$ ,  $y_1$  (Figure 3.1). Here, only the derivations for the analytical expressions for the



occurrence of the second failure mechanism are illustrated in detail, as the derivation for the analytical expressions for the first failure can be found in (Utili, 2013, Utili and Abd, 2016).

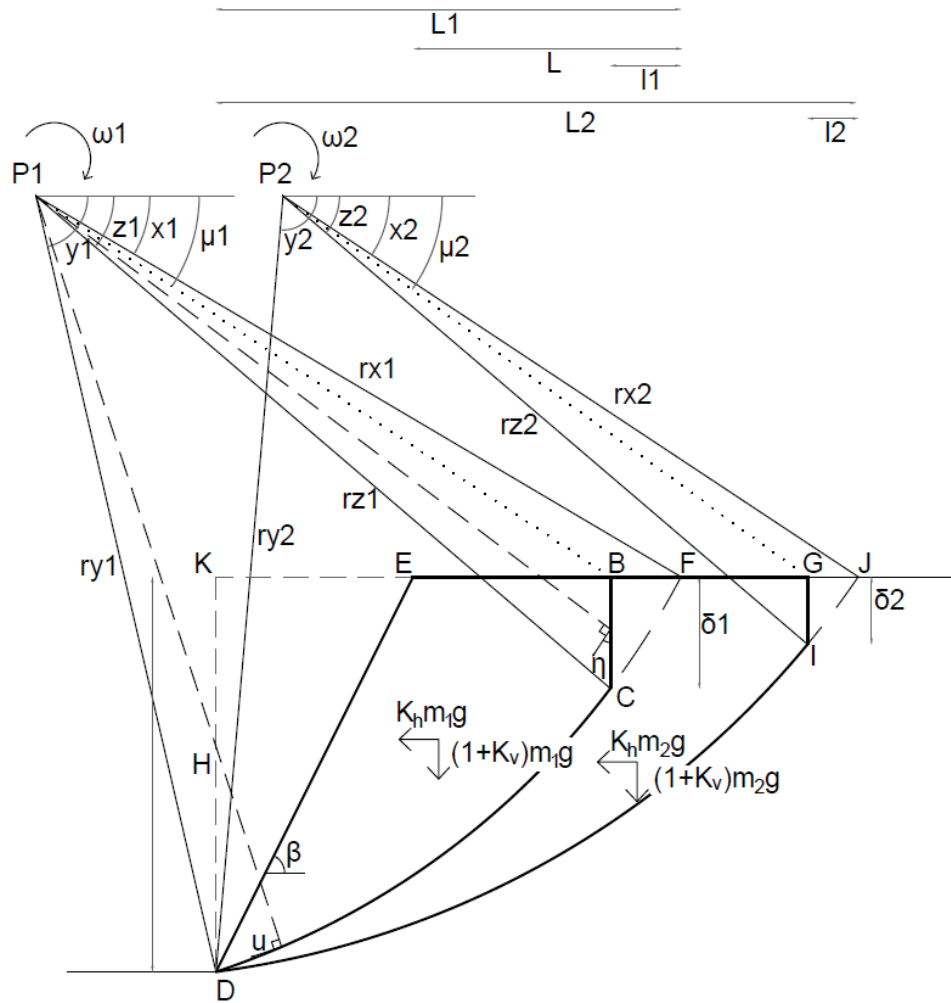


*Figure 3.1. First and second failure mechanisms: Region of soil EBCD slides away rotating around point  $P_1$  and then region of soil GIDCB rotates around point  $P_2$ .*

### 3.2.1. Tension crack

The calculation of  $\dot{W}_d$  accounting for the energy dissipated along the log-spiral segment BC is reported in (Utili, 2013). Cracks may develop from the slope face (DE) and / or from the upper part of the slope (EF) (see Figure 3.1). Here cracks are treated as no-tension non-cohesive perfectly smooth (no friction) interfaces, therefore the angle  $\eta$  between the velocity vector and the crack surface (Figure 3.1) is  $0^\circ < \eta < 180^\circ$ .

Following (Michalowski, 2013), two types of cracks can be considered: cracks existing in the slope before the formation of any failure mechanism, called pre-existing cracks by Michalowski, and cracks forming as part of the failure process due to the exceedance of the ground tensile strength, here called tension cracks, that take place contemporaneously to the formation of localized deformations leading to the failure of the slope.

A pre-existing crack may have been formed in the past by tensile stresses that are no longer acting on the slope, for instance due to tectonic movements. Tension cracks instead indicate cracks that are generated by tensile stresses exceeding the current ground tensile strength leading to the formation of a failure mechanism (Terzaghi, 1950, Baker, 1981). Although the presence of pre-existing cracks can be easily accounted for in limit analysis (Utili, 2013), in this model only tension cracks are considered. This is because the evolution of a slope subject to material strength deterioration is ruled by the deterioration of the ground strength, and therefore of tensile strength, leading to the onset of tension cracks whereas pre-existing cracks generated in the course of the geological history of the slope formation are likely to affect the formation of the first failure mechanism only. Moreover, position and depth of pre-existing cracks need to be postulated whereas position and depth of

tension cracks can be clearly related to a physical property of the ground: its tensile strength (Baker, 1981, Michalowski, 2013).

The most critical failure mechanism is the one associated with the highest cohesion, and as it has been showed in (Utili, 2013) the most critical failure mechanism for a planar slope subject to tension cracks is the one passing through the slope toe. For this reason, only this case is considered here.

The tensile strength of a cohesive geomaterial obeying the Mohr-Coulomb failure criterion,  $f_t$  is defined by  $f_t = c/\tan\phi$ . To calculate the energy dissipated by the formation of a crack with limit analysis, Michalowski (2013) has considered limiting the Mohr Coulomb linear envelope by the stress circle of an unconfined uniaxial tensile strength test with the circle being tangent to the linear envelope (see Figure 3.2). This failure criterion is realistically non-linear in the tension zone and on the other hand lends itself to limit analysis calculations. The energy expended for the formation of a tension crack,  $\dot{D}S_{(B-C)}$  turns out to be (Michalowski, 2013):

$$\dot{W}_{cf} = r_{x1}^2 \omega \left( \frac{\sin x_1}{\tan \mu_1} \right)^2 \left( \frac{f_c^{M-C}}{2} \int_{\mu_1}^{z_1} \frac{1 - \sin \theta}{\cos^3 \theta} d\theta + \frac{f_t}{1 - \sin \phi} \int_{\mu_1}^{z_1} \frac{\sin \theta - \sin \phi}{\cos^3 \theta} d\theta \right) \quad [3.13]$$

with  $\mu_1$  being the angle made by the segment P-B with the horizontal (see Figure 3.1),  $f_c^{M-C}$  being the Mohr-Coulomb unconfined compressive strength of the ground and  $f_t$  the unconfined tensile strength as measured from laboratory experiments (see Figure 3.2). It is convenient to introduce a dimensionless coefficient,  $t$ , defined as the ratio of the unconfined tensile strength measured in laboratory experiments,  $f_t$ , over the full unconfined

tensile strength predicted by the Mohr-Coulomb criterion,  $f_t^{M-C}$  (see Figure

3.2a):

$$t = \frac{f_t}{f_t^{M-C}} \quad [3.14]$$

It is straightforward to observe that  $0 < t < 1$ . Also, both  $f_c^{M-C}$  and  $f_t^{M-C}$  are uniquely related to  $c$  and  $\phi$ :

$$f_c^{M-C} = 2c \left( \frac{\cos \phi}{1 - \sin \phi} \right) \quad [3.15]$$

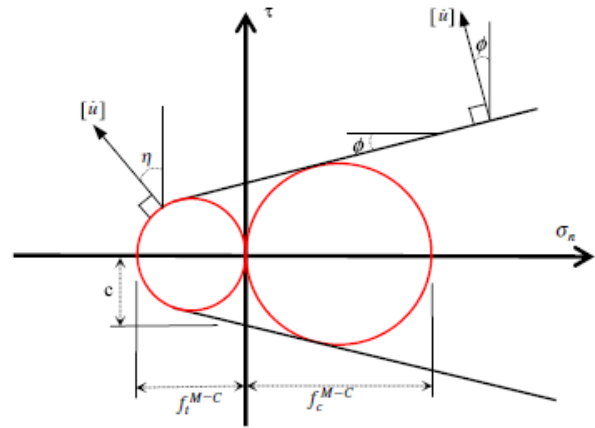
$$f_t^{M-C} = 2c \left( \frac{\cos \phi}{1 + \sin \phi} \right) \quad [3.16]$$

Now substituting equations [3.13], [3.14] and [3.15] into Eq. [3.12], the following expression is obtained:

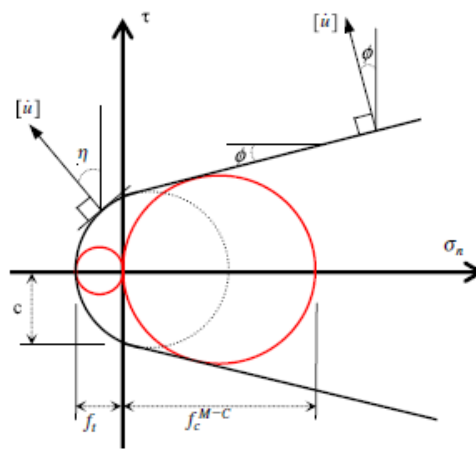
$$\begin{aligned} \dot{W}_{cf} &= c r_{x1}^2 \omega \left( \frac{\sin x_1}{\tan \mu_1} \right)^2 \left( \left( \frac{\cos \phi}{1 - \sin \phi} \right) \int_{\mu_1}^{z_1} \frac{1 - \sin \theta}{\cos^3 \theta} d\theta + \frac{2t \cos \phi}{1 - \sin^2 \phi} \int_{\mu_1}^{z_1} \frac{\sin \theta - \sin \phi}{\cos^3 \theta} d\theta \right) \\ &= \omega \gamma r_{x1}^2 f_d(x_1, z_1, \theta_1, \phi) \end{aligned} \quad [3.17]$$

Three different conditions controlling crack formation are tackled here:

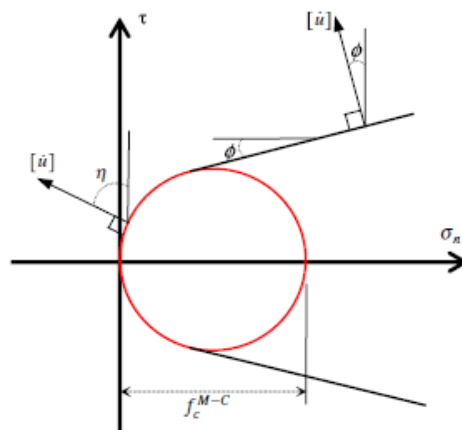
- tension cut-off ( $t=0$ )
- slopes with soil tensile strength limited to  $t=0.2$  and
- slopes with soil tensile strength limited to  $t=0.5$



(a)



(b)



(c)

Figure 3.2. Mohr-Coulomb failure criteria illustrating the failure mechanisms associated with soil of: (a) full unconfined tensile strength ( $t=1$ ). (b) limited tensile strength ( $t=0.5$ ). (c) zero tensile strength ( $t=0$ ), after (Michalowski, 2013).

### 3.2.2. Seismic action

The earthquake load is adding an extra driving force (work rate) to the work balance equation. The seismic action is accounted for by employing the so-called pseudo-static approach (Terzaghi, 1950) following the approach presented in (Chang et al., 1984, Utili and Abd, 2016). The rate of external work for the sliding wedge EBCD,  $\dot{W}_{ext}$ , is made by two contributions:

$$\dot{W}_{ext} = \dot{W}_\gamma + \dot{W}_w \quad [3.18]$$

with  $\dot{W}_\gamma$  representing the external work done by the weight of the wedge and  $\dot{W}_w$  representing the work done by the water pressure.

$\dot{W}_\gamma$  is calculated as the work of block EDF minus the work of block BCF. In turn the work of block EDF is calculated by algebraic summation of the work of blocks P<sub>1</sub>DF, P<sub>1</sub>EF and P<sub>1</sub>DE (Chen, 1975) and the work of block BCF is calculated by summation of the work of blocks P<sub>1</sub>CF, P<sub>1</sub>BF and P<sub>1</sub>CB (Utili and Nova, 2007, Utili and Crosta, 2011a, Utili, 2013). Note that here, in addition to the weight force, a horizontal pseudo-static force,  $F_{psh} = mK_h g = \gamma K_h A$ , with  $g$  being the gravitational acceleration and  $m$  the mass of the wedge, and a vertical one,  $F_{psv} = mK_v g = \gamma K_v A$ , are added to account for seismic action (Chen and Liu, 2012, Utili and Abd, 2016). The expressions of the rates of each soil block  $\dot{W}_1 \sim \dot{W}_6$  are found in Chen and Liu (2012) and Utili and Abd (2016) and here only the final expressions are provided.

Considering the region P<sub>1</sub>FD (Figure 3.1):

$$\begin{aligned}\dot{W}_1 &= \omega \gamma r_{x1}^3 \left[ (1+k_v) f_{1_v}(x_1, y_1, \varphi) + k_h f_{1_h}(x_1, y_1, \varphi) \right] \\ &= \omega \gamma r_{x1}^3 \left[ (1+k_v) \frac{\exp[3 \tan \varphi (y_1 - x_1)] (3 \tan \varphi \cos y_1 + \sin y_1) - 3 \tan \varphi \cos x_1 - \sin x_1}{3(1+9 \tan^2 \varphi)} \right. \\ &\quad \left. + k_h \frac{\exp[3 \tan \varphi (y_1 - x_1)] (3 \tan \varphi \sin y_1 - \cos y_1) - 3 \tan \varphi \sin x_1 + \cos x_1}{3(1+9 \tan^2 \varphi)} \right] \end{aligned} \quad [3.19]$$

with  $\omega$  being the rate of angular displacement of the failing wedge.

Considering the region P<sub>1</sub>FE:

$$\begin{aligned}\dot{W}_2 &= \omega \gamma r_{x1}^3 \left[ (1+k_v) f_{2_v}(x_1, y_1, \varphi) + k_h f_{2_h}(x_1, y_1, \varphi) \right] \\ &= \omega \gamma r_{x1}^3 \left[ (1+k_v) \frac{1}{6} \frac{L}{r_{x1}} (2 \cos x_1 - \frac{L}{r_{x1}}) \sin x_1 + \right. \\ &\quad \left. k_h \frac{1}{3} \frac{L}{r_{x1}} \sin^2 x_1 \right] \end{aligned} \quad [3.20]$$

Considering the region P<sub>1</sub>ED:

$$\begin{aligned}\dot{W}_3 &= \omega \gamma r_{x1}^3 \left[ (1+k_v) f_{3_v}(x_1, y_1, \varphi) + k_h f_{3_h}(x_1, y_1, \varphi) \right] \\ &= \omega \gamma r_{x1}^3 \left[ (1+k_v) \frac{1}{6} [\exp(\tan \varphi (y_1 - x_1)) \left( \sin(y_1 - x_1) - \frac{L}{r_{x1}} \sin y_1 \right) \right. \\ &\quad \left. \left( \cos x_1 - \frac{L}{r_{x1}} + [\exp(\tan \varphi (y_1 - x_1)) \cos y_1] \right) + \right. \\ &\quad \left. k_h \frac{1}{6} [\exp(\tan \varphi (y_1 - x_1)) \left( \sin(y_1 - x_1) - \frac{L}{r_{x1}} \sin y_1 \right) \right. \\ &\quad \left. (\sin x_1 + [\exp(\tan \varphi (y_1 - x_1)) \sin y_1]) \right] \end{aligned} \quad [3.21]$$

Considering the region P<sub>1</sub>FC:

$$\begin{aligned}\dot{W}_4 &= \omega \gamma r_{x1}^3 \left[ (1+k_v) f_{4_v}(x_1, z_1, \varphi) + k_h f_{4_h}(x_1, z_1, \varphi) \right] \\ &= \omega \gamma r_{x1}^3 \left[ (1+k_v) \frac{\exp[3 \tan \varphi (z_1 - x_1)] (3 \tan \varphi \cos z_1 + \sin z_1) - 3 \tan \varphi \cos x_1 - \sin x_1}{3(1+9 \tan^2 \varphi)} + \right. \\ &\quad \left. k_h \frac{\exp[3 \tan \varphi (z_1 - x_1)] (3 \tan \varphi \sin z_1 - \cos z_1) - 3 \tan \varphi \sin x_1 + \cos x_1}{3(1+9 \tan^2 \varphi)} \right] \end{aligned} \quad [3.22]$$

Considering the region P<sub>1</sub>FB:

$$\begin{aligned}\dot{W}_5^n &= \omega \gamma r_{x1}^3 \left[ (1+k_v) f_{5_v}(x_1, z_1, \varphi) + k_h f_{5_h}(x_1, z_1, \varphi) \right] \\ &= \omega \gamma r_{x1}^3 \frac{l_1}{r_{x1}} \left[ (1+k_v) \frac{1}{6} (2 \cos x_1 - \frac{l_1}{r_{x1}}) \sin x_1 + k_h \sin^2 x_1 \right] \end{aligned} \quad [3.23]$$

Finally, considering the region P<sub>1</sub>BC:

$$\begin{aligned}
\dot{W}_6 &= \omega \gamma r_{x1}^3 \left[ (1 + k_v) f_{6_v}(x_1, z_1, \varphi) + k_h f_{6_h}(x_1, z_1, \varphi) \right] \\
&= \omega \gamma r_{x1}^3 \frac{1}{3} \left[ (1 + k_v) [\exp(\tan \varphi (z_1 - x_1)) \sin z_1 - \sin x_1] \cos^2 z_1 \exp(2 \tan \varphi (z_1 - x_1)) + \right. \\
&\quad \left. k_h \frac{1}{2} [\exp(2 \tan \varphi (z_1 - x_1)) \sin^2 z_1 - \sin^2 x_1] \cos z_1 \exp(\tan \varphi (z_1 - x_1)) \right] \quad [3.24]
\end{aligned}$$

### 3.2.3. Pore pressure

To account for the influence of the pore pressure, the work of pore-water pressure on the deformation of the soil along the failure surface, and the work of the water pressure on the crack surface, as documented in (Viratjandr and Michalowski, 2006, Michalowski, 2013, Michalowski, 1995a), has to be included in the energy balance equation. Pore-water pressure,  $u$ , is accounted for in the model using the coefficient  $r_u$  (Bishop and Morgenstern, 1960), as:

$$r_u = \frac{u}{\gamma h} \quad [3.25]$$

with  $u$  being the total pore pressure in the considered point of the failure line,  $\gamma_{\text{sat}}$  the ground bulk unit weight and  $h$  the depth of the point considered from the ground surface. The assumption of uniform  $r_u$  is a strong one (Barnes, 2010), since the use of the  $r_u$  coefficients for calculating the pore water pressures in a slope treats the groundwater flow in a rather idealized manner. Therefore, the calculated pressures are not necessarily as accurate as those determined from more sophisticated analyses. However the method provides a practical and convenient method of assessing the stability of multiple slopes, is consistent with the level of accuracy of the other slope stability parameters, and it is still commonly used in slope stability analyses in engineering practice (Barnes, 2010).



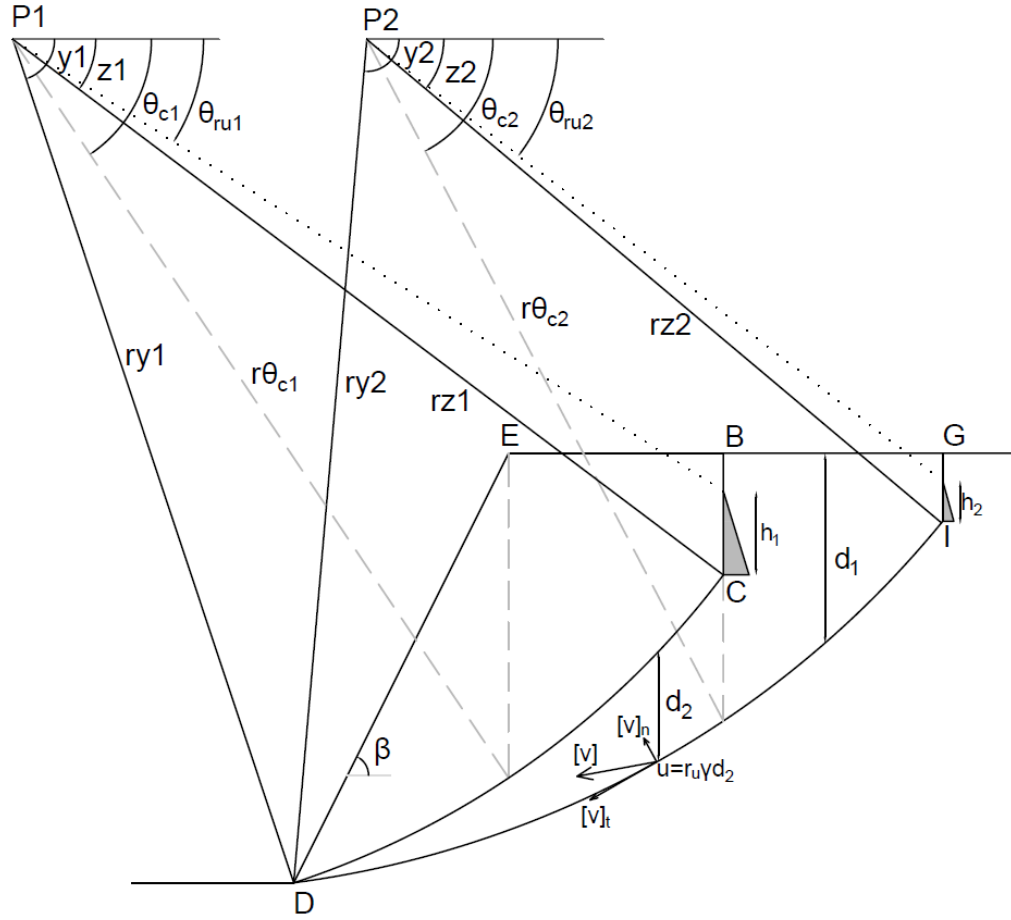


Figure 3.3. Presence of pore pressure in the calculation of the most critical failure mechanism.

The work of the water along the crack BC and along the log-spiral part CD can be calculated as an integral over the whole surface (Michalowski, 1995a, Michalowski, 2013) by:

$$W_w = W_{BC} + W_{CD}$$

$$\dot{W}_w = \dot{W}_{BC} + \dot{W}_{CD} = \int_{\theta_{ru1}}^{z1} u[v]_n dS_{BC} + \int_{z1}^{y1} u[v]_n dS_{CD} \quad [3.26]$$

where  $[v]_n$  is the normal component of the boundary velocity (Figure 3.3) and

$$\tan \theta_{ru1} = \frac{r_z \sin z_1 - h_1}{r_z \cos z_1} = \frac{\exp(\tan \varphi(z_1 - x_1)) \sin z_1 - \frac{r_u \gamma}{\gamma_w} (\exp(\tan \varphi(z_1 - x_1)) \sin z_1 - \sin x_1)}{\exp(\tan \varphi(z_1 - x_1)) \cos z_1}$$

The detailed equations for the calculation of the work of water along the log-spiral part CD and the crack BC for the first failure are well documented and can be found in (Michalowski, 1995a).

### 3.2.4. Calculation of the first failure mechanism

Substituting Eqs [3.17], [3.18] and [3.26] into Eq [3.11], the final equation to calculate the stability factor,  $N=\gamma H/c$ , is obtained:

$$\begin{aligned} \frac{\gamma H}{c} &= g(x_1, y_1, z_1, \varphi, \beta, K_h, \lambda, r_u) \\ &= \frac{f_{d1} + f_{cf}}{(1 + \lambda K_h)(f_{1_v} - f_{2_v} - f_{3_v} - f_{4_v} + f_{5_v} + f_{6_v}) + K_h(f_{1_h} - f_{2_h} - f_{3_h} - f_{4_h} + f_{5_h} + f_{6_h}) + r_u f_w} \end{aligned} \quad [3.27]$$

with  $\lambda=K_v/K_h$  (consistently with Figure 3.1, the + sign indicates vertical downward acceleration, whereas the – sign indicates vertical upward acceleration). The global minimum of  $g(x_1, y_1, z_1, \phi, \beta, K_h, \lambda)$  over the three geometrical variables  $x_1, y_1, z_1$  provides the least (best) upper bound on the stability factor for the case that has been considered. The static case is a particular case obtained setting  $K_h=K_v=0$ .

In Figure 3.4 the influence of the seismic action on the crack depth is investigated for a slope with friction angle  $\varphi=30^\circ$  for the first failure and for different kinds of crack formation. It can be seen, that the lower the tensile strength, the lower the depth of the crack that will lead the slope to failure. For slope inclinations higher than  $72^\circ$  and for the case of tension cut off when  $K_h=0.2$ , a translational failure mechanism takes place, for this reason no curve is shown in the graph.

Unlike the case of intact slopes, failure mechanisms may in principle daylight on the slope face above the slope toe; however in (Utili and Abd, 2016) no potential mechanism passing above the slope toe turned out to be the most critical, therefore no potential failure mechanisms passing above the toe were considered in this analysis.

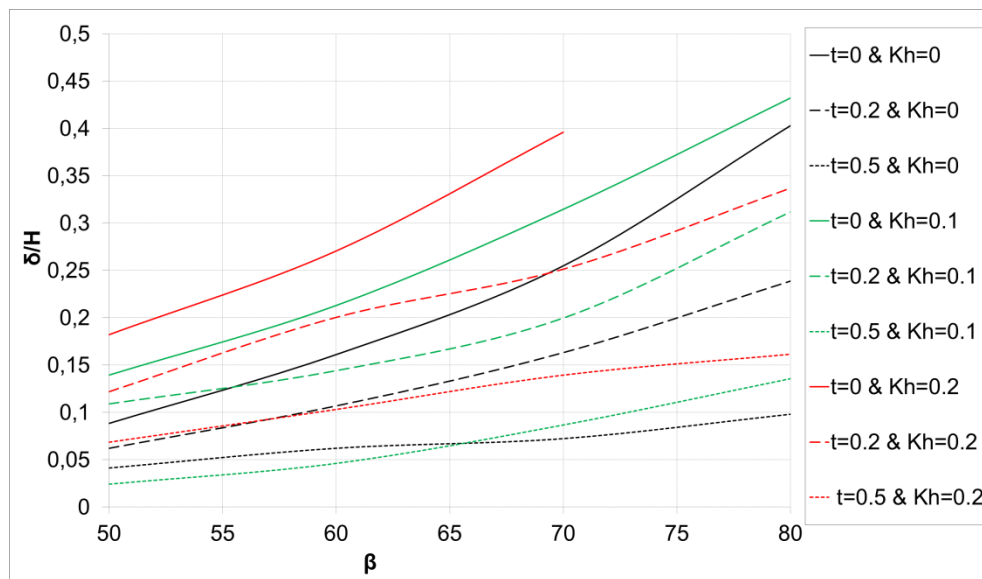


Figure 3.4. Crack depth against slope inclination for friction angle  $\phi=30^\circ$  for the first failure and for different kind of crack formation for seismic coefficient  $K_h=0$ ,  $K_h=0.1$  and  $K_h=0.2$  (for slope inclinations higher that  $72^\circ$  and for the case of tension cut off when  $K_h=0.2$ , a translational failure mechanism takes place - no curve).

### 3.3. Second and successive failures (landslides)

The analytical expressions for the second failure also apply to every successive failure that will take place. After the region EBCD (Figure 3.1) has slipped away and due to further weathering, at some point a second landslide will occur. The double logarithm spiral shaped area GIDCB will rigidly rotate

around the center of rotation  $P_2$ , yet undefined, with the material below the logarithmic spiral ID and right of the vertical crack GI remaining at rest. The mechanism is now defined by six variables  $x_1, z_1, y_1, x_2, z_2, y_2$ , where  $x_1, y_1, z_1$  are the angles defining the first log spiral failure line (i.e., the current slope profile produced by the previous failure), that will be called 'old' landslide and  $x_2, y_2, z_2$  are the angles defining the second log spiral failure line (see Figure 3.1), that will be called 'new' landslide.

Two contributions constitute the rate of the external work for the sliding wedge GIDCB; the work done by the weight of the wedge that slides away  $\dot{W}_\gamma$  and the work done by the water pressure  $\dot{W}_w$ . The weight of the wedge that slides away  $\dot{W}_\gamma$  is calculated this time as the work by block JDE minus the work of blocks BCDE and JIG. More specifically, the rate of the work of the block JDK is given by three contributors as  $\dot{W}_1^n - \dot{W}_2^n - \dot{W}_3^n$ , where  $\dot{W}_1^n, \dot{W}_2^n$  and  $\dot{W}_3^n$  are the rates of work done by regions  $P_2JD, P_2JK$  and  $P_2KD$  respectively. The rate of the work of the region BCDE is given by six contributors as  $\dot{W}_1^o - \dot{W}_2^o - \dot{W}_3^o - (\dot{W}_4^o - \dot{W}_5^o - \dot{W}_6^o)$ , where  $\dot{W}_1^o$  to  $\dot{W}_6^o$  are the rates of work done by regions  $P_1FD, P_1FK, P_1KD, P_1FC, P_1FB$  and  $P_1BC$  respectively. The rate of the region JIG is also given by three contributors as  $\dot{W}_4^n - \dot{W}_5^n - \dot{W}_6^n$ , where  $\dot{W}_4^n, \dot{W}_5^n$  and  $\dot{W}_6^n$  are the works done by regions  $P_2JI, P_2JG$  and  $P_2GI$  respectively. Therefore, the rate of external work due to the weight of the soil  $\dot{W}_\gamma$  is a total of twelve different contributors, given by the following equation:

$$\dot{W}_{ext} = \dot{W}_1^n - \dot{W}_2^n - \dot{W}_3^n - \dot{W}_4^n + \dot{W}_5^n + \dot{W}_6^n - \dot{W}_1^o + \dot{W}_2^o + \dot{W}_3^o + \dot{W}_4^o - \dot{W}_5^o - \dot{W}_6^o \quad [3.28]$$

with  $n$  and  $o$  referring to the new and the old landslide respectively.

The calculations of the expressions for  $\dot{W}_1^n, \dot{W}_2^n, \dot{W}_3^n$  etc. for all the aforementioned blocks and for  $\dot{W}_w$  are provided in detail. Note that the second

(and every successive) mechanism could pass through any point since the current slope profile is no longer straight, as presented in Figure 3.5. Therefore, failure mechanisms daylighting at any point of the slope profile left after the first failure has occurred have to be considered. To this end, the slope profile was divided into a discrete number of points ( $n$ ) and each point has been assumed as the toe of a sub-slope whose height,  $h_i$ , is smaller than the overall height  $H$  (see Figure 3.5). The most critical mechanism among all the possible mechanisms has to be found. The critical cohesion values,  $c_i$ , and angles,  $x_i$ ,  $y_i$  and  $z_i$ , associated with the critical failure mechanism, were determined for all  $n$  sub-slopes of different height,  $h_i$ , with the parameter  $y_i$  assuming a different value associated with each sub-slopes analysed. The most critical failure mechanism among the  $n$  potential mechanisms is the one with the highest cohesion value. As long as a sufficiently large value of  $n$  is chosen,  $n$  does not affect the obtained result.

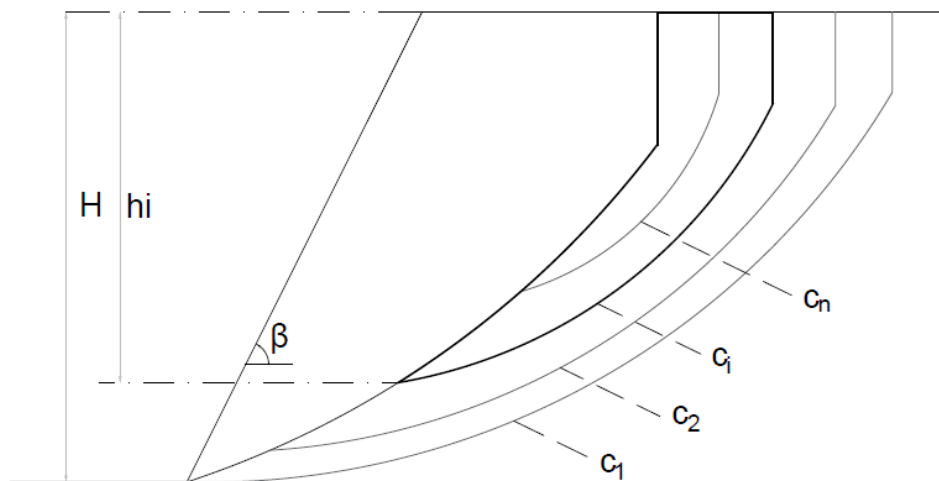


Figure 3.5. Potential failure mechanisms for the second failure, relative to different mechanisms considered (for different critical heights  $h_i$ ).

### 3.3.1. Weathering simulated by cohesion decrease

By applying the procedure described above, it is possible to determine as many failure mechanisms as needed to follow the slope evolution until full degradation of the soil strength has taken place. Strength degradation has been considered to end at  $c=0$ , while  $\varphi=\varphi_{\text{const}}$ . Here, the friction angle is assumed to remain constant in time and only cohesion decreases, since experimental evidence (failure envelopes obtained from tests on a granitic rock subject to various degrees of weathering) from the weathering of rocks and cemented soils as illustrated in Figure 3.6, have shown that weathering causes mainly a decrease in the cohesion and to a much lesser extend to the friction angle of the material (Kimmance, 1998). However, extension of the model to account for a decrease of both cohesion and friction angle is straightforward. The case of both  $c$  and  $\varphi$  decreasing for geomaterials with infinite tensile strength is reported in (Utili and Crosta, 2011a).

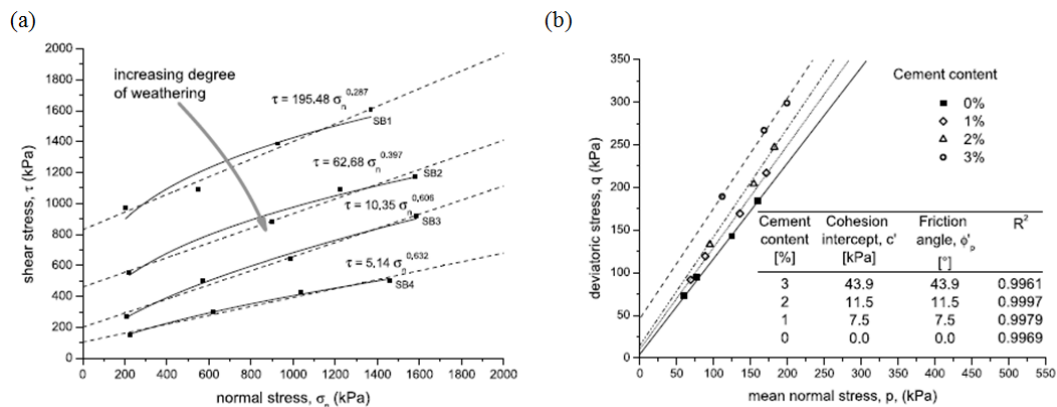


Figure 3.6. (a) Weathering of granite, after (Kimmance, 1988) , (b) failure loci of cemented sands for different cement contents, after (Wang and Leung, 2008)

Computations have been carried out using Matlab for a wide range of parameters (friction angle  $\varphi$  and initial slope inclination  $\beta$  for intact slopes ( $t=1$ ), slopes with soil tensile strength limited to  $t=0.2$  and  $t=0.5$  of that described by the classical Mohr–Coulomb yield condition and slopes with no tensile strength,  $t=0$  (tension cut-off) and under different seismic and groundwater scenarios.

### 3.3.2. Effect of seismic acceleration

In the following, the log spiral of the current slope profile and the log spiral of the failure line of the second (and each subsequent) mechanism are denoted by the superscripts o (old) and n (new), respectively. The equations for the static case and seismic case with the inclusion of crack and pore water pressure are reported, based on the analysis for the intact case (Utili and Crosta, 2011a). The calculations that refer to the ‘new’ failure line are derived in the same way as the calculations for the first failure and are given below. Note that for the calculation of the rates of the external works, the front of the slope is considered vertical for the simplicity of the calculations and that is the reason why the inclination of the slope  $\beta$  does not appear in the calculations. After subtracting  $\dot{W}_2$  and  $\dot{W}_3$  from  $\dot{W}_1$  the result is the same.

Considering the region  $P_2JD$  (Figure 3.1):

$$\begin{aligned} \dot{W}_1^n &= \omega \gamma r_{x2}^3 \left[ (1 + k_v) f_{l_v}^n(x_1, y_1, x_2, y_2, \varphi) + k_h f_{l_h}^n(x_1, y_1, x_2, y_2, \varphi) \right] \\ &= \omega \gamma r_{x2}^3 \left[ (1 + k_v) \frac{\exp[3 \tan \varphi (y_2 - x_2)] (3 \tan \varphi \cos y_2 + \sin y_2) - 3 \tan \varphi \cos x_2 - \sin x_2}{3(1 + 9 \tan^2 \varphi)} + \right. \\ &\quad \left. k_h \frac{\exp[3 \tan \varphi (y_2 - x_2)] (3 \tan \varphi \sin y_2 - \cos y_2) - 3 \tan \varphi \sin x_2 + \cos x_2}{3(1 + 9 \tan^2 \varphi)} \right] \quad [3.29] \end{aligned}$$

with  $\omega$  being the rate of angular displacement of the failing wedge.

Considering the region  $P_2JK$  (Figure 3.1):

$$\begin{aligned}
\dot{W}_2^n &= \omega \gamma r_{x_2}^3 \left[ (1+k_v) f_{2_v}''(x_2, y_2, \varphi) + k_h f_{2_h}''(x_2, y_2, \varphi) \right] \\
&= \omega \gamma r_{x_2}^3 \frac{L_2}{r_{x_2}} \left[ (1+k_v) \frac{1}{6} (2 \cos x_2 - \frac{L_2}{r_{x_2}}) \sin x_2 + k_h \sin^2 x_2 \right]
\end{aligned} \quad [3.30]$$

Considering the region P<sub>2</sub>KD (Figure 3.1):

$$\begin{aligned}
\dot{W}_3^n &= \omega \gamma r_{x_2}^3 \left[ (1+k_v) f_{3_v}''(x_2, y_2, \varphi) + k_h f_{3_h}''(x_2, y_2, \varphi) \right] \\
&= \omega \gamma r_{x_2}^3 \frac{1}{3} \left[ (1+k_v) [\exp(\tan \varphi (y_2 - x_2)) \sin y_2 - \sin x_2] \cos^2 y_2 \exp(2 \tan \varphi (y_2 - x_2)) + \right. \\
&\quad \left. k_h \frac{1}{2} [\exp(2 \tan \varphi (y_2 - x_2)) \sin^2 y_2 - \sin^2 x_2] \cos y_2 \exp(\tan \varphi (y_2 - x_2)) \right]
\end{aligned} \quad [3.31]$$

Considering the region P<sub>2</sub>JI (Figure 3.1):

$$\begin{aligned}
\dot{W}_4^n &= \omega \gamma r_{x_2}^3 \left[ (1+k_v) f_{4_v}''(x_2, z_2, \varphi) + k_h f_{4_h}''(x_2, z_2, \varphi) \right] \\
&= \omega \gamma r_{x_2}^3 \left[ (1+k_v) \frac{\exp[3 \tan \varphi (z_2 - x_2)] (3 \tan \varphi \cos z_2 + \sin z_2) - 3 \tan \varphi \cos x_2 - \sin x_2}{3(1+9 \tan^2 \varphi)} + \right. \\
&\quad \left. k_h \frac{\exp[3 \tan \varphi (z_2 - x_2)] (3 \tan \varphi \sin z_2 - \cos z_2) - 3 \tan \varphi \sin x_2 + \cos x_2}{3(1+9 \tan^2 \varphi)} \right]
\end{aligned} \quad [3.32]$$

Considering the region P<sub>2</sub>JG (Figure 3.1):

$$\begin{aligned}
\dot{W}_5^n &= \omega \gamma r_{x_2}^3 \left[ (1+k_v) f_{5_v}''(x_2, z_2, \varphi) + k_h f_{5_h}''(x_2, z_2, \varphi) \right] \\
&= \omega \gamma r_{x_2}^3 \frac{L_2}{r_{x_2}} \left[ (1+k_v) \frac{1}{6} (2 \cos x_2 - \frac{L_2}{r_{x_2}}) \sin x_2 + k_h \sin^2 x_2 \right]
\end{aligned} \quad [3.33]$$

Finally, considering the region P<sub>2</sub>GI (Figure 3.1):

$$\begin{aligned}
\dot{W}_6^n &= \omega \gamma r_{x_2}^3 \left[ (1+k_v) f_{6_v}''(x_2, z_2, \varphi) + k_h f_{6_h}''(x_2, z_2, \varphi) \right] \\
&= \omega \gamma r_{x_2}^3 \frac{1}{3} \left[ (1+k_v) [\exp(\tan \varphi (z_2 - x_2)) \sin z_2 - \sin x_2] \cos^2 z_2 \exp(2 \tan \varphi (z_2 - x_2)) + \right. \\
&\quad \left. k_h \frac{1}{2} [\exp(2 \tan \varphi (z_2 - x_2)) \sin^2 z_2 - \sin^2 x_2] \cos z_2 \exp(\tan \varphi (z_2 - x_2)) \right]
\end{aligned} \quad [3.34]$$

Note that the rate of the external work of the regions above could have also been achieved by calculating the moment of the considered soil regions accounting as the center of rotation the center of the log-spiral P<sub>2</sub>. The calculations of the rate of the external work for the six regions that refer to the occurrence of the 'old' landslide should also be achieved by calculating the moment of each soil region around point P<sub>2</sub>.



For the region P<sub>1</sub>FD, whose center of rotation is G<sub>1</sub>, the rate of the external work is calculated for an infinitesimal slice, as illustrated in Figure 3.7a, considering this time, as the center of rotation the point P<sub>2</sub>:

$$d\dot{W}_{1v}^o = \omega \left( \frac{2}{3} r_\theta \cos \theta - r_{y_1} \cos y_1 + r_{y_2} \cos y_2 \right) \left( \frac{1}{2} \gamma r_\theta^2 d\theta \right)$$

$$d\dot{W}_{1h}^o = \omega \left( \frac{2}{3} r_\theta \sin \theta - r_{y_1} \sin y_1 + r_{y_2} \sin y_2 \right) \left( \frac{1}{2} \gamma r_\theta^2 d\theta \right)$$

After integration by parts, manipulations and substitutions the obtained expression is:

$$\begin{aligned} \dot{W}_1^o &= \dot{W}_{1v}^o + \dot{W}_{1h}^o = \omega \gamma r_{x2}^3 \left[ (1+k_v) f_{1v}^o(x_1, y_1, x_2, y_2, \varphi) + k_h f_{1h}^o(x_1, y_1, x_2, y_2, \varphi) \right] \\ &= \omega \gamma r_{x2}^3 \left[ (1+k_v) \left( \left( \frac{r_{x1}}{r_{x2}} \right)^2 \frac{[\exp(\tan \varphi (y_2 - x_2) \cos y_2 (\exp(2 \tan \varphi (y_1 - x_1) - 1))]}{4 \tan \varphi} \right. \right. \\ &\quad \left. \left. + \left( \frac{r_{x1}}{r_{x2}} \right)^3 \frac{\left( \frac{\exp(3 \tan \varphi (y_1 - x_1)) (\sin y_1 + 3 \tan \varphi \cos y_1) - \sin x_1 - 3 \tan \varphi \cos x_1}{3(1 + 9 \tan^2 \varphi)} \right)}{4 \tan \varphi} \right) \right. \\ &\quad \left. + k_h \left( \left( \frac{r_{x1}}{r_{x2}} \right)^2 \frac{[\exp(\tan \varphi (y_2 - x_2) \sin y_2 (\exp(2 \tan \varphi (y_1 - x_1) - 1))]}{4 \tan \varphi} \right. \right. \\ &\quad \left. \left. + \left( \frac{r_{x1}}{r_{x2}} \right)^3 \frac{\left( \frac{\exp(3 \tan \varphi (y_1 - x_1)) (3 \tan \varphi \sin y_1 - \cos y_1) - 3 \tan \varphi \sin x_1 + \cos x_1}{3(1 + 9 \tan^2 \varphi)} \right)}{4 \tan \varphi} \right) \right] \quad [3.35] \end{aligned}$$

Considering the region P<sub>1</sub>FK, whose center of rotation is G<sub>2</sub>, the rate of the external work is calculated for an infinitesimal slice, as illustrated in Figure 3.7b:

$$\dot{W}_{2v}^o = \omega \left[ \frac{1}{3} (2r_{x1} \cos x_1 - L_1) + r_{y_2} \cos y_2 - r_{y_1} \cos y_1 \right] \left( \frac{1}{2} \gamma L_1 r_{x1} \sin x_1 \right)$$

$$\dot{W}_{2h}^o = \omega \left( \frac{2}{3} r_{x1} \sin x_1 + r_{y_2} \cos y_2 - r_{y_1} \cos y_1 \right) \left( \frac{1}{2} \gamma L_1 r_{x1} \sin x_1 \right)$$

And after manipulations and substitutions the following expression is obtained:

$$\begin{aligned}
\dot{W}_2^o &= \dot{W}_{2v}^o + \dot{W}_{2h}^o = \omega \gamma r_{x2}^3 \left[ (1+k_v) f_{2v}^o(x_1, y_1, x_2, y_2, \varphi) + k_h f_{2h}^o(x_1, y_1, x_2, y_2, \varphi) \right] \\
&= \omega \gamma r_{x2}^3 \frac{1}{2} \frac{L_1}{r_{x1}} \left( \frac{r_{x1}}{r_{x2}} \right)^2 \sin x_1 \left[ \begin{aligned} &(1+k_v) \left( \frac{1}{3} \frac{r_{x1}}{r_{x2}} (\cos x_1 - 2 \exp(\tan \varphi (y_1 - x_1) \cos y_1) \right. \\ &\quad \left. + \exp(\tan \varphi (y_2 - x_2) \cos y_2) \right) \\ &+ k_h \left( \frac{2}{3} \frac{r_{x1}}{r_{x2}} (\sin x_1 - 2 \exp(\tan \varphi (y_1 - x_1) \sin y_1) \right. \\ &\quad \left. + \exp(\tan \varphi (y_2 - x_2) \sin y_2) \right) \end{aligned} \right] \quad [3.36]
\end{aligned}$$

Considering the region P<sub>1</sub>KD, whose center of rotation is G<sub>3</sub>, the rate of the external work is calculated for an infinitesimal slice, as illustrated in Figure 3.7c:

$$\dot{W}_{3v}^o = \omega \left( \frac{2}{3} r_{y1} \cos y_1 - r_{y1} \cos y_1 + r_{y2} \cos y_2 \right) \left( \frac{1}{2} \gamma H r_{y1} \cos y_1 \right)$$

$$\dot{W}_{3h}^o = \omega \left[ \frac{1}{3} (r_{x1} \sin x_1 + r_{y1} \sin y_1) - r_{y1} \sin y_1 + r_{y2} \sin y_2 \right] \left( \frac{1}{2} \gamma H r_{y1} \cos y_1 \right)$$

And after manipulations and substitutions the obtained expression is:

$$\begin{aligned}
\dot{W}_3^o &= \dot{W}_{3v}^o + \dot{W}_{3h}^o = \omega \gamma r_{x2}^3 \left[ (1+k_v) f_{3v}^o(x_1, y_1, x_2, y_2, \varphi) + k_h f_{3h}^o(x_1, y_1, x_2, y_2, \varphi) \right] \\
&= \omega \gamma r_{x2}^3 \frac{1}{2} \left( \frac{r_{x1}}{r_{x2}} \right)^2 \left[ \exp(\tan \varphi (y_1 - x_1) \sin y_1 - \sin x_1) \exp(\tan \varphi (y_1 - x_1) \cos y_1 \right. \\
&\quad \left. (1+k_v) \left( \exp(\tan \varphi (y_2 - x_2) \cos y_2 - \frac{1}{3} \frac{r_{x1}}{r_{x2}} [\exp(\tan \varphi (y_1 - x_1) \cos y_1]) + \right. \right. \\
&\quad \left. \left. k_h \left( \exp(\tan \varphi (y_2 - x_2) \sin y_2 + \frac{r_{x1}}{r_{x2}} \left( \frac{1}{3} \sin x_1 - \frac{2}{3} [\exp(\tan \varphi (y_1 - x_1) \sin y_1] \right) \right) \right) \right] \quad [3.37]
\end{aligned}$$

The external work for the region P<sub>1</sub>FC is calculated in a similar way with that of the rate of the external work  $\dot{W}_1^o$  and is given below:

$$\begin{aligned}
 \dot{W}_4^o &= \omega \gamma r_{x2}^3 \left[ (1+k_v) f_{4_v}^o(x_1, y_1, z_1, x_2, y_2, z_2, \varphi) + k_h f_{4_h}^o(x_1, y_1, z_1, x_2, y_2, z_2, \varphi) \right] \\
 &= \omega \gamma r_{x2}^3 \left[ (1+k_v) \left( \left( \frac{r_{x1}}{r_{x2}} \right)^2 \frac{[\exp(\tan \varphi (y_2 - x_2) \cos y_2 (\exp(2 \tan \varphi (z_1 - x_1) - 1))]}{4 \tan \varphi} \right. \right. \\
 &\quad \left. \left. + \left( \frac{r_{x1}}{r_{x2}} \right)^3 \frac{(\exp(3 \tan \varphi (z_1 - x_1)) (\sin z_1 + 3 \tan \varphi \cos z_1) - \sin x_1 - 3 \tan \varphi \cos x_1)}{3(1 + 9 \tan^2 \varphi)} \right. \right. \\
 &\quad \left. \left. - \frac{[\exp(\tan \varphi (y_1 - x_1) \cos y_1 [\exp(2 \tan \varphi (z_1 - x_1) - 1)]]}{4 \tan \varphi} \right) \right] \\
 &\quad + k_h \left( \left( \frac{r_{x1}}{r_{x2}} \right)^2 \frac{[\exp(\tan \varphi (y_2 - x_2) \sin y_2 (\exp(2 \tan \varphi (z_1 - x_1) - 1))]}{4 \tan \varphi} \right. \\
 &\quad \left. + \left( \frac{r_{x1}}{r_{x2}} \right)^3 \frac{(\exp(3 \tan \varphi (z_1 - x_1)) (3 \tan \varphi \sin z_1 - \cos z_1) - 3 \tan \varphi \sin x_1 + \cos x_1)}{3(1 + 9 \tan^2 \varphi)} \right. \\
 &\quad \left. \left. - \frac{[\exp(\tan \varphi (y_1 - x_1) \sin y_1 [\exp(2 \tan \varphi (z_1 - x_1) - 1)]]}{4 \tan \varphi} \right) \right] \quad [3.38]
 \end{aligned}$$

Considering the region P<sub>1</sub>FB, the external work is calculated similar to that of the rate of the external work  $\dot{W}_2^o$  and is given below:

$$\begin{aligned}
 \dot{W}_5^o &= \omega \gamma r_{x2}^3 \left[ (1+k_v) f_{5_v}^o(x_1, y_1, z_1, x_2, y_2, z_2, \varphi) + k_h f_{5_h}^o(x_1, y_1, z_1, x_2, y_2, z_2, \varphi) \right] \\
 &= \omega \gamma r_{x2}^3 \frac{1}{2} \frac{l_1}{r_{x1}} \left( \frac{r_{x1}}{r_{x2}} \right)^2 \sin x_1 \left[ (1+k_v) \left[ \frac{r_{x1}}{r_{x2}} \left( \frac{1}{3} (2 \cos x_1 - \frac{l_1}{r_{x1}}) - \exp(\tan \varphi (y_1 - x_1) \cos y_1) + \exp(\tan \varphi (y_2 - x_2) \cos y_2) \right) \right] \right. \\
 &\quad \left. + k_h \left[ \frac{2}{3} \frac{r_{x1}}{r_{x2}} (\sin x_1 - 2 \exp(\tan \varphi (y_1 - x_1) \sin y_1)) \right. \right. \\
 &\quad \left. \left. + \exp(\tan \varphi (y_2 - x_2) \sin y_2) \right] \right] \quad [3.39]
 \end{aligned}$$

Finally, considering the region P<sub>1</sub>BC:

$$\begin{aligned}
 \dot{W}_6^o &= \omega \gamma r_{x2}^3 \left[ (1+k_v) f_{6_v}^o(x_1, y_1, z_1, x_2, y_2, z_2, \varphi) + k_h f_{6_h}^o(x_1, y_1, z_1, x_2, y_2, z_2, \varphi) \right] \\
 &= \omega \gamma r_{x2}^3 \frac{1}{2} \left( \frac{r_{x1}}{r_{x2}} \right)^2 \left[ \exp(\tan \varphi (z_1 - x_1) \sin z_1 - \sin x_1) \exp(\tan \varphi (z_1 - x_1) \cos z_1) \right. \\
 &\quad \left. (1+k_v) \left( \exp(\tan \varphi (y_2 - x_2) \cos y_2 + \frac{r_{x1}}{r_{x2}} \left( \frac{2}{3} \exp(\tan \varphi (z_1 - x_1) \cos z_1) - \exp(\tan \varphi (y_1 - x_1) \cos y_1) \right) \right) + \right. \\
 &\quad \left. k_h \left( \exp(\tan \varphi (y_2 - x_2) \sin y_2 + \frac{r_{x1}}{r_{x2}} \left( \frac{1}{3} (\sin x_1 + \exp(\tan \varphi (z_1 - x_1) \sin z_1) - [\exp(\tan \varphi (y_1 - x_1) \sin y_1)] \right) \right) \right) \right] \quad [3.40]
 \end{aligned}$$

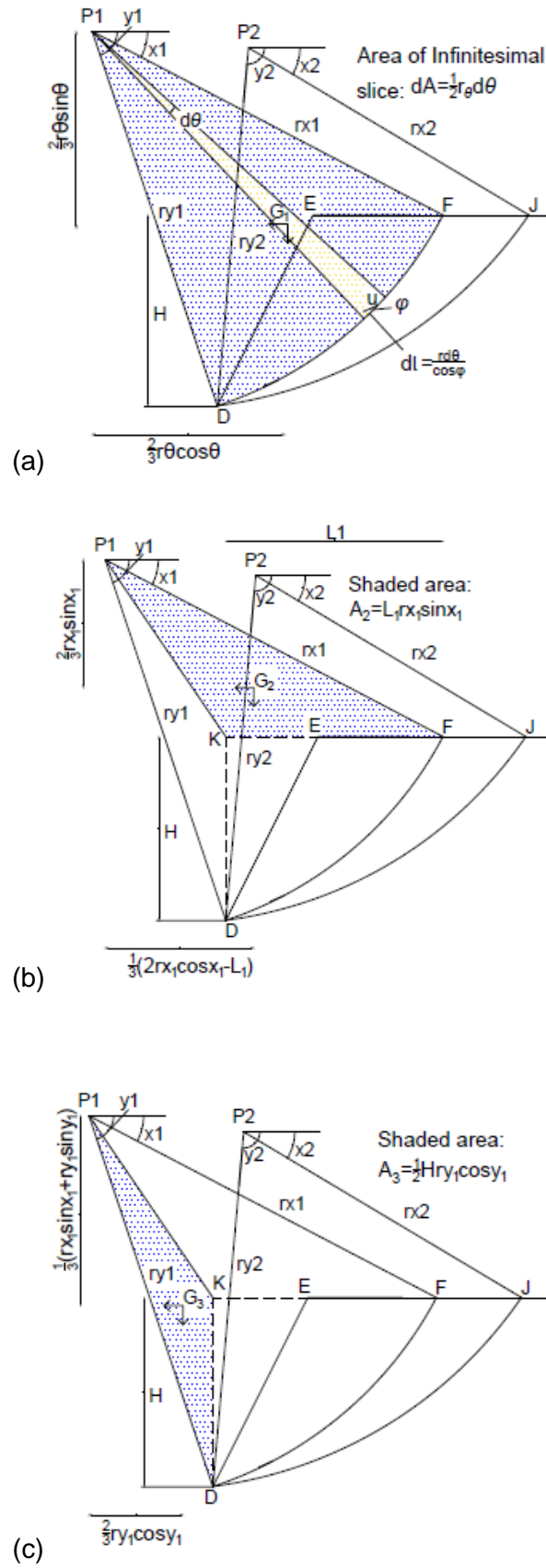


Figure 3.7. Calculation for the rate of the external work for each 'old' landslide

### 3.3.3. Work of water during the second failure

For the second and each successive failure, the calculation of the work of the water  $\dot{W}_w$  is calculated over the mechanism boundaries which include the shear surface ID and the crack surface GI (Michalowski, 2013) and is here illustrated, as arising from Figure 3.3:

$$\dot{W}_w = \dot{W}_{GI} + \dot{W}_{ID} = \int_{\theta_{ru2}}^{z_2} u[v]_n dS_{GI} + \int_{z_2}^{y_2} u[v]_n dS_{ID} \quad [3.41]$$

where the work of water along the long spiral part is given:

$$\dot{W}_{ID} = \omega \gamma r_{x2}^2 \tan \varphi r_u \left( \int_{z_2}^{\theta_{c2}} d_1 \exp[2 \tan \varphi (\theta - x_2)] d\theta + \int_{\theta_{c2}}^{y_2} d_2 \exp[2 \tan \varphi (\theta - x_2)] d\theta \right)$$

and  $\theta_{ru2}$ ,  $d_1$ ,  $d_2$  and  $\theta_{c2}$  (Figure 3.3):

$$\tan \theta_{ru2} = \frac{r_z \sin z_2 - h_2}{r_z \cos z_2} = \frac{\exp(\tan \varphi (z_2 - x_2)) \sin z_2 - \frac{r_u \gamma}{\gamma_w} (\exp(\tan \varphi (z_2 - x_2)) \sin z_2 - \sin x_2)}{\exp(\tan \varphi (z_2 - x_2)) \cos z_2}$$

$$d_1 = r_{\theta 2} \sin \theta_2 - r_{x2} \sin x_2$$

$$d_2 = r_{\theta 2} \sin \theta_2 - r_{\theta 1} \sin \theta_1 + r_{x1} \sin x_1 - r_{x2} \sin x_2$$

$$\cos \theta_{c2} \exp[\tan \varphi (\theta_{c2} - x_2)] = \frac{r_{x1}}{r_{x2}} (\cos x_1 - \exp[\tan \varphi (y_1 - x_1)] \cos y_1) + \cos y_2$$

The distance between the two ( $d_2$ ) log-spirals has been approximated employing Simpon's rule (see Appendix C- MATLAB SCRIPTS).

### 3.3.4. Calculation of the second failure mechanism

Substituting Eq [3.16], [3.19] and [3.21] into Eq [3.11] and dividing all terms by  $\dot{\theta}$  and  $r_{x2}$ , and rearranging, the stability factor,  $N_s = \gamma H/c$ , is obtained:

$$\frac{\gamma H}{c} = g(x_1, y_1, z_1, x_2, y_2, z_2, \phi, K_h, \lambda, r_u) \quad [3.42]$$

$$= \frac{f_{d2} + f_{cf} [\exp(\tan \phi (y_2 - x_2)) \sin y_2 - \sin x_2]}{\left[ (1 + \lambda K_h) (f_{1_v}^n - f_{2_v}^n - f_{3_v}^n - f_{1_v}^o + f_{2_v}^o + f_{3_v}^o + f_{4_v}^o - f_{5_v}^o - f_{6_v}^o - f_{4_v}^n + f_{5_v}^n + f_{6_v}^n) + \right. \\ \left. K_h (f_{1_h}^n - f_{2_h}^n - f_{3_h}^n - f_{1_h}^o + f_{2_h}^o + f_{3_h}^o + f_{4_h}^o - f_{5_h}^o - f_{6_h}^o - f_{4_h}^n + f_{5_h}^n + f_{6_h}^n) + r_u f_w \right]}$$

The global minimum of  $g(x_1, y_1, z_1, x_2, y_2, z_2, \phi, \beta, K_h, \lambda)$  over the three geometrical variables  $x_2, y_2, z_2$ , provides the least (best) upper bound on the stability factor for the second and any successive landslide.

### 3.4. Geometric approximations

In Figure 3.8, the evolution of initially steep slopes, with very limited or completely absent tensile strength, is shown. It emerges that this type of slope exhibits a peculiar type of evolution: several successive small failure mechanisms made of thin slices (from vertical line FC to vertical line GI) until a much larger failure mechanism takes place (mechanism JMK). The occurrence of thin slice mechanisms, which in the limit case of an initially vertical slope ( $\beta=90^\circ$ ) become infinitesimally thin slices, is described and physically explained in (Utili, 2013).

In Figure 3.9 the typical evolution undergone by a slope subject to weathering is shown. The features of the morphological evolution exhibited by the slopes are similar to what shown in (Utili and Crosta, 2011a) apart from the upper part of the failure mechanism which is always made by a vertical part due to the presence of cracks. A number of successive failures of decreasing area and depth of mechanism occur until a deeper mechanism of much larger area takes place (see Figure 3.9). To calculate the deeper mechanism, the slope profile, which is composed of several log-spiral pieces, was approximated by a straight line obtained as the linear envelope of the piecewise log-spiral profile.

### 3.4.1. Slope profile after each failure

As it is well known that a vertical slope profile is more critical among slopes with angle lower than  $90^\circ$ . After the first failure takes place the new profile is no longer a straight line but it is made of a log spiral part CD and a vertical part FC as shown in Figure 3.8. The search for the most critical failure mechanism for some cases of steep initial slopes and for the case of tension cut-off; and following the procedure described above a failure line departing from point C (Figure 3.8) turns out to be the most critical one, with a crack depth for the second failure mechanism slightly shorter than that on the first mechanism. Following this second failure, a number of 'small' failures will take place forming the line IC, until a 'significant' failure (Figure 3.8) becomes more critical than the 'small' one and takes place. The line IC is formed by a number of very small log-spiral parts of every successive 'small' failure.

A technique is used to avoid being trapped in the CI line when looking for the most critical successive failure mechanism. An illustrative example is presented in Figure 3.8 to explain how the second 'significant' failure is identified. A slope with inclination  $\beta=80^\circ$  and  $\varphi=40^\circ$  is selected; the second 'significant' failure takes place when the stability number of this failure is lower than the stability number of any successive 'small' failure.

Since the analytical formulation for a slope profile made up of more than one log-spiral line becomes prohibitive, the search for the second failure mechanism is always searched above the intersection of the two previous mechanisms. In the case of the 'small' failures developed in the vertical part of the slope, the line IC which is formed by small log spiral parts can be assumed to be linear with a specific inclination for every combination of  $\beta$  and  $\varphi$ . Then the profile is formed by a log-spiral and a planar part which makes the calculation of the stability number possible. A comparison is made between

the stability number of every successive 'small' failure mechanism and a failure mechanism for an initial profile I'CD, when the stability number for JMK is smaller than that for the next 'small' failure then the procedure is stopped as the second 'significant' failure becomes the most critical. The determination of the second significant failure mechanism with GCD being the starting profile for the second failure, can be a time consuming iterative procedure as it demands the calculation and comparison of the stability numbers for many profiles in order to identify the correct sequence.

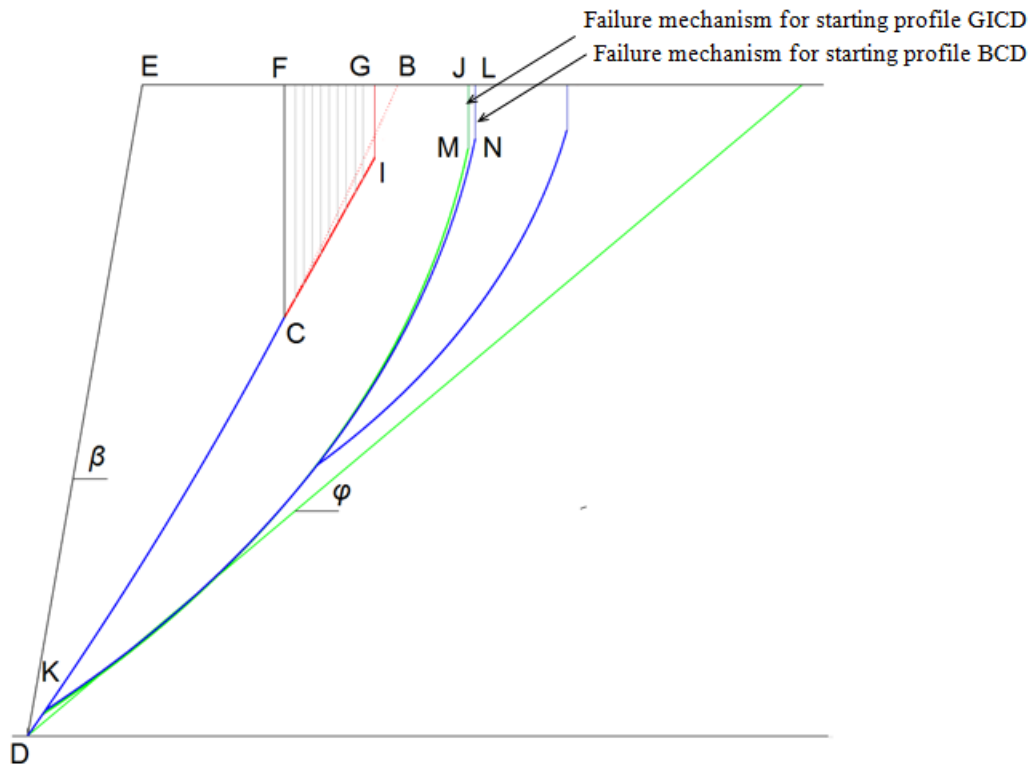


Figure 3.8. Most critical failure mechanism for the second 'significant' failure for slope with initial slope inclination  $\beta=80^\circ$  and friction angle  $\varphi=40^\circ$  (tension cut off).



*Table 3.1. Stability number and crack depth for second 'significant' failure for different starting slope profiles for the second 'significant' failure*

<b>Starting profile</b>	<b>BCD</b>	<b>GICD</b>
<b>Stability Number</b>	30.95	31.05
<b>Crack Depth</b>	0.084	0.082
<b>Sliding Area</b>	0.146	0.144

For this reason the stability number, the failure mechanism and the depth of the critical crack for the second failure mechanism with BCD being the starting slope profile have been compared with these when GICD is the starting profile and the results are presented in Table 3.1 and in Figure 3.8. The results presented in this example present the larger difference among all the results in this paper and even so they are almost identical. For the sake of simplicity, the whole log spiral BCD is considered as the starting profile for each successive failure for the case of a pre-existing crack when a number of successive 'small' failures are more critical than the next 'significant' one. Note that this approximation is only made to define the second 'significant' failure, after that the second and for every successive  $n+1$  failure the initial profile is the one predicted from the model for the previous ( $n$ ) failure.

#### **3.4.2. Slope profile after a number of failures**

In the model, as described above, it has been assumed that after the second failure and to find each new failure mechanism, the potential failure lines have been searched only above the point of intersection of the two previous mechanisms. However, a closer look on the failure mechanisms and the final condition of the slope after a number successive failures (Figure 3.9); suggests that a deep mechanism involving more than one log spiral as an initial slope profile should also be considered in the case of pre-existing

cracks. As the failures progress, the cohesion of the soil decreases; the final condition of a slope made of a purely frictional material should be lower than the friction angle for the profile to be stable.

In order to search for a deep-seated mechanism a slope profile made by more than 2 log spirals should be considered. A slope made by  $n$  spirals requires 2 times  $n$  number of parameters for its complete description, then the calculation of the external work by a sliding area enclosed in  $n+1$  log-spirals would make the analytical equations involved in the energy balance for the calculation of the stability number far complicated. For this reason, a procedure similar to the one described above has been adopted.

After  $m$  number of failures an almost planar profile is formed by  $m$  log-spiral parts. To account for the deep-seated failure mechanism, a linear envelope to the piecewise log spiral profile after  $m$  successive failures for a slope with an initial slope inclination  $\beta=70^\circ$  has been drawn (Figure 3.9). This envelope line is assumed as the new slope profile with  $\beta^*=26.3^\circ$  and  $\varphi=20^\circ$ ; the minimization procedure of limit analysis is then performed for this plane profile. The calculated stability number  $N^*$  for this new profile is compared with the stability number of each failure mechanism  $i$  ( $2 < i < m$ ). The mechanism with the lower stability number will take place first. If the stability number  $N^*$  becomes lower than  $N^i$ , the new slope profile is made by the single log spiral failure surface associated with this mechanism and all the subsequent failures will depart from this profile (Utili and Crosta, 2011a).

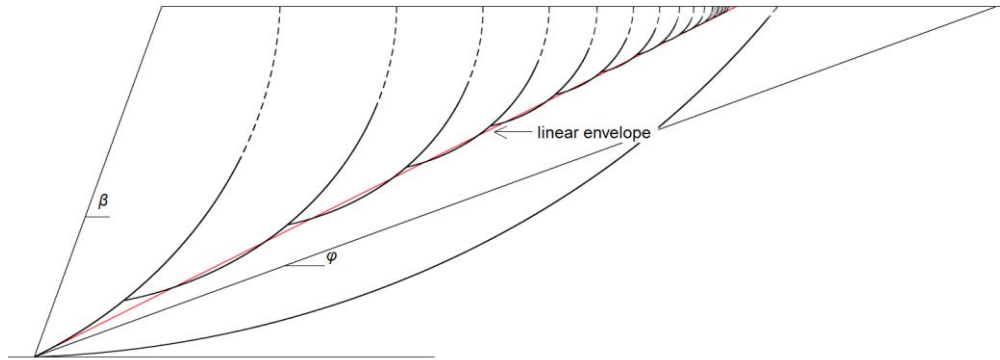


*Figure 3.9. Deep seated failure mechanism for a slope with  $\beta=70^\circ$  and initial friction angle  $\varphi=20^\circ$*

As in (Utili and Crosta, 2011a), during this process an approximation has been introduced. When calculating the deep log spiral failure mechanism, the slope profile is assumed to be planar, but the calculated log spiral failures from  $i+1$  to  $m$  do not take place in reality, which means that the slope profile is not entirely a plane. It should be approximated by a plane in its lower part, a log spiral in its medium part and a vertical line in its upper part (see the shaded area in Figure 3.9). As it is obvious in Figure 3.9 the region delimited by the log spiral and the vertical line is small in comparison with the size of the failure mechanisms, therefore this approximation is acceptable and its influence on the calculation of the successive mechanisms can be neglected.

### 3.5. Results

#### 3.5.1. Parametric analysis of slope evolution for various hydrogeological scenarios

In Figure 3.10 the effect of the seismic action is analysed for various values of tensile strength. For each failure, numbered in chronological order, the area of the sliding mass is plotted. The results indicate that the influence of

the tensile strength on the sliding area is small, with seismic action having the effect of amplifying the small differences. To investigate the influence of seepage instead, the critical height for a slope with initial slope inclination  $\beta=60^\circ$  and  $\varphi=20^\circ$  is plotted in Figure 3.11 for 6 successive failures.

In Figure 3.12, the step-like relationship between the dimensionless normalised cohesion and crest retreat is plotted for 8 successive failures for various seismic scenarios ( $K_h=0$ ,  $K_h=0.1$  and  $K_h=0.2$ ). It can be observed that if the first two failures are excluded, the values of critical cohesion and crest retreat lie on straight lines in agreement to what observed in (Utili and Crosta, 2011a) for static dry slopes not subject to crack formation. However, when there is also seismic action this is not more the case for slopes with limited tensile strength. From the figure, it also emerges that the tensile strength does not affect significantly either the normalised cohesion or crest retreat although this is less the case for slopes subject to substantial seismic action. Same plots showing the relationship between the dimensionless normalized cohesion and crest retreat for inclination  $\beta=70^\circ$  and  $\varphi=20^\circ$ , only for intact slopes for intact slopes under seismic action and the influence of pore pressure is plotted in Figure 3.13.

The evolution of the critical height ( $\gamma H/c$ ) and the dimensionless cliff retreat ( $L/H$ ) as a function of the friction angle represented in the same graph as curves from the analysis of six successive failures, for initial slope inclination  $\beta=60^\circ$ ,  $\beta=70^\circ$  and  $\beta=80^\circ$  demonstrating the effect of limited tensile strength, seismic action and existence of water are plotted in Figure 3.14, Figure 3.15 and Figure 3.16. Solid black lines are used for the critical height and dashed lines for the dimensionless crest retreat, while the corresponding number of failure is marked on the curves. It is evident the influence of the tensile strength and the presence of cracks on the stability of the slopes is

more important in steep slopes. When seismic acceleration is taken into consideration the influence on both critical height and cliff retreat is significant (Figure 3.15). In Figure 3.16 and as explained by (Michalowski, 2013), the adverse influence of pore-water pressure on the dimensional critical height increases for larger values of the internal friction angle is illustrated.

Note that for some cases of slopes with low friction angle, after a number of failures, the model predicts a much larger landslide in terms of area (volume), but not in terms of crest retreat (Figure 3.9) so this is more of interest for anthropic constructions at the toe of the slope. If the slope is a cliff by the ocean - an environment where there is a continuous wash away action – it is reasonable to expect the erosion of the excised material before the next mechanism occurs. In this case, the model illustrates an important feature for cliffs made of geomaterials with limited tensile strength. Instead, in case of less exposed cliffs (e.g. inland and less exposed by the sea) we can expect that this deep mechanism will not take place due to the stabilising action of the weight of the debris and therefore it is reasonable to disregard it.

To make meaningful comparisons, the values of the crest retreat normalised by the initial slope height, the sliding area normalised by the square of the initial height and the associated crack depth normalised by the height are listed for initial slope inclinations  $\beta=60^\circ$ ,  $\beta=70^\circ$  and  $\beta=80^\circ$  and for friction angles  $\varphi=20^\circ$ ,  $\varphi=30^\circ$  and  $\varphi=40^\circ$  for the three different cases of the formation of the crack are reported in Table 3.2. The results of the parametric investigation in terms of normalised crest retreat and normalised sliding area for intact slopes under seismic action and the existence of water are reported in Table 3.3.

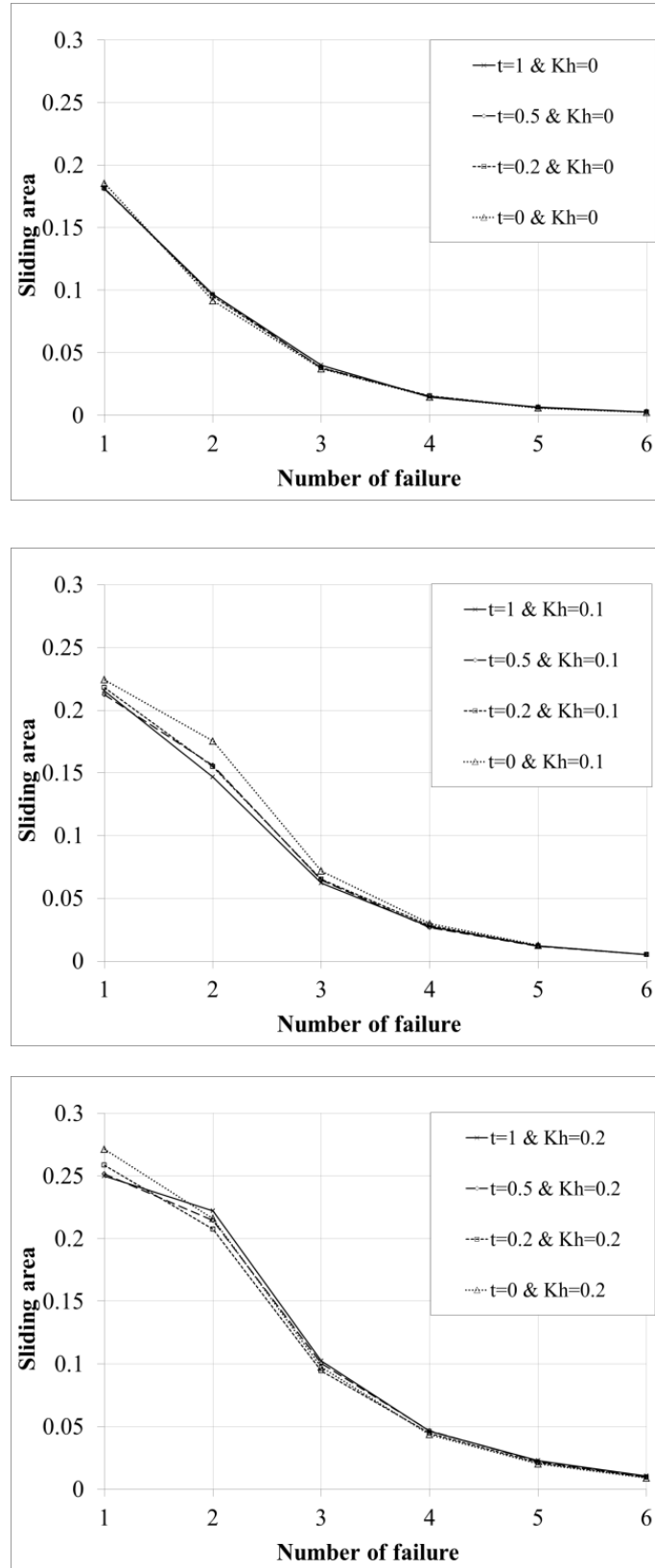


Figure 3.10. Dimensionless normalized sliding area for inclination  $\beta=70^\circ$  and for friction angle  $\varphi=40^\circ$ , showing the influence of the tensile crest on the evolution of slopes for different  $Kh$ , for 6 successive failures

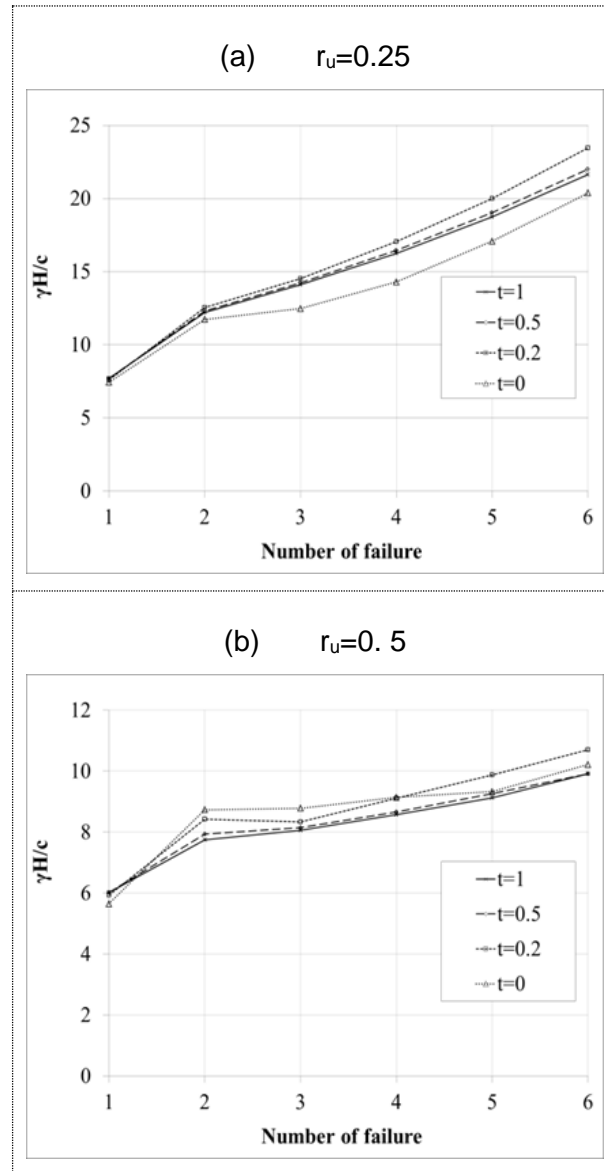
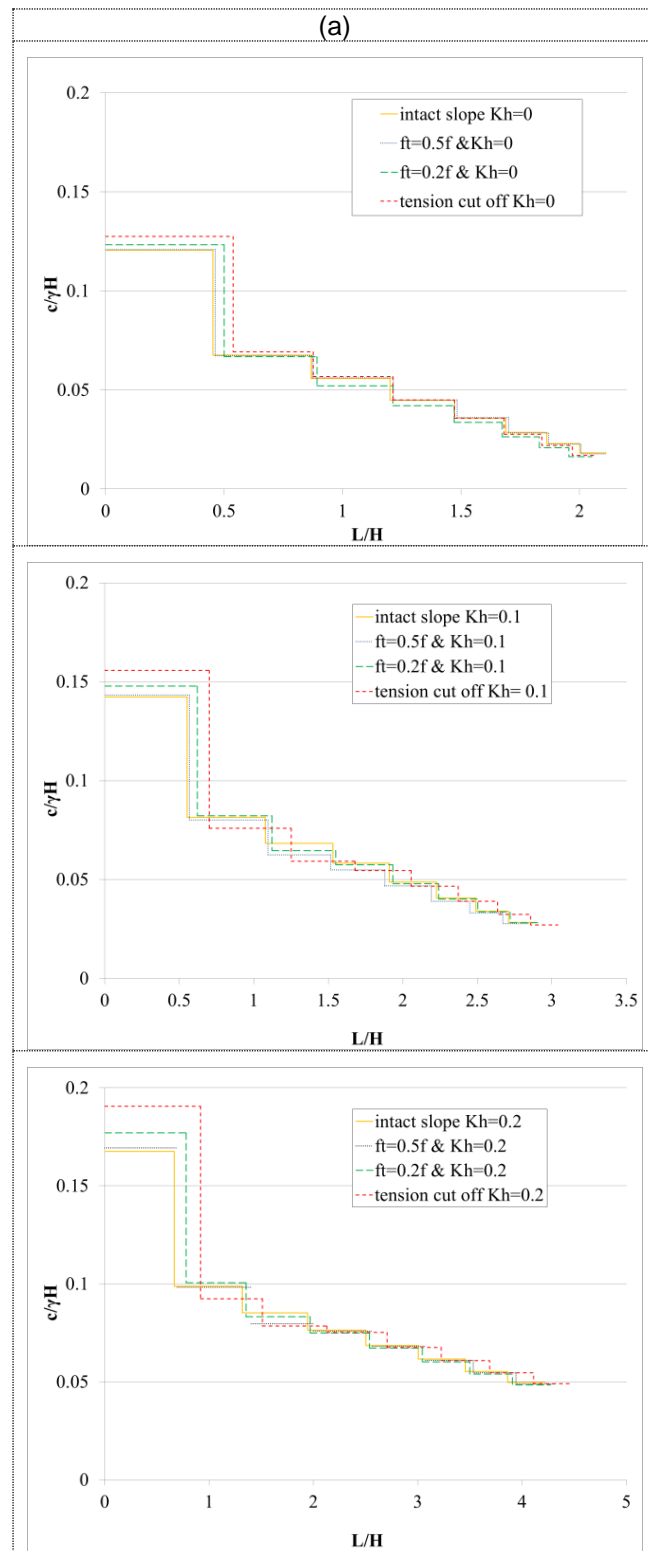


Figure 3.11. Critical height ( $\gamma H/c$ ) for six successive failures for slope inclination  $\beta=60^\circ$  and  $\phi=20^\circ$  for soil of full unconfined tensile strength ( $t=1$ ), soil of limited tensile strength ( $t=0.5$  and  $t=0.2$ ) and soil of zero tensile strength ( $t=0$ ), (a) for  $r_u=0.25$  and (b) for  $r_u=0.50$ .





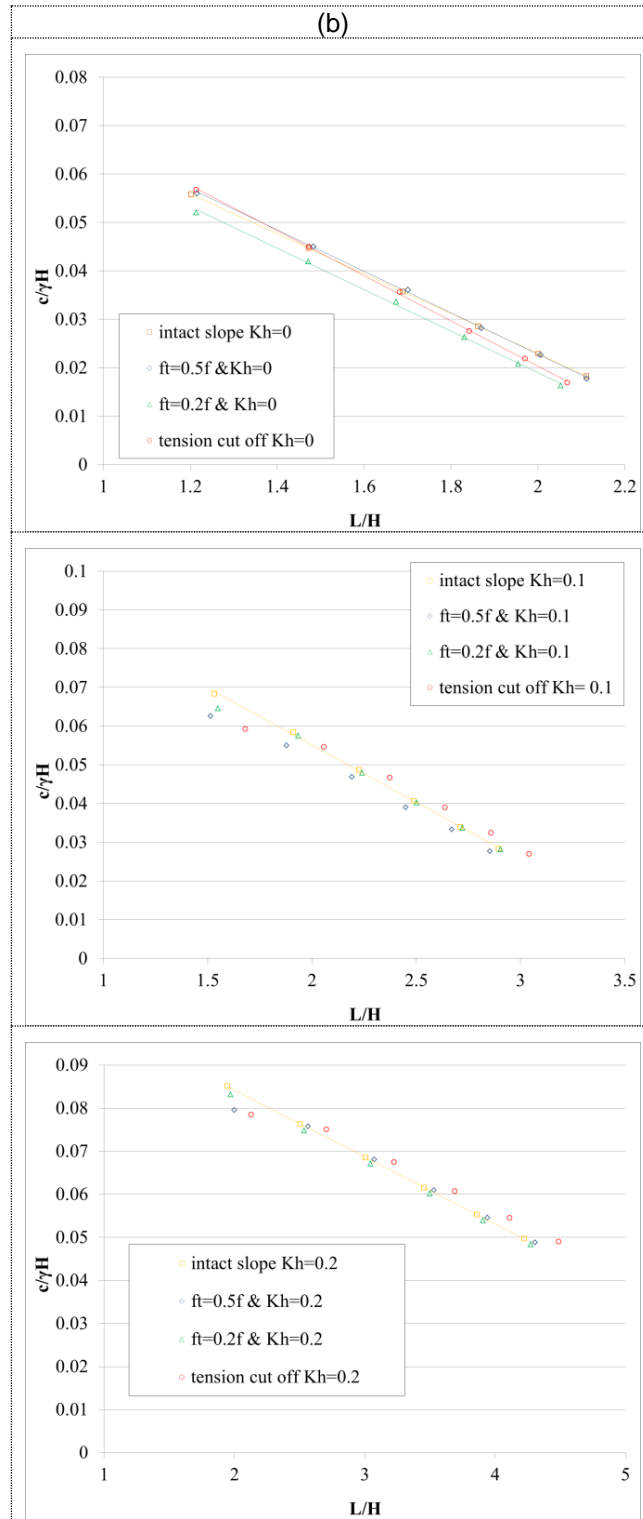


Figure 3.12. Dimensionless normalized cohesion versus crest retreat for inclination  $\beta=70^\circ$ , (a) step-like relationship obtained for  $\phi = 20^\circ$ , for different tensile strengths for  $Kh=0$ ,  $Kh=0.1$  and  $Kh=0.2$ , for 8 successive failures (b) If the first two failures are excluded, the values of critical cohesion and crest retreat lie on straight lines only for intact slopes.

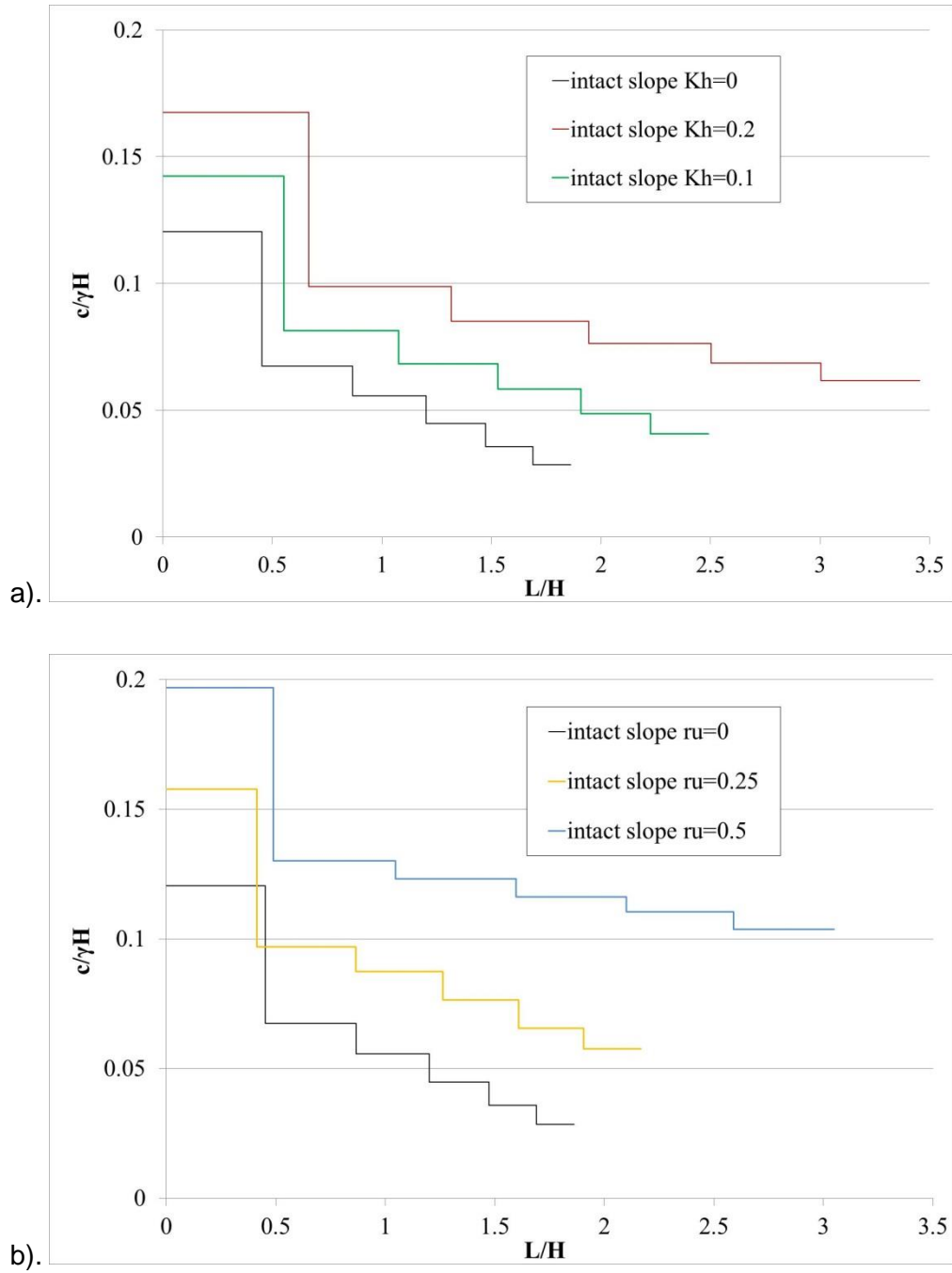
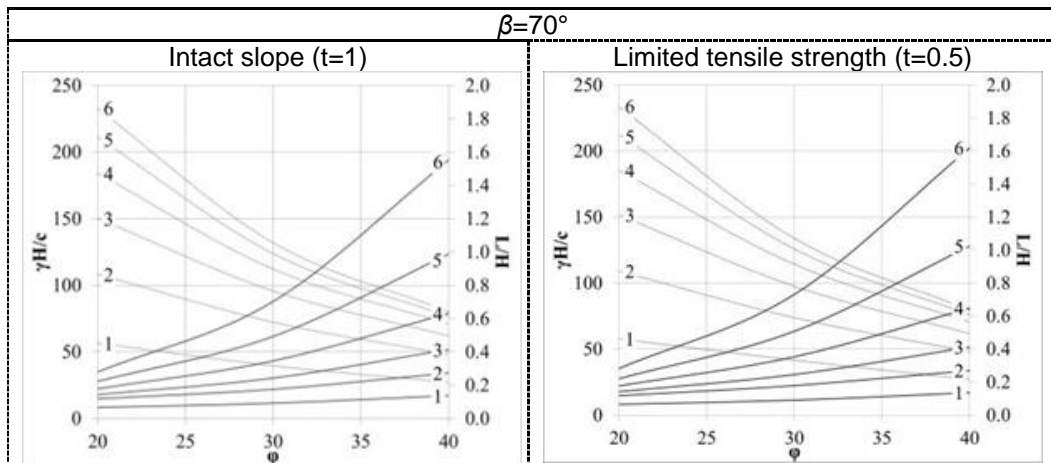
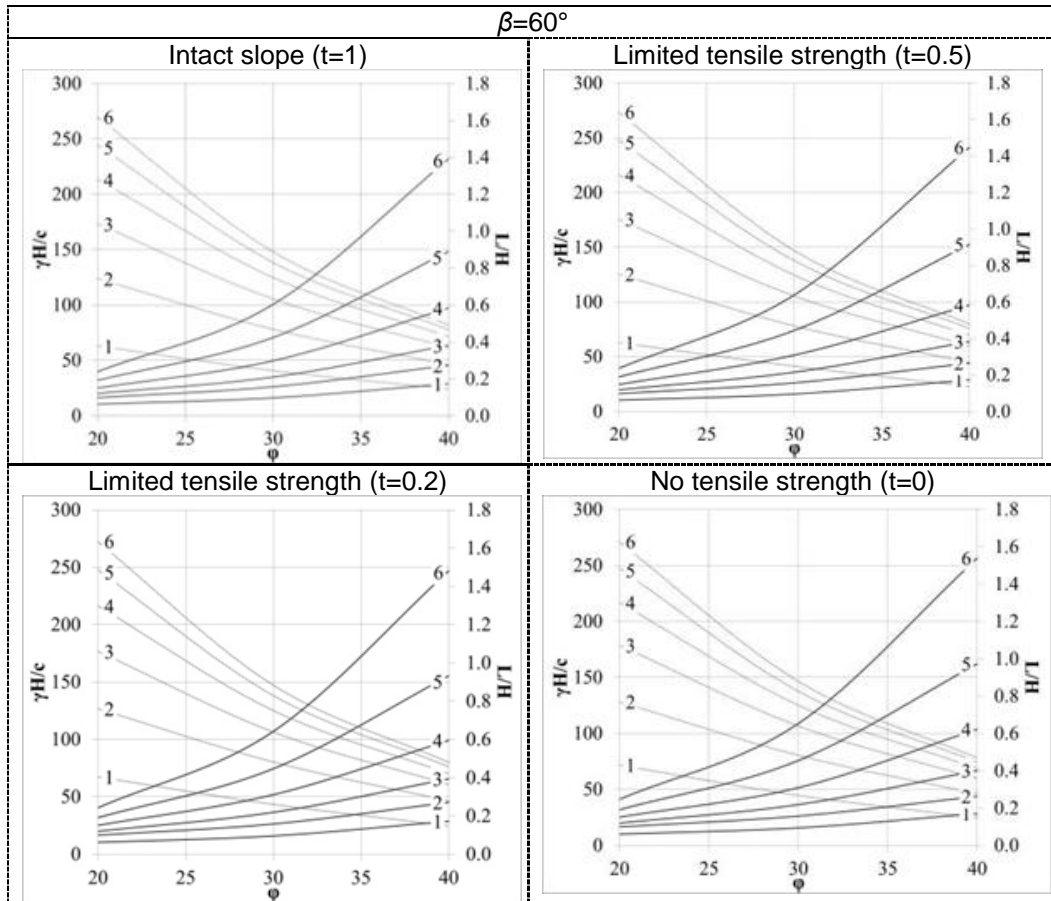


Figure 3.13. Dimensionless normalized cohesion versus crest retreat for inclination  $\beta=70^\circ$ , step-like relationship between cohesion and crest retreat obtained for  $\phi=20^\circ$ , for intact slopes (dry case) a) slope evolution for various  $Kh$  values and b) slope evolution for various  $r_u$  values for 6 successive failures (static case)



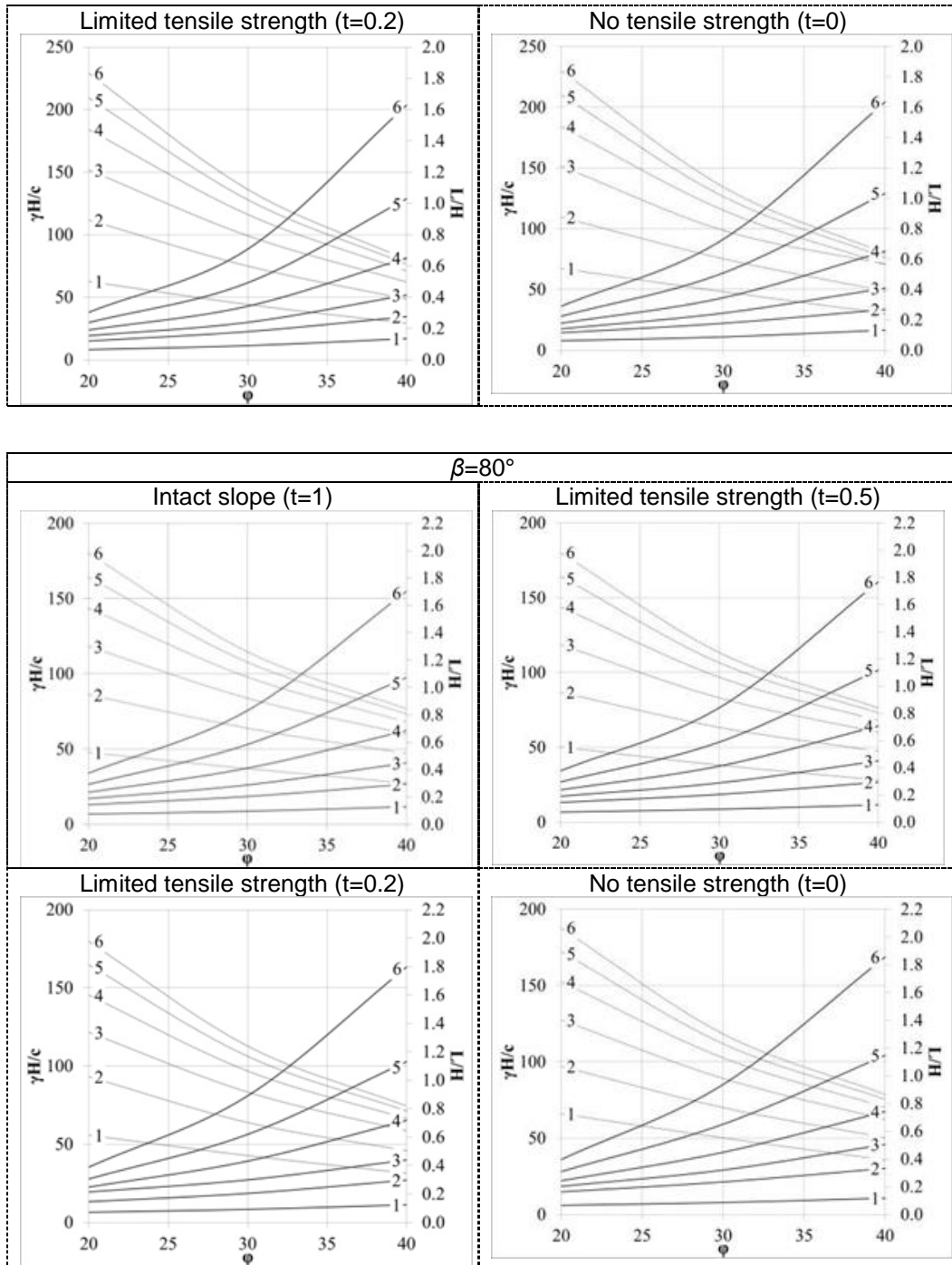


Figure 3.14. Critical height ( $\gamma H/c$ ) and dimensionless cliff retreat ( $L/H$ ) as a function of the friction angle represented in the same graph as curves for six successive failures for slope inclinations  $\beta=60^\circ$ ,  $\beta=70^\circ$  and  $\beta=80^\circ$  for the case of intact slope, for soil of full unconfined tensile strength, soil of limited tensile strength and soil of zero tensile strength. Solid black lines are used for the critical height and dashed lines for the dimensionless crest retreat. The corresponding failure number is marked on the curves.

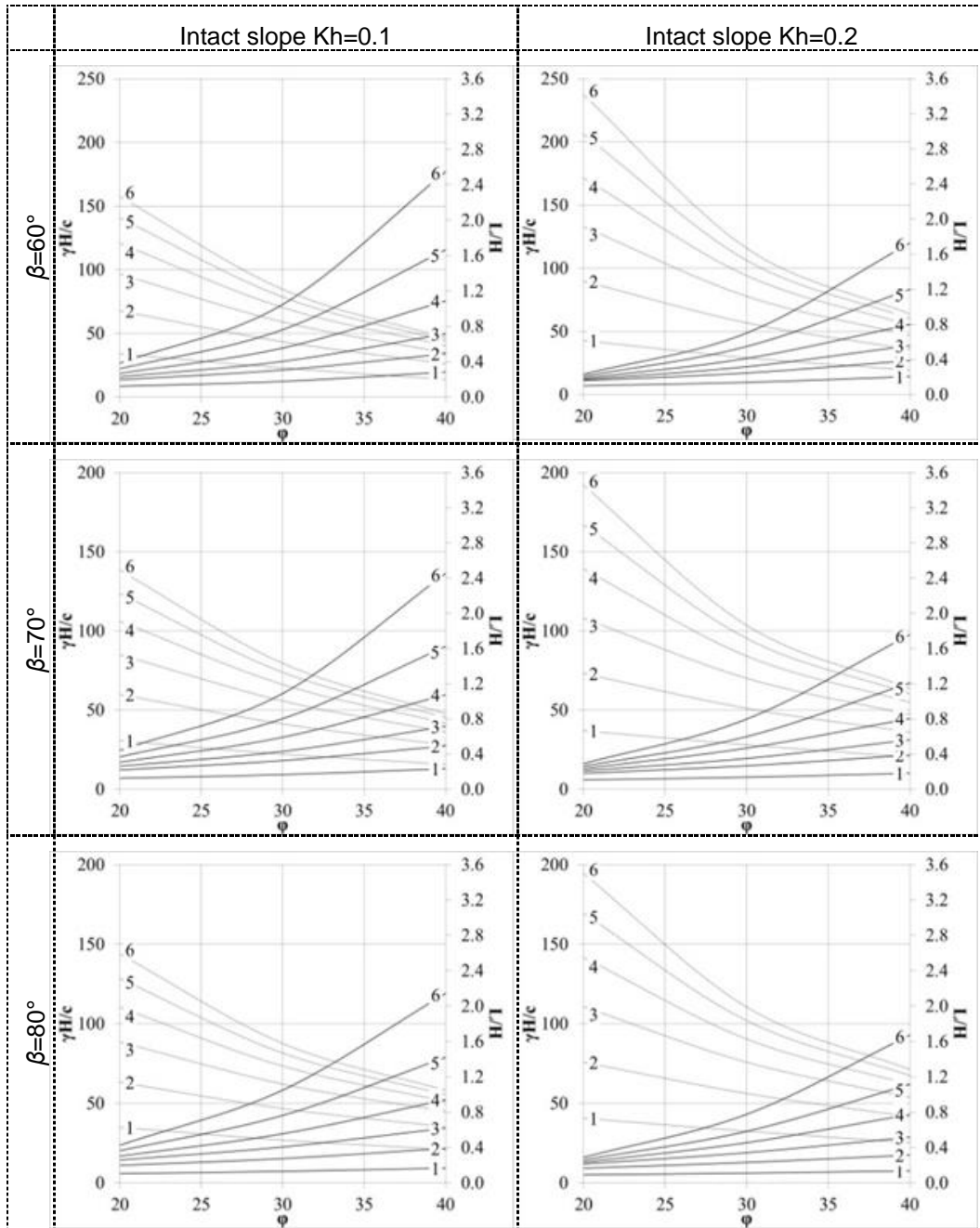


Figure 3.15. Critical height ( $\gamma H/c$ ) and dimensionless cliff retreat ( $L/H$ ) as a function of the friction angle represented in the same graph as curves for six successive failures for slope inclinations  $\beta=60^\circ$ ,  $\beta=70^\circ$  and  $\beta=80^\circ$  for intact slopes and for seismic scenarios with coefficient  $Kh=0.1$  and  $Kh=0.2$ . Solid black lines are used for the critical height and dashed lines for the dimensionless crest retreat. The corresponding failure number is marked on the curves.

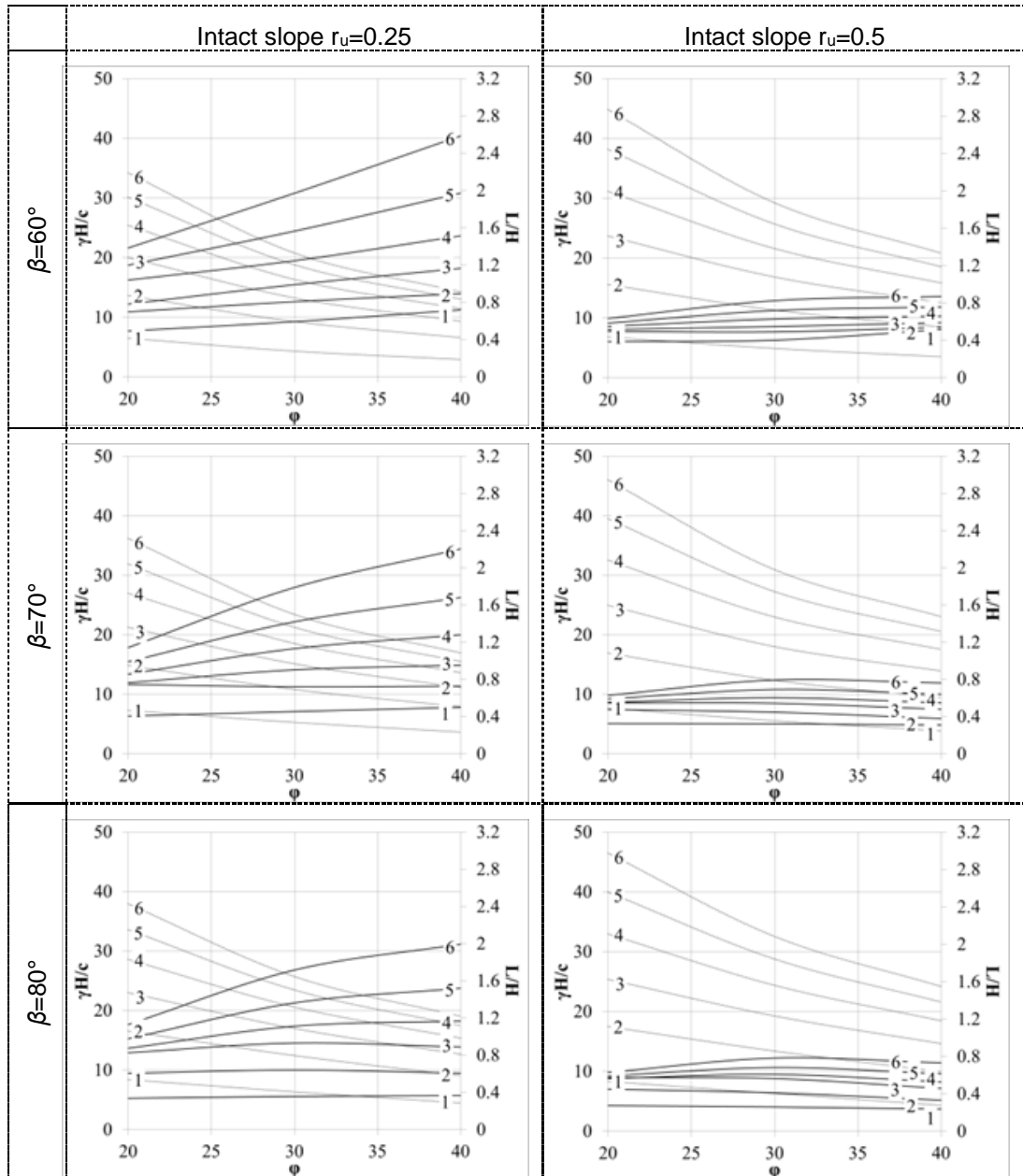


Figure 3.16. Critical height ( $\gamma H/c$ ) and dimensionless cliff retreat ( $L/H$ ) as a function of the friction angle represented in the same graph as curves for six successive failures for slope inclinations  $\beta = 60^\circ$ ,  $\beta = 70^\circ$  and  $\beta = 80^\circ$  for the case of intact slope and for pore pressure with coefficient  $r_u = 0.25$  and  $r_u = 0.5$ . Solid black lines are used for the critical height and dashed lines for the dimensionless crest retreat. The corresponding failure number is marked on the curves.

Table 3.2. Values for Associated Crest Retreat, Sliding Area and Crack Depth for Slopes with Initial Inclination  $\beta$  and Friction Angle  $\varphi$ , for slopes with  $t=1.0$ ,  $t=0.5$ ,  $t=0.2$  and  $t=0$ .

	$\beta=60^\circ$						$\beta=70^\circ$						$\beta=80^\circ$					
	$\varphi=20^\circ$		$\varphi=30^\circ$		$\varphi=40^\circ$		$\varphi=20^\circ$		$\varphi=30^\circ$		$\varphi=40^\circ$		$\varphi=20^\circ$		$\varphi=30^\circ$		$\varphi=40^\circ$	
	L/H	Area	L/H	Area	L/H	Area	L/H	Area	L/H	Area	L/H	Area	L/H	Area	L/H	Area	L/H	Area
<b>Failure</b>	<b>Intact slope <math>t=1.0</math></b>																	
1	0,377	0,356	0,244	0,244	0,145	0,162	0,453	0,345	0,317	0,255	0,218	0,181	0,525	0,345	0,407	0,269	0,301	0,207
2	0,742	0,270	0,468	0,141	0,277	0,072	0,867	0,353	0,578	0,178	0,386	0,097	0,947	0,364	0,702	0,239	0,518	0,154
3	1,039	0,171	0,632	0,066	0,369	0,027	1,202	0,216	0,766	0,085	0,497	0,040	1,300	0,241	0,922	0,117	0,659	0,064
4	1,279	0,105	0,748	0,033	0,428	0,011	1,473	0,138	0,898	0,042	0,568	0,016	1,580	0,151	1,076	0,058	0,748	0,025
5	1,466	0,067	0,830	0,016	0,466	0,004	1,689	0,088	0,990	0,021	0,613	0,006	1,806	0,093	1,184	0,028	0,808	0,010
6	1,616	0,041	0,887	0,008	0,490	0,002	1,862	0,056	1,055	0,010	0,642	0,003	1,981	0,059	1,260	0,014	0,844	0,004
<b>Failure</b>	<b>limited tensile strength <math>t=0.5</math></b>																	
1	0,378	0,349	0,248	0,246	0,137	0,159	0,463	0,344	0,334	0,257	0,217	0,181	0,552	0,350	0,419	0,269	0,310	0,206
2	0,753	0,287	0,469	0,134	0,269	0,068	0,874	0,362	0,591	0,182	0,385	0,097	0,955	0,359	0,697	0,232	0,521	0,156
3	1,054	0,175	0,633	0,065	0,360	0,027	1,215	0,224	0,782	0,088	0,495	0,038	1,306	0,238	0,914	0,113	0,660	0,060
4	1,297	0,108	0,747	0,031	0,418	0,011	1,484	0,140	0,915	0,042	0,565	0,015	1,583	0,149	1,066	0,055	0,748	0,024
5	1,486	0,069	0,827	0,015	0,456	0,004	1,701	0,086	1,008	0,021	0,609	0,006	1,808	0,092	1,172	0,027	0,804	0,010
6	1,639	0,043	0,882	0,007	0,479	0,002	1,870	0,055	1,072	0,010	0,638	0,002	1,981	0,059	1,246	0,013	0,839	0,004
<b>Failure</b>	<b>limited tensile strength <math>t=0.2</math></b>																	
1	0,404	0,354	0,260	0,251	0,148	0,163	0,501	0,354	0,353	0,259	0,233	0,182	0,614	0,364	0,470	0,278	0,346	0,214
2	0,760	0,284	0,481	0,133	0,278	0,066	0,893	0,328	0,599	0,191	0,388	0,095	1,025	0,343	0,702	0,213	0,505	0,136
3	1,060	0,171	0,638	0,062	0,364	0,025	1,214	0,203	0,793	0,091	0,497	0,038	1,337	0,232	0,917	0,110	0,644	0,055
4	1,298	0,107	0,750	0,030	0,421	0,010	1,471	0,127	0,929	0,044	0,567	0,015	1,598	0,138	1,065	0,053	0,730	0,023
5	1,485	0,066	0,828	0,015	0,457	0,004	1,674	0,076	1,023	0,021	0,612	0,006	1,810	0,084	1,168	0,026	0,784	0,009
6	1,633	0,041	0,883	0,007	0,479	0,002	1,831	0,047	1,089	0,010	0,640	0,002	1,976	0,052	1,240	0,012	0,818	0,004
<b>Failure</b>	<b>tension cut-off <math>t=0</math></b>																	
1	0,431	0,359	0,268	0,248	0,148	0,163	0,539	0,357	0,386	0,266	0,243	0,185	0,726	0,389	0,552	0,299	0,393	0,218
2	0,770	0,280	0,483	0,133	0,276	0,062	0,876	0,344	0,603	0,177	0,389	0,091	1,068	0,391	0,771	0,237	0,554	0,150
3	1,072	0,171	0,639	0,062	0,359	0,023	1,213	0,220	0,790	0,088	0,499	0,037	1,403	0,239	0,981	0,114	0,686	0,064
4	1,301	0,103	0,751	0,029	0,412	0,009	1,473	0,133	0,923	0,041	0,567	0,015	1,678	0,142	1,129	0,053	0,773	0,025
5	1,485	0,062	0,826	0,014	0,446	0,004	1,682	0,080	1,012	0,020	0,610	0,006	1,896	0,087	1,231	0,025	0,830	0,010
6	1,625	0,039	0,879	0,007	0,468	0,001	1,842	0,050	1,075	0,009	0,637	0,002	2,065	0,053	1,302	0,012	0,865	0,004

Table 3.3. Values for Associated Crest Retreat and Sliding Area with Initial Inclination  $\beta$  and Friction Angle  $\varphi$ , for intact slopes under seismic action or with the existence of water.

	$\beta=60^\circ$						$\beta=70^\circ$						$\beta=80^\circ$					
	$\varphi=20^\circ$		$\varphi=30^\circ$		$\varphi=40^\circ$		$\varphi=20^\circ$		$\varphi=30^\circ$		$\varphi=40^\circ$		$\varphi=20^\circ$		$\varphi=30^\circ$		$\varphi=40^\circ$	
	L/H	Area	L/H	Area	L/H	Area	L/H	Area	L/H	Area	L/H	Area	L/H	Area	L/H	Area	L/H	Area
<b>Failure</b>	<b>Kh=0.1</b>																	
1	0,490	0,415	0,330	0,293	0,199	0,194	0,553	0,393	0,400	0,293	0,286	0,216	0,628	0,390	0,485	0,302	0,380	0,238
2	0,977	0,407	0,626	0,203	0,379	0,101	1,078	0,478	0,744	0,274	0,504	0,147	1,139	0,458	0,841	0,289	0,635	0,194
3	1,391	0,288	0,850	0,106	0,501	0,042	1,531	0,344	1,004	0,143	0,652	0,062	1,595	0,349	1,118	0,164	0,809	0,084
4	1,738	0,196	1,013	0,056	0,582	0,018	1,910	0,234	1,191	0,076	0,751	0,028	1,987	0,244	1,321	0,088	0,922	0,037
5	2,026	0,136	1,132	0,030	0,635	0,008	2,226	0,163	1,330	0,041	0,817	0,012	2,311	0,176	1,470	0,046	0,998	0,016
6	2,267	0,095	1,218	0,016	0,669	0,003	2,490	0,114	1,431	0,023	0,860	0,005	2,590	0,123	1,577	0,025	1,048	0,007
<b>Failure</b>	<b>Kh=0.2</b>																	
1	0,618	0,483	0,420	0,337	0,281	0,238	0,667	0,455	0,505	0,340	0,366	0,250	0,731	0,442	0,586	0,349	0,456	0,270
2	1,292	0,649	0,817	0,301	0,516	0,146	1,317	0,616	0,920	0,356	0,652	0,222	1,366	0,570	1,011	0,355	0,750	0,229
3	1,913	0,535	1,121	0,174	0,676	0,068	1,945	0,524	1,262	0,209	0,850	0,102	1,993	0,541	1,365	0,224	0,969	0,115
4	2,469	0,421	1,356	0,099	0,790	0,031	2,503	0,423	1,514	0,124	0,989	0,046	2,550	0,423	1,627	0,133	1,114	0,055
5	2,968	0,339	1,530	0,059	0,865	0,015	3,004	0,342	1,714	0,072	1,085	0,023	3,050	0,340	1,835	0,077	1,215	0,025
6	3,415	0,273	1,668	0,034	0,917	0,007	3,455	0,276	1,863	0,043	1,148	0,010	3,498	0,274	1,989	0,046	1,283	0,012
<b>Failure</b>	<b>r<sub>u</sub>=0.25</b>																	
1	0,415	0,402	0,276	0,304	0,188	0,233	0,143	0,236	0,338	0,291	0,233	0,228	0,537	0,364	0,406	0,292	0,286	0,228
2	0,873	0,390	0,593	0,228	0,422	0,147	0,354	0,131	0,691	0,275	0,507	0,195	1,059	0,388	0,796	0,276	0,578	0,197
3	1,280	0,287	0,847	0,139	0,598	0,083	0,514	0,070	0,968	0,169	0,714	0,108	1,472	0,346	1,087	0,201	0,810	0,140
4	1,625	0,211	1,045	0,086	0,732	0,048	0,630	0,038	1,185	0,105	0,872	0,065	1,829	0,241	1,317	0,120	0,984	0,080
5	1,926	0,158	1,203	0,054	0,834	0,027	0,720	0,021	1,360	0,066	0,993	0,038	2,150	0,179	1,502	0,073	1,117	0,046
6	2,187	0,119	1,329	0,034	0,913	0,016	0,788	0,012	1,498	0,041	1,085	0,022	2,427	0,134	1,645	0,045	1,218	0,027
<b>Failure</b>	<b>r<sub>u</sub>=0.5</b>																	
1	0,436	0,444	0,313	0,357	0,280	0,406	0,490	0,404	0,355	0,327	0,246	0,268	0,533	0,378	0,403	0,310	0,277	0,250
2	0,997	0,531	0,723	0,343	0,676	0,327	1,083	0,511	0,790	0,347	0,605	0,269	1,119	0,450	0,857	0,323	0,636	0,248
3	1,515	0,445	1,077	0,248	1,014	0,232	1,597	0,468	1,152	0,276	0,891	0,201	1,624	0,474	1,233	0,304	0,937	0,221
4	1,993	0,382	1,382	0,183	1,305	0,166	2,082	0,386	1,471	0,199	1,123	0,131	2,110	0,395	1,560	0,218	1,182	0,146
5	2,443	0,324	1,644	0,136	1,555	0,123	2,526	0,330	1,744	0,147	1,315	0,088	2,557	0,331	1,842	0,156	1,382	0,095
6	2,868	0,292	1,871	0,098	1,770	0,089	2,944	0,280	1,979	0,106	1,475	0,061	2,974	0,280	2,083	0,115	1,548	0,066



### 3.5.2. Case study

The use of the model presented in this chapter can be twofold; for example, it can be used to identify the magnitude of past earthquake events by back analysis of the shape and the extent of the landslide, or to predict possible future failures. In what follows, an illustrative example is described to show how the model can be used for real cases. The case study described below is one of the most seismically active areas in the world (located south of Iquique in northern Chile), where the presence of large rockslide and avalanches occurred at different times is well documented.

The study area lies along the hypo-arid coastal area of the Atacama Desert (Figure 3.17), with mean annual precipitation of about 1 mm, south of Iquique in northern Chile (Tarapaca province - between latitude  $20^{\circ}6'S$  and  $20^{\circ}26'S$ , longitude  $70^{\circ}05'W$  and  $70^{\circ}10'W$ ). The hypo-arid climate persists in this region since a few million years. This area coincides today with one of the most important seismic areas along the subduction zone of the Nazca plate without major earthquakes since those 1868 and 1877 (Beck and Ruff, 1989, Lomnitz, 2004, Baker et al., 2013). The area is characterized by a sequence of layered sedimentary rocks, prevalently marls and limestones, dipping with the slope (cataclinal) and covered at the cliff top by alluvial conglomerates characterized by polygenic angular to subangular clasts in a brownish sandy-silty matrix (Crosta et al., in press). In this area along the coastal scarp and the coastal plain, some huge rock avalanches and rotational landslides have been mapped (Crosta et al., 2012b, Crosta et al., 2014a). An example of a rock avalanche with a sequence of deposits is given in Figure 3.18.

In Figure 3.18a the elevation profiles of the slope before the failures and the present situation are illustrated. The pre-failure profile is obtained from

the slope beside the area of interest that has not yet suffered failures. The average initial slope angle is  $27^\circ$  and the final average angle is approximately  $22^\circ$ .



*Figure 3.17. Area of interest for the case study.*

As visible in Figure 3.18b, a series of rock avalanche deposits can be recognized from events occurring in a sequence all from the same source area. More rock avalanche groups have been recognized in the same area. The geometrical relationships among the various deposits of each group allow to define a relative age or order of occurrence for the various events (Crosta et al., in press). This makes evident a progressive decrease in rock avalanche size with time or order of occurrence within the sequence. Furthermore, field observations and aerial photointerpretation support the hypothesis that the main failure surface (or failure surfaces envelope) daylights about 250 m

above the slope toe. This is an important feature of these phenomena, which must be stressed because it could be an indicator of a possible seismic triggering. In fact, earthquake induced rockslides generally affect the middle-upper portions of steep rock slopes where major seismic amplification effects are focused and a minor groundwater role is recognized.

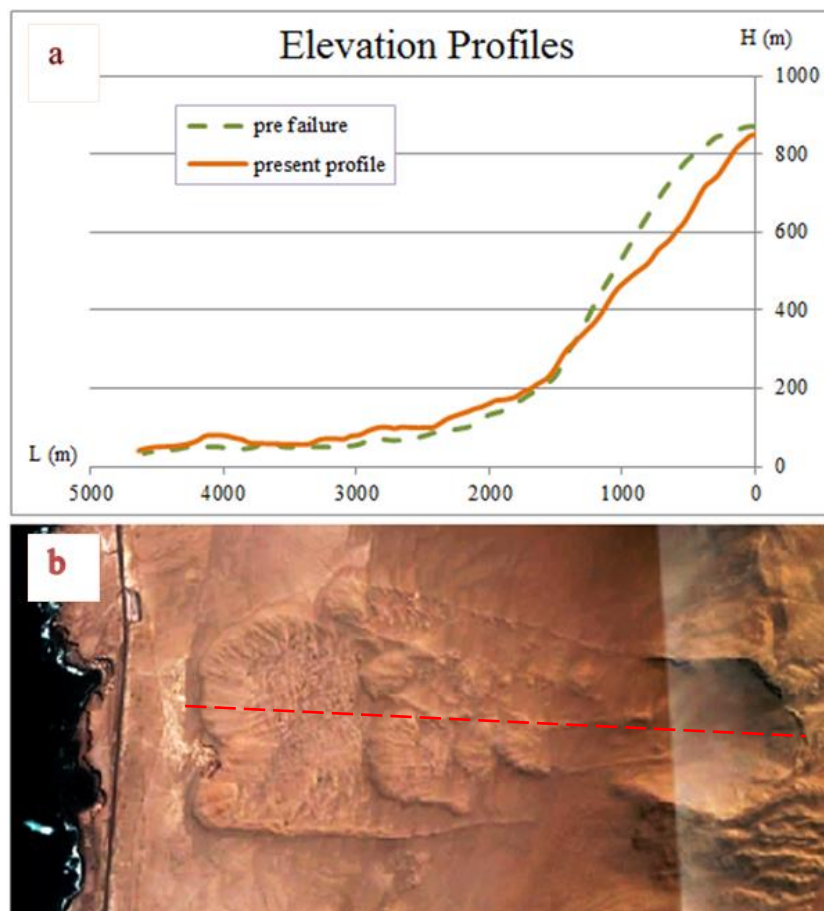


Figure 3.18. a. Elevation profiles for the rock avalanche area before and after the failures, b. group of rock avalanches studied here. The failure surface envelope daylight above the slope toe.

The implementation of the model either looking for the yield acceleration of past events or for the most critical failure mechanism under

various seismic accelerations is presented in this section. First the model is applied to a simplified slope based on the case described above and the yield acceleration of past events is estimated. Then the evolution of a slope under different seismic accelerations is presented.

The model calibration is performed by looking for the sequence of failures with cross sectional areas (i.e. volumes in three dimensions) similar to the observed ones. In particular, there should be a relationship between real and computed volumes (or cross sectional areas). The final geometry of the landslide alcove, generated by the complete sequence of failures, is also considered for calibration

For all the results presented in this section, either looking for the slope yield acceleration or the most critical slip surface, only horizontal seismic action has been assumed ( $\lambda=0$ ).

### ***Calculation of yield acceleration for past events***

The proposed model was applied to a simplified slope with initial slope angle  $\beta=27^\circ$  (the average angle of the initial profile in the study area deriving from Figure 3.18a) as illustrated in Figure 3.19 and four successive failures were assumed based on the results of (Crosta et al., in press). The characteristics of the soil (friction and cohesion) during each failure are also based on the results of (Crosta et al., in press) regarding the study area discussed in the previous section, while the height of each failure event is proportional of the volume obtained in the same paper. Unfortunately, relatively few data are available about the geomechanical characteristics of the rock masses, because of the poor outcropping conditions.

The estimated height and cohesion for every landslide are presented in Table 3.4. A constant bulk unit weight of 25kN/m<sup>3</sup> was assigned and the friction angle is assumed to be the same for every event  $\varphi=35^\circ$ . Note that the results presented here are based only on assumptions on the landslide heights as the geometric parameters of each failure cannot be calculated in detail (height and retreat length).

*Table 3.4. Estimated yield acceleration for four past failure events*

<b>Failure</b>	<b>1</b>	<b>2</b>	<b>3</b>	<b>4</b>
<b>c (kPa)</b>	300	250	250	200
<b>H (m)</b>	480	230	160	115
<b>K<sub>y</sub></b>	0.33	0.27	0.26	0.32

For the first failure, and from (Crosta et al., in press) observations, the total height of the failure was estimated to be around 450-500 m. The reason that the mechanism for the first failure did not pass from the slope toe, as this would have been the most critical failure mechanism for the static case, can be due to inhomogeneity of the material or can be related straight to the seismic activity in the region. This height was also assigned to the model to calculate the most yield acceleration of the first failure.

Given the characteristics described above and by solving equations [3.27] and [3.42] to  $K_y$ , the final profile of the slope and the yield coefficient of acceleration (Table 3.4) for the first and each successive failure can be obtained respectively. For the first failure, the equation of the yield acceleration coefficient is:

$$K_y = \frac{\frac{c}{\gamma H} f_{d1} \{ \exp[\tan \varphi (y_1 - x_1)] \sin y_1 - \sin x_1 \} - (f_{1_v} - f_{2_v} - f_{3_v})}{\lambda(f_{1_v} - f_{2_v} - f_{3_v}) + (f_{1_h} - f_{2_h} - f_{3_h})}$$

and for the second and each successive failure:

$$K_y = \frac{\frac{c}{\gamma H} f_{d2} \{ \exp[\tan \varphi (y_2 - x_2)] \sin y_2 - \sin x_2 \} - (f_{1_v}^n - f_{2_v}^n - f_{3_v}^n - f_{1_v}^o + f_{2_v}^o + f_{3_v}^o)}{\lambda (f_{1_v}^n - f_{2_v}^n - f_{3_v}^n - f_{1_v}^o + f_{2_v}^o + f_{3_v}^o) + (f_{1_h}^n - f_{2_h}^n - f_{3_h}^n - f_{1_h}^o + f_{2_h}^o + f_{3_h}^o)}$$

The final profile after the four successive failures is close to the situation as observed today with an average inclination of  $22^\circ$  (Figure 3.19). In Figure 3.20, the areas calculated by limit analysis and the volumes as extrapolated from the DTM topographic dataset in (Crosta et al., in press) for each failure, are plotted. Area and volume values in the plot are normalized to the areas and volume of the first failure respectively. By looking at Figure 3.20, it is evident that the older events are characterized by larger sliding areas and volumes; a progressive decrease in area and volume is recorded for the successive events (Crosta et al., in press).

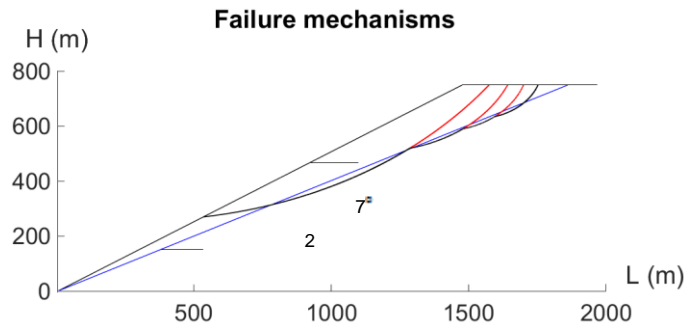


Figure 3.19. Past failure mechanisms for a simplified slope profile with initial slope inclination  $\beta=27^\circ$ .

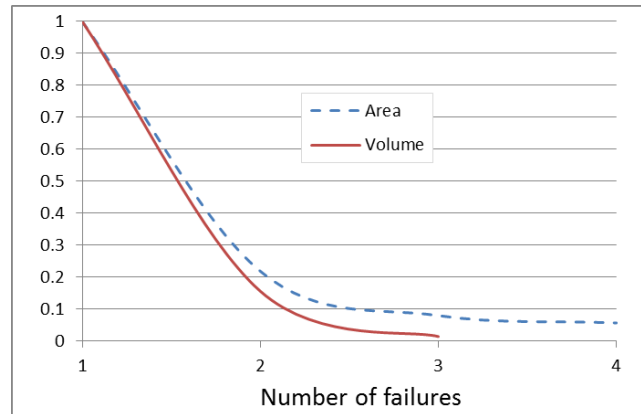


Figure 3.20. Sliding volumes and areas normalised to the first failure

### Prediction of future events

Using the same model solving equations [3.27] and [3.42], the most critical failure mechanisms can be obtained for slopes of any given height, angle and friction angle. The model is applied to a slope of initial slope inclination  $\beta=40^\circ$  and friction angle  $\phi=35^\circ$ . Three different seismic scenarios causing four successive failures each are considered and the failure mechanisms are obtained.

In Table 3.5, the stability number of each failure and for different coefficient of yield acceleration is illustrated. To make meaningful comparisons, the outcome of calculations, the associated crest retreat normalised by the initial slope height and the sliding area normalised by the square of the initial height are listed for all seismic scenarios and for four failures. In

Figure 3.21, the slope evolution is illustrated for the three different seismic scenarios. Solid line is illustrating the slope evolution after four failures, applying a horizontal seismic acceleration to the slope  $Kh=0.2$ , dashed line is used for the seismic acceleration is  $Kh=0.3$  and dotted line for  $Kh=0.4$ . It is obvious that the magnitude of the seismic acceleration can cause a significant

change in the stability of the slope but also can alter the failure mechanism; leading to larger amount of soil sliding away and larger cliff retreat for higher seismic acceleration. Combinations of different seismic acceleration for each failure as well as vertical seismic acceleration can easily be applied to the model. Note that the first failures for all seismic scenarios have been assumed to pass through the slope toe and the cases of failure surfaces passing below or above the toe failure have not been considered. In fact, failures below the slope toe can generally occur only for very low friction angles (Chen, 1975) and failures above the toe cannot occur for intact slopes for reasons of similarity. Moreover, after the second failure and to find each new failure mechanism, the potential failure lines have been searched only above the point of intersection of the two previous mechanisms.

*Table 3.5. Results for Associated Stability Number  $\gamma H/c$ , Crest Retreat normalized by the initial height of the slope  $CR/H$  and Sliding Area normalized by the square initial height of the slope  $A/H^2$  for slopes with initial inclination  $\beta=40^\circ$  and friction angle  $\phi=35^\circ$ , for horizontal seismic acceleration  $Kh=0.2$ ,  $Kh=0.3$  and  $Kh=0.4$ .*

	Failure	1	2	3	4
$K_h=0.2$	$\gamma H/c$	28.234	32.879	40.495	56.255
	$CR/H$	0.196	0.403	0.560	0.679
	$A/H^2$	0.295	0.129	0.056	0.0316
$K_h=0.3$	$\gamma H/c$	17.989	23.540	28.426	39.223
	$CR/H$	0.280	0.592	0.826	1.003
	$A/H^2$	0.359	0.218	0.101	0.061
$K_h=0.4$	$\gamma H/c$	12.628	18.007	22.535	27.310
	$CR/H$	0.422	0.842	1.189	1.479
	$A/H^2$	0.454	0.291	0.194	0.131



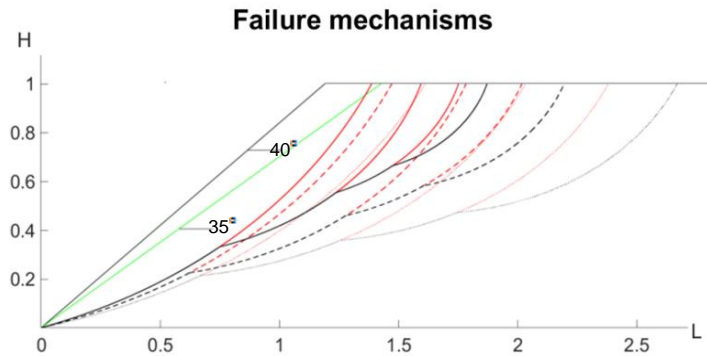


*Figure 3.21. Slope evolution during four successive failures under three different earthquake scenarios for slope with initial inclination  $\beta=40^\circ$  and friction angle  $\varphi=35^\circ$ . Solid lines refer to failure mechanisms under horizontal acceleration  $K_h=0.2$ , dashed lines to  $K_h=0.3$  and dotted to  $K_h=0.4$ .*

### 3.5. Conclusions

In this chapter, the upper bound theorem of limit analysis and the pseudo-static approach have been adopted for the assessment of the stability of homogeneous  $c, \varphi$  slopes subject to seismic action providing rigorous upper bounds to the true collapse values. The influence of pore water pressure has also been implemented in the model using the  $r_u$  coefficient. The limit analysis upper bound method was applied to determine each discrete landslide event occurring over time in a sequence of ordered events assuming the complete removal of the failed mass occurring before the onset of the successive mechanism.

Analytical solutions have been presented to investigate the effect of weathering induced strength degradation, seismic action, crack formation and various seepage scenarios on the geomorphological evolution of homogeneous slopes, employing the upper bound limit analysis method. Slopes are characterised by uniform cohesion, angle of shearing resistance, and finite tensile strength. The solutions were obtained considering a succession of discrete failure events (landslides) progressively altering the slope morphology over time and can be used to achieve a first rough estimation of the past or future evolution of a slope knowing a limited amount of information.

The location and the depth of the crack as well as the most critical failure mechanism for every failure were calculated through an optimisation procedure. Solutions were provided for the evolution of cohesive slopes with full tensile strength, with a prescribed limited tensile strength or no tensile strength at all (tension cut-off) for a range of friction angle and slope inclination of engineering interest and more results can be obtained using the Matlab code that is provided in the Appendix.

A comprehensive parametric analysis has been carried out to investigate the relative influence on slope evolution of the physical phenomenon considered, i.e. weathering induced strength degradation, seismic action, crack formation and seepage. It emerges that strength degradation, seismic action and seepage may significantly accelerate slope failure, exhibiting a stronger influence than the formation of cracks on the morphologic evolution of slopes. High seismic acceleration and / or seepage forces cause larger slope failure mechanisms and therefore larger slope crest retreats. Tension cracks forming due to exceedance of the limited tensile strength influence the first slope failures more than the subsequent ones. In

conclusion, the model here introduced allows in principle, to predict the evolution of natural cliffs subject to weathering processes and seismic events for cohesive geomaterials of limited (or nil) tensile strength.

Moreover, a case study in northern Chile was presented showing that the model can be used to identify the minimum magnitude of past earthquake events by back analysis of the shape and extent of previous landslides, and also to predict possible future scenarios. The kinematic approach of limit analysis can be used to calculate the least upper bound on the yield coefficient of acceleration  $K_y$  for a given slope with uniform cohesion  $c$  and internal friction angle  $\varphi$ . The yield acceleration can be defined as the minimum level of horizontal acceleration (vertical acceleration being proportional to the horizontal acceleration) that can cause the slope to fail. However, when performing such an analysis the assumptions behind the model (e.g. that the failed debris is carried away before the occurrence of a second failure) should be considered.

## **Chapter 4 : Experimental Methodology**

---

This work aims at the morphologic evolution of natural cliffs made of weakly cemented materials subject to progressive retreat under various causes. Physical modelling of landslide processes in the laboratory can potentially create well documented, highly-instrumented case-studies of slope behaviour in which the material properties, initial state, and boundary conditions are well defined. To this end, an experimental apparatus was designed and scaled slope models were built in a transparent flume. Rainfall was applied on them until failure was reached, while soil moisture content and suction were monitored by sensors buried inside the slope model. High resolution cameras record the behaviour of the slope model during the tests and GeoPIV software and Matlab image analysis are used to analyse the frames and obtain the deformations of the slope model and the movement of the water front. The reproduction of the slope failure process at a greatly reduced scale is not fully representative of full scale behaviour (Camponuovo, 1977), it is however a good approximation to approach the problem and to gain insight in the most important parameters.

The goal of this experiment is to develop a physical model able to replicate retrogressive slope failures due to various actions. A set of

experiments is carried out on soil with limited tensile strength; after a short period of rainfall and due to degradation of the soil strength, vertical cracks appear in the slope model and significant vertical deformations start to occur around the crack, until a failure occurs. The experimental results help quantifying the correlation between moisture content and landslide onset and highlight how debris propagation and deposition affect the stability of the remaining slope.

The present chapter reports on the laboratory apparatus and the experimental methodology that were designed and used for this research. The experimental program was carried out both at the Department of Geological Sciences and Geotechnologies of the University of Bicocca in Milano and at the Geotechnical laboratory of the University of Warwick in Coventry. Preliminary tests and soil characterization tests were carried out at the University of Bicocca, while the main experimental work was conducted at the University of Warwick.

#### **4.1. Preliminary tests**

Choosing the appropriate material to be used in the experiments was the first concern of the experimental set up. For this reason, the initial part of the experimental research was conducted at the Department of Geological Sciences and Geotechnologies of the University of Bicocca in Milano and included a set of preliminary experiments to conclude to the right material that would be used for the tests.

The material being sought should be able to simulate weathering in laboratory timescales and be easily produced. The objective was to reproduce and visualize the formation and destruction of the depositional bonds during wetting. In order to support the above described short-term mechanism, ad

hoc experiments were carried out and are reported below. Four different artificial materials to be bound by depositional bonds only were used: a mixture of powder of crushed calcarenite and glass beads or silica sand, and a mixture formed by powder of gypsum and glass beads or silica sand with different proportions. Also, some ideas on how to get the specimen to fail were verified in practice.

#### **4.1.1. Selection and design of (artificial) weakly bonded geomaterial suitable for laboratory weathering**

The preliminary tests were of a very small scale, and for this reason it was possible to test 20 alternative combinations (Table 4.1) of the materials mentioned above without using large amounts of materials. More specifically, small cylindrical specimens were prepared following the procedure proposed by (Soulié et al., 2007) and subsequently by (Ciantia et al., 2015a) and pictured in Figure 4.2b, with dimensions of diameter 13.00mm and height 28.00mm (Figure 4.2). Once the cylindrical sample is extruded (Figure 4.2b), it is oven dried for 24 h at 105° Celsius to evaporate all the water. The particle size of the materials used is <0.20mm for calcarenite powder and gypsum, 1.00 - 1.50mm for silica sand and 0.40 - 0.80mm for glass beads. The percentages used for each specimen are reported in Table 4.1. The name of each specimen illustrates the materials that it contains and the percentage of each material. The first letter stands for: B for glass beads and Q for silica sand, the second letter stand for: G for gypsum and C for calcarenite, the third letter inform about the percentage of water used for the preparation of each specimen and the last one (S) describes the percentage of fine silica sand.

Three specimens of each different combination were created (Figure 4.1 and Figure 4.2) and after being left to dry, they were tested under load in order to measure their strength (Figure 4.3a). Specimens 9 and 10 were very

loose and were destroyed only by touching them before testing. Because there was also an interest in the behavior of the material when encountering water, specimens were then tested under half of the load their dry peak strength, while at the same time water was gradually added to wet their base (see Figure 4.3b). The water at the base of the specimen was added gradually, starting from 2mm for the first two minutes and adding another 2.00mm every 2min. Results from dry and wet tests are presented in Table 4.1.

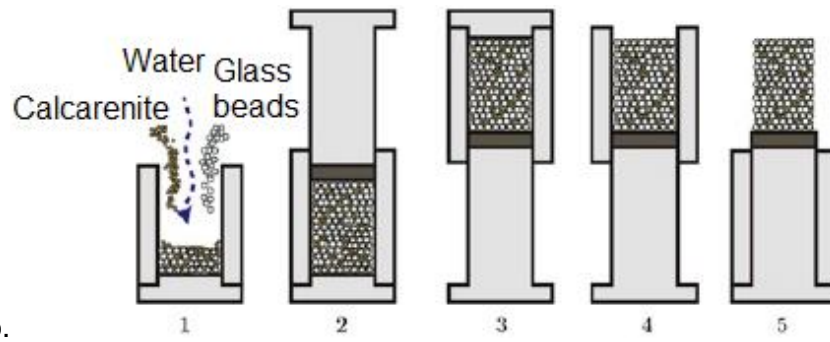


Figure 4.1. Twenty different specimens tested

The results of the tests suggested that the best candidates for the purpose of this research are number 1, 6, 19, 20. The next step of the procedure was to build small cubic models (15.00x8.00x6.00cm) with vertical front (Figure 4.4), in a small apparatus that was specially designed for this goal and test these four mixtures and their ability to form a slope model where a failure mechanism could develop under the influence of water.



a.



b.

Figure 4.2. a. Small specimen b. glass and powder structured sample preparation (Ciantia et al., 2015a)



a.



b.

Figure 4.3. Specimen under load a. dry b. with water at its base



Tests on the cubic specimens, have been carried out in order to identify a geomaterial giving rise to more than one failure under rainfall in a reasonable timespan. The specimens were prepared and left to dry, then a simple mechanism to wet them was built and placed on top of them and a digital camera to record the evolution of the slope was used. The results suggested that only the specimens containing calcarenite could be destroyed and demonstrate 'failure' in laboratory time (Figure 4.4), because those containing gypsum would not fail even after 5 days under constant wetting. After the completion of these preliminary tests, the material that fitted the desired characteristics was selected to carry out the main experiments for this research.

The mixture for all the slope models tested for the needs of this thesis consists of 43.5% w/w calcarenite, 43.5% w/w glass beads and 13% w/w water. This mixture has proved to be able to fail in laboratory time only under the influence of water, and a second failure was observed in the preliminary small scale slope model. In addition a similar material has been already studied and characterised by (Ciantia and Castellanza, 2015, Ciantia et al., 2015b) proving that real weakly bonds are created and can be destroyed just with water. The geotechnical properties of the calcarenite and the glass beads used for the construction of the slope models of the main experiments are illustrated in Table 4.2.

Table 4.1. List of the 20 specimens tested

	Name	F (g)	$\sigma$ (kPa)	50% F (g)	Water	Time
1	B40C40W20	40	3.1	20	2.00mm	<4min
2	B30C46W23	130	9.8	65	2.00mm	<1min
3	B60C26W13	22	1.7	11	destroyed	
4	B45C45W10	46	3.5	23	2.00mm	<2min
5	B43G43W14	170	10.3	85	2.00mm	4-5min
6	B60G24W16	3000	226	1500	Filled	n/d
7	B40G40W20	3000	226	1500	Filled	n/d
8	B70G20W10	3000	226	1500	Filled	n/d
9	Q70C20W10	0	0	0		
10	Q60C25W15	0	0	0		
11	Q40C40W20	44	3.3	22	2.00mm	<2min
12	Q30C50W20	130	9.8	65	2.00mm	<2min
13	Q70G20W10	3000	226	1500	Filled	3 days
14	Q55G32W13	3000	226	1500	Filled	n/d
15	Q80G16W6	3000	226	1500	Filled	n/d
16	Q65G10W10S15	2500	188.4	1250	Filled	n/d
17	G65G10W10S15	2500	188.4	1250	Filled	n/d
18	Q50G15W10S25	2500	188.4	1250	20.00mm	n/d
19	Q75G10W7S8	1100	82.9	550	20.00mm	6-7min
20	G80G7W5S8	1500	113	750	2.00mm	<1min

Note that B is for Glass beads, C for calcarenite, G for Gypsum, Q for Silica sand, S for fine silica sand and W for Water.

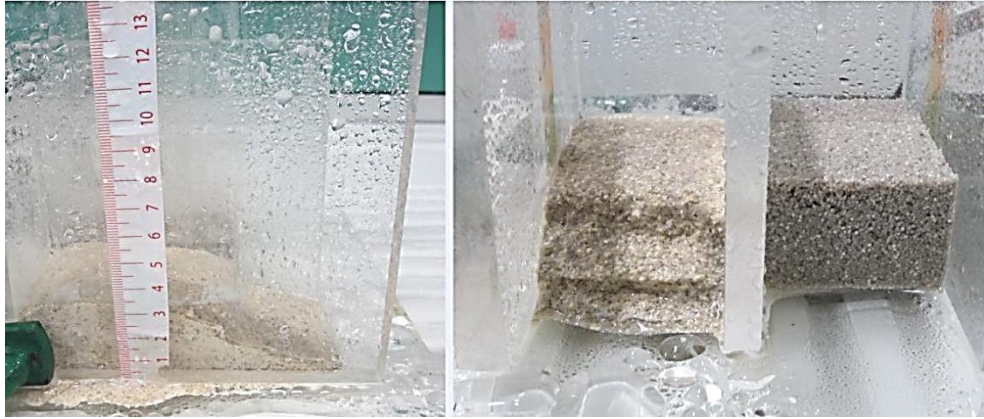


Figure 4.4. Small slope models (15.00x8.00x6.00cm) with vertical front

Table 4.2. Geotechnical properties of the materials used in the experiments.

**Geotechnical Properties of calcarenite (Castellanza et al., 2009)**

$\gamma_d$ (kN/m <sup>3</sup> )	$\gamma_{sat}$ (kN/m <sup>3</sup> )	Gs (-)	n (-)	e (-)
13.92	18.82	2.73	0.49	0.96

**Geotechnical Properties of glass beads**

$\gamma_d$ (kN/m <sup>3</sup> )	Gs (-)	Micron range
14.715	1.75	840-590

#### 4.1.2. Microstructure characterisation of the selected material

The Grain Size Distribution performed with sieve analysis is presented in Figure 4.5. The effective particle size D10 of the mixture is 0.12mm, the average particle size D50 is 0.6mm and the uniformity coefficient  $C_u = D_{60}/D_{10}$  is 5.83.

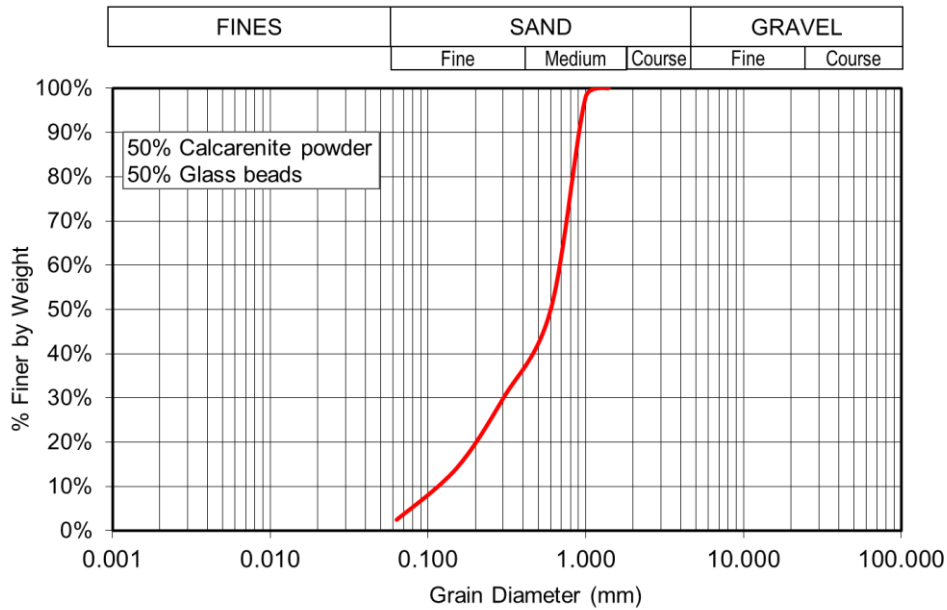
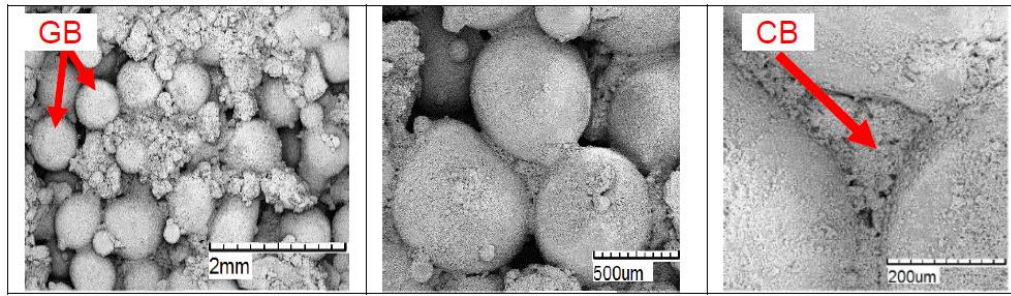


Figure 4.5. Sieve Analysis - Particle size distribution curve

By means of scanning electron microscope (SEM) analyses and mercury intrusion porosimetry (MIP), the microstructure both in 2D and 3D and the porosity of the material by different methods was defined. In what follows, only the most important results of such intensive micromechanical investigation of the material are reported. In Figure 4.6, a SEM image of the sample is used to show the grains and the bonds between the materials. In

Figure 4.7, a typical thin-section obtained from samples hardened with epoxy resin is photographed by means of a high-resolution camera connected to an optical microscope to illustrate the bonds between the materials.



*Figure 4.6. SEM images of 3D microstructure observations at increasing magnification (where GB stands for Glass beads and CB for calcarenite bonds)*

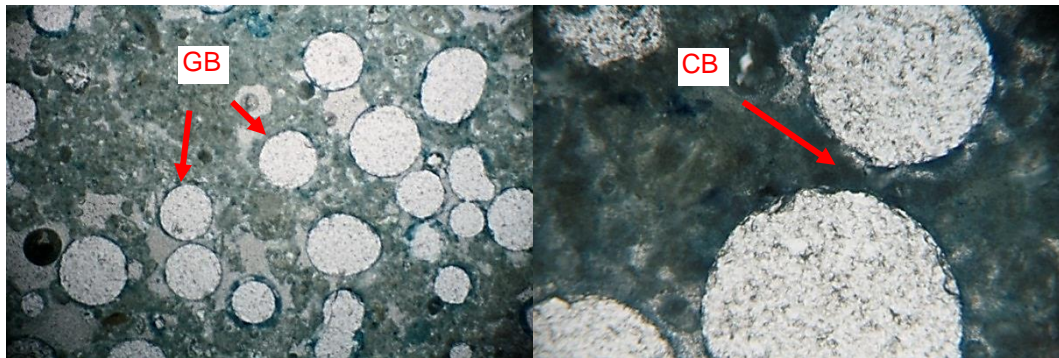


*Figure 4.7. Typical thin-sections obtained at an optical microscope (where GB stands for Glass beads and CB for calcarenite bonds)*

The results of the porosimetry test by means of mercury intrusion porosimetry MIP are illustrated in

Figure 4.8. The porosimetry samples that were prepared for this test are also shown in the figure. The porosity values calculated by the standard weighing method are summarised with those determined by MIP tests and 2D thin section image analysis in Table 4.3.

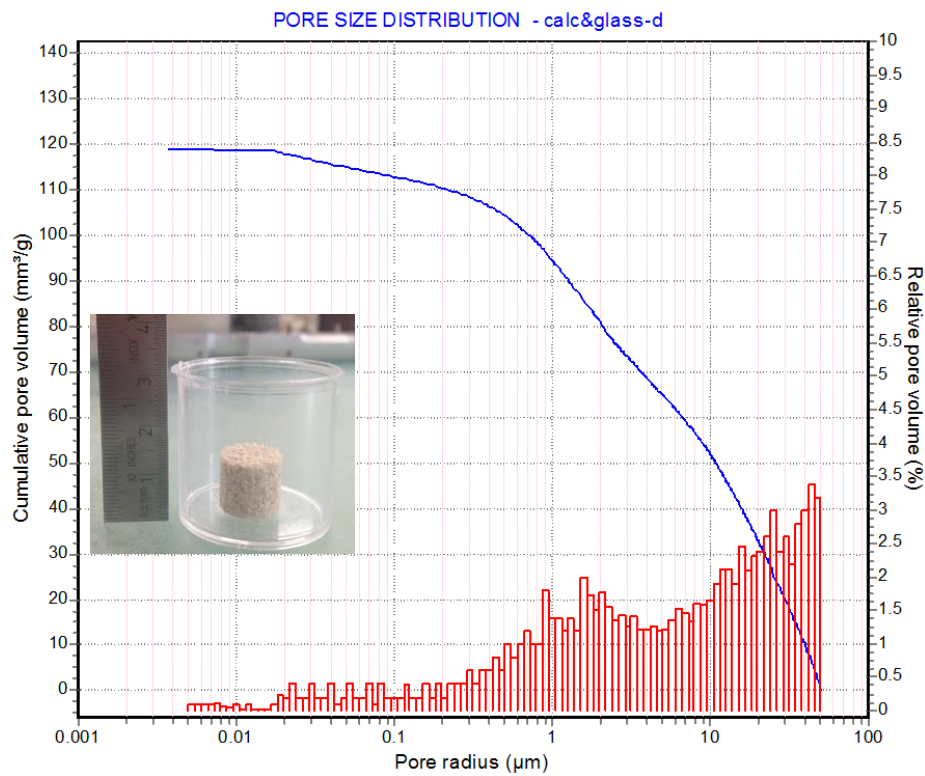


Figure 4.8. Porosimetry (blue curve for the cumulative pore volume and red columns for relative pore volume)

Table 4.3. Porosity values calculated by means of the standard weighting method, mercury intrusion porosimetry MIP, and 2D image analysis

	Weighting method	MIP	2D - thin section
Porosity n	0.34	0.25	0.30

#### 4.1.3. Macro scale tests to show the short term debonding process

In this part of the thesis, macro experimental investigations performed on the selected material are shown; short- and long-term debonding processes are leading to the macro-scale weakening mechanisms of the

weakly cemented material. The dry strength is first investigated by means of UCT using strain controlled (0.25mm/s and 0.05mm/s) uniaxial compression test equipment. In Figure 4.9a and b the dry and wet soil sample after failure during the uniaxial test are illustrated and in Figure 4.9c the stress strain curve is shown at different saturation degrees of the material. In Figure 4.10 the soil water characteristic curve (SWCC) of the material obtained by pressure plates and ku-pF tests are plotted. Ku-pF is a laboratory instrument for the automatic determination of any saturated hydraulic conductivity  $k_u$  and the pf curve (water tension curve).

Soil strength can be expressed by two parameters, cohesion  $c$  and internal friction angle  $\phi$ , according to the Mohr-Coulomb yield criterion. Hence, to characterise the strength of the material under different water contents, shear box tests have been carried out.

Specimens of the exact same characteristics (components and density) as those used in the main experiments and with different moisture content, therefore various degrees of weathering were tested and the failure envelopes were obtained. The failure envelopes obtained from the direct shear tests are illustrated in Figure 4.11. The tests were carried out in dry samples, samples with moisture content 15% that were left for approximately an hour after the water was added and before the initiation of the test and saturated samples that were tested approximately 24 hours after the water was added to the soil. As shown in Figure 4.11, the increase in water content results in a decrease of the strength characteristics of the material. It causes mainly a decrease in the cohesion and a lower decrease in the friction angle of the material.

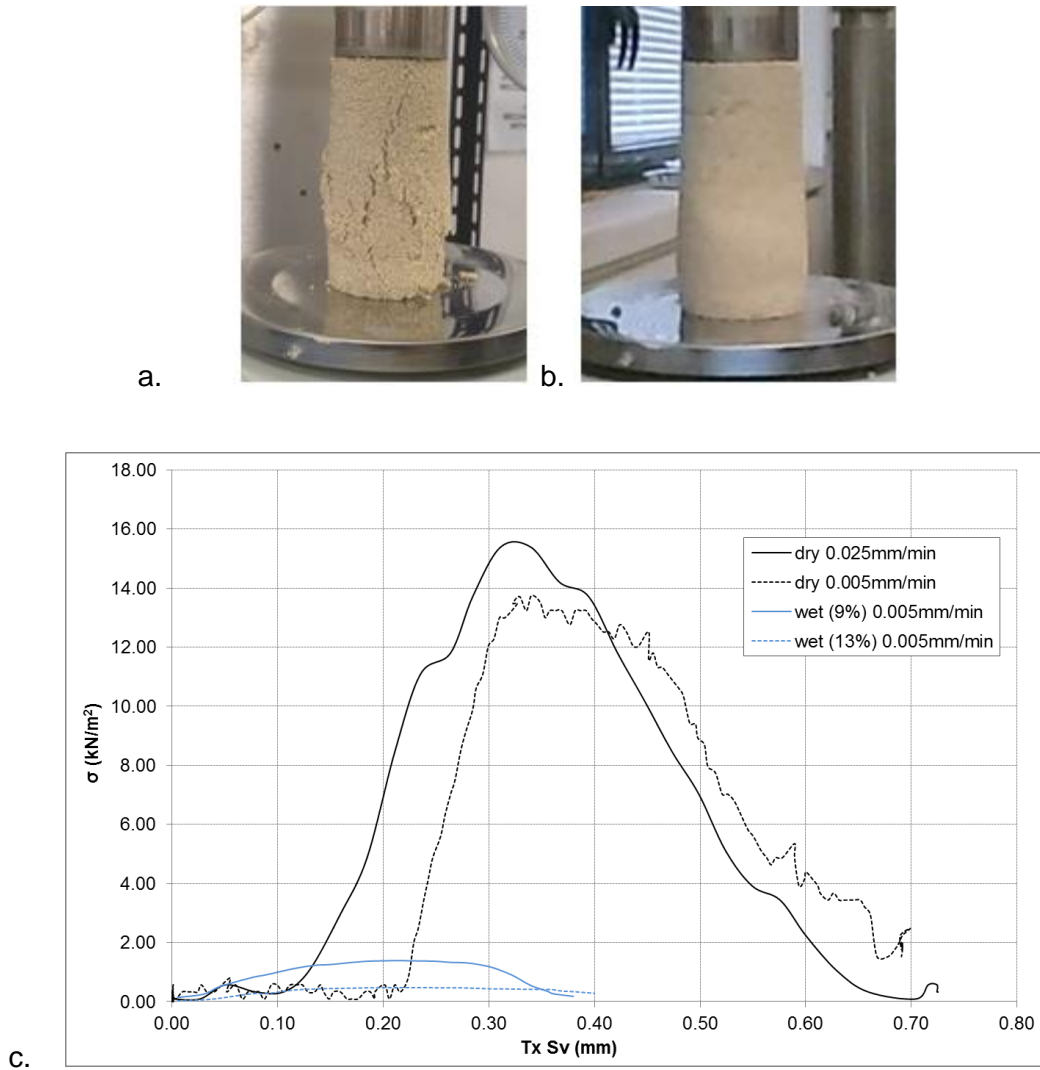


Figure 4.9. a. Dry soil sample after failure during the uniaxial test b. a. Wet soil sample after failure during the uniaxial test c. Stress strain curve at different moisture contents



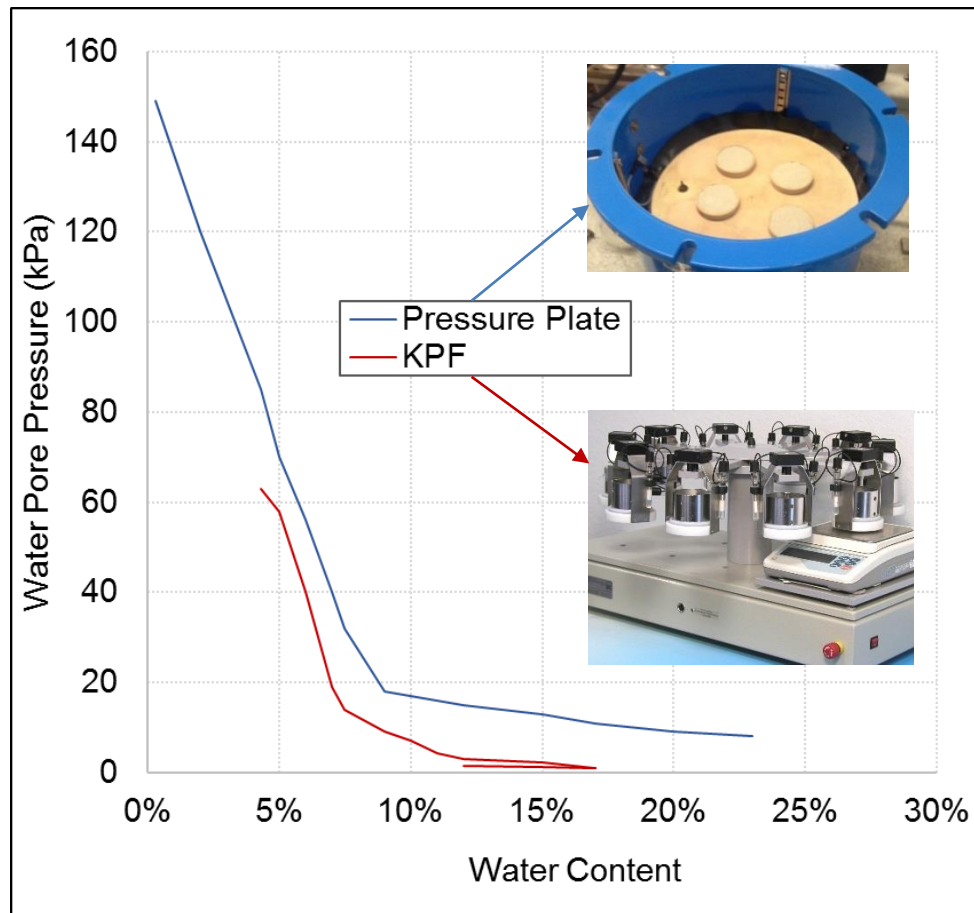


Figure 4.10. Comparison of SWCC derived from pressure plate tests and  $k_u$ - $pF$  and from measurements taken during calibration box tests

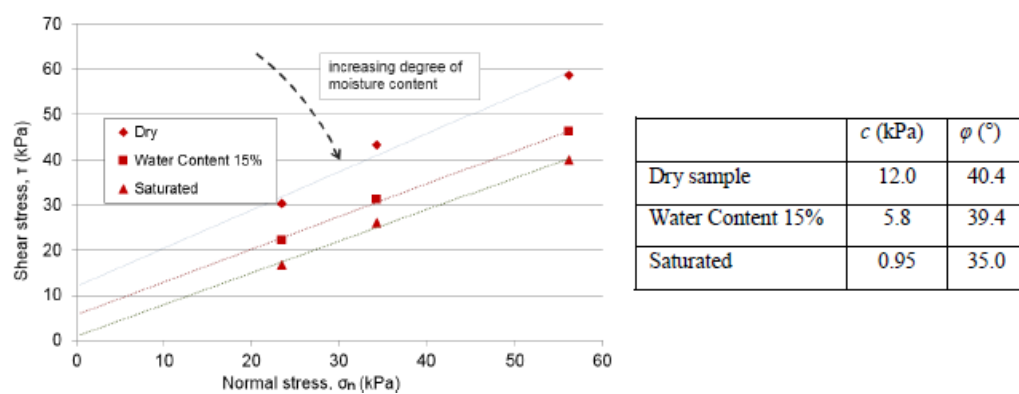
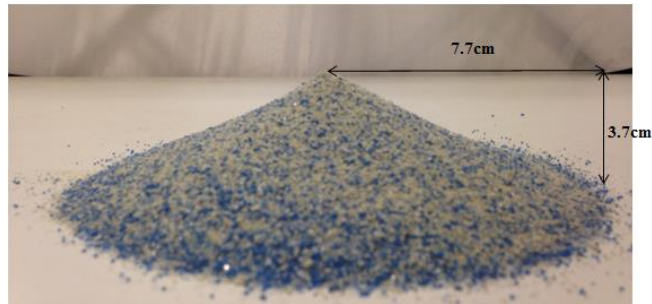
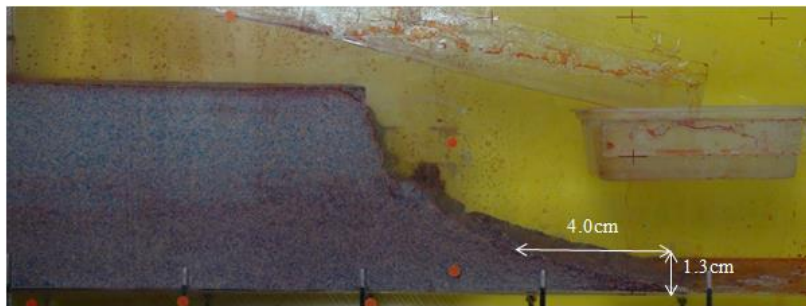


Figure 4.11. Shear box tests for different water contents

Finally, to conclude on the length of the flume where the slope models were prepared the repose angle of the material was estimated both for dry mixture and for a saturated sample, as can be seen in Figure 4.12.



*Angle of repose of dry mixture:  $\arctan (3.7/7.7) = 25.7^\circ$*



*Angle of repose of saturated sample:  $\arctan (1.3/4.0) = 18^\circ$*

*Figure 4.12. Repose angle of dry and saturated sample*

## 4.2. Physical Model

The main experimental program was carried out in the University of Warwick and involved two parts. First, a calibration box was built and a set of calibration tests were carried out to verify that the construction procedure of the slope models was accurate enough and that the test was repeatable. Second, the main apparatus was designed and constructed as well as the

rainfall simulation device and slope models were of different geometries were tested under different scenarios.

#### **4.2.1. Dimensional Analysis**

The main challenge is to provide rational analyses of large scale landslides via small scale laboratory tests. Since a model test is employed to study the progressive failure mechanism of a slope, a number of physical parameters that are used have to be related between the model and the prototype by satisfying three necessary conditions for complete similarity between a model and a prototype (Cengel, 2010):

- Geometric similarity - the model must be the same shape as the prototype, but may be scaled by some constant scale factor.
- Kinematic similarity - the velocity at any point in the model must be proportional (by a constant scale factor) to the velocity at the corresponding point in the prototype.
- Dynamic similarity - When all forces in the model scale by a constant factor to corresponding forces in the prototype (force-scale equivalence).

When the above conditions are met the reliability and feasibility of the test are ensured.

Dimensional analysis is a means of simplifying a physical problem by appealing to dimensional homogeneity to reduce the number of relevant variables. The three primary purposes of dimensional analysis are to:

- Generate non-dimensional parameters that help in the design of experiments (physical and / or numerical) and in the reporting of experimental results.

- Obtain scaling laws so that prototype performance can be predicted from model performance.
- Predict (sometimes) trends in the relationship between parameters.

By means of dimensional analysis, the governing parameters of the problem are identified, and then the independent and dependent dimensionless groups are formulated. The parameters include soil and geometric properties, rainfall intensity, velocity of the weathering front and characteristic times, where the units are expressed using fundamental dimensions L, M and T, for length, mass and time respectively, as listed in Table 4.4. Based on how these parameters are related during the test they are categorized as independent and dependent ones.

*Table 4.4. The governing parameters of the slope model*

	Parameter	Symbol	Dimension	Unit
<b>Independent parameters</b>	Initial slope height	$H_i$	[L]	m
	Initial slope length	$L_i$	[L]	m
	Slope width	$W$	[L]	m
	Gravitational acceleration	$g$	$[LT^{-2}]$	$m/s^2$
	Friction angle	$\phi$	[-]	
	Cohesion	$c$	$[M/LT^2]$	$kN/m^2$
	Rainfall intensity	$r$	$[L/T]$	mm/h
	Weathering velocity	$v_w$	$[LT^{-1}]$	$m/s^2$
<b>Dependent parameters</b>	Failure location	$L_{fi}$	[L]	m
	Failure duration time	$t_f$	[T]	s
	Particle velocity	$v_f$	$[LT^{-1}]$	$m/s^2$

The objective of this research is to investigate the location and the time of the successive failures. For that reason, the dependent parameters are the

location of each failure ( $L_{fi}$ ), the particle velocity ( $v_i$ ) and the failure duration time ( $t_i$ ). The other parameters are set as the independent ones.

Greek letter Pi ( $\Pi$ ) denotes a non-dimensional parameter. In a general, in a dimensional analysis problem, there is one  $\Pi$  called the dependent  $\Pi$ , giving it the notation  $\Pi_1$ . The parameter  $\Pi_1$  is in general a function of several other  $\Pi$ 's, called independent  $\Pi$ 's. The functional relationship is:

$$\Pi_1 = f(\Pi_2, \Pi_3, \dots, \Pi_k)$$

To ensure complete similarity between the model test and the real case, the model and prototype must be geometrically similar, and all independent groups ( $\Pi$ ) must be identical between model and prototype (Cengel, 2010). Under these conditions the dependent  $\Pi$  of the model ( $\Pi_{1,m}$ ) is guaranteed to also equal the dependent  $\Pi$  of the prototype ( $\Pi_{1,p}$ ). Mathematically, the conditional statement for achieving similarity can be written:

$$\text{If } \Pi_{2,m} = \Pi_{2,r} \text{ and } \Pi_{3,m} = \Pi_{3,r} \dots \text{ and } \Pi_{k,m} = \Pi_{k,r} \text{ then } \Pi_{1,m} = \Pi_{1,r}.$$

Assuming the above, that a link exists between the independent and the dependent parameters a general functional relationship can be written as:

$$(L_{fi}, v_i, t_i) = f(H_i, L_i, W_i, g, \phi, c, r, v_w)$$

In Table 4.5, the relationship between the physical quantities of the real and the model slope is illustrated (Roscoe, 1968, Chen et al., 2012), obtained from similarity analysis. The scaling factor ( $\lambda$ ) between the length of the real slope ( $L_r$ ) and the slope model ( $L_m$ ) is  $\lambda = L_r/L_m$  and the materials used in the model slope have the same unit weight with the real slope. According to (Askarinejad et al., 2012) the seepage time in the model is  $\lambda$  times less than that of the real slope as the seepage length in the model is  $\lambda$  times shorter, therefore the duration of the rainfall in the  $\lambda$  times scaled down model is  $\lambda$

times less than that of the real slope. Moreover, the length equivalent of the total precipitated rainfall in the model is  $\lambda$  times less than that of the real slope, making the rainfall intensity which is the ration between the total rain and the rain duration equal between the model and the real slope.

*Table 4.5. Dimensional analysis of the physical quantities in model test*

Physical Quantity	Relationship
Length	$L_m = (1/\lambda) L_r$
Slope angle	$\theta_m = \theta_r$
Unit weight	$\gamma_m = (1/\rho) \gamma_r = \gamma_r$
Friction angle	$\phi_m = \phi_r$
Pore water pressure (or stress)	$u_m = (1/\lambda) u_r$
Strain	$\epsilon_m = \epsilon_r$
Time	$t_m = (1/\lambda) i_r$
Rainfall intensity or velocity	$i_m = i_r$
Hydraulic conductivity	$k_m = (1/\lambda) k_r$

*Note that  $\lambda$ , and  $\rho$  are the scaling factors for length and unit weight respectively. In this study, the value of chosen to be  $\lambda$  was equal to 100 and  $\rho$  was equal to 1.*

To choose the appropriate scaling factor, the procedure that is simulated need to be studied. For example, weathering processes can have different velocities depending on the type of weathering, the changes and the evolution of natural slopes range from decades to thousands years depending on the type of soil and the weathering processes. To manage to model the weathering of a slope in the laboratory, a scaling factor should be chosen that will allow the progressive failure of the slope model to occur in laboratory time.

#### 4.2.2. Main test Apparatus

During laboratory testing, there are practical constraints such as space and material quantities making large scale modelling costly and prohibitive. To this end an apparatus was designed able to accommodate the needs of this research. The experimental apparatus is illustrated in Figure 4.13 (all dimensions are in centimetres). The main apparatus consists of a soil container made of 10mm thick Plexiglas supported by a steel frame, a rainfall simulation device, eight soil moisture sensors, two tensiometers and two high speed cameras to record the movement of the slope model during the tests. The container, with transparent sides, is 120.00cm long, 12.00cm wide and 50.00cm high (inner dimensions).

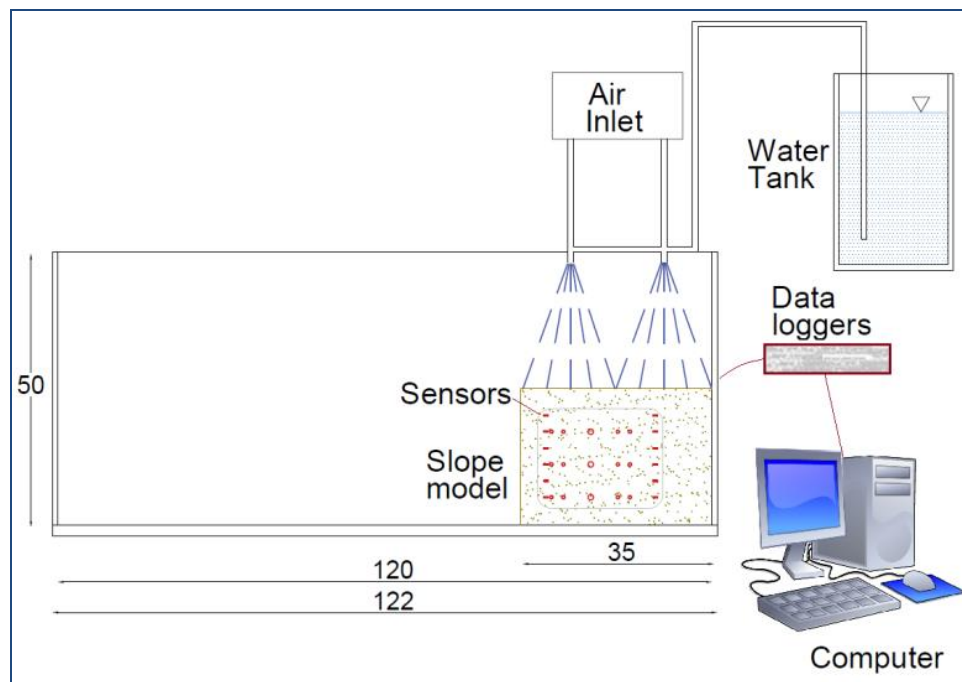


Figure 4.13. Arrangement of the experimental apparatus

Starting at longitudinal distance  $x = 10.00\text{cm}$  from one end of the flume and at latitudinal distance  $y = 28.00\text{cm}$  from the top of the flume, a mesh of

small holes is drilled. The holes are located 1.50cm far from one another (vertically and horizontally) and are used to place the soil moisture sensors and the tensiometers. The other end of the sensors is connected to an Arduino microcontroller and / or a Delta-T GP2 data logger that allow the data to be logged in on a computer for further analysis.

Two water nozzles are placed above the container, which under constant pressure; induce steady and uniform rainfall on the model. Finally, two high resolution cameras (25fps) are also used to monitor the test process from both sides of the flume.

#### 4.2.3. Slope model

For the experiments, homogeneous slope models made of the material described in paragraph 4.1 above are constructed. Although non planar slope profiles are more common in nature and they may be more stable than planar ones (Utili and Nova, 2007), all the experiments were performed with planar slopes for sake of simplicity.

*Table 4.6. General characteristics of the slope model (height  $H=15.00\text{cm}$ )*

<b>Number of layers</b>	<b>15</b>
Layer Width (cm)	12
Layer Length (cm)	35
Layer Height (cm)	1.00
Weight of layer (g)	714
Weight of the model (g)	10710
Volume of the model (cm <sup>3</sup> )	6300
Wet Bulk density (g/cm <sup>3</sup> )	1.700
Dry Bulk density (g/cm <sup>3</sup> )	1.478



The dimensions of a typical vertical slope model were height: 15.00cm, width: 12.00cm and length: 35.00cm and the general characteristics are illustrated in Table 4.6. For the construction of homogeneous slope models, the materials were manually mixed and layered inside the box in 15 layers of 714gr each. Each layer was compacted by a specifically designed plexiglass plate into 1.00cm height to achieve uniformity of the slope model, obtaining a wet density of  $1.7\text{g/cm}^3$ . The soil moisture sensors and tensiometers were buried inside the slope model during the construction phase (Figure 4.14), to cause the least possible disturbance to the soil.

Transparent silicon oil was applied on the sides of the container to avoid friction between the slope model and the container. Tests have also been carried out without applying the silicon oil on the sides of the container. Soil material would stick to the sides not allowing for a failure mechanism to develop.

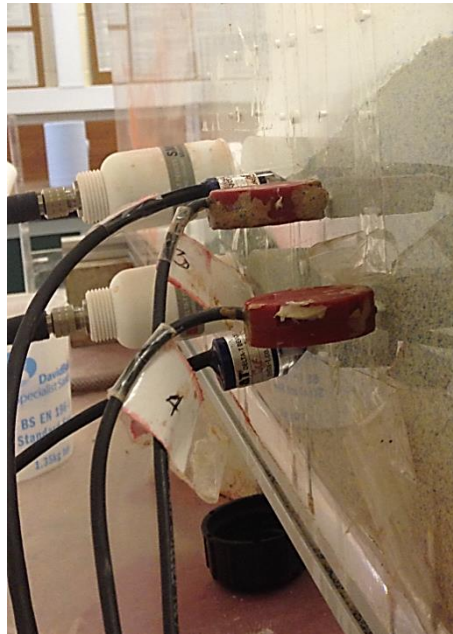


*Figure 4.14. Picture during the construction phase and placing the sensors*

Moreover, thin plastic drainage rails were glued to both sides to prevent water from coming into the slope model from the sides (Figure 4.17).



*Figure 4.15. Transparent plastic drainage rails at the sides of the container*

#### **4.2.4. Rainfall simulation device**

Two different artificial rainfall systems were developed and used. For higher rainfall intensities, the artificial rainfall system consists of a 1x12v diaphragm pump, a control set including a pressure gauge and a pressure regulating valve, plastic pipes and two M1 - Mini nozzles (Figure 4.16a), providing rainfall intensity of approximately at 40 - 60 mm/h. The flow rates of these nozzles are 0.04 l/h and 0.045 l/h, operating at 3 and 4 bars respectively. Different pressures can be set and flow rates can be determined. The desired surface of the slope crest can be wetted by adjusting the nozzle in different heights. In these experiments the nozzles are placed 32.00cm above the slope crest. For lower rainfall intensities, two GSC1 gravity atomising nozzles (Figure 4.16b) were used to achieve small drop size and to provide rainfall intensities of 5 - 30 mm/h by adjusting the inlet pressure.

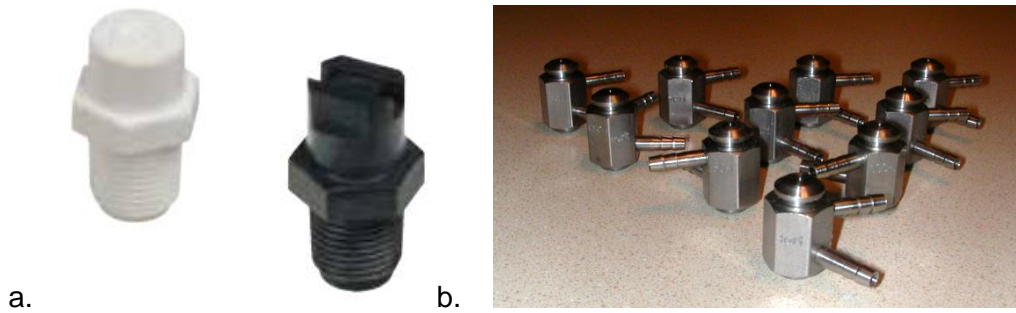


Figure 4.16. a.M1 - Mini Nozzles, b. GSC1 gravity nozzles

The nozzles are placed directly above the container and guarantee uniformity and accuracy. The uniformity of the nozzles was tested using small containers and measuring the flow rate at different pressures. Moreover, during all tests small containers were placed on the top of the slope to measure the rainfall intensity.

#### 4.2.5. Monitoring System

In the following, the main geotechnical and geophysical measurements of the monitoring system are described. The main technical features of all the probes used in the monitoring program (e.g., the manufacturer, accuracy, and operational range) are given in Table 4.7.

*Table 4.7. Main Technical Features of Probes Used for Monitoring*

<b>Device</b>	<b>Product name</b>	<b>Manufacturer</b>	<b>Accuracy and operational range</b>
Moisture sensors	SM300	Delta-T Devices ( <a href="http://www.delta-t.co.uk/">http://www.delta-t.co.uk/</a> )	$\pm 0.025\text{m}^3.\text{m}^{-3}$ (2.5%) - Full accuracy over 0 to $0.5\text{m}^3.\text{m}^{-3}$
Moisture sensors	Vegetronix VH400	Vegetronix ( <a href="http://www.vegetronix.com/">http://www.vegetronix.com/</a> )	2% at 25°C
Tensiometers	SWT-5x	Delta-T Devices ( <a href="http://www.delta-t.co.uk/">http://www.delta-t.co.uk/</a> )	$\pm 0,5$ kPa From -160kPa to 160kPa

### **Soil Moisture Sensors**

To record the changes in the volumetric water content of the soil by time, six Vegetronix VH400 soil moisture sensors were initially buried horizontally in one side of the slope model. The location of the soil moisture sensors is shown in Figure 4.13. The accuracy of these sensors is 2% and they measure volumetric soil moisture content, using transmission line techniques to detect the dielectric constant of the soil. The size of the sensors is very small, 9.40cm long and 0.70cm thick, thus causing minimal disturbance to the surrounding soil.

The water content of the soil is recorded at frequency 1/s. Since reliable measurements are very important while performing experiments, two SM300 soil moisture and temperature sensors were also obtained later on during the tests and were also buried inside the slope model for independent measurements. These sensors are even smaller than the VH400 sensors causing least disturbance to the soil, their accuracy is 2.5% for the moisture content and 0.5°C for the temperature and they give continuous readings. The

SM300 sensors are used in combination with the others to ensure correct readings.

Vegetronix VH400 soil moisture sensors were connected with an Arduino microcontroller and a code was written to obtain readings every second while SM300 sensors were connected to a GP2 Delta-T devices Data Logger obtaining continuous measurements.

Soil moisture content tests took place in the laboratory to calibrate the output voltages of the sensors prior to the main tests. Moreover, some preliminary tests for the response time of these sensors were conducted, using small samples of the same density as that of the slope model and with known water contents which showed that the sensors responded accurately in less than 1s of contact with the soil.

### ***Tensiometers***

The suction of the soil can have a considerable influence on the slope stability (Fredlund et al., 1978); therefore it is essential to determine the suction of the slope during the test to evaluate the likelihood of a slope failure. In order to capture the changes in the soil suction during the tests, two tensiometers (SWT-5x) were employed. The accuracy of these tensiometers is  $\pm 0.5$  kPa while the small size of the shaft (5mm diameter and 5mm length) causes very small disturbance to the soil. These sensors were also connected to the GP2 Delta T devices Data Logger to obtain the readings.

### ***GeoPIV analysis***

The displacement vectors were obtained using GeoPIV. GeoPIV is a Matlab module which combines the technologies of digital imaging, close range photogrammetry and the image-processing technique of Particle Image Velocimetry (PIV) in a manner suited to geotechnical testing (White and Take,

2002, White et al., 2003, White et al., 2005). The analysis technique used is based on the principles of PIV, which is a digital image-based surface displacement measurement method that compares a reference image to a series of deformed images. It measures whole velocity fields by taking two images in successive time instants and calculating the distance individual particles travel within these instants. Since the accuracy of displacement measurements using particle image analysis is strongly dependent on the surface contrast of the soil, some of the glass beads were painted blue and white to be used as markers, in order to have unique and easy to track patches (Figure 4.17) for the GeoPIV analysis.

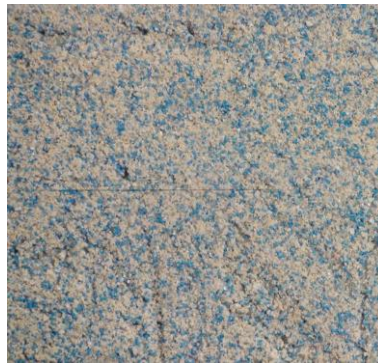


*Figure 4.17. Soil texture after using blue and white paint for some glass beads*

During the event, two high resolution cameras were aimed at both sides of the container, to record the process of the test and the movement of the soil. These cameras have a video resolution of 1920 x 1080 pixels and a maximum frame rate of 25 fps. There were two cameras to verify that the wetting front is moving homogeneously through the model at both sides; the displacement vectors were obtained by analysing the images of the video only at one side via Particle Image Velocimetry (PIV). Frames were extracted from the video and were analysed to measure the displacement vectors of the soil

and the velocity of the wetting front, without causing any disturbance to the slope model.

### ***Matlab Image Processing***

When the experiment starts, the readings of every sensor are steady and after some time the moisture sensors readings start to increase due to the infiltration of the water. This is an indication that the wetting front has reached to the corresponding location of the sensor. To validate the accuracy of the sensors, the idea was to use red coloured water for the rainfall and the movement of the red colour could then be tracked through Matlab image processing, thus giving the movement of the wetting front and then compare these results were with those obtained from the soil moisture sensors, regarding the movement of the wetting front.

## **4.3. Experimental Procedure**

### **4.3.1. Camera setting**

Since GeoPIV is a digital image - based surface displacement measurement method, its success relies heavily on the quality of the images used. Any displacement measured by the software will be made up of two components: the true displacement, and a certain amount of noise, caused by camera shake, lens distortion, misalignment of the camera and the plane of interest, refraction of light etc. The aim is to obtain displacement vectors that reflect the real movements within the soil. For that reason, noise effects should be minimised while setting up the experiment and post processing should take place in order to remove the noise from the frames. The camera should be positioned orthogonally to the plane of interest to capture images at regular time intervals. For every test the same set-up, same lighting and same camera to container distance were used.

#### 4.3.2. Orthogonality between Plane of Interest and Camera

The camera lens should be positioned orthogonally to the plane of interest to capture images at regular time intervals and their position must be identical for every frame taken.

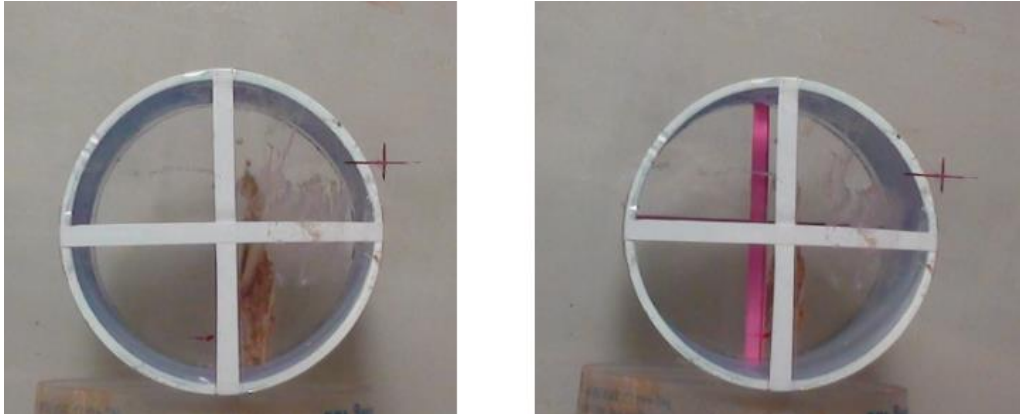


*Figure 4.18. Cylinder for the orthogonal set-up*

To ensure that the plane of particles and the camera were orthogonal, a hollow Plexiglas cylinder with crosses as markers at both ends was attached inside the container before setting the camera (Figure 4.18). By looking through the eyepiece it was possible to align the camera by matching the points on either end of the cylinder. Before each test, the aforementioned cylinder should be installed to ensure that the camera and the container are orthogonal.

#### 4.3.3. Camera shake

Even though the camera is still during the tests, placed on a steady tripod, camera shake cannot be completely avoided. Camera shake accounts for small apparent movements in the photograph due to external factors, such as the camera moving relative to the object being photographed between



images. It is due to the shutter mechanism of the camera, and to random floor vibrations due to activity around the testing area. To minimise the effects of camera shake, image post processing should take place to remove this 'noise' when necessary. To achieve that, markers (coloured stickers) were placed on the front plane of the container, which are known to stay static during the tests. A PIV analysis takes place, identifying the markers in the first image and determining their apparent movement in the series of images.

After acquiring the displacement data for the markers known to be static during the test and once the detected movement is significant, this 'noise' is removed from the GeoPIV analysis results for the deformation of the slope.

#### **4.3.4. Lens Distortion**

Lens distortion is a nonlinear and generally radial distortion; it is a deviation from a projection in which straight lines in a scene remain straight in an image. The photograph is affected by optical distortions caused by the lens which can be linear or nonlinear and causes elements of the image to appear altered from their original state. Most common types of distortion are:

- Barrel distortion, where image magnification decreases with distance from the optical axis (Figure 4.19a)
- Pincushion distortion, where image magnification increases with distance from the optical axis (Figure 4.19b)

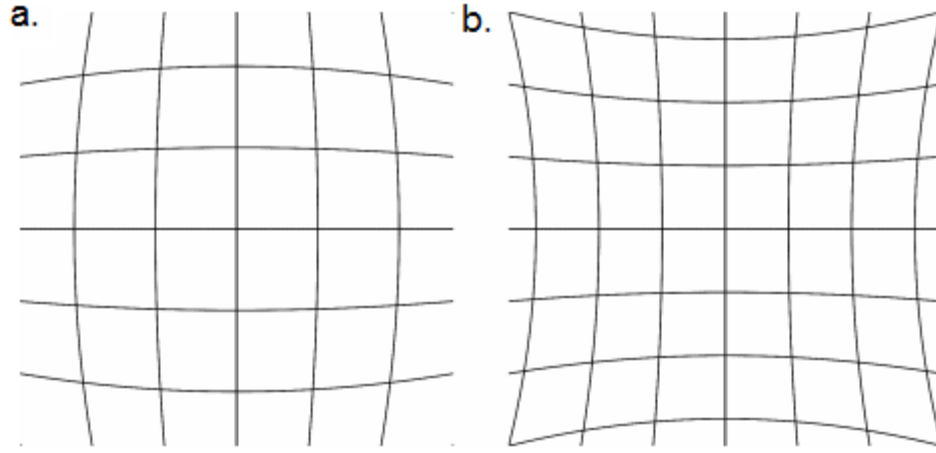
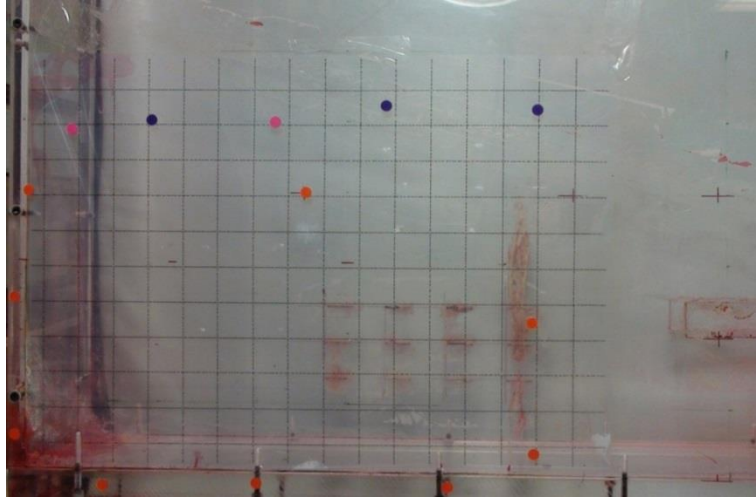


Figure 4.19. a. Barrel distortion, b. Pincushion Distortion (Hugemann, 2010)

Distortion can be defined as the difference between the original location  $(x_u, y_u)$  of an element in the photo and its distorted location  $(x_d, y_d)$ .

$$\text{Distortion: } r = \sqrt{(x_u - x_c)^2 - (y_u - y_c)^2} - \sqrt{(x_d - x_c)^2 - (y_d - y_c)^2}$$

To determine the effect of distortion on the images, a calibration mesh was created in the form of a sheet of with a mesh of square elements of 250mm printed on it. This sheet was stuck in the inner side of the Plexiglas as seen in Figure 4.20 and was photographed by the SONY-HDR-SR12, under test conditions and by means of image analysis the distances between all the points were calculated. The results suggested ignoring lens distortion since no larger than 1.00 pixel distortions were calculated.



*Figure 4.20. Calibration mesh for the effect of distortion*

#### **4.3.5. Refraction of light**

Light refraction is a second parameter of image distortion, since light travels through mediums of different refractive indexes. The plane in the images will be magnified by the light refraction as it crosses the boundary between the different mediums; in this case air and Plexiglas. In the present experiment, there is no need to account for the refraction of light since the pure magnification of the real dimensions will be the same for all the images and will be accounted for when calculating the scaling factor in the GeoPIV analysis to transform from image-space (pixels) to object-space dimensions (mm or cm).

## **Chapter 5 : Experimental Study**

---

In the previous chapter the experimental apparatus and the experimental procedure to study the evolution of slopes due to progressive retreat has been described in detail. This chapter reports on the experiments that have been carried out for this aim. Twenty-eight main experiments have been carried out in total; applying different rainfall intensities, using different bottom surfaces for the failed material to slide on, removing manually the failed debris and also testing slopes with different initial slope inclinations.

A calibration box has also been designed and one dimension tests were conducted prior to the main experiments and are reported in this Chapter. The aim of these 1D tests was to verify that the slope models were homogeneous and to measure the moisture content using not only the sensors but also the traditional oven-dry method. Moreover, some other techniques were used to verify the validity of the tests and are described in this chapter.

Finally, the experimental analysis is presented together with the main conclusions of this study. The deformations of the slope were estimated through GeoPIV analysis during the tests and the experimental results are reported and discussed in this chapter.

### 5.1. Preliminary one dimensional tests

To gather an initial feel of the water movement inside the soil, a calibration box was designed and tests were carried out prior to the model tests in order to obtain the infiltration rate of the soil. For this, a soil model 100.00\*100.00\*160.00 mm (L : W : H, inner dimensions) was created, in the manner outlined in paragraph 3.2.3. The calibration box was placed within the testing flume and then the model was constructed in it (Figure 5.1).

To conduct the oven-dry test to measure moisture content, a mesh of holes was drilled on one side of the calibration box, in order to take the samples through them (Figure 5.1a). Four thin metal stripes were placed to block the holes and were removed each time that a sample needed to be taken. Clear Rimmed Test Tubes (83.00\*11.00mm) were used to take samples at four different depths at four times during the test (Figure 5.1b). Samples were taken at 1.00cm, 4.00cm, 7.00cm and 10.00cm from the slope top and at a: 10 minutes, b: 40 minutes, c: 100 minutes and d: 160 minutes after the beginning of the test. The rainfall intensity during these calibration tests was approximately 16mm/hr.

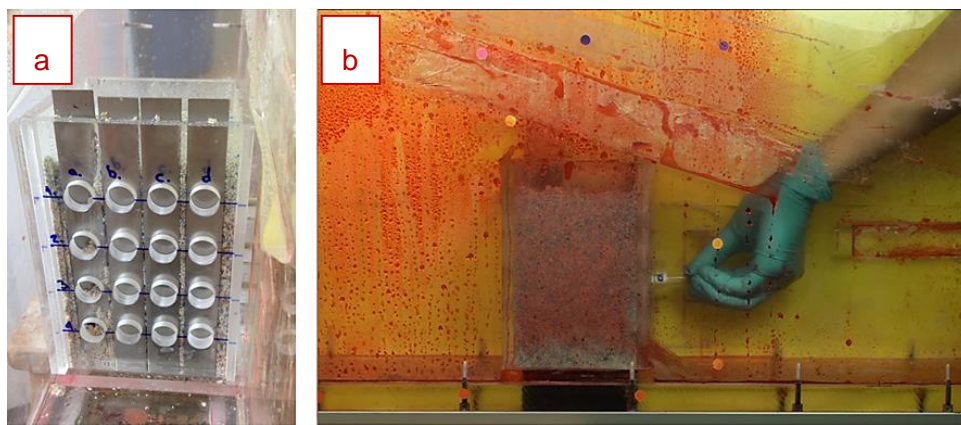


Figure 5.1. Calibration box and sample extraction

All tests were carried out into two stages stages to minimise possible 3D effects. Samples being extracted from two columns for each sub-test (e.g. samples from holes: a1, c2, a3, c4), to achieve minimum disturbance to the sample inside the calibration box and not affect the infiltration rate of the water inside the slope model. A new model was then created and the procedure was repeated to extract the samples from the other two columns.

*Table 5.1. Water content during calibration box test*

Sample Number	Jar mass (g)	wet soil mass + container (g)	dry soil mass and container (g)	Mass of water (g- cm <sup>3</sup> ) (m <sub>w</sub> )	Dry soil mass (g) (m <sub>s</sub> )	Gravimetric water content (g/g)	Dry Density (g/cm <sup>3</sup> )	Volumetric Water Content (cm <sup>3</sup> /cm <sup>3</sup> )
		before oven	after oven			(m <sub>w</sub> /m <sub>s</sub> )		
<b>time: 10min</b>								
<b>A1</b>	2.13	5.93	5.41	0.54	3.26	0.159	1.478	0.245
<b>A2</b>	2.15	6.11	5.56	0.56	3.40	0.161	1.478	0.243
<b>A3</b>	2.15	6.24	5.66	0.58	3.51	0.165	1.478	0.244
<b>A4</b>	2.2	7.16	6.44	0.72	4.24	0.170	1.478	0.251
<b>time: 40min</b>								
<b>B1</b>	2.14	5.92	5.39	0.54	3.24	0.163	1.478	0.246
<b>B2</b>	2.14	6.55	5.92	0.64	3.77	0.167	1.478	0.251
<b>B3</b>	2.17	6.13	5.54	0.59	3.37	0.175	1.478	0.259
<b>B4</b>	2.16	6.47	5.79	0.68	3.63	0.187	1.478	0.277
<b>time: 100min</b>								
<b>C1</b>	2.13	5.41	4.94	0.47	2.81	0.167	1.478	0.247
<b>C2</b>	2.13	6.45	5.82	0.63	3.69	0.171	1.478	0.252
<b>C3</b>	2.19	6.51	5.84	0.67	3.65	0.184	1.478	0.271
<b>C4</b>	2.16	6.85	6.07	0.78	3.91	0.199	1.478	0.295
<b>time: 160min</b>								
<b>D1</b>	2.12	5.89	5.35	0.54	3.23	0.167	1.478	0.247
<b>D2</b>	2.11	6.41	5.78	0.63	3.67	0.172	1.478	0.254
<b>D3</b>	2.17	6.43	5.76	0.67	3.59	0.187	1.478	0.276
<b>D4</b>	2.19	6.29	5.57	0.72	3.38	0.213	1.478	0.315

All the samples that were extracted from the calibration box were then weighted and placed in the oven at 100°C for 48 hours. After that, the soil and the containers were left to cool and their mass was measured again to calculate the dry mass of the sample and the soil gravimetric water content. Since the characteristics of the soil are known the gravimetric water content can be transformed into volumetric water content by using the dry unit weight of the mixture:  $\gamma_d=14.5\text{kN/m}^3$ . All the results are presented in Table 5.1. The gravimetric water content is illustrated in Figure 5.2. It is seen that the moisture content is higher in greater depth and this can be due to the infiltration rate inside the slope being higher than the wetting rate (rainfall intensity).

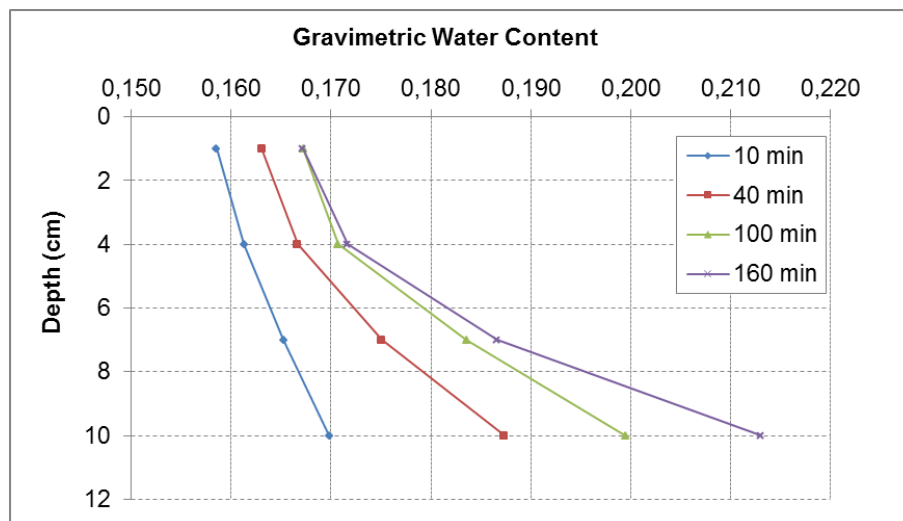


Figure 5.2. Gravimetric water content from oven-dry test during the calibration box test

Apart from the samples, three Vegetronix VH400 were buried inside the model at different depths to measure the moisture content. In Figure 5.3, the results in terms of volumetric water content as obtained from the

Vegetronix VH400 soil moisture sensors are illustrated, with MS0, MS1, MS2 being at depths 5.00cm, 8.00cm and 11.00cm from the slope top respectively. The results obtained during the calibration test by the oven dry method and those from the soil moisture sensors' readings showed good agreement.

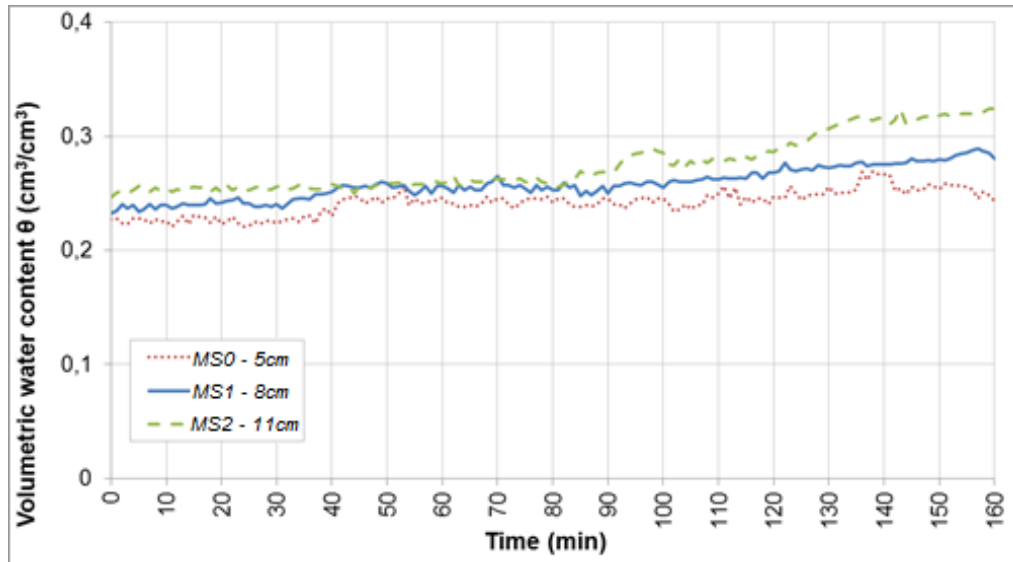


Figure 5.3. Volumetric water content from sensors readings during the calibration box test

## 5.2. Other verification techniques

In most tests, soil moisture sensors were buried inside the slope model (Table 5.2) during the construction phase, so as to cause the least possible disturbance to the soil. However, tests without the soil moisture sensors were also carried out to verify that the existence of the moisture sensors inside the slope model did not cause any difference to the behaviour of the model and to the location of the failure mechanisms and the failure surface that developed.

Moreover, since the aim was to capture the propagation of the wetting and thus the weathering front, red dye was used to make it possible to capture



the wetting front by the use of image analysis. A Matlab code was developed to capture the movement of the red part in the series of frames extracted from the videos. Frames were extracted every second and results from the Matlab image analysis are shown in Figure 5.4 at three different times during rainfall infiltration, showing that the red water - water front - is moving homogeneously across the length of the slope (blue lines are almost horizontal). Moreover, the height of the wet part of the slope can be calculated at each point. Thus the infiltration rate at any time can be also calculated.

The initial idea was to use the red dye to gather an extra measurement of the velocity of the wetting front inside the slope model and to verify whether water infiltrates uniformly inside the slope. The wetting - infiltration front is also monitored by soil moisture sensors. A change in the reading of the moisture sensors implies that the wetting front has reached the location of the sensors. However, calibration test and comparison between the location of the red dye from the image analysis and the sensors' readings showed that the red dye front is not moving at the same velocity as the wetting front. A hysteresis between the wetting front and the front of the red dye was observed, owing possibly to the size of the dye particles being filtered by the soil particles. Nevertheless, the red dye is still useful as it can be used as a way to verify the homogeneity of the wetting front downward the slope, since it was not possible to calculate the hysteresis, which changes with the saturation degree of the soil.

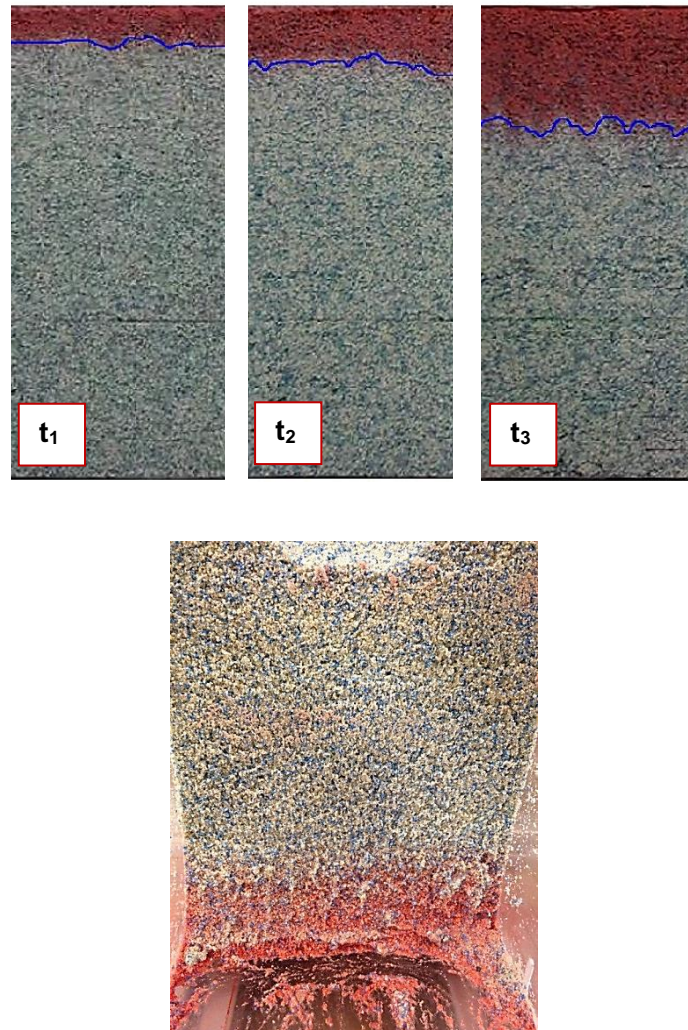


*Figure 5.4. a. Sequence of photographs showing the advancing wet dye front and b. vertical slice of the model during the test showing uniform movement of water also inside the model*

Finally, experiments were carried out to test the correctness of the apparatus and the repeatability of the experiments. With regard to repeatability, identical tests (slopes with the exact same geometry, material, construction procedure and rainfall intensity) were carried out with the slopes exhibiting very similar failure mechanisms occurring at the same time after the initiation of the rainfall. Also slopes of two different heights (with a ratio of 1.5-2.5 between the two) were tested under the same rainfall intensity.

In Figure 5.5 and Figure 5.6 the location and the time of failure (first) against rainfall intensity is illustrated respectively for all tests that have been carried out with vertical initial profile and height  $H=15.00\text{cm}$ . The location of the failure is measured as the distance from the slope crest to the failure line. It is seen that for the same rainfall intensity the location and the time at which the failure occurs do not present significant differences, thus validating the repeatability of the experimental procedure.

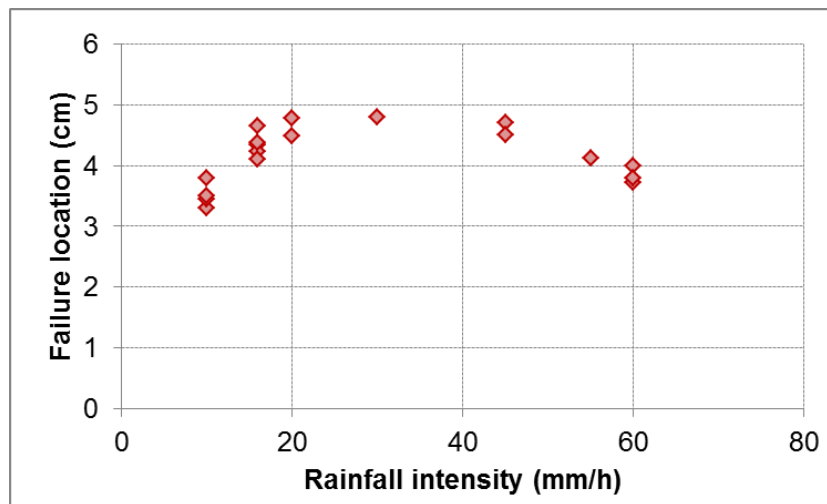


Figure 5.5. Location of the failure vs. rainfall intensity

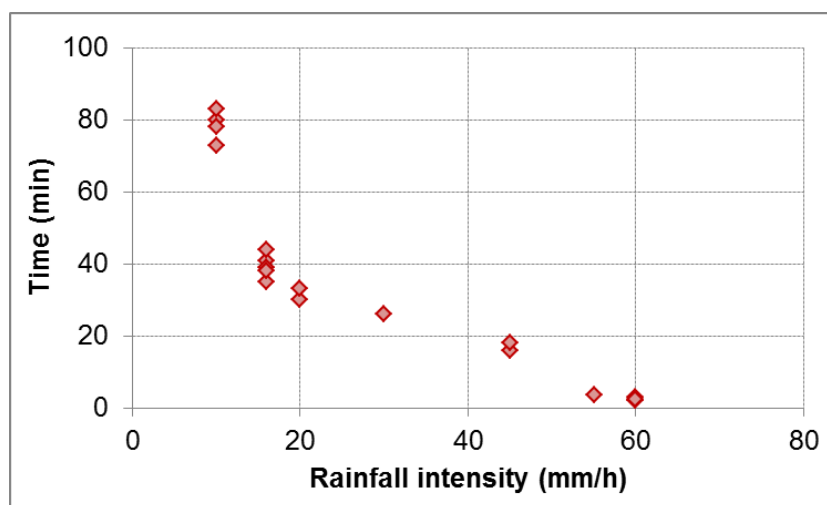


Figure 5.6. Time of failure vs. rainfall intensity

Finally, Figure 5.7 illustrates the time at which the readings of SM300 soil moisture sensor  $m_1$  (buried 4.00cm from slope top) started changing. From this plot, the mean infiltration rate for different rainfall intensities can be calculated.

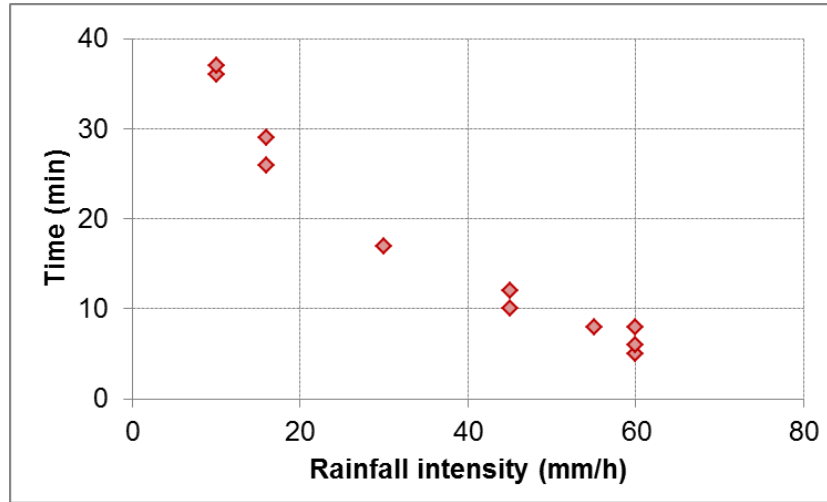


Figure 5.7. Time when water front reaches moisture sensor  $m_1$  vs. rainfall intensity

### 5.3. GeoPIV analysis

In Paragraph 4.2.5, it has already been mentioned, that a Matlab module based on PIV principles and suited to geotechnical testing, called GeoPIV will be employed in the analysis of the experiments. Frames from the videos that were recorded during the tests were extracted at a frame rate of 25 frames per second and were analysed to measure the soil displacements.

To run the GeoPIV analysis and avoid misleading or incorrect displacement data, suitable input variables for the module should be chosen (White and Take, 2002). On the other hand, the computation time should also be considered, when for example setting the search range over which GeoPIV

searches for a displaced patch. More specifically, a search zone set too small or a frame rate set too low leads to wild displacement vectors appearing in the results while if set too large it will lead to an impractically long computation time, on the other hand if the patch size is set too large then displacement resolution is lost while if set too small it can lead to wild vectors. Generally, the user needs to manually examine typical pairs of images and pick the input values. More details on how to choose the most appropriate input variables for the GeoPIV launcher file can be found in (White and Take, 2002). For this work, some analyses have been carried out using different input variables; e.g. different patch sizes (Figure 5.8), to see which ones can capture better the deformations of the soil and follow the failure mechanism, and select the values used for the analysis of the experiments. After several trials, the patch size and mesh spacing used for all the experiments presented in this thesis was chosen to be 24 pixels.

Once the GeoPIV analysis has been carried out, some post processing of the data needs to take place. An additional analysis is carried out for the markers that are placed on the container which remains static during the test to account for the camera-ground shake (noise) which should be removed from the data to obtain valid results. In Figure 5.9, the identified displacement of a marker versus time for the whole duration of an experiment is illustrated to show that no significant movement was captured during the test. This was expected as there were not people walking around the laboratory during the test, nor was there the disturbance due to the camera shutter since there was video recording and for this reason it was not considered necessary to remove it from the GeoPIV analysis results for the deformation of the slope.

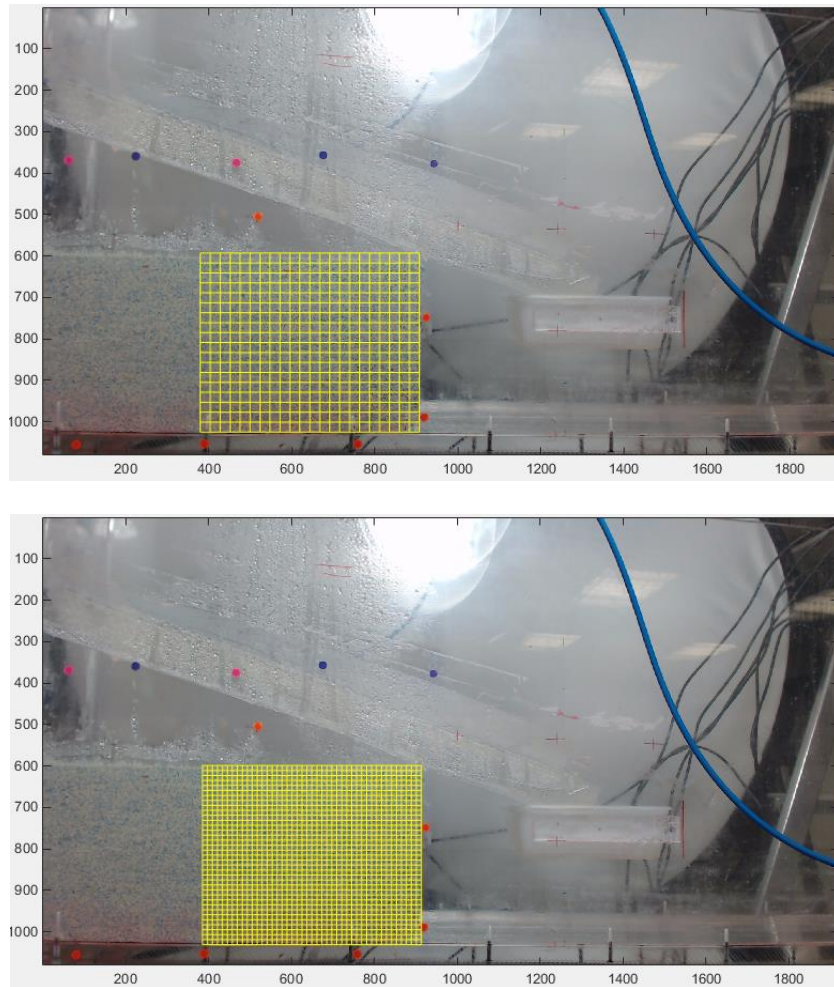


*Figure 5.8. Different patch size used in the analysis*

Moreover, once the results from the analysis are obtained, suitable scaling factor should be used to convert image-space (PIV) measurements into object-space values, that means to say that coordinates in terms of pixels in the image are converted to coordinates in the observed soil. Here, the image-space to object-space conversion process was carried out by assuming a constant image scale.

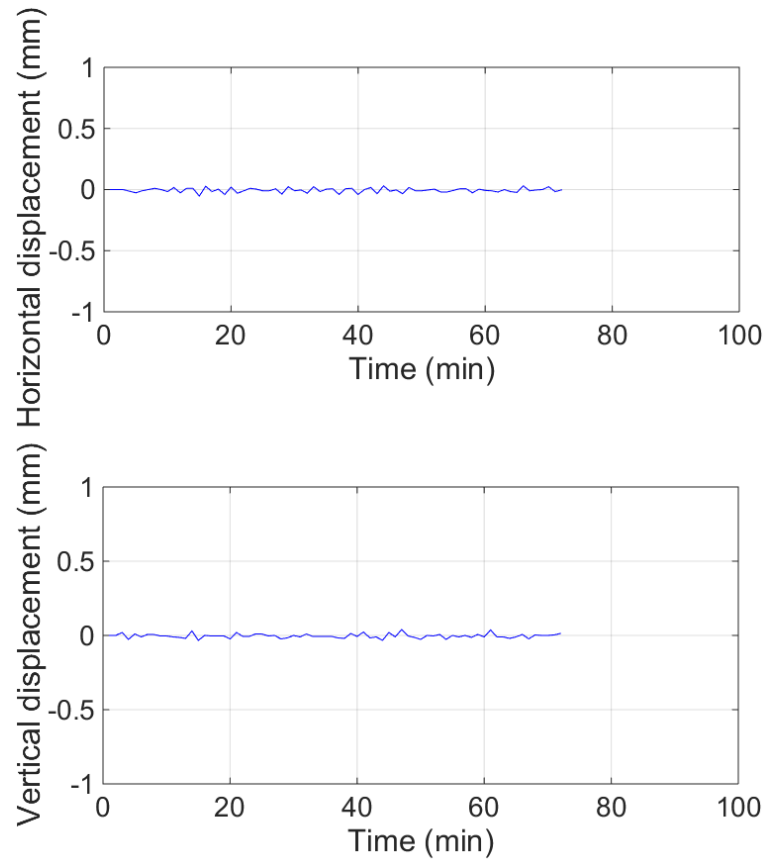


*Figure 5.9. Identified noise during the test*

#### **5.4. Experiments and Results**

The initial aim of these experiments was to build a model test able to simulate weathering and compare the results with the analytical model. The idea was to use lightly rainfall to decrease the mechanical properties of the soil material. However, the procedure is more complicated since there is also the increase of the soil weight due to the water infiltration that changes the behavior of the soil. For this reason, it was decided to investigate other aspects of the slope behavior subject to successive failures, with the triggering factor being the water infiltration. Different patterns were used to investigate:

- the influence of rainfall intensity on slope evolution (for low rainfall intensity the experiment can simulate a weathering procedure),
- the effect of the flume bottom surface on the debris propagation and as a result on the slope evolution and
- the effect of the debris itself that was manually removed in some experiments just after failure occurred.

The experimental procedure is designed and described in Chapter 3, and twenty-eight tests have been carried out. In Table 5.2, the main characteristics of these tests are summarised.

*The general characteristics of the slope model are shown in*

Table 5.3 for a typical vertical slope 15.00cm high. In some cases, different heights were used during the experiments as shown in the Table. A drawing illustrating the locations of the sensors is illustrated in Figure 5.10. In what follows a description of the experimental technique used in each case together with the findings from the experiments are presented. The model slope is heavily instrumented to quantitatively capture the pore water pressure, soil moisture and deformations during the test.

In what follows the main aspects of the observations made during the tests is presented. Fourteen of the experiments are selected and analysed in detail in this Chapter.



Table 5.2. Tests characteristics

		Rainfall intensity (mm/h)	Sensors	Soil bottom	Soil removal
1	S90_H15_L35_1	55	✓		
2	S90_H15_L35_2	60	✓		
3	S90_H15_L35_3	16	✓		
4	S90_H15_L35_4	20			
5	S90_H15_L35_5	16	✓		
6	S90_H15_L35_6	10	✓		
7	S90_H15_L35_7	16	✓		
8	S90_H15_L35_8	16			
9	S90_H15_L35_9	10	✓		
10	S90_H15_L35_10	10			
11	S90_H15_L35_11	16	✓		
12	S90_H15_L35_12	60	✓		✓
13	S90_H15_L35_13	60	✓		✓
14	S90_H15_L35_14	45	✓		✓
15	S90_H15_L35_15	10	✓		
16	S90_H15_L35_16	45	✓		
17	S90_H15_L35_17	30	✓		
18	S90_H15_L35_18	10		✓	
19	S90_H15_L35_19	20		✓	
20	S90_H25_L35_20	16	✓		
21	S90_H25_L35_21	30	✓		
22	S90_H10_L35_22	16	✓		
23	S60_H15_L35_23	10	✓		
24	S60_H15_L35_24	30	✓		
25	S60_H25_L35_25	30	✓		
26	S60_H15_L35_26	16	✓		
27	S45_H15_L35_27	16	✓		
28	S45_H15_L35_28	60	✓		

Table 5.3. Model and soil characteristics

Characteristic	Symbol	Type	Value
Glass beads	$W_b$		43.5%
Calcarene	$W_c$		43.5%
Water	$W_w$		13.0%
Number of layers			15
Layer Width (cm)			10.00
Length (cm)			10.00
Height (cm)			1.00
Weight of layer (g)			170
Weight of soil model (g)	$W_T$		10710
Volume of soil sample (cm <sup>3</sup> )	$V_T$		6300
Glass beads specific gravity	$\gamma_b$		1.75
Calcarene specific gravity	$\gamma_c$		2.73
Mixture specific gravity	$\gamma_m$		2.24
Water density (g/cm <sup>3</sup> )	$\rho_w$		1.0
Water specific weight (kN/m <sup>3</sup> )	$\gamma_w$		9.81
Dry weight of soil (g)	$W_s$		9313.04
Weight of water (g)	$W_w$	$=W_T-W_s$	1396.96
Volume of water (g)	$V_w$	$=W_w/\gamma_w$	1396.96
Volume of soil (cm <sup>3</sup> )	$V_s$	$=W_s/\gamma_s$	745.435
Volume of voids (cm <sup>3</sup> )	$V_v$	$=V_T-(V_s+V_w)$	561.98
Void ratio	$e$	$=(V_w+V_v)/V_s$	0.515
Degree of saturation	$S$	$=V_w/(V_w+V_v)$	65.21%
Total density (g/cm <sup>3</sup> )	$\rho_T$	$=W_T/V_T$	1.700
Total unit weight (kN/m <sup>3</sup> )	$\gamma_T$		16.672
Dry density (g/cm <sup>3</sup> )	$\rho_d$	$=W_s/V_T$	1.478
Dry unit weight (kN/m <sup>3</sup> )	$\gamma_d$		14.497
Saturated density (g/cm <sup>3</sup> )	$\rho_{sat}$	$=W_T/V_T (S=1)$	2.040
Saturated unit weight	$\gamma_{sat}$		20.007
Gravimetric water content	$w$	$=W_w/W_s$	15.00%
Volumetric water content		$=V_w/V_T (w*\gamma_d/g)$	22.17%
Gravimetric water content at saturation	$w$	$=W_{w(sat)}/W_s$	34.01%
Volumetric water content at saturation		$=w*\gamma_d/g$	44.01%

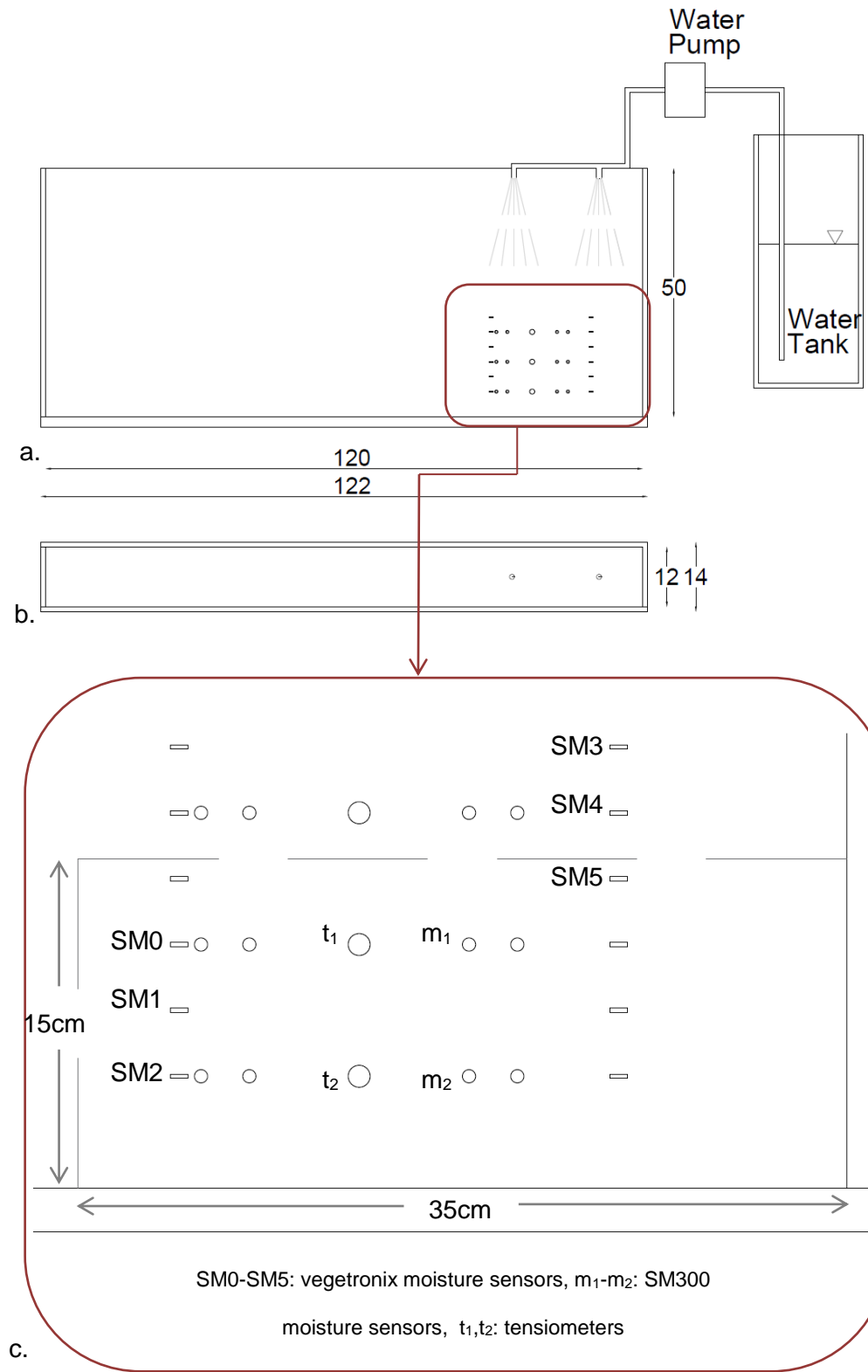


Figure 5.10. Experimental apparatus a. front view, b. plan view, c. location of soil moisture sensors & tensiometers (all dimensions are in cm)

All the experiments presented in this thesis were performed on planar slopes for sake of simplicity during the construction phase. Most of the experiments were performed on vertical profiles, however slope inclinations  $\beta=60^\circ$  and  $\beta=45^\circ$  were also tested.

### **5.5. Slope behaviour under different rainfall intensities**

From the observation of the slope model behaviour during the tests described above, it can be stated that the setting was successful in inducing successive failure in the slope and the formation of cracks. Matlab image processing of the videos from both sides of the flume, suggested that the wetting front moves homogeneously inside the slope model.

In this part, two experiments of the same geometry and soil characteristics but under different rainfall intensities are presented and analysed. More specifically, experiments S90\_H15\_L35\_3 and S90\_H15\_L35\_2 being subject to a rainfall of  $I_r=16\text{mm/h}$  and  $I_r=60\text{mm/h}$  respectively.

In all the experiments, after the onset of rainfall, the moisture content starts to increase over time towards a saturated value due to the ingress of water. Increase of the moisture content leads to a decrease of the slope material strength as well as to an increase of the weight of the soil mass, causing initial deformation to the soil that will lead the soil mass to slide away.

After a short period of rainfall, vertical cracks start to form in the upper part of the slope model (Figure 5.11) with vertical deformations near the crack progressively increasing. When the shear band developing from the slope toe joins the vertical crack, failure occurs (Utili, 2013) and a soil wedge slides away. After some time, the constant rainfall induced by the nozzles cause further degradation to the soil strength and additional water weight due to

water infiltration and further deformations are observed until a second failure occurs (in the case of heavy rainfall scenarios).

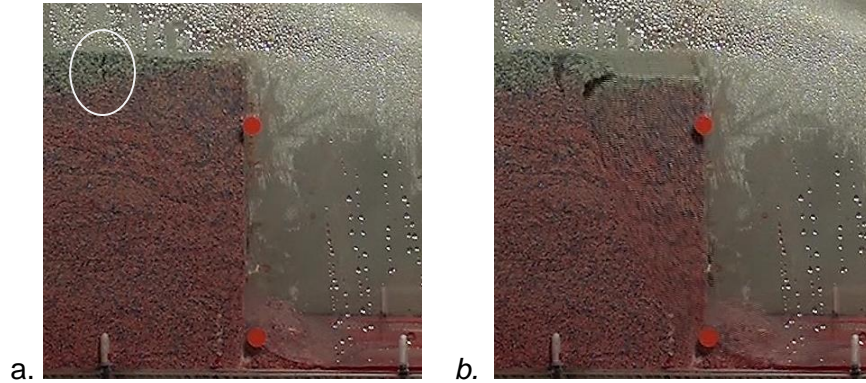


*Figure 5.11. a. Vertical crack in the upper part of the slope and b. initiation of failure*

The time histories of the volumetric water contents at the location of the sensors can be obtained from the soil moisture sensors' readings. Generally, three different phases can be observed (Figure 5.12), the first one featured by constant moisture readings when the water has not yet reached the point in question, the second one, featured by a significant increase of the volumetric water content due to the ingress of the wetting front and the third one when a steady moisture level is reached (Figure 5.12).

In case of light rainfall events, slopes exhibit only minor deformations until a first failure takes place but no second failure occurs. On the other hand, during heavy rainfall events, after the first failure larger displacements occurred to the slopes which progressively increased with time, as shown in Figure 5.26, until a global failure takes place and following the same pattern after some time of constant rainfall a second smaller failure took place.

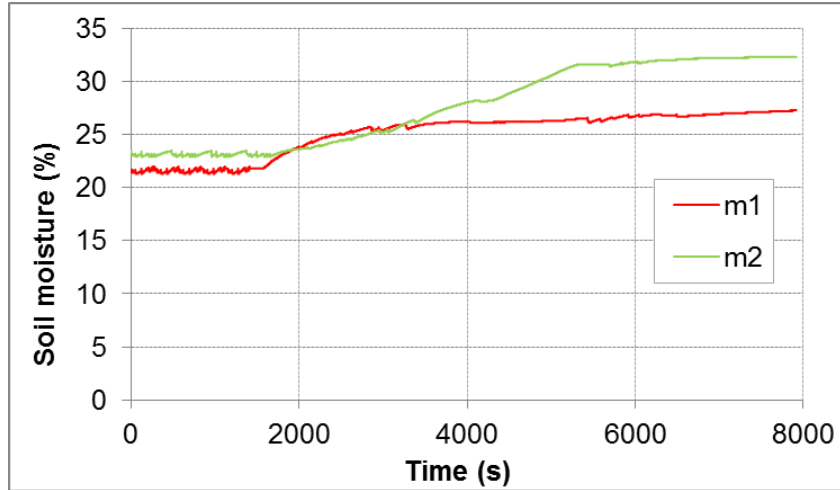


Figure 5.12. Time history of water content during test S90\_H15\_L35\_3

It was observed that at low rainfall intensities failure takes place much later and once the water front reached the toe of the slope, leading to the conclusion that the failure was caused due to the degradation of the slope material due to the ingress of water and then no second failure was observed. However, for intense rainfall scenarios, e.g.  $I_r=60\text{mm/h}$ , the first failure takes place after a few minutes of constant rainfall leading to the conclusion that in this case the failure occurred mainly due to the rapid increase of the weight of the soil mass. Also, vertical cracks were clearly noted on the slope crest causing the failure to occur sooner.

#### 5.5.1. First failure

##### $I_r=16\text{mm/h}$

For rainfall intensity  $I_r=16\text{mm/h}$  during experiment S90\_H15\_L35\_3 and at about  $t^{16}=30\text{min}$  from rainfall initiation, surface cracks perpendicular to the slope started to form at the top of the slope, and small-scale deformation started to occur, until the first failure took place. As shown in Figure 5.13, the arrival of the water at the location of tensiometer  $t_1$  (4.00cm from the slope

top) at time approximately  $t_1^{16}=30\text{min}$  starts destroying a portion of the soil suction very rapidly at the shallow location of  $t_1$  and then it becomes asymptotic to a small negative value, while at the deeper location of  $t_2$  the value decreases once the moisture content starts to increase and diminishes to zero once the soil moisture reaches almost saturation value. Readings from the tensiometers cannot be taken into consideration to represent the real value of the suction in the soil, as the initial suction in the soil was not more than  $u=1.00\text{kPa}$  when the accuracy of the sensor is  $\pm 0.5\text{ kPa}$ , however the trend to decrease as the moisture content increases is clear.

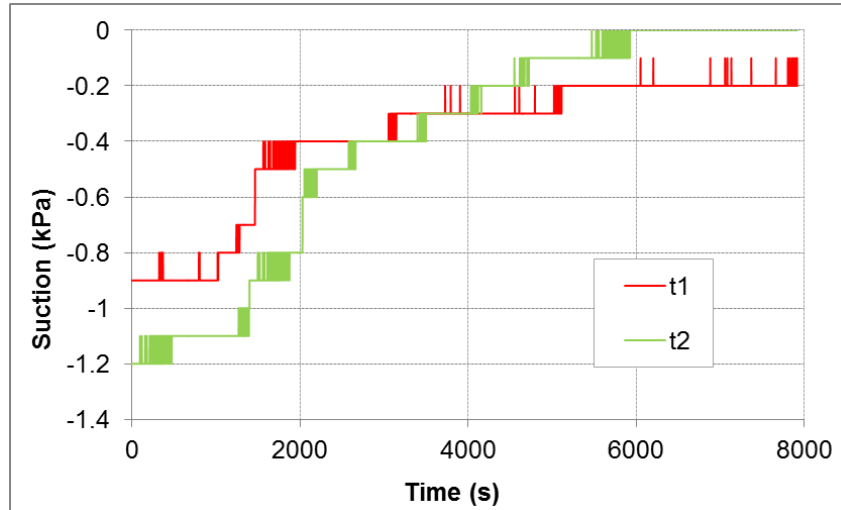
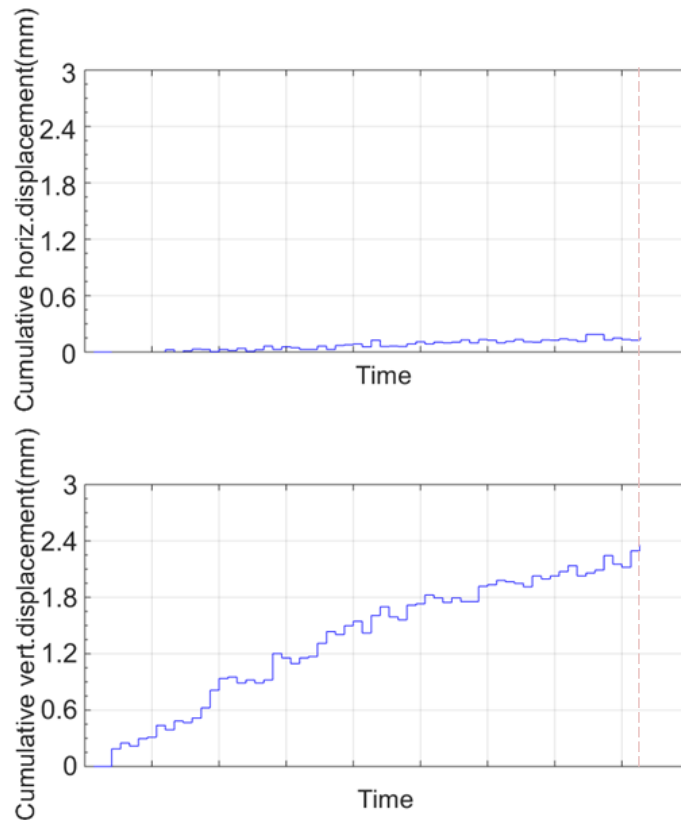


Figure 5.13. Soil suction during test S90\_H15\_L35\_3

At approximately  $t_1^{16}=41\text{min}$  after the test initiation, the water front has progressed toward to slope toe and the slope mass is observed to accelerate. Using GeoPIV module, successive digital images extracted from the video captured during the tests are compared to determine the displacements of thousand patches where the failure is likely to take place by tracking the soil texture.

The cumulative pre-failure displacements from the beginning of the test until the onset of failure are plotted in Figure 5.14, in both x and y directions for a soil element on the slope crest (see Figure 5.17). For a better understanding of the displacements that are developed within the slope model, the incremental horizontal and vertical displacement contours are plotted in Figure 5.15 for one second before the onset of the first failure event.



*Figure 5.14. Accumulated soil element displacements before the onset of the first failure for a point on the slope crest (test: S90\_H15\_L35\_3)*

It is seen that just after the initiation of the test and as the water infiltrates in the slope small movements are recorded on the slope crest. As the water moves further inside the slope soil consolidation deduced by the observed small vertical displacements, becomes more significant with time



and then failure is reached. The observed pre-failure displacements are a warning for the onset of a failure. It must be noted however, that no significant crack was observed before the failure for this rainfall intensity.

The spatial distribution of displacement vectors is illustrated in Figure 5.16, at a second before the onset of the failure. The region of instability observed during the first failure is clearly identified. As can be seen, at the onset of failure, displacements are predominantly vertical. In the next second a rotational failure mechanism occurs (Figure 5.17b) and the affected region of soil accelerates towards the toe, leading to a debris run-out shown by the two digital images in Figure 5.17b. Then the slope mass is observed to progressively decelerate. In Figure 5.17b a clear brittle failure mechanism is observed.

Rainfall carries on for another 100 minutes; small deformations are observed but no further failure, with the failed debris sliding slowly downward the slope. Investigating propagation of the debris is not within the scope of this thesis, however, it was observed that for low rainfall intensities the debris moved at slower velocities and the failed mass did not propagate to the same distance as in the case of heavy rainfall intensities creating shorter run out, explaining to some extent the occurrence of a second failure during heavy rainfall scenarios.

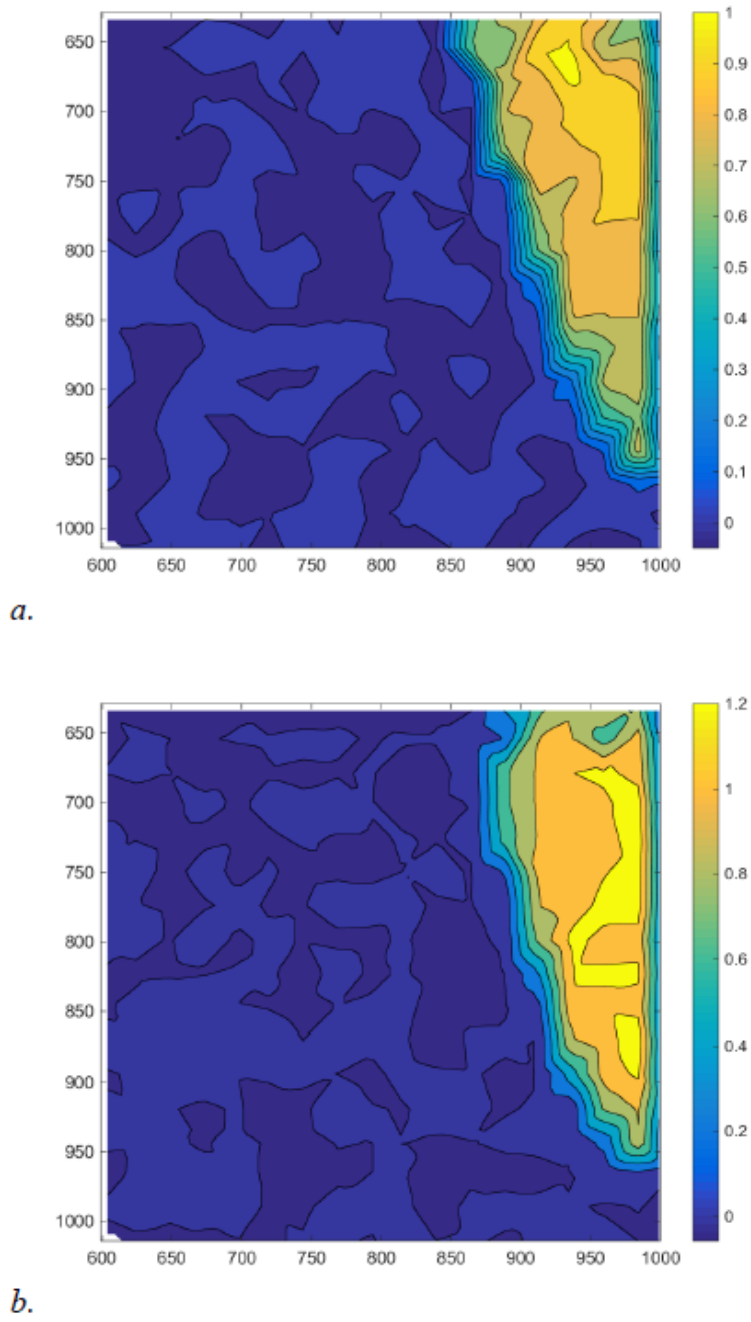


Figure 5.15. Incremental *a.* horizontal and *b.* vertical displacement contours at the initiation of the first failure event (test S90\_H15\_L35\_3)

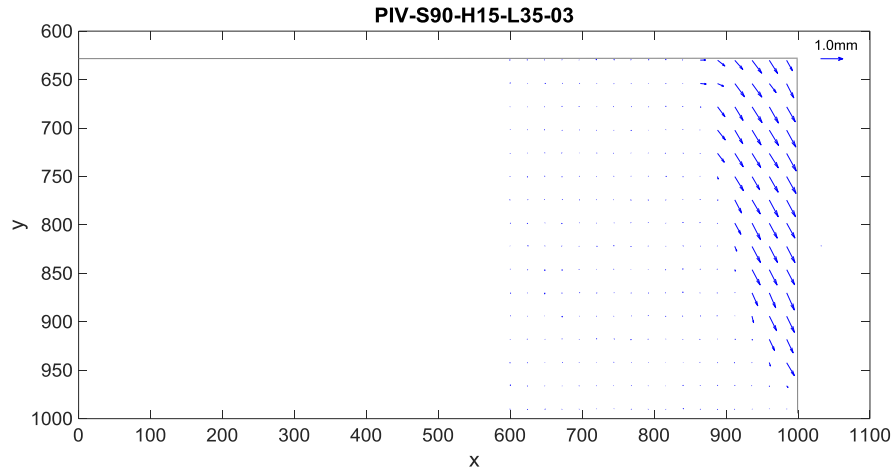


Figure 5.16. Observed displacement vectors at the initiation of the first failure event for test S90\_H15\_L35\_3

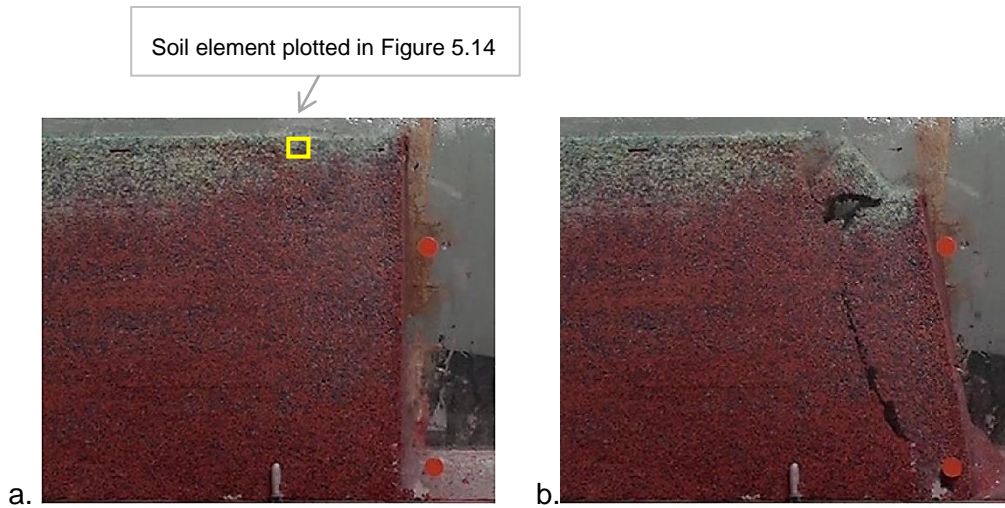
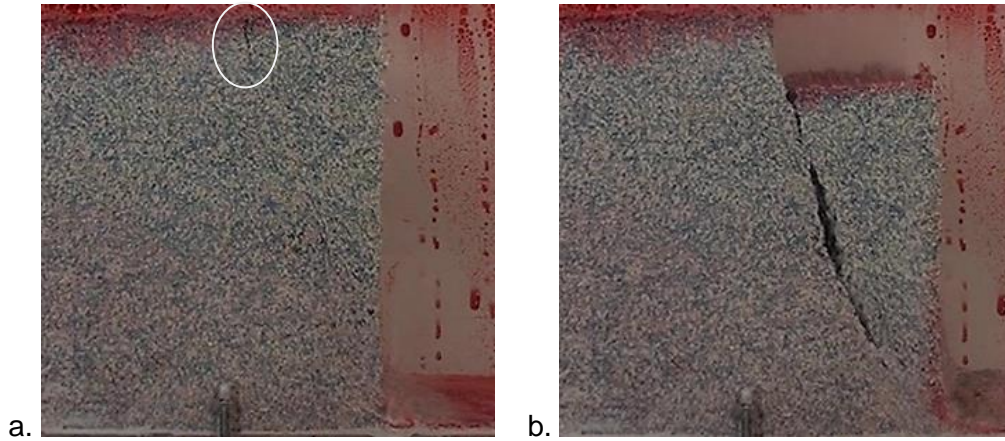


Figure 5.17. Digital images a. before and b. after the first failure during test S90\_H15\_L35\_3

**$I_r=45\text{mm/h}$**

For a higher rainfall intensity  $I_r=45\text{mm/h}$  during experiment S90\_H15\_L35\_16 and much sooner than for the case of  $I_r=16\text{mm/h}$  at about  $t_1^{45}=16\text{min}$  from rainfall initiation, a failure takes place. At about 5min from the

start of rainfall, vertical cracks started to form from the slope top (Figure 5.18a). Small deformation could be observed, until the first failure took place.



*Figure 5.18. Digital images a. before and b. after the first failure during test*

*S90\_H15\_L35\_16*

The spatial distribution of displacement vectors, at the initiation of the failure is illustrated in Figure 5.19a, for a timespan of one second before the onset of the failure. The region of instability observed during the first failure is clearly defined. Vectors are also plotted on top of the digital image of the slope model illustrate the affected region that will eventually slide away (Figure 5.19b). The vectors appear to be larger for this higher rainfall intensity than the previous one ( $I_r=16\text{mm/h}$ ) in terms of size and again they are predominantly vertical. There is however a strong horizontal component at the top of the slope which disappears towards the slope toe.

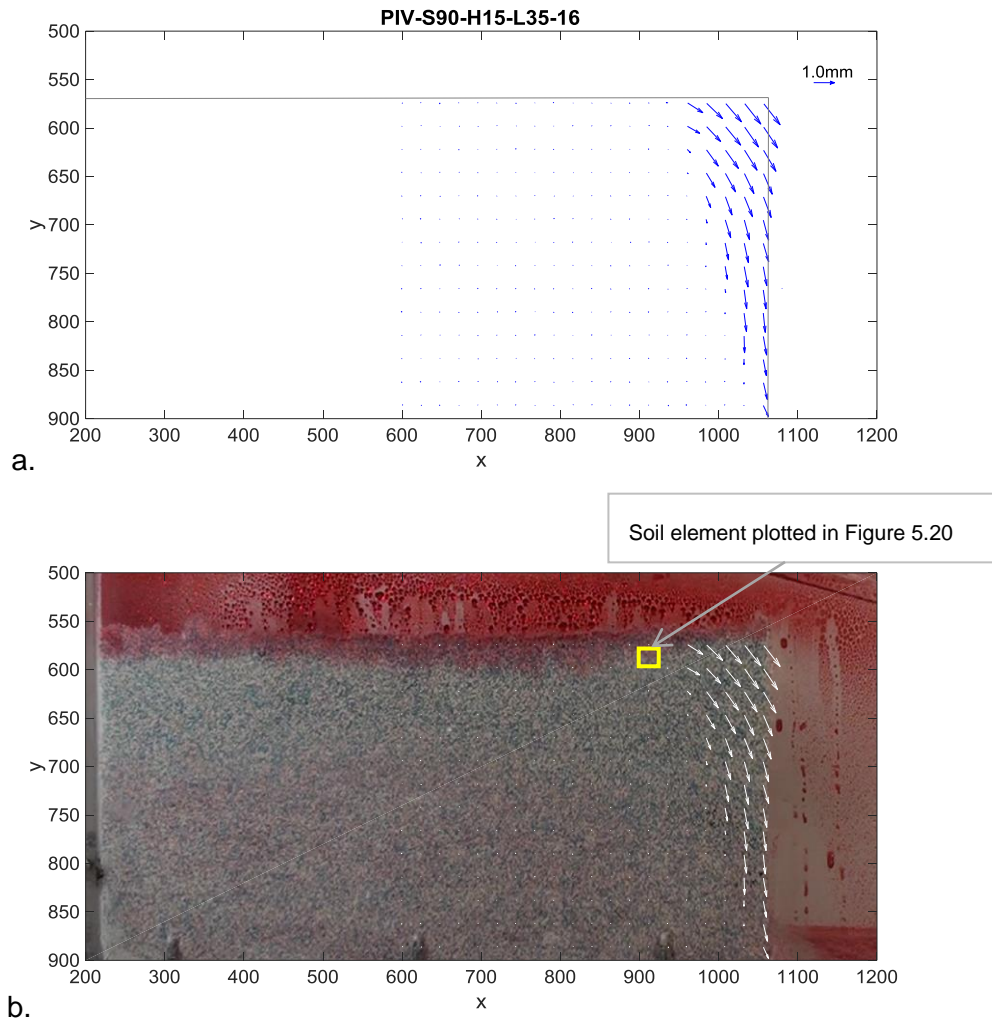


*Figure 5.19. Observed displacement vectors before the first failure event for test S90\_H15\_L35\_16*

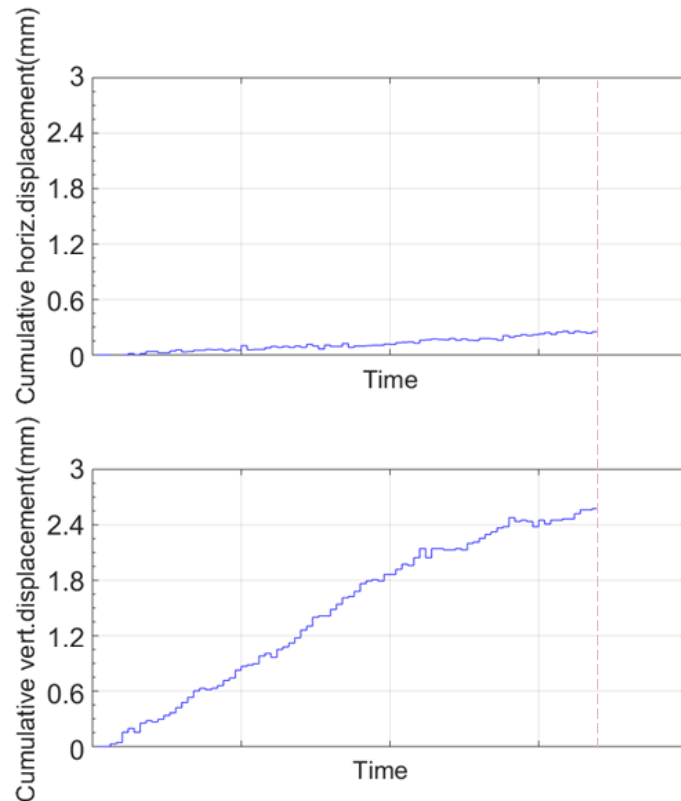


*Figure 5.20. Accumulated soil element displacements before the onset of the first failure for a point on the slope crest (test: S90\_H15\_L35\_16)*

A more clear picture is given in Figure 5.20, where the accumulated soil element displacements for an element on the slope top (see Figure 5.19) before the failure are plotted in the horizontal and vertical direction. The cumulative pre-failure displacements show that the pre-failure displacements were much larger than before, even in the horizontal direction warning that an event is about to happen. Once the first failure took place, further deformations occurred at the slope mass as the failed material slides away and a second failure is observed which is described in detail in the next paragraph.

**$I_r=60\text{mm/h}$**

For the event of heavy rainfall intensity of  $I_r=60\text{mm/h}$  during experiment S90\_H15\_L35\_2, vertical cracks made their appearance on the slope crest much earlier than in the cases described above, at about  $t^{60}=2\text{min}$  from the start of rainfall and are shown in Figure 5.21. Just a few seconds after the appearance of the cracks a sudden failure takes place. The wedge of soil that failed, slides away fast creating a low angle run-out within few seconds from the onset of the failure (Figure 5.27e). No changes in the soil moisture sensors readings were recorded until the occurrence of the first failure. Since the first sensor was buried 4.00cm from the slope crest and the first failure took place just 2min after the initiation of the rainfall, there was not enough time for the water to infiltrate to this depth.

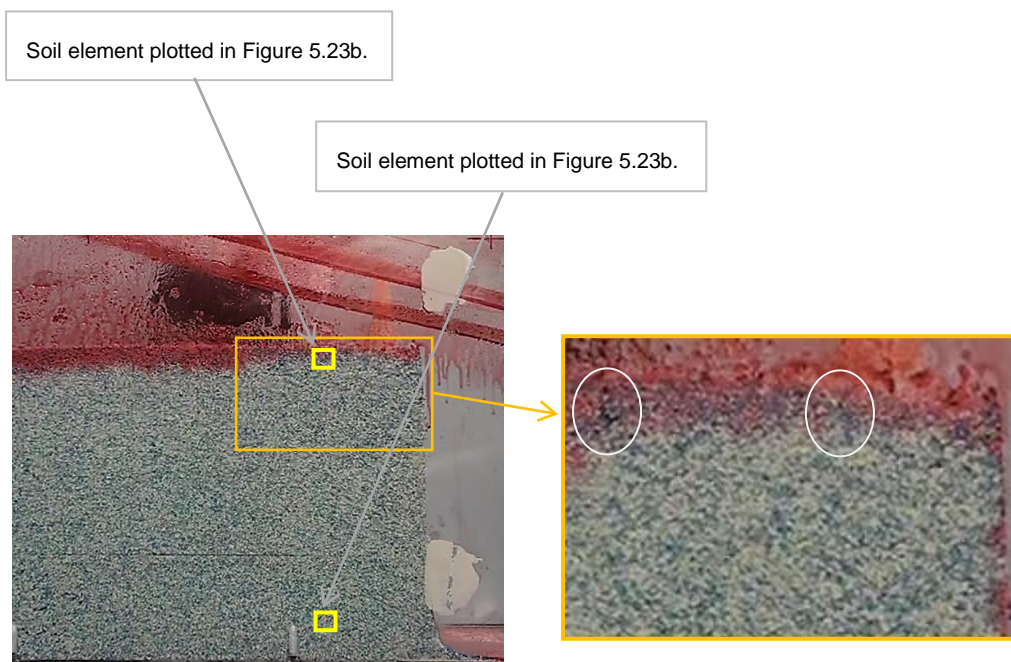


*Figure 5.21. Crack forming in the slope during test S90\_H15\_L35\_2*



The spatial distribution of the displacement vectors is illustrated in Figure 5.22. The region of instability during the first failure is defined by the vectors, which are predominantly vertical, with maximum vectors magnitude appearing at the crest of the slope. It was observed that higher rainfall intensities lead much faster the slope to failure and the velocity of the mass that slides away at failure is higher.

Figure 5.23 shows the accumulated horizontal and vertical displacements of two typical points (see Figure 5.21) of the slope during the test before failure is reached. In Figure 5.23a the cumulative displacement of a point at the slope top is illustrated showing the increase of the displacement in time, while in Figure 5.23b no significant movement at the bottom of the slope is recorded. It is obvious that the crest goes through significant deformation due to the infiltration of water, while no apparent movement is recorded inside the slope.

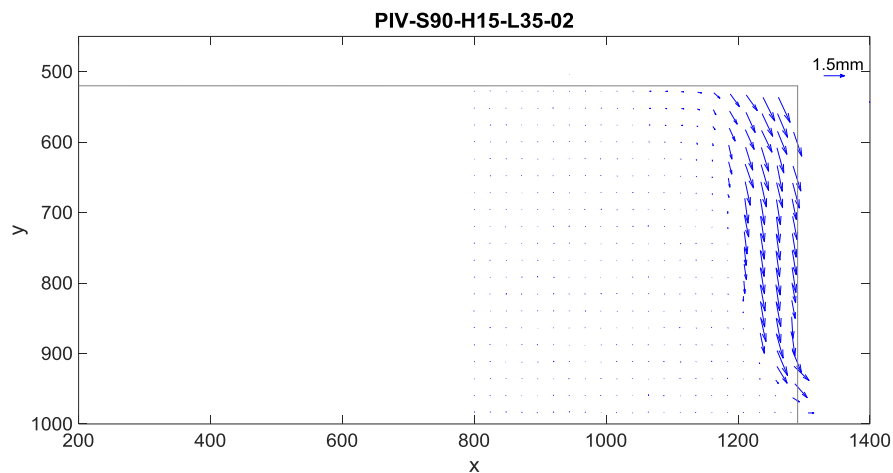


*Figure 5.22. Observed displacement vectors before the first failure event for test S90\_H15\_L35\_2*



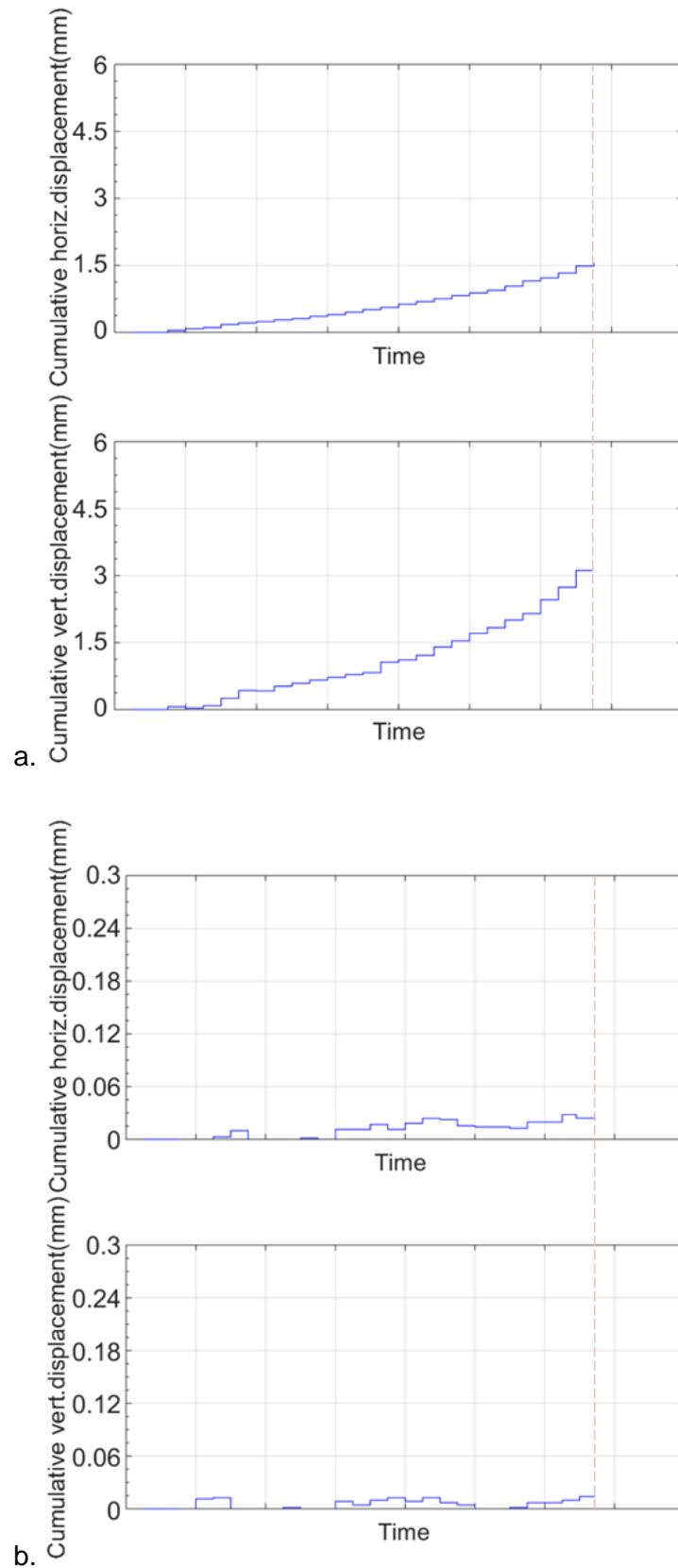


Figure 5.23. Accumulated soil element displacements before the onset of the first failure for a point a. on the slope top and b. at the slope bottom (test:

S90\_H15\_L35\_2)

### 5.5.2. Second failure

As stated before, a second or any successive failure occurred only for slopes under heavy rainfalls. Although the slope model experienced further deformations after the first failure, a second failure has not been triggered in every case. The non-appearance of a second event however, in certain circumstances does not mean that the event will never occur under any circumstance, e.g. bigger duration of rainfall. Therefore, the conventional understanding of successive failure triggering factors should not be dismissed on the evidence of only a few laboratory tests. Furthermore, there are also factors arising out of small scale testing that may indeed have influenced against the occurrence of a second failure, e.g. different stresses developed during the tests than in real conditions etc.

#### ***$I_r=45\text{mm/h}$***

After the first failure and as the nozzles continue to produce constant rainfall  $I_r=45\text{mm/h}$  during experiment S90\_H15\_L35\_16, a second failure occurs at  $t_2^{45}=25\text{min}$ . The occurrence of the failure was not as clear as the first one, where an almost rigid body of soil was observed to slide away. Therefore, it was not possible to capture the displacement vectors just before the occurrence of the failure. However, the spatial distribution of the displacement vectors during the failure is shown in Figure 5.24 to illustrate the affected region that slides away during the second failure.

When compared to the region of soil that slides away during the first failure for the same test, it is clear that the region during the second failure is significantly smaller. Moreover, the velocity of the sliding mass during the second failure is lower than that of the first failure.

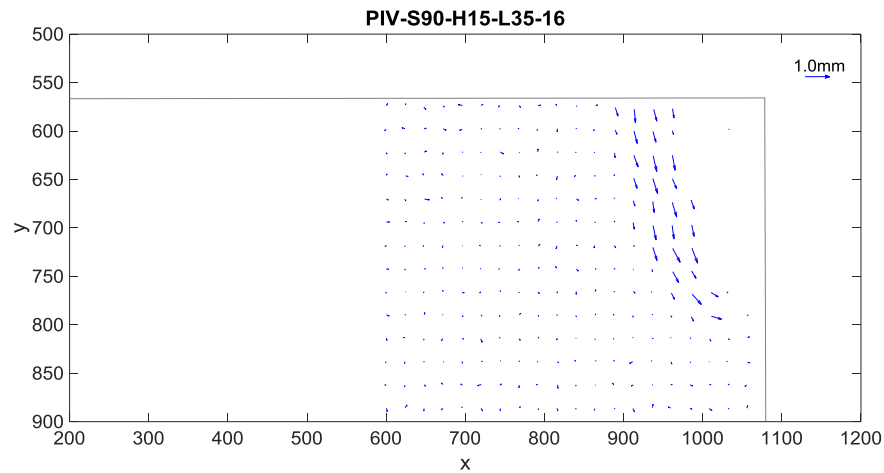


*Figure 5.24. Observed displacement vectors during the second failure event  
for test S90\_H15\_L35\_16*

It can be observed that this second failure (see Figure 5.25b) does not go through the slope toe as it happens for the first failure, but through a point much higher. In fact, the point through which the second failure passes, is the intersection of the slope with the failed debris from the first failure (Figure 5.25a). In Figure 5.25, a sequence of the digital images extracted from the video is presented, showing the slope before and during the second failure with the displacement vectors as calculated by GeoPIV. The evolution of the slope and the mass of soil that slides away during the second failure is illustrated.

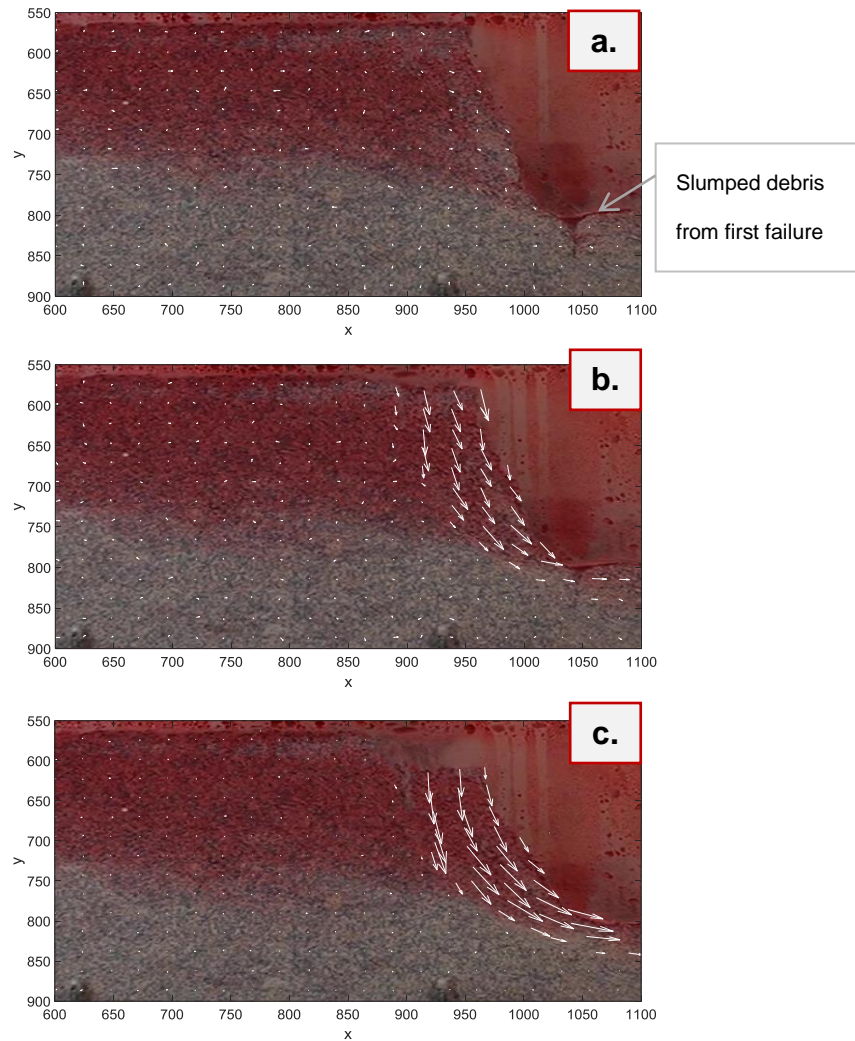
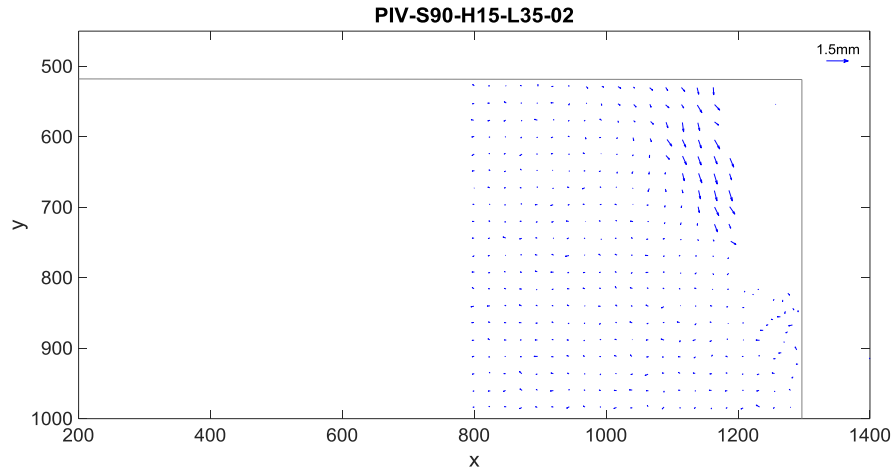


Figure 5.25. Digital images showing the evolution of second failure during test

*S90\_H15\_L35\_16*

**$I_r=60\text{mm/h}$**

As rainfall continues during the experiment S90\_H15\_L35\_2, and as the failed debris slides away (Figure 5.27e) further deformations are observed in the slope until a second failure is reached. The observed mechanism for the occurrence of the second failure is similar to that for  $I_r=45\text{mm/h}$ . The displacement vectors during the second failure are illustrated in Figure 5.26, defining the region of soil that slides away.



*Figure 5.26. Observed displacement vectors during the second failure event  
for test S90\_H15\_L35\_2*

As for the case of  $I_r=45\text{mm/h}$ , the region of soil that is affected and slides away is significantly smaller than that during the first failure and also the failure event takes place at a lower velocity. It is interesting to observe that as expected the second failure does not pass through the slope toe and passes again through the intersection between the slope and soil mass that has failed previously and is deposited downhill the slope (Figure 5.27f). After the second failure and due to further rainfall infiltration more deformations occurred until flow of the upper part of the soil was observed (Figure 5.27h) due to the increase of the water content and the material flows downhill. Then the nozzles were turned off and the experiment ended.



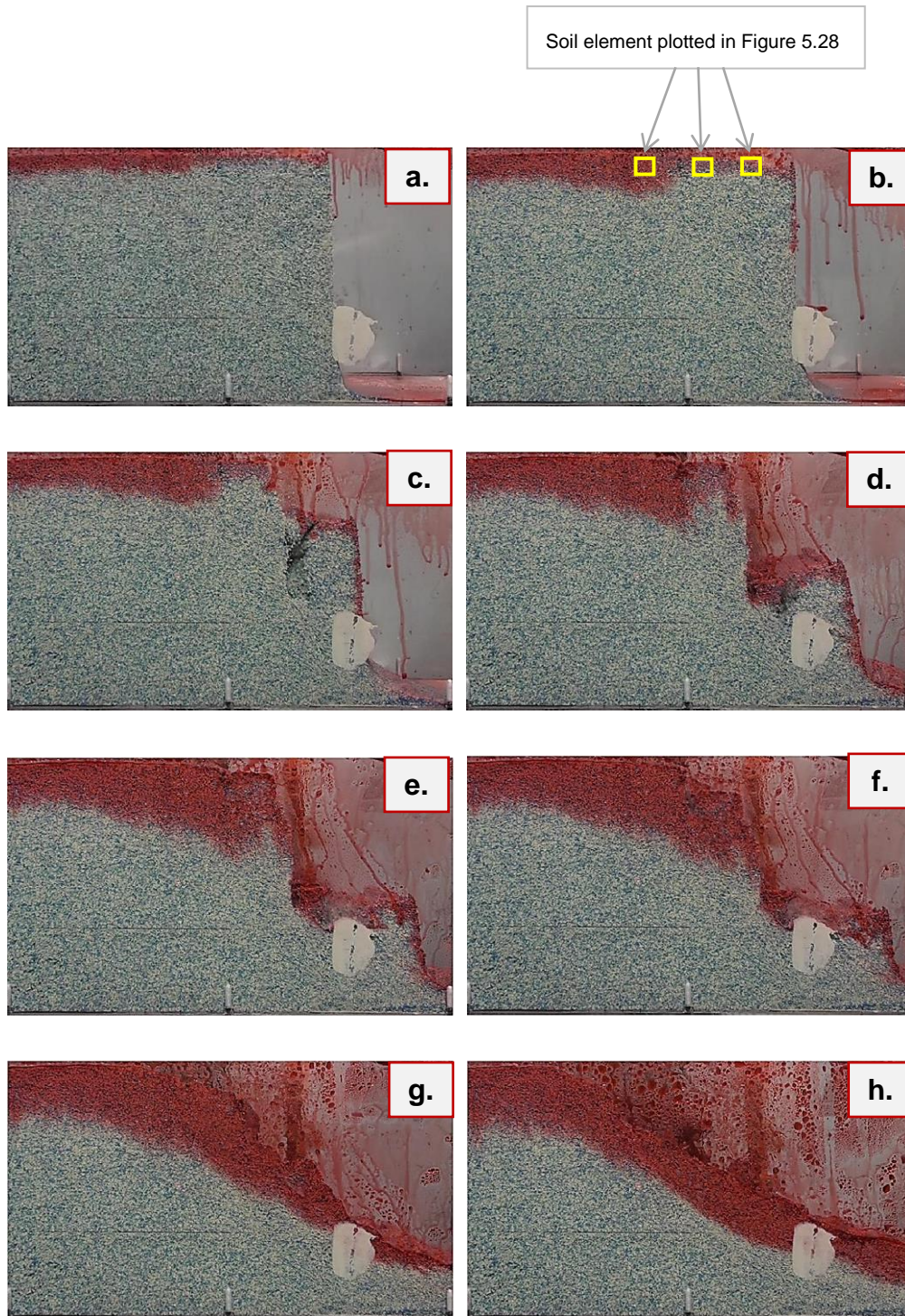


*Figure 5.27. Digital images showing the slope profile during test*

*S90\_H15\_L35\_2, observation of two slides and then flow occurs in the model*

All visible cracks that appeared during the tests on the slope model were almost vertical and led to slope failure a few minutes after their

formation. In Figure 5.27, digital images showing the slope face during the test S90\_H15\_L35\_2 can be seen. The first failure took place with an amount of soil moving mainly downwards at the onset of the failure and then horizontally away from the rest of the slope. Then after a second failure occurred, a third failure was not observed in the form of rigid body slide, however soil was flowing downwards the slope (Figure 5.27h).

The evolution of the velocity of the sliding mass for the three different failure events recorded for test S90\_H15\_L35\_2 is illustrated in Figure 5.28. For the sake of comparison, the velocity is estimated from GeoPIV results for soil elements on the top of the slope as shown in Figure 5.27b.

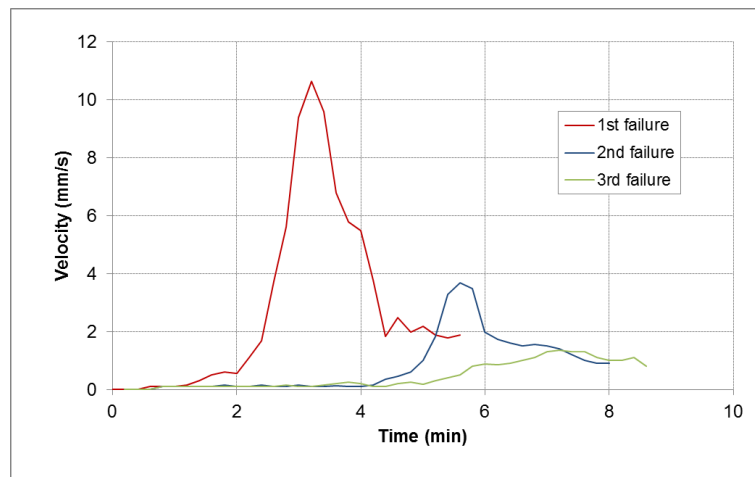


Figure 5.28. Velocity of sliding masses during test S90\_H15\_L35\_2

It is observed that the first and the second failure are discrete events. For failures one and two a peak velocity is reached and then the mass of soil that failed slows down. More specifically, while before the first and the second failure small displacements were observed in the slope before the failure until at some point the mass of soil suddenly slides downwards the slope, during the third event it was not easy to distinguish between the small deformations

and the actual failure. However, for the third failure an almost constant velocity is developed, since no clear rigid body is observed to slide away. The peak velocity is higher during the first failure event.

### **5.5.3. General observations**

The aim of the described set of experiments was to investigate the slope behaviour under different rainfall intensities. From the observed displacements vectors at different rainfall intensities and according to the image-based measurements seen in Figure 5.16, Figure 5.19 and Figure 5.22, it can be concluded that the displacement of the slope increased with increasing rainfall amount and decreased from the surface to the interior of the slope as a whole.

The deformation was mainly concentrated near the surface of the slope at the beginning of each test, as it mainly depends on the rainfall infiltration. This is also apparent in Figure 5.23, where the accumulated soil displacement is plotted for two patches until the onset of the first failure and when the water has not yet infiltrated deep inside the model. Although the displacements of the element on the slope top are significant, both in the vertical but also in the horizontal direction (Figure 5.23a), no movement is recorded for the soil element on the slope bottom (Figure 5.23b). By observing the water infiltration behaviour one can predict in principal the deformation behaviour of the slope, since there seems to be a close relationship.

When a second failure was observed, for the cases of higher rainfall intensities, it was seen that the soil mass that slides away during the second failure is significantly smaller than that of the first failure. In Figure 5.29, the areas of each failure are plotted for every experiment, where a successive failure was observed, normalised to the area of the first failure.



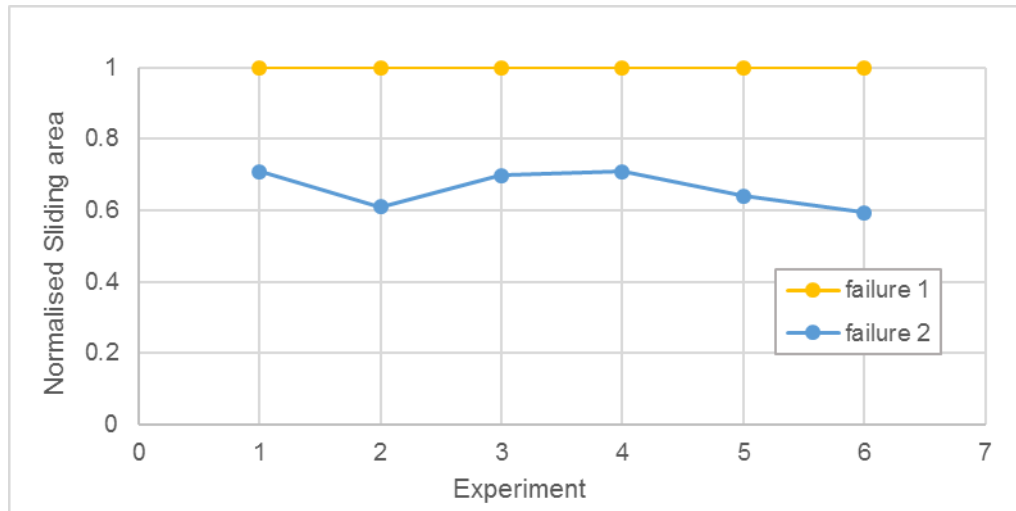


Figure 5.29. Sliding area of each failure normalised to the area of the first failure

### 5.6. Effect of flume bottom on the evolution of the slope

Another aspect that was investigated was the effect of the material at the bottom of the container on the sliding behaviour of the failed mass and thus on slope evolution. Two different surfaces were examined to explore the difference on debris propagation and its effect on slope evolution: in one case the bottom of the container was Plexiglas (Figure 5.30a), leaving the material to slide freely on it, while in the other case soil particles were glued on the bottom of the flume to mimic sliding on the same type of material as the one making the slope (Figure 5.30b).

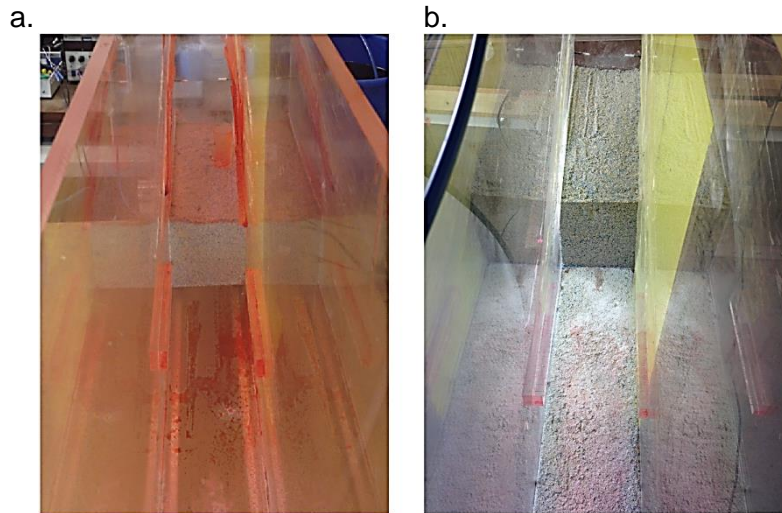


Figure 5.30. Container bottom made of a. Plexiglas and b. Soil particles layer

Experimental results of two sets of experiments under the same rainfall intensity are presented in this part. The experimental results presented below concern comparisons between S90\_H15\_L35\_6 and S90\_H15\_L35\_18 with a steady rainfall intensity of  $I_r=10\text{mm/h}$  applied on the slope and S90\_H15\_L35\_4 with S90\_H15\_L35\_19 with a steady rainfall intensity of  $I_r=20\text{mm/h}$  (see Table 5.2).

In the first batch of experiments, the slope material that failed, was left to slide on the Plexiglas bottom of the container (see Figure 5.30a), while for the next batch, a thin layer (1.00-1.50mm) of soil particles was glued to the floor of the container (see Figure 5.30b) to create friction and to inhibit direct sliding of the slope base along the soil - container interface.

In Figure 5.31 and Figure 5.32, the final profile of the slope for the case of Plexiglas bottom and for soil particles glued on the bottom is illustrated for of  $I_r=10\text{mm/h}$  and  $I_r=20\text{mm/h}$  respectively. The failure mechanisms that were develop for both cases, were similar and occurred at the same time after the start of rainfall. In no case a second failure was observed, since the rainfall

intensity was kept low, however the debris propagation is different for different bottom surfaces.

In Figure 5.31a and Figure 5.32a the slope profile for Plexiglas bottom after a certain time of rainfall is illustrated, while in Figure 5.31b and Figure 5.32b the slope profile for soil particles glued in the bottom of the container. It can be seen that when soil particles are glued on the bottom of the container, the friction that is developed between the failed mass and the bottom does not allow the debris to propagate as much as in the case that the bottom is made of Plexiglas. Especially for the case of  $I_r=20\text{mm/h}$  and when soil particles are glued on the bottom, the friction developed between the failed mass and the container bottom does not let the failed mass to slide and a few minutes after the failure, toppling was observed (Figure 5.32b).

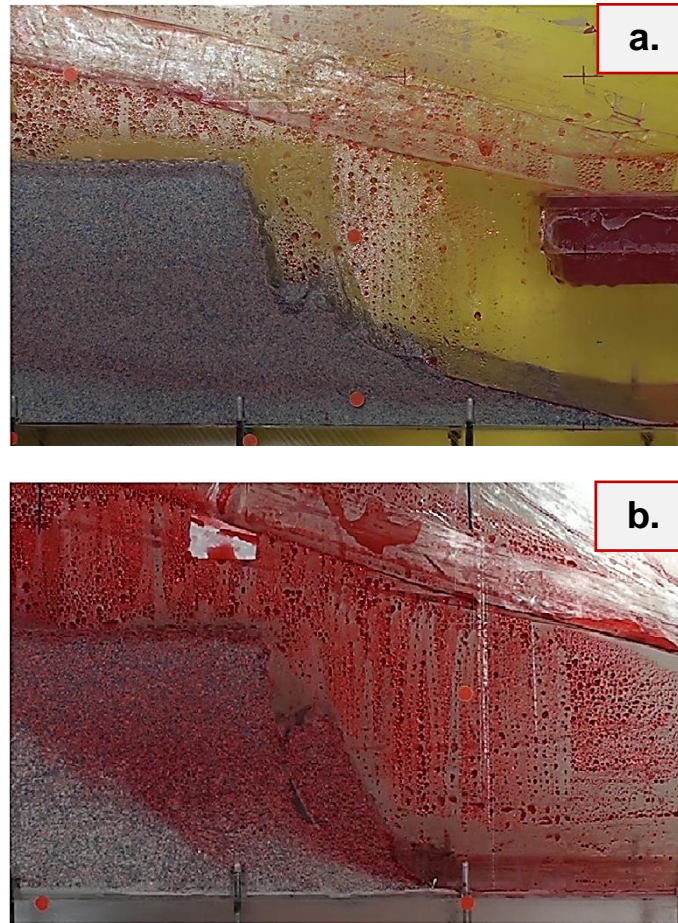


Figure 5.31. Slope profile at  $t=105\text{min}$  from the initiation of rainfall for  $I_r=10\text{mm/h}$  and after the occurrence of one failure for a. Plexiglas bottom (test: S90\_H15\_L35\_6) b. soil particles glued on the bottom of the container (test: S90\_H15\_L35\_18)

The aim of this comparison was to investigate the effect of the material on which the debris slides on the debris propagation. It was shown, that the friction between the bottom material and the failed mass affects the debris propagation. More specifically, once the friction is higher the debris propagates less and as a result the failed mass acts as a stabilising force on the rest of the slope. In the next paragraph the stabilising effect of the failed mass is studied.

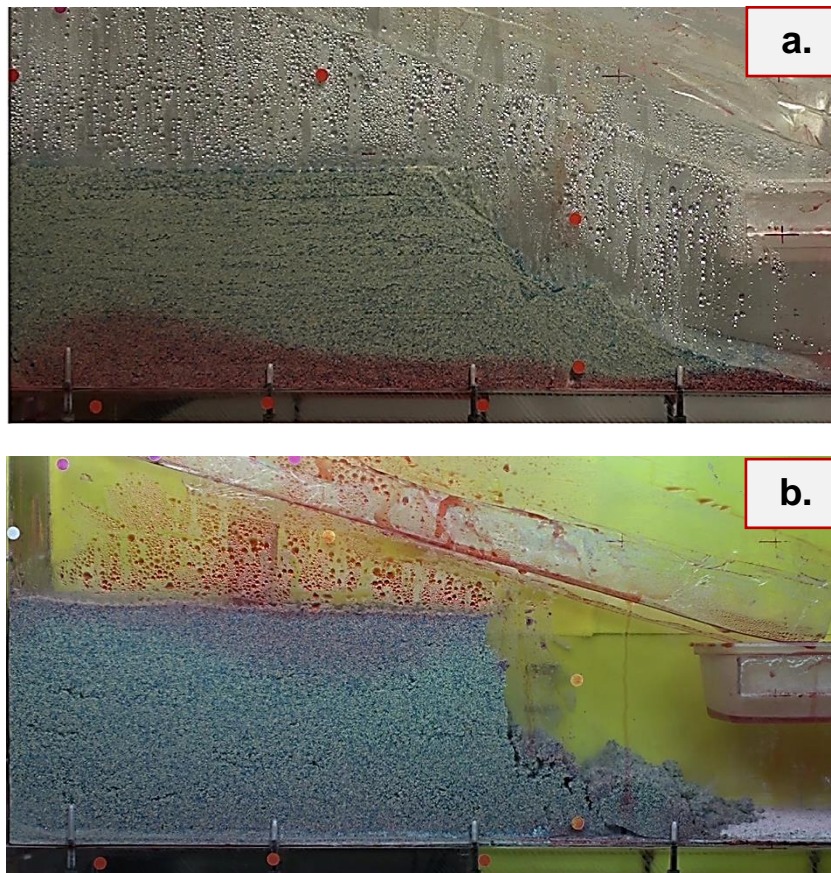


Figure 5.32. Slope profile at  $t=40\text{min}$  from the initiation of rainfall for  $I_r=20\text{mm/h}$  and after the occurrence of one failure for a. Plexiglas bottom (test: S90\_H15\_L35\_4) b. soil particles glued on the bottom of the container (test: S90\_H15\_L35\_19)

### 5.7. Stabilising effect of the failed mass

In this part, the stabilizing effect of the slumped debris on slope stability is examined. To this end, slope models were built in the transparent flume and were subjected to heavy rainfall. Two different cases are presented here; in one case debris is manually removed after the occurrence of each, while in the other one, debris is allowed to accumulate at the slope toe.

Experimental results of two sets of experiments under the same rainfall intensity are presented. The experiments presented below are



S90\_H15\_L35\_14 and S90\_H15\_L35\_16 (see Table 5.2). A steady rainfall intensity of  $I_r=45\text{mm/h}$  was applied on the slopes. In the first batch of experiments the debris accumulating at the slope toe after each failure is manually removed to mimic the effect of strong atmospheric agents or fluvial or marine erosion that remove all the debris before a new landslide develops. The debris is carefully removed just after a landslide has occurred using a scoop, following the line of the failure mechanism (Figure 5.33), in order to avoid any changes to the new slope profile.



*Figure 5.33. Removal of slumped debris after the occurrence of each failure  
(test: S90\_H15\_L35\_14)*

In Figure 5.34 and Figure 5.35, the evolution of the slope is illustrated for the case that debris is removed from the toe and where debris is left in situ respectively. Figure 5.34b and Figure 5.35b show the slope during the first failure that occurred approximately 16 minutes after the rainfall started. In Figure 5.34c and Figure 5.35c the second failure is plotted. In the case of the removed debris from the slope toe (Figure 5.34c), the second failure takes place earlier at  $t_2=22\text{min}$  than in the case of debris left at the slope toe (Figure 5.35c) where the second failure occurs at  $t_2'=25\text{min}$ . Moreover, the wedge coming off the slope face is larger with the failure mechanism being deeper in case of removed debris (see Figure 5.34c and Figure 5.35c). Also note that at

the onset of the second failure the position of the waterfront is shallower in the case of removed debris than the position in the case of debris left in situ, because it occurs much before the second failure in the case of debris left in situ allowing less time for water to infiltrate.

In Figure 5.34d the slope at  $t_3=33\text{min}$  after initiation of rainfall is plotted when the third failure takes place in the slope with the debris being removed from the toe. Instead, in case of debris left in situ on the slope toe no third failure is observed (see Figure 5.35d). The experiment lasted for 45 minutes in total until the rainfall was stopped. One more failure took place at  $t_4=44\text{min}$  in the case of debris removal, whereas no further failure was observed on the slope where the debris was left on the slope toe.

In Figure 5.36a and Figure 5.36b the slope is photographed after 45 min for the case of debris removal and debris left in situ respectively. It can be observed that when the debris is removed from the slope toe, the slope front retreats further inwards since more failures occur for the same rainfall intensity and duration. This is in agreement with analytical and numerical models of cliffs subject to weathering (Utili and Nova, 2008, Utili and Crosta, 2011a, Utili and Crosta, 2011b) where it is shown that the weight of the soil debris accumulating on the slope toe contribute to resist subsequent failures and decrease the total final inward retreat of the slope.

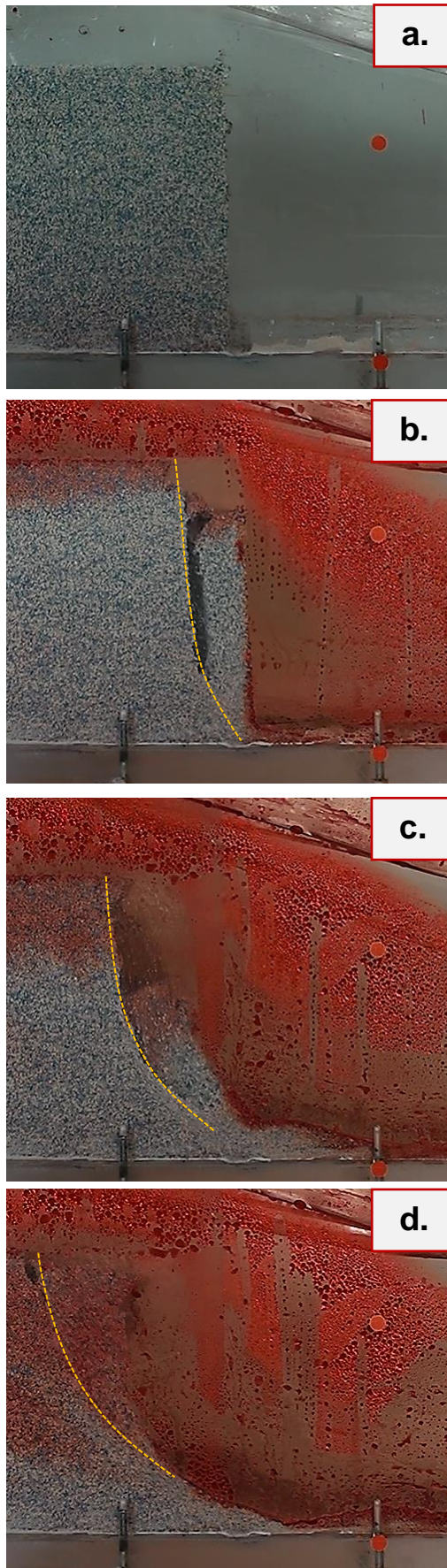


Figure 5.34. Initiation of three successive failure when debris is removed from the slope toe (test: S90\_H15\_L35\_14), a. initial state ( $t_0 = 0$  min) b. first failure ( $t_1 = 16$  min) c. second failure ( $t_2 = 22$  min) d. third failure ( $t_3 = 33$  min)



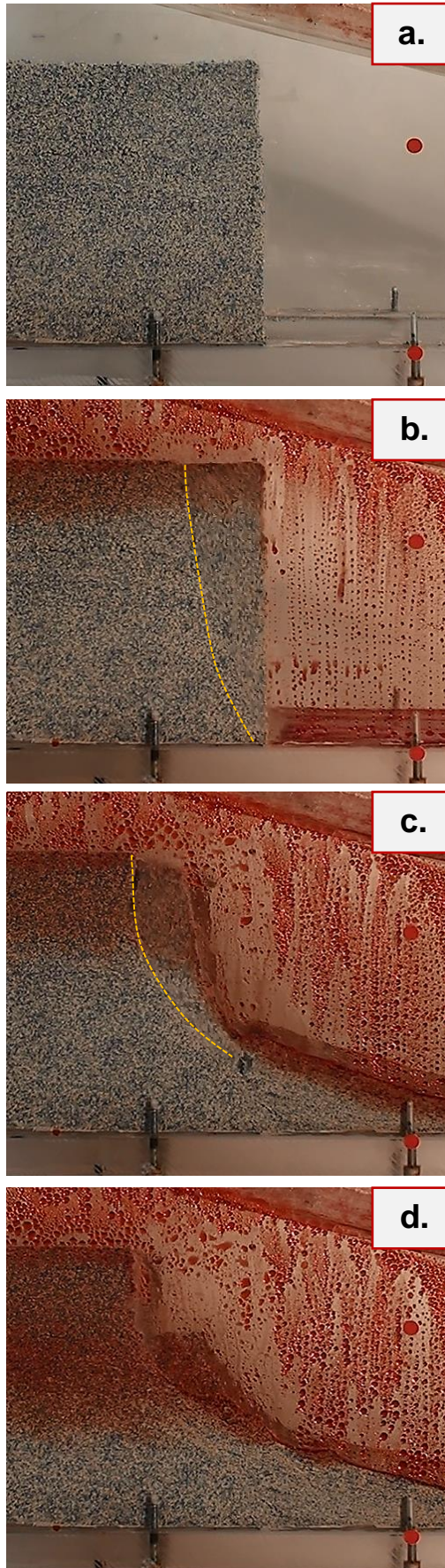


Figure 5.35. Initiation of successive failure without debris removal (test: S90\_H15\_L35\_16) a. initial state ( $t_0' = 0$  min) b. first failure ( $t_1' = 16$  min) c. second failure ( $t_2' = 25$  min) d. at the end of the test ( $t_3' = 45$  min)

The aim of this part was to investigate progressive rainfall-induced slope failures and the stabilizing effect of debris accumulated at the slope toe and the following conclusions can be drawn:

- The results suggested that when the debris that accumulated at the slope toe is removed before a new landslide develops; the new failure takes place earlier than in the case where the soil remains at the slope toe.
- It was illustrated that the cliff retreat is faster when the accumulated debris is removed and the amount of soil slides away in the case of soil removal is larger.
- The slumped debris contributes to the stability of the slope, acting as a stabilizing force. This, if not accounted for, can alter the stability number and the failure mechanisms when performing slope stability analyses.



*Figure 5.36. Slope profile at  $t=45\text{min}$  from the initiation of rainfall after the occurrence of a. four failures (debris removal) b. two failures (no debris removal)*

### 5.8. Experimental results for inclined slope front

The experiments were also extended for cases with no vertical slope front. Experiments 23 to 28 (see Table 5.2) have been carried out for an inclined initial slope profile with inclinations  $\beta=60^\circ$  (23-26) and  $\beta=45^\circ$  (27-28). For the construction of the slopes with inclined profile, a vertical slope was first built following the procedure described in Paragraph 4.2.3 and then the abundant material was cut out to achieve the desired slope inclination (Figure 5.37).

It was not possible to capture a rotational failure for the inclined slopes although the rainfall intensity varied from low  $I_r=16\text{mm/h}$  to very intense where  $I_r=60\text{mm/h}$ . In the cases of inclined slope, a local failure that occurred near the slope toe after some time of constant rainfall was observed, which was larger for higher rainfall intensities. However, no global failure occurred in any case. The phenomenon is illustrated in Figure 5.38 for slope with initial inclination  $\beta=60^\circ$  and in Figure 5.39 for slope with initial inclination  $\beta=45^\circ$  for all rainfall intensities that were tested.

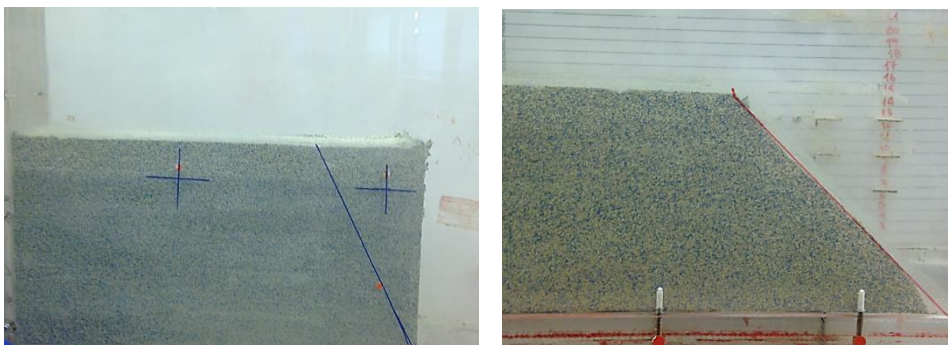


*Figure 5.37. Construction of inclined slope profile*



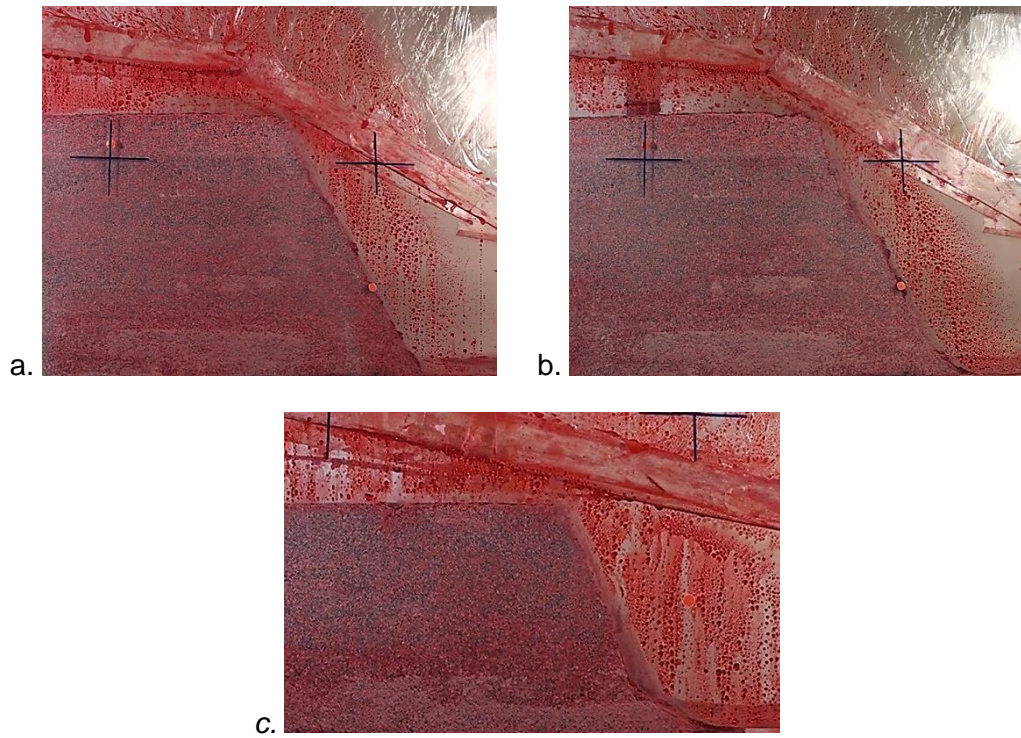


Figure 5.38. Local slope failure for initial slope inclination  $\beta=60^\circ$  and for rainfall intensity a.  $I_r=10\text{mm/h}$ , b.  $I_r=16\text{mm/h}$  and c.  $I_r=30\text{mm/h}$

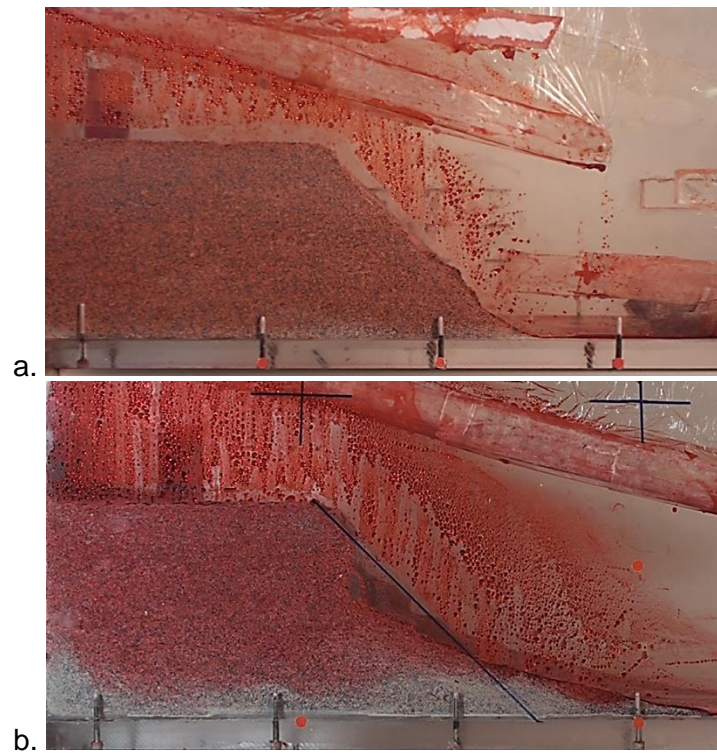


Figure 5.39. Local slope failure for initial slope inclination  $\beta=45^\circ$  and for rainfall intensity a.  $I_r=16\text{mm/h}$  and b.  $I_r=60\text{mm/h}$

### 5.10. Conclusions

In this chapter, the experiments that have been carried out for the needs of this thesis together with the main experimental results have been illustrated. Slope failure was induced in the slopes by water infiltration under different rainfall conditions. From the observation of the slope model's behaviour during the tests described above, it can be stated that this setting performs well and satisfies the aim of this research to study the retrogressive retreat of the slope, as successive failures with cracks were recorded. Matlab image processing of the digital frames from both sides of the flume, suggested that the wetting front was moving homogeneously inside the slope model.

Failure mechanisms of similar geometries have been observed in all vertical slope models, while for inclined slope with  $\beta=60^\circ$  and  $\beta=45^\circ$  no major failure was recorded. Generally, failures that were developed, formed clear brittle failure mechanisms.

The displacement process can be divided into three phases, first one where soil displacements are small and gradually increasing, second one when the main failure takes place and the displacements are increasing rapidly and the final one that failure has taken place and the mass of soil slides slowly away. Water infiltration causes mainly vertical deformation in the soil rather than horizontal one until the failure was reached.

Results showed that more intense rainfall events cause greater soil displacement and overall larger amounts of soil slides away, while the retreat of the cliff moves deeper inside the slope for the same rainfall duration. As for the occurrence of successive failures, it was seen that the soil amount that slides away during the first failure is larger than during a second one.

Moreover, the experiments showed that the material on which the debris slides can affect the debris propagation; once the friction is higher the debris propagates less and as a result the failed mass acts as a stabilising force on the rest of the slope. When the material that slides away was manually removed, the cliff retreat proved to be faster and the mass that slides away larger.

However, as in every experimental effort, there are some limitations and things that could be enhanced in the future. The size of the experiment was kept small and the degree of saturation inside the slope model was high at the initiation of the test, thus not allowing large differences in the moisture content. Regarding the first issue it will be beneficial to repeat some of the tests in a large-scale model or maybe even in a centrifuge to ensure that the results are comparable. Moreover, experiments could also be carried out on dry slopes to observe larger changes in the moisture content of the soils and get a more clear relationship between the moisture content and the displacement of the soil. Also, if the slopes are dry at the initiation of the test it will be possible to observe the movement of the water front from the images.

## Chapter 6 : Conclusions

---

In this thesis, the analytical upper bound theorem of limit analysis and a series of small scale laboratory tests have been employed to investigate the stability of slopes under various actions and to study their morphological evolution. More specifically, the aim of the thesis is to provide general solutions for the stability of intact slopes and slopes with cracks under the influence of water presence and seismic acceleration as well as to predict the morphological evolution of slopes in time due to degradation of the slope material. Solutions are provided through a number of stability charts for a range of friction angle and slope inclination of engineering interest available in this thesis to be used by engineers and practitioners, while more results can be obtained using the Matlab code in the Appendix.

Moreover, through a series of laboratory tests, where failure is achieved through water infiltration, an approximation of the evolution of the slope was attempted to be modeled. In cases, successive failures were achieved.

### 6.1. Analytical model

A comprehensive parametric analysis has been carried out to investigate the effect of weathering of slopes with different tensile strength or

under seismic action and existence of water on the evolution of slopes after a number of failures and until the material becomes almost cohesionless, employing the upper bound limit analysis method together with the pseudo static approach. The evolution of slopes under the aforementioned actions has been compared to the intact, static and dry case.

When cracks are formed in a slope they can cause changes in their evolution, compared to the evolution of intact slopes, especially during the first two failures, leading to different stability numbers, different failure mechanisms and sliding masses. Seismic action and presence of water can lead to faster slope failure and change significantly the morphologic evolution of slopes as the shape and the location of the failure mechanisms vary under different driving forces. In this paper, a model based on the kinematic approach of limit analysis to predict evolution of slopes under various scenarios has been proposed. The location and the depth of the crack as well as the most critical failure mechanism for every failure were calculated through an optimisation procedure. Solutions were provided for different types of problem; determination of the evolution of slopes for slopes with no tensile strength (tension cut-off) where crack forming requires work to open and slopes with soil tensile strength limited to 0.2 and 0.5 of that described by the classical Mohr–Coulomb yield condition have been examined. The influence of seismic acceleration was studied; acting either independently or synergistically with cracks and also the effect of the presence of water was explored. With this model, it is possible to relate the evolution of natural slopes by a sequence of rotational sliding block failures to the degradation of material strength properties. It can be concluded that with the proposed model it is possible, in principle, to predict the evolution by successive failures of any cliff under various actions, knowing the strength degradation over time.



## 6.2. Experimental model

A series of small scale laboratory tests was designed and performed to investigate the onset of failure on slope caused by various actions as well as the evolution of slope due to successive failures. Slope failure was reached by increasing the degree of saturation within the slope through steady rainfall that was applied on the slope crest. For the simulation of the rainfall a bespoke device was designed and constructed. This is made of a distribution system which includes two atomising mist nozzles placed above a container to provide a uniform and steady rainfall to the model. Soil moisture sensors and tensiometers were buried inside the slope model during the construction phase to avoid causing any disturbance to the soil around them. The sensors were connected to a data acquisition system with readings being logged every second. Moreover, high resolution cameras were recording the slope behaviour throughout the duration of the test and GeoPIV was used to analyse the digital images and obtain the deformation of the slope.

Constant rainfall was applied to the slope crest and minor slope displacements were recorded and, in cases, vertical cracks appeared prior to the failure. Slope failure in the case of low rainfall intensity occurred when the soil moisture content within the region that failed and across the failure mechanism reached nearly its saturation value. However, for higher rainfall intensities the failure occurred before the wetting front reaching the slope toe. Once the first failure was triggered, soil region accelerated downwardly, after that, additional deformations occurred in the rest of the slope. For the cases of high rainfall intensities this led to the occurrence of a second failure, however when rainfall intensity was kept low water infiltration alone was not sufficient to induce a second failure.

### 6.3. Comparison of experimental with analytical results

In this part, a comparison between experimental observations and the analytical model described in Chapter 3 is carried out. When designing the experiment, an effort was made to simulate the conditions adopted in the analytical model. However, due to the complexity of the experimental conditions it was not possible to achieve the desired similarity.

The initial idea was to use water infiltration to simulate the material strength degradation and thus achieve successive failures due to material deterioration in time. In the analytical model, it is assumed that the cohesion of the soil is the same through the whole slope. Also, the failure occurs solely due to the uniform degradation of the cohesion in time which leads to successive events. During the experiments, it was not possible to achieve the same moisture content inside the model, thus the strength of the soil was not the same inside the whole slope. Moreover, the use of water during the tests, leads to slope failure due to a combination of factors, that is to say increase of the weight of the soil and also decrease of the soil strength due to changes in moisture content and suction. For these reasons, there are some shortcomings when it comes to comparing experimental to analytical results.

Since the experimental model is wet at the time of the first failure and the moisture content is significant but has not yet its saturation value (Figure 5.12), the comparison is made with results from the analytical model both for  $r_u=0.25$  and  $r_u=0.50$ . It should be noted, that this is an additional difference to the experimental conditions since moisture content was different at different depths at the time of the failure during experiments while for the analytical model the water presence is assumed to be the same in the whole slope.

In Figure 6.1, the slope model is illustrated at the occurrence of the first failure during test S90\_H15\_L35\_3 for rainfall intensity  $I_r=16\text{mm/h}$ . The solution from the analytical model is calculated for a slope with height and friction angle same as these for the slope model during the experiment. More specifically the input height for the analytical model is  $H=15\text{cm}$  and the shear resistance of the soil  $\phi=40^\circ$ . Based on the shear box tests shown in Figure 4.11,  $\phi$  is likely to vary from approximately  $40^\circ$  to  $37^\circ$  during the test, as the failure is reached before the soil becomes fully saturated. Since the soil used in the experiments is a weakly cemented geomaterial, the failure line is calculated from the analytical model for the case of slopes with soil tensile strength limited to  $t=0.5$ . The failure lines as derived from the analytical model are superimposed on a digital image illustrating the slope model during the failure and represented by the blue line for  $r_u=0.25$ , while the green line is for  $r_u=0.50$ . The dashed yellow line is illustrating the failure mechanism developed during the experiment. If lower  $\phi$  is used in the analytical model the failure line moves further away from the slope crest.

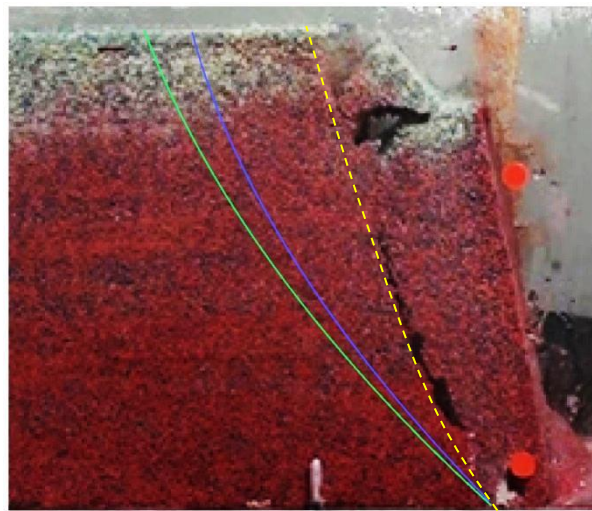


*Figure 6.1. Failure mechanism developed during test S90\_H15\_L35\_3 and failure lines as derived from the analytical model*

It is seen that the mechanisms from the analytical model and that from the experimental results are of similar geometries. However, there is a significant difference in the location that the failure occurs. The failure mechanism derived from the analytical solution includes almost the double amount of soil sliding away. The differences in the failure mechanism between the analytical and the experimental results might be due to the assumptions made to obtain the analytical solutions as well to the limitations of the experimental procedure as described above.

As far as a second failure is concerned a comparison between experimental and analytical results has not been carried out. The comparison of the first failure showed that different mechanisms were derived from the analytical model than those observed during the experiment, making a comparison of the second failure not meaningful. It must be noted however that when a second failure occurred during the experiments, the soil mass that slides away is decreased during the second failure event and that the second failure does not pass through the slope toe, which comes in good agreement with the analytical results.

The analytical solution provided in Chapter 3 is modelling the degradation of the material of a slope in time; a physical phenomenon different from rainfall. Both phenomena cause a decrease of strength inside exposed slopes that drives the onset of successive mass movements and also there is a similarity between these two phenomena in causing slope inward retreat. However, the complexity of the experimental procedure does not allow for uniform conditions inside the slope model (moisture content, cohesion etc.) as assumed in the analytical model. Moreover, during the experiments the failure was reached both because of the decrease in the material strength due to the increase in moisture content and the debonding of the soil particles, but also

because of the increase of the soil weight due to the ingress of water which is not accounted for in the analytical model.

#### **6.4. Recommendations for future work**

This thesis has tackled the problem of the evolution of slopes subject to a progressive retreat. This is especially interesting for many coastal or not areas characterized by moderate to steep cliffs. The results of this thesis could become useful for possible spatially distributed analysis of cliff stability both at a local and at a distributed scale in the UK and internationally, wherever the described phenomena often endanger the coastline.

The analytical model is tested against a real case study for a group of landslides detached from a specific source area in a relatively clear sequence. This case study is interesting as it fits well with the assumptions made for the analytical model, because of the topography of the area leads the mass of soil that fails during each failure (deposits) to move to a distance away from the slope, therefore not affecting the stability of the remaining slope for the various successive failures. The solution could also be applied in other planetary conditions where similar types of landslides have been recognised (Crosta et al., 2012a, Crosta et al., 2014b) and for which rock mass mechanical properties determination could be of great interest.

As far as the analytical part of this work is concerned, the model described in this thesis is a 2D model, which in general is well known to be more conservative than 3D models. A 3D analysis of the problems presented here, although it might be complicated, is required to achieve results closer to the real values.

Regarding the experimental procedure described in this thesis, there are many limitations as in every experiment. The size of the model does not

allow to extract reliable results on the behaviour of the soil, it is however a good indicator. The experiments showed that prediction of slope failure initiation is possible by monitoring changes in soil moisture contents and displacements within the slope prior to the failure. Further studies based on larger scale experiments and in-situ monitoring of actual slopes during rainfall are recommended to verify this conclusion and to develop a comprehensive warning system based on changes in soil moisture content.

Experiments should also be carried out on dry slopes where the identification of the water front will be easier to capture even through image analysis. More experiments can be carried out to validate all the results obtained here, as well as experiments on non - linear initial profiles since they are more common in nature and they have been proven to be more stable than planar ones (Utili and Nova, 2007).

The analytical model developed in this work is a simplified model of what is happening in a real slope, with strong assumptions being made, e.g. uniformity as far as the water presence or the cohesion of the soil. However, while conducting experiments it was not possible to model the same conditions as reality is more complicated. An analysis using more detailed numerical methods could be developed to make more meaningful comparisons with the experimental results.

## Appendices

---

### Appendix A - SOIL MOISTURE SENSORS

#### Calibration

The VEGETRONIX VH400 soil moisture sensors used in these experiments measure the volumetric water content of the soil by measuring the dielectric constant of the soil. Since, not all soils have identical electrical properties, due to variations in soil bulk density, mineralogy, texture and salinity, a generic calibration for these sensors was necessary. For higher precision, repeatability, and sensor to sensor agreement, each specific soil sensor was calibrated for that particular soil type.

The soil was packed into the calibration container at approximately the model bulk density ( $\rho = 1.67 \text{ g/cm}^3$ ). Soil into the containers was added into layers; packing each layer before adding the next. Then the soil moisture sensor was inserted vertically directly and fully into the full soil container. Soil around the exposed portion of the sensor was packed carefully to prevent air gaps while maintaining the desired bulk density. When the above procedure was completed sensors' reading were recorded. There was generally some small variability (a few raw counts), so an average of 10 readings was taken. Next step was to measure the mass of the wet soil with the container, record the mass in Table 1 and put the specimen in the oven for 24 hours at 105°. After 24 hours, the soil containers were removed from the oven and allowed to cool, before measuring the mass of the dry soil and the containers.

This was repeated for another 4 samples, each of them containing different amount of water (Table 1).

From Table 1 it is obvious that all the 6 sensors give almost the same output for the same water content. For that reason, only one calibration curve is exported for all the sensors (Figure 1).

*Table 0.1. Soil moisture content calibration*

sample number	0 sensor output (raw counts)	1 sensor output (raw counts)	2 sensor output (raw counts)	3 sensor output (raw counts)	4 sensor output (raw counts)	5 sensor output (raw counts)	Jar mass (g)	Sample volume (cm <sup>3</sup> )	wet soil mass + container (g)	dry soil mass and container (g)	Mass and volume of water (cm <sup>3</sup> )	Dry soil mass (g)	Soil bulk density (g/cm <sup>3</sup> )	VWC (cm <sup>3</sup> /cm <sup>3</sup> )
									pre oven	after oven				$\theta$
0	219	217	223	240	223	228	33	1020	1266	1266	0	1233	1.21	0.00
1	317	315	306	315	314	317	33	1020	1366	1266	100	1233	1.21	0.10
2	346	353	347	349	356	353	32	1020	1416	1266	150	1234	1.21	0.15
3	420	419	437	420	428	430	33	1020	1466	1266	200	1233	1.21	0.20
4	601	615	615	610	609	616	33	1020	1516	1266	250	1233	1.21	0.25

Calculations for the numbers obtained in Table 1 are illustrated below:

The volumetric water content is defined as the volume of water per volume of bulk soil:

$$\theta = V_w/V_t \quad (1)$$

Where  $\theta$  is volumetric water content (cm<sup>3</sup>/cm<sup>3</sup>),  $V_w$  is the volume of water (cm<sup>3</sup>) and  $V_t$  is the total volume of bulk soil sample (cm<sup>3</sup>).  $V_t$  of the sample is already known.  $V_w$  is the volume of the water that is lost from the soil sample during oven drying:

$$m_w = m_{wet} - m_{dry} \quad (2)$$



$$V_w = m_w/\rho_w \quad (3)$$

Where  $m_w$  is the mass of water,  $m_{wet}$  is the mass of moist soil (g),  $m_{dry}$  is the mass of the dry soil, and  $\rho_w$  is the density of water (1 g/cm<sup>3</sup>). In addition to the volumetric water content, the bulk density of the soil sample can also be calculated. Bulk density ( $\rho_b$ ) is defined as the density of dry soil (g/cm<sup>3</sup>):

$$\rho_b = m_{dry}/V_{soil} \quad (4)$$

Using the trend line function in Excel, a logarithmic line was found to fit best the calibration results, as shown in Figure 1.

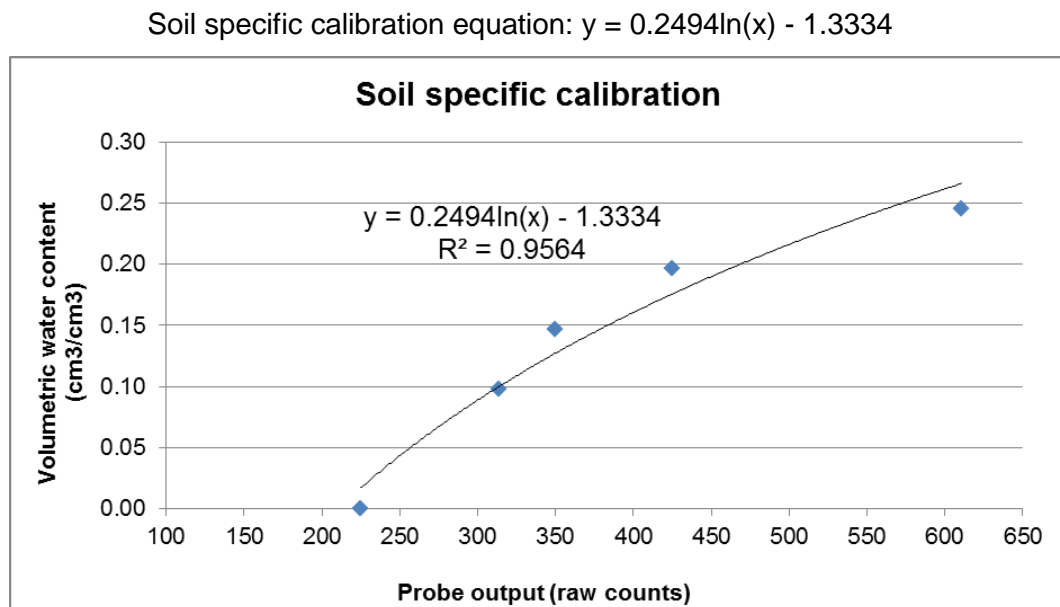


Figure 0.1. Plot of calibration data and soil specific calibration equation.

## ARDUINO Code for data logging

```
int timer = 100;    // The higher the number, the slower
the timing.

void setup() {
  /* Setup the serial port for displaying the status of the
  sensor */
  Serial.begin(9600);
}

int voltage;
void loop() {
  // loop from the lowest pin to the highest:
  for (int i=3; i<6; i++) {
    /* Read the sensors analogue output & send it to the
    serial port */

    Serial.print("DATA,TIME,,");
    Serial.print(analogRead(i));

    Serial.print(",");
    Serial.println(i);
    delay(1000);    // wait for a second
  }
}
```

## Appendix B - ANALYTICAL CALCULATIONS

The analytical calculations for each successive failure are given below.

The areas are shown in Figure 0.2.

Considering the region P<sub>2</sub>JD:

$$\begin{aligned} W_1^n &= W_{P_2JD} = \left(\omega \frac{2}{3} r \theta \cos \theta\right) \left(\frac{1}{2} \gamma r \theta^2 d\theta\right) \\ &= \omega \gamma r_{x_2}^3 \frac{\exp[3 \tan \varphi (y_2 - x_2)] (3 \tan \varphi \cos y_2 + \sin y_2) - 3 \tan \varphi \cos x_2 - \sin x_2}{3(1 + 9 \tan^2 \varphi)} \\ &= \omega \gamma r_{x_2}^3 f_1^n(x_2, y_2, \varphi) \end{aligned}$$

Considering the region P<sub>2</sub>JE:

$$\begin{aligned} W_2^n &= W_{P_2JE} = \left[\omega \frac{1}{3} (2r_{x_2} \cos x_2 - L_2)\right] \left(\frac{1}{2} \gamma L_2 r_{x_2} \sin x_2\right) \\ &= \omega \gamma r_{x_2}^3 \frac{1}{6} \frac{L_2}{r_{x_2}} (2 \cos x_2 - \frac{L_2}{r_{x_2}}) \sin x_2 \\ &= \omega \gamma r_{x_2}^3 f_2^n(x_2, y_2, \varphi) \end{aligned}$$

Considering the region P<sub>2</sub>ED:

$$\begin{aligned} W_3^n &= W_{P_2ED} = \left(\omega \frac{2}{3} r_{y_2} \cos y_2\right) \left(\frac{1}{2} \gamma H r_{y_2} \cos y_2\right) \\ &= \omega \gamma r_{x_2}^3 \frac{1}{3} [\exp(\tan \varphi (y_2 - x_2)) \sin y_2 - \sin x_2] \cos^2 y_2 \exp(2 \tan \varphi (y_2 - x_2)) \\ &= \omega \gamma r_{x_2}^3 f_3^n(x_2, y_2, \varphi) \end{aligned}$$

Considering the region P<sub>2</sub>JI, the rate of the external work is calculated for an infinitesimal slice, as illustrated in Figure 0.2:

$$dW_4^n = u_4 dF_4 = \omega |x_{G_4} - x_P| \gamma dA = \omega \frac{1}{3} r^3 \gamma \cos \theta d\theta$$

where  $u_4$  is the displacement rate of the infinitesimal region,  $dF_4$  is the weight force, and  $x_{G_4}$  and  $x_P$  are the x coordinates of the gravity center of the soil region and of the center of rotation P<sub>2</sub> respectively. Integrating over the whole region, the rate of the work of the region P<sub>2</sub>JI is calculated:

$$\begin{aligned}
W_4^n &= W_{P_2H} = \left(\omega \frac{2}{3} r_\theta \cos \theta\right) \left(\frac{1}{2} \gamma r_\theta^2 d\theta\right) \\
&= \omega \gamma r_{x_2}^3 \frac{\exp[3 \tan \varphi (z_2 - x_2)] (3 \tan \varphi \cos z_2 + \sin x_2) - 3 \tan \varphi \cos x_2 - \sin x_2}{3(1 + 9 \tan^2 \varphi)} \\
&= \omega \gamma r_{x_2}^3 f_4^n(x_2, z_2, \varphi)
\end{aligned}$$

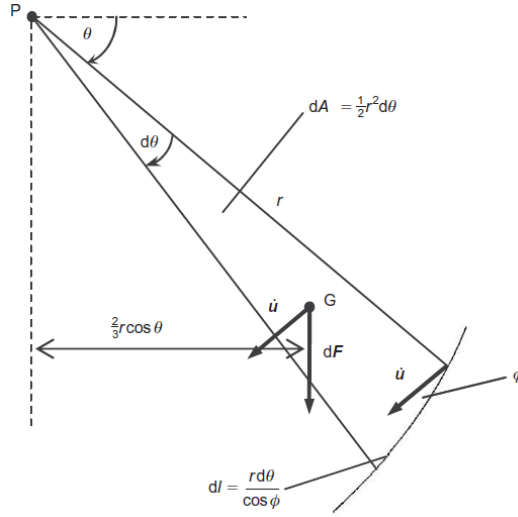


Figure 0.2. Infinitesimal slice of logarithmic spiral regions

Considering the region  $P_2JG$ :

$$\begin{aligned}
W_5^n &= W_{P_2AB} = \left[\omega \frac{1}{3} (2r_{x_2} \cos x_2 - l_2)\right] \left(\frac{1}{2} \gamma l_2 r_{x_2} \sin x_2\right) \\
&= \omega \gamma r_{x_2}^3 \frac{1}{6} \frac{l_2}{r_{x_2}} (2 \cos x_2 - \frac{l_2}{r_{x_2}}) \sin x_2 \\
&= \omega \gamma r_{x_2}^3 f_5^n(x_2, z_2, \varphi)
\end{aligned}$$

Finally, considering the region  $P_2GI$ :

$$\begin{aligned}
W_6^n &= W_{P_2GI} = \left(\omega \frac{2}{3} r_{y_2} \cos z_2\right) \left(\frac{1}{2} \gamma H r_{z_2} \cos z_2\right) \\
&= \omega \gamma r_{x_2}^3 \frac{1}{3} [\exp(\tan \varphi (z_2 - x_2)) \sin z_2 - \sin x_2] \cos^2 z_2 \exp(2 \tan \varphi (z_2 - x_2)) \\
&= \omega \gamma r_{x_2}^3 f_6^n(x_2, z_2, \varphi)
\end{aligned}$$

For the region P<sub>1</sub>FD, the rate of the external work is calculated for an infinitesimal slice, similar to W<sub>4</sub><sup>n</sup> (Figure 0.). Considering this time, as the center of rotation the point P<sub>2</sub>:

$$dW_1^o = (\omega \frac{2}{3} r_{\theta} \cos \theta - r_{y_1} \cos y_1 + r_{y_2} \cos y_2) (\frac{1}{2} \gamma r_{\theta}^2 d\theta)$$

And after integration by parts, manipulations and substitutions of the obtained expression:

$$\begin{aligned} W_1^o &= W_{P_1FD} \\ &= \omega \gamma r_{x2}^3 \left[ \left( \frac{r_{x1}}{r_{x2}} \right)^2 \frac{[\exp(\tan \varphi (y_2 - x_2) \cos y_2 (\exp(2 \tan \varphi (y_1 - x_1) - 1) - 1)]}{4 \tan \varphi} \right. \\ &\quad + \left( \frac{r_{x1}}{r_{x2}} \right)^3 \frac{\exp(3 \tan \varphi (y_1 - x_1)) (\sin y_1 + 3 \tan \varphi \cos y_1) - \sin x_1 - 3 \tan \varphi \cos x_1}{3(1 + 9 \tan^2 \varphi)} \\ &\quad \left. - \left( \frac{r_{x1}}{r_{x2}} \right)^3 \frac{[\exp(\tan \varphi (y_1 - x_1) \cos y_1 [\exp(2 \tan \varphi (y_1 - x_1) - 1)] - 1)]}{4 \tan \varphi} \right] \\ &= \omega \gamma r_{x2}^3 f_1^o(x_1, y_1, x_2, y_2, \varphi) \end{aligned}$$

Considering the region P<sub>1</sub>FE:

$$W_2^o = W_{P_1FE} = \left[ \frac{1}{3} (2r_{x1} \cos x_1 - L_1 + r_{y_2} \cos y_2 - r_{y_1} \cos y_1) \right] \left( \frac{1}{2} \gamma L_1 r_{x1} \sin x_1 \right)$$

And after manipulations and substitutions of the obtained expression, the following expression is obtained:

$$\begin{aligned} W_2^o &= \omega \gamma r_{x2}^3 \frac{1}{2} \frac{L_1}{r_{x1}} \left( \frac{r_{x1}}{r_{x2}} \right)^2 \sin x_1 \left[ \frac{1}{3} \frac{r_{x1}}{r_{x2}} (\cos x_1 - 2 \exp(\tan \varphi (y_1 - x_1) \cos y_1 + \exp(\tan \varphi (y_2 - x_2) \cos y_2) \right. \\ &\quad \left. - \exp(\tan \varphi (y_1 - x_1) \cos y_1) \right] \\ &= \omega \gamma r_{x2}^3 f_2^o(x_1, y_1, x_2, y_2, \varphi) \end{aligned}$$

Considering the region P<sub>1</sub>ED:

$$W_3^o = W_{P_1ED} = (\omega \frac{2}{3} r_{y_1} \cos y_1 - r_{y_1} \cos y_1 + r_{y_2} \cos y_2) (\frac{1}{2} \gamma H r_{y_1} \cos y_1)$$

And after manipulations and substitutions of the obtained expression:

$$\begin{aligned}
W_3^o &= \omega \gamma r_{x2}^3 \frac{1}{2} \left( \frac{r_{x1}}{r_{x2}} \right)^2 \left[ \exp(\tan \varphi (y_1 - x_1) \sin y_1 - \sin x_1) \exp(\tan \varphi (y_1 - x_1) \cos y_1) \right. \\
&\quad \left. \left[ \exp(\tan \varphi (y_2 - x_2) \sin y_2 - \frac{1}{3} \frac{r_{x1}}{r_{x2}} [\exp(\tan \varphi (y_1 - x_1) \cos y_1] \right] \right] \\
&= \omega \gamma r_{x2}^3 f_3^o(x_1, y_1, x_2, y_2, \varphi)
\end{aligned}$$

The external work for the region P<sub>1</sub>FC is calculated similar to that of the rate of the external work W<sub>1</sub><sup>o</sup> and:

$$dW_4^o = (\omega \frac{2}{3} r_\theta \cos \theta - r_{y1} \cos y_1 + r_{y2} \cos y_2) (\frac{1}{2} \gamma r_\theta^2 d\theta)$$

And after integration by parts, manipulations and substitutions of the obtained expression:

$$\begin{aligned}
W_4^o &= W_{P_1FC} \\
&= \omega \gamma r_{x2}^3 \left[ \left( \frac{r_{x1}}{r_{x2}} \right)^2 \frac{\exp(\tan \varphi (y_2 - x_2) \cos y_2 (\exp(2 \tan \varphi (z_1 - x_1) - 1))}{4 \tan \varphi} \right. \\
&\quad \left. + \left( \frac{r_{x1}}{r_{x2}} \right)^3 \frac{\exp(3 \tan \varphi (z_1 - x_1)) (\sin z_1 + 3 \tan \varphi \cos z_1) - \sin x_1 - 3 \tan \varphi \cos x_1}{3(1 + 9 \tan^2 \varphi)} \right. \\
&\quad \left. - \left( \frac{r_{x1}}{r_{x2}} \right)^3 \frac{\exp(\tan \varphi (y_1 - x_1) \cos y_1 [\exp(2 \tan \varphi (z_1 - x_1) - 1)]}{4 \tan \varphi} \right] \\
&= \omega \gamma r_{x2}^3 f_4^o(x_1, z_1, x_2, z_2, \varphi)
\end{aligned}$$

Considering the region P<sub>1</sub>FB:

$$W_5^o = W_{P_1FB} = \left[ \frac{1}{3} (2r_{x1} \cos x_1 - l_1 - r_{y1} \cos y_1 + r_{y2} \cos y_2) \right] \left( \frac{1}{2} \gamma l_1 r_{x1} \sin x_1 \right)$$

And after manipulations and substitutions of the obtained expression and dividing by r<sub>x2</sub><sup>3</sup>, the following expression is obtained:

$$\begin{aligned}
W_5^o &= \omega \gamma r_{x2}^3 \frac{1}{2} \frac{l_1}{r_{x1}} \left( \frac{r_{x1}}{r_{x2}} \right)^2 \sin x_1 \left[ \frac{r_{x1}}{r_{x2}} \left( -\frac{1}{3} (2 \cos x_1 - \frac{l_1}{r_{x1}}) - \exp(\tan \varphi (y_1 - x_1) \cos y_1) + \exp(\tan \varphi (y_2 - x_2) \cos y_2) \right] \right. \\
&= \omega \gamma r_{x2}^3 f_2^o(x_1, y_1, z_1, x_2, y_2, z_2, \varphi)
\end{aligned}$$

Finally, considering the region P<sub>1</sub>BC:

$$W_6^o = W_{P_1BC} = (\omega \frac{2}{3} r_{z1} \cos z_1 - r_{y1} \cos y_1 + r_{y2} \cos y_2) (\frac{1}{2} \gamma H r_{z1} \cos z_1)$$

And after manipulations and substitutions of the obtained expression and dividing by  $r_{x2}^3$ , the following expression is obtained:

$$\begin{aligned}
 W_6^o &= \omega \gamma r_{x2}^3 \frac{1}{2} \left( \frac{r_{x1}}{r_{x2}} \right)^2 \left[ \exp(\tan \varphi (z_1 - x_1) \sin z_1 - \sin x_1) \exp(\tan \varphi (z_1 - x_1) \cos z_1 \right. \\
 &\quad \left. \exp(\tan \varphi (y_2 - x_2) \cos y_2 + \frac{r_{x1}}{r_{x2}} \left( \frac{2}{3} \exp(\tan \varphi (z_1 - x_1) \cos z_1) - \exp(\tan \varphi (y_1 - x_1) \cos y_1) \right) \right] \\
 &= \omega \gamma r_{x2}^3 f_3^o(x_1, y_1, z_1, x_2, y_2, z_2, \varphi)
 \end{aligned}$$

## Appendix C- MATLAB SCRIPTS

### Successive failures with cracks

```
% Main program
% -----
% -----
clear;

% -----
% -----
% Input data
% -----
% -----
% save the results with this filename
filename = 'b_70_f_40_f1_kh01';

% friction angle [deg]
phi_deg=40
% initial slope height [m]
H_ini=1;
% initial slope inclination [deg]
beta_deg=90
% unit weight [KN/m^3]
gamma=18;
gamma_w=9.807;
% n1= number of points used to divide the spiral
n1=100;
% n2+1= number of failures to be determined
n2=0;
% seismic coefficients
seismic=1; %if looking for the critical cohesion seismic=1 if
looking for the yield acceleration seismic=2
lamda=0.0; % ratio between vertical acceleration
coeffecient to the horizontal one ?= Kv/Kh
K_h=0.0; % assigned horizontal acceleration (for static
case K_h=0)
cohesion=300;
cgH=0.024;%cohesion/(gamma*H_ini);%0.0812;

%way==1 for the case that i do not remove the vertical part
from the new profile
%way==2 to use the whole logspiral as the second/third... slope
front
%way==3 to remove planar part (trapezoid)
way=0;
%water
ru=0.5;
%calculation of the energy needed for the crack formation,
%pre-existing crack: formation ==0 / tension cut-off:
formation==1 / reduced
%tensile strength to 0.2*fc: formation==3 / and formation==2
for tensile strength
%limited to 0.5*fc
formation=2;
info=[way;ru;formation;seismic;K_h;lamda;cgH]
```



```

% -----
% Determination of the first spiral
% -----
h_norm(1)=1;
x_guess_deg=58;
y_guess_deg=89;
z_guess_deg=89;
delta_deg=5;
X0=[x_guess_deg;y_guess_deg;z_guess_deg]

% -----
% Determination of the second spiral
% -----
% starting values for the search of the minimum
of funM
x_guess_deg(1)=50;
y_guess_deg(1)=107;
z_guess_deg(1)=55;

delta_deg_2=6;
% -----
if seismic==2
    n1=1;
    %parameters to change when looking for the most critical
    yield acceleration
    %inputs for each failure: const= the height of the
    slope and and
    %the cohesion of the soil const= the normalised height
    of the new
    %failure/slope
    cohesion=300;
    hi(1)=300;
    const(1)=hi(1)/H_ini;
    covergH(1)=cohesion/(gamma*hi(1));
    cohesion=300;
    hi(2)=280;
    const(2)=hi(2)/H_ini;
    covergH(2)=cohesion/(gamma*hi(2));
    cohesion=300;
    hi(3)=250;
    const(3)=hi(3)/H_ini;
    covergH(3)=cohesion/(gamma*hi(3));
    hi(4)=220;
    const(4)=hi(4)/H_ini;
    covergH(4)=cohesion/(gamma*hi(4));
end

% -----
% derived variables
% -----
% determination of angles in radians
beta=beta_deg/180*pi;
phi=phi_deg/180*pi;
b=tan(phi);

```

```

beta_grad_low=phi_deg+3;
deltabeta_grad=1.0;
beta_grad=beta_grad_low;
min_stability_number=2*tan(pi/4+phi/2);

%critical depth = 3.83*c*tan(pi/4+phi/2)/gamma
d_max_upper=3.83*tan(pi/4+phi/2);
d_max_lower=2*tan(pi/4+phi/2);

% determination of the minimum of funI (stability number)
[X,M_,K_y]=funI_num(X0,delta_deg,b,beta,phi,ru,gamma,gamma_w,formation,K_h,seismic);
%=====funI
    M(i)=M_
    x(i)=X(1);
    y(i)=X(2);
    z(i)=X(3);
    K_y(1)=K_y;
    X0=X;
    c_norm(1)=h_norm(1)/M(1);
    end

% geometrical variables
rx_norm(1)=h_norm(1)/(exp(b*(y(1)-x(1)))*sin(y(1))-sin(x(1)));
d_norm1=rx_norm(1)*(exp(b*(z(1)-x(1)))*sin(z(1))-sin(x(1)));
L_norm1=rx_norm(1)*(exp(b*(z(1)-x(1)))*cos(z(1))-exp(b*(y(1)-x(1)))*cos(y(1)));
Xcir_norm(1)=-rx_norm(1)*exp(b*(y(1)-x(1)))*cos(y(1));
Ycir_norm(1)=rx_norm(1)*exp(b*(y(1)-x(1)))*sin(y(1));
retreat_norm(1)=Xcir_norm(1)+rx_norm(1)*cos(x(1))-cot(beta);
M_norm(1)=M_;

% normalised area of the landsliding mass: area/H_ini^2
area1_norm=rx_norm(1)^2*(exp(2*b*(y(1)-x(1)))-1)/(4*b);
area2_norm=1/2*rx_norm(1)^2*sin(x(1))*(-exp(b*(y(1)-x(1)))*cos(y(1))+cos(x(1)));
area3_norm=1/2*rx_norm(1)*exp(b*(y(1)-x(1)))*cos(y(1));
area4_norm=cot(beta)/2;
area_norm(1)=area1_norm-area2_norm-area3_norm-area4_norm;

% -----
% -----
% Determination of the successive spirals
% -----
% -----
for j=1:n2;
    x_old=x(j);
    y_old=y(j);
    z_old=z(j);
    h_norm_old=h_norm(j);
    rx_norm_old=h_norm_old/(exp(b*(y_old-x_old))*sin(y_old)-sin(x_old));

    deltax=(y_old-z_old)/n1;
    x1=x_old;
    y1=y_old;
    z1=z_old;
    if j>1
        way=1;
    end
end

```

```

        if frictionchange==1
            %changing the friction angle
            phi_deg=phi_deg-(phi_deg_in-phi_deg_fn)/n2;
            phi=phi_deg/180*pi
            b=tan(phi);
        end
    for i=1:n1
        X0=[x_guess_deg(i);y_guess_deg(i);z_guess_deg(i)];
        if seismic==1
            % determination of the minimum of funM (stability
number)

[X,fval,fK_y]=funM_num(X0,delta_deg_2,x1,y1,z1,b,phi,info,gamma
,gamma_w);%=====
=====funM
            x_iter(i)=X(1);
            y_iter(i)=X(2);
            z_iter(i)=X(3);
            M_iter(i)=fval;
            h_norm_iter(i)=rx_norm_old*(exp(b*(y1-
x_old))*sin(y1)-sin(x_old));
            c_norm_iter(i)=h_norm_iter(i)/M_iter(i);
        elseif seismic==2
            options = optimset('TolX',1e-18);
            [yh,exitflag,output] =
fzero(@(yh) rx_norm_old*(exp(b*(yh-x_old))*sin(yh)-sin(x_old))-
const(j),[x1 y1],options);
            y1=yh;
            cgH=covergH(j)
            [X,fval]=funM_num(X0,Xdelta,x1,y1,z1,b,phi,info);
            x_iter(i)=X(1);
            y_iter(i)=X(2);
            z_iter(i)=X(3);
            K_y_iter(i)=fK_y;
            h_norm_iter(i)=rx_norm_old*(exp(b*(y1-
x_old))*sin(y1)-sin(x_old));
            M_iter(i)=fval*h_norm_iter(i);
            c_norm_iter(i)=h_norm_iter(i)/M_iter(i);
        end
        x_guess_deg(i+1)=X(1)*180/pi;
        y_guess_deg(i+1)=X(2)*180/pi;
        z_guess_deg(i+1)=X(3)*180/pi;
        y1=y1-deltay;
        delta_deg_2=2;
    end
    if seismic==1
        [d,ii]=max(c_norm_iter);
        % if ii==n1
        %   check=1
        %   break;
        % end
        M_new=M_iter(ii);
        theta_old=y_old-deltay*(ii-1);
        x_new=x_iter(ii);
        y_new=y_iter(ii);
        z_new=z_iter(ii);
        K_y_new=fK_y;
        h_norm_new=h_norm_iter(ii);
        rx_norm_new=h_norm_new/(exp(b*(y_new-x_new))*sin(y_new)-
sin(x_new));
        c_norm_new=c_norm_iter(ii);
    end
end

```

```

M_norm_new=1/c_norm_iter(ii);
elseif seismic==2
    [d,ii]=min(K_y_iter);
    M_new=M_iter(ii)
    K_y_new=K_y_iter(ii);
    theta_old=y1;
    x_new=x_iter(ii);
    y_new=y_iter(ii);
    z_new=z_iter(ii);
    K_y_new=fK_y;
    h_norm_new=h_norm_iter(ii);
    rx_norm_new=h_norm_new/(exp(b*(y_new-x_new))*sin(y_new)-
sin(x_new));
    c_norm_new=c_norm_iter(ii);
    M_norm_new=1/c_norm_iter(ii);
end

theta(j)=theta_old;
x(j+1)=x_new;
y(j+1)=y_new;
z(j+1)=z_new;
x_guess_deg(1)=x_new*180/pi;
y_guess_deg(1)=y_new*180/pi;
z_guess_deg(1)=z_new*180/pi;
rx_norm(j+1)=rx_norm_new;
M(j+1)=M_new;
h_norm(j+1)=h_norm_new;
c_norm(j+1)=c_norm_new;
M_norm(j+1)=M_norm_new;
Xcir_norm(j+1)=rx_norm(j)*exp(b*(theta(j)-
x(j)))*cos(theta(j))-rx_norm(j+1)*exp(b*(y(j+1)-
x(j+1)))*cos(y(j+1))+Xcir_norm(j);
Ycir_norm(j+1)=rx_norm(j+1)*exp(b*(y(j+1)-
x(j+1)))*sin(y(j+1))+1-h_norm(j+1);
rx_norm(j+1)=rx_norm_new;

d_norm(1)=d_norm1;
L_norm(1)=L_norm1;
L_norm(j+1)=rx_norm(j+1)*(exp(b*(z(j+1)-x(j+1)))*cos(z(j+1))-
exp(b*(y(j+1)-x(j+1)))*cos(y(j+1)));
d_norm(j+1)=rx_norm(j+1)*(exp(b*(z(j+1)-x(j+1)))*sin(z(j+1))-
sin(x(j+1)));

% area of the landsliding mass
area1_norm_new=rx_norm_new^2*(exp(2*b*(y_new-x_new))-
1)/(4*b);
area2_norm_new=1/2*rx_norm_new^2*sin(x_new)*(-exp(b*(y_new-
x_new))*cos(y_new)+cos(x_new));
area3_norm_new=1/2*rx_norm_new^2*exp(b*(y_new-
x_new))*cos(y_new)*(exp(b*(y_new-x_new))*sin(y_new)-
sin(x_new));
area1_norm_old=rx_norm_old^2*(exp(2*b*(theta_old-x_old))-
1)/(4*b);
area2_norm_old=1/2*rx_norm_old^2*sin(x_old)*(-
exp(b*(theta_old-x_old))*cos(theta_old)+cos(x_old));
area3_norm_old=1/2*rx_norm_old^2*exp(b*(theta_old-
x_old))*cos(theta_old)*(exp(b*(theta_old-
x_old))*sin(theta_old)-sin(x_old));
area_norm(j+1)=area1_norm_new - area2_norm_new -
area3_norm_new - (area1_norm_old - area2_norm_old -
area3_norm_old);

```

```

% Storing of values in arrays
theta(j)=theta_old;
x(j+1)=x_new;
y(j+1)=y_new;
h_norm(j+1)=h_norm_new;
c_norm(j+1)=c_norm_new;
M(j+1)=M_new;
K_y(j+1)=K_y_new;
rx_norm(j+1)=rx_norm_new;

% storing of other geometrical variables gotten from the
above values
A(j+1)=-rx_norm(j+1)*exp(b*(y(j+1)-x(j+1)))*cos(y(j+1));
B(j+1)=rx_norm(j+1)*exp(b*(y(j+1)-x(j+1)))*sin(y(j+1));
Xcir_norm(j+1)=rx_norm(j)*exp(b*(theta(j)-
x(j)))*cos(theta(j))+A(j+1)+Xcir_norm(j);
Ycir_norm(j+1)=B(j+1)+1-h_norm(j+1);
retreat_norm(j+1)=Xcir_norm(j+1)+rx_norm(j+1)*cos(x(j+1))-
cot(beta);
end

%   phi_deg=phi_deg_in;
%   phi=phi_deg/180*pi
%   b=tan(phi);

% creation of further geometrical variables
x_deg=x*180/pi
y_deg=y*180/pi
z_deg=z*180/pi
theta(n2+1)=0;
theta_grad=theta*180/pi;

% determination of dimensional variables
h=h_norm*H_ini;
rx=rx_norm*H_ini;
Xcir=Xcir_norm*H_ini;
Ycir=Ycir_norm*H_ini;
c=c_norm*gamma*H_ini;
%to plot at the same plot (existing)
hold on

% Plotting
plot_line1(H_ini,beta,'k')
axis equal
hold on
plot_line1(H_ini,phi,'g')
% Spiral plotting
plot_spirals1
hold off

save(filename)

```

```

function
% for the first failure
[X,M_,K_y]=funI_num(X0,delta_deg,b,beta,phi,ru,gamma,gamma_w,fo
rmation,K_h,seismic)

step=1;
x_range_deg=(-delta_deg+X0(1)):step:(delta_deg+X0(1));
y_range_deg=(-delta_deg+X0(2)):step:(delta_deg+X0(2));
z_range_deg=(-delta_deg+X0(3)):step:(delta_deg+X0(3));

x_range=x_range_deg/180*pi;
m=size(x_range);
n3=m(2);
y_range=y_range_deg/180*pi;
m=size(y_range);
n4=m(2);
z_range=z_range_deg/180*pi;
m=size(z_range);
n5=m(2);
for k=1:n3
    for l=1:n4
        for j=1:n5
            if (x_range(k)>y_range(l)-10e-6) |
(x_range(k)>z_range(j)-10e-6) | (z_range(j)>y_range(l)-10e-6)
                funI(k,l,j)=NaN;
            else
                g=exp(2*b*(z_range(j)-
x_range(k)))*(exp(2*b*(y_range(l)-z_range(j)))-
1)*(exp(b*(y_range(l)-x_range(k)))*sin(y_range(l))-
sin(x_range(k)))/(2*b);
                f1=(exp(3*b*(y_range(l)-
x_range(k)))*(sin(y_range(l))+3*b*cos(y_range(l)))-
3*b*cos(x_range(k))-sin(x_range(k)))/(3*(1+9*b^2));
                fLrx=sin(y_range(l)-
x_range(k))/sin(y_range(l))-
sin(y_range(l)+beta)/(sin(y_range(l))*sin(beta))*(exp(b*(y_rang
e(l)-x_range(k)))*sin(y_range(l))-sin(x_range(k)));
                f2=1/6*fLrx*sin(x_range(k))*(2*cos(x_range(k))-
fLrx);
                f3=1/6*exp(b*(y_range(l)-
x_range(k)))*(sin(y_range(l)-x_range(k))-
fLrx*sin(y_range(l)))*(cos(x_range(k))-
fLrx*cos(y_range(l))*exp(b*(y_range(l)-x_range(k))));
                f4=(exp(3*b*(z_range(j)-
x_range(k)))*(sin(z_range(j))+3*b*cos(z_range(j)))-
3*b*cos(x_range(k))-sin(x_range(k)))/(3*(1+9*b^2));
                f5=1/6*sin(x_range(k))*((cos(x_range(k)))^2-
exp(2*b*(z_range(j)-x_range(k)))*(cos(z_range(j)))^2);
                f6=1/3*exp(2*b*(z_range(j)-
x_range(k)))*(cos(z_range(j)))^2*(sin(z_range(j))*exp(b*(z_rang
e(j)-x_range(k)))-sin(x_range(k)));
                % here are the functions for horizontal coeffecient Kh:
                f1_h=(exp(3*b*(y_range(l)-x_range(k)))*(-
cos(y_range(l))+3*b*sin(y_range(l)))-
3*b*sin(x_range(k))+cos(x_range(k)))/(3*(1+9*b^2));
                f2_h=1/3*fLrx*(sin(x_range(k)))^2;
                f3_h=1/6*exp(b*(y_range(l)-
x_range(k)))*(sin(y_range(l)-x_range(k))-

```

```

fLrx*sin(y_range(1)))*(exp(b*(y_range(1)-
x_range(k)))*sin(y_range(1))+sin(x_range(k)));
f4_h=(exp(3*b*(z_range(j)-
x_range(k)))*(3*b*sin(z_range(j))-cos(z_range(j)))-
3*b*sin(x_range(k))+cos(x_range(k)))/(3*(1+9*b^2));
lrx=cos(x_range(k))-exp(b*(z_range(j)-
x_range(k)))*cos(z_range(j));
f5_h=1/3*lrx*(sin(x_range(k)))^2;
f6_h=1/6*exp(b*(z_range(j)-
x_range(k)))*cos(z_range(j))*(exp(2*b*(z_range(j)-
x_range(k)))*sin(z_range(j))^2-sin(x_range(k))^2);

if formation==0
    fcf=0;
elseif formation==1
    %energy for crack formation with cut off

tan_theta_c=sin(x_range(k))/((exp(b*(z_range(j)-
x_range(k))))*cos(z_range(j)));
theta_c=atan(tan_theta_c);
if theta_c<phi

fcf=50000000000000000000000000000000;
else
    int_fcf = integral(@(theta) (1-
sin(theta))./(cos(theta)).^3,theta_c,z_range(j));

fcf=((sin(x_range(k))/tan_theta_c)^2)*(cos(phi)/(1-
sin(phi)))*int_fcf*(exp(b*(y_range(1)-
x_range(k)))*sin(y_range(1))-sin(x_range(k)));
end
elseif formation==3
    %energy for crack formation with limited
tensile

    %strength (=0.2)

tan_theta_c=sin(x_range(k))/((exp(b*(z_range(j)-
x_range(k))))*cos(z_range(j)));
theta_c=atan(tan_theta_c);
if theta_c<phi

fcf=50000000000000000000000000000000;
else
    int_fcf1 = integral(@(theta) (1-
sin(theta))./(cos(theta)).^3,theta_c,z_range(j));
    int_fcf2 = integral(@(theta)
(sin(theta)-sin(phi))./(cos(theta)).^3,theta_c,z_range(j));

fcf=((sin(x_range(k))/tan_theta_c)^2)*((cos(phi)/(1-
sin(phi)))*int_fcf1+0.4*(cos(phi)/(1-
sin(phi).^2))*int_fcf2)...
    *(exp(b*(y_range(1)-
x_range(k)))*sin(y_range(1))-sin(x_range(k)));
end
elseif formation==2
    %energy for crack formation with limited
tensile

    %strength (=0.5)

tan_theta_c=sin(x_range(k))/((exp(b*(z_range(j)-
x_range(k))))*cos(z_range(j)));

```





```

                                                (exp(2*b*(theta_z1-
x_range(k)))).*b),z_range(j),theta1);
        int_z2=integral(@(theta_z2) ((exp(b*(theta_z2-
x_range(k))).*sin(theta_z2)-sin(y_range(1))).*...
                                                exp(b*(y_range(1)-
x_range(k)))+(exp(b*(theta_z2-x_range(k))).*cos(theta_z2)-...

cos(y_range(1))*exp(b*(y_range(1)-
x_range(k)))).*tan(beta)).*...

(exp(2*b*(theta_z2-x_range(k))))*b,theta1,y_range(1));
        %total energy dissipated along the failure line due
to the water pore pressure
        fw=int_z0+int_z1+int_z2;
    end
end
% -----
-----

        %stability number
        funI(k,l,j)=(g+fcf)/(f1-f2-f3-f4+f5+f6+K_h*(f1_h-
f2_h-f3_h-f4_h+f5_h+f6_h)+ru*fw);
%    end
        if (funI(k,l,j) < 1.0) | (funI(k,l,j) > 1000)
            funI(k,l,j)=NaN;
        end
    end
end
end
i=1;
for k=2:(n3-1)
    for l=2:(n4-1)
        for j=2:(n5-1)
            if (funI(k,l,j)<Inf)
                if (funI(k-1,l,j)>funI(k,l,j)) &&
(funI(k+1,l,j)>funI(k,l,j)) && (funI(k,l-1,j)>funI(k,l,j)) &&
(funI(k,l+1,j)>funI(k,l,j)) && (funI(k,l,j-1)>funI(k,l,j)) &&
(funI(k,l,j+1)>funI(k,l,j)) && (funI(k-1,l-1,j)>funI(k,l,j)) &&
(funI(k-1,l+1,j)>funI(k,l,j)) && (funI(k+1,l-1,j)>funI(k,l,j))
&& (funI(k+1,l+1,j)>funI(k,l,j)) && (funI(k-1,l,j-
1)>funI(k,l,j)) && (funI(k-1,l,j+1)>funI(k,l,j)) &&
(funI(k+1,l,j-1)>funI(k,l,j)) && (funI(k+1,l,j+1)>funI(k,l,j))
&& (funI(k,l-1,j-1)>funI(k,l,j)) && (funI(k,l-
1,j+1)>funI(k,l,j)) && (funI(k,l+1,j-1)>funI(k,l,j)) &&
(funI(k,l+1,j+1)>funI(k,l,j)) && (funI(k-1,l-1,j-
1)>funI(k,l,j)) && (funI(k+1,l+1,j+1)>funI(k,l,j))
                    potminima(i)=funI(k,l,j);
                    potx(i)=k;
                    poty(i)=l;
                    potz(i)=j;
                    i=i+1;
            end
        end
    end
end
end
end

if seismic==1
    [M_,II]=min(potminima);
    K_y=K_h;
    k=potx(II);

```

```

        l=poty(II);
        j=potz(II);
        X(1)=x_range(k);
        X(2)=y_range(l);
        X(3)=z_range(j);
elseif seismic==2
    [M_,II]=min(potminima);
    k=potx(II);
    l=poty(II);
    j=potz(II);
    X(1)=x_range(k);
    X(2)=y_range(l);
    X(3)=z_range(j);
end

function
%for second and each successive failure
[X,fval,fK_y]=funM_num(X0,delta_deg_2,x1,y1,z1,b,phi,info,gamma
,gamma_w);
step=1;
x_range_deg=(-delta_deg_2+X0(1)):step:(delta_deg_2+X0(1));
y_range_deg=(-delta_deg_2+X0(2)):step:(delta_deg_2+X0(2));
z_range_deg=(-delta_deg_2+X0(3)):step:(delta_deg_2+X0(3));

way=info(1);
ru=info(2);
formation=info(3);
seismic=info(4);
K_h=info(5);
lamda=info(6);
cgH=info(7);

% vertical seismic coefficient
K_v=lamda*K_h;

t=45*pi/180;
tan_theta=sin(x1)/(exp(b*(z1-x1))*cos(z1)+(exp(b*(z1-
x1))*sin(z1)-sin(x1))*tan(t));
theta=atan(tan_theta);

x_range=x_range_deg/180*pi;
m1=size(x_range);
n3=m1(2);
y_range=y_range_deg/180*pi;
m2=size(y_range);
n4=m2(2);
z_range=z_range_deg/180*pi;
m3=size(z_range);
n5=m3(2);
for k=1:n3
    for l=1:n4
        for j=1:n5
            if (x_range(k)>y_range(l)-10e-6) |
(x_range(k)>z_range(j)-10e-6) | (z_range(j)>y_range(l)-10e-6)
                funM(k,l,j)=NaN;
            else
                g=exp(2*b*(z_range(j)-
x_range(k)))*(exp(2*b*(y_range(l)-z_range(j)))-

```

```

1)*(exp(b*(y_range(1)-x_range(k)))*sin(y_range(1))-
sin(x_range(k)))/(2*b);

f1n=(exp(3*b*(y_range(1)-
x_range(k)))*(3*b*cos(y_range(1))+sin(y_range(1)))-
3*b*cos(x_range(k))-sin(x_range(k)))/(3*(1+9*b^2));
L2_rx2=cos(x_range(k))-
cos(y_range(1))*exp(b*(y_range(1)-x_range(k)));

f2n=1/6*L2_rx2*sin(x_range(k))*(2*(cos(x_range(k)))-L2_rx2);
f3n=1/3*exp(2*b*(y_range(1)-
x_range(k)))*((cos(y_range(1)))^2)*(exp(b*(y_range(1)-
x_range(k)))*sin(y_range(1))-sin(x_range(k)));

f4n=(exp(3*b*(z_range(j)-
x_range(k)))*(3*b*cos(z_range(j))+sin(z_range(j)))-
3*b*cos(x_range(k))-sin(x_range(k)))/(3*(1+9*b^2));
l2_rx2=cos(x_range(k))-
cos(z_range(j))*exp(b*(z_range(j)-x_range(k)));

f5n=1/6*l2_rx2*sin(x_range(k))*(2*(cos(x_range(k)))-l2_rx2);
f6n=1/3*exp(2*b*(z_range(j)-
x_range(k)))*((cos(z_range(j)))^2)*(exp(b*(z_range(j)-
x_range(k)))*sin(z_range(j))-sin(x_range(k)));
rx1_rx2=(exp(b*(y_range(1)-
x_range(k)))*sin(y_range(1))-sin(x_range(k)))/(exp(b*(y1-
x1))*sin(y1)-sin(x1));

f1o=(rx1_rx2^2)*exp(b*(y_range(1)-
x_range(k)))*cos(y_range(1))*(exp(2*b*(y1-x1))-
1)/(4*b)+(rx1_rx2^3)*((exp(3*b*(y1-
x1))*(sin(y1)+3*b*cos(y1))...
-sin(x1)-3*b*cos(x1))/(3*(1+9*b^2))-
exp(b*(y1-x1))*cos(y1)*(exp(2*b*(y1-x1))-1)/(4*b));
L1_rx1=cos(x1)-exp(b*(y1-x1))*cos(y1);

f2o=1/2*(rx1_rx2^2)*L1_rx1*sin(x1)*(exp(b*(y_range(1)-
x_range(k)))*cos(y_range(1))+1/3*rx1_rx2*(cos(x1)-2*exp(b*(y1-
x1))*cos(y1)));
f3o=1/2*(rx1_rx2^2)*((exp(b*(y1-x1))*sin(y1)-
sin(x1))*exp(b*(y1-x1))*cos(y1)*(exp(b*(y_range(1)-
x_range(k)))*cos(y_range(1))-1/3*rx1_rx2*exp(b*(y1-
x1))*cos(y1)));

f4o=(rx1_rx2^2)*exp(b*(y_range(1)-
x_range(k)))*cos(y_range(1))*(exp(2*b*(z1-x1))-
1)/(4*b)+(rx1_rx2^3)*((exp(3*b*(z1-
x1))*(sin(z1)+3*b*cos(z1))...
-sin(x1)-3*b*cos(x1))/(3*(1+9*b^2))-
exp(b*(y1-x1))*cos(y1)*(exp(2*b*(z1-x1))-1)/(4*b));
l1_rx1=cos(x1)-exp(b*(z1-x1))*cos(z1);

f5o=1/2*(rx1_rx2^2)*l1_rx1*sin(x1)*(exp(b*(y_range(1)-
x_range(k)))*cos(y_range(1))+1/3*rx1_rx2*(2*(cos(x1))-l1_rx1)-
rx1_rx2*exp(b*(y1-x1))*cos(y1));
f6o=1/2*(rx1_rx2^2)*((exp(b*(z1-x1))*sin(z1)-
sin(x1))*exp(b*(z1-x1))*cos(z1)*(exp(b*(y_range(1)-
x_range(k)))*cos(y_range(1))+...
rx1_rx2*(2/3*exp(b*(z1-
x1))*cos(z1)-exp(b*(y1-x1))*cos(y1)));

```





```

1)/(4*b)+rx1_rx2^3*((exp(3*b*(y1-x1))*(3*b*sin(y1)-cos(y1))-
3*b*sin(x1)+cos(x1))/(3*(1+9*b^2))...
-exp(b*(y1-x1))*sin(y1)*(exp(2*b*(y1-x1))-
1)/(4*b));

f2o_h=1/2*rx1_rx2^2*L1_rx1*sin(x1)*(exp(b*(y_range(1)-
x_range(k)))*sin(y_range(1))+rx1_rx2*((2/3)*sin(x1)-exp(b*(y1-
x1))*sin(y1)));
f3o_h=1/2*rx1_rx2^2*(exp(b*(y1-x1))*sin(y1)-
sin(x1))*exp(b*(y1-x1))*cos(y1)*(exp(b*(y_range(1)-
x_range(k)))*sin(y_range(1))+...
rx1_rx2*((1/3)*sin(x1)-(2/3)*exp(b*(y1-
x1))*sin(y1)));
f4o_h=rx1_rx2^2*exp(b*(y_range(1)-
x_range(k)))*sin(y_range(1))*(exp(2*b*(z1-x1))-
1)/(4*b)+rx1_rx2^3*((exp(3*b*(z1-x1))*(3*b*sin(z1)-cos(z1))-
3*b*sin(x1)+cos(x1))/(3*(1+9*b^2))...
-exp(b*(y1-x1))*sin(y1)*(exp(2*b*(z1-x1))-
1)/(4*b));

f5o_h=1/2*rx1_rx2^2*l1_rx1*sin(x1)*(exp(b*(y_range(1)-
x_range(k)))*sin(y_range(1))+rx1_rx2*((2/3)*sin(x1)-exp(b*(y1-
x1))*sin(y1)));
f6o_h=1/2*rx1_rx2^2*(exp(b*(z1-x1))*sin(z1)-
sin(x1))*exp(b*(z1-x1))*cos(z1)*(exp(b*(y_range(1)-
x_range(k)))*sin(y_range(1))+...
rx1_rx2*((1/3)*(sin(x1)+exp(b*(z1-
x1))*sin(z1))-exp(b*(y1-x1))*sin(y1)));
% -----
% -----
% Energy dissipation due to water pore pressure
% -----
% -----
if ru==0
    fw=0;
else
    %work of water along the crack
    z0=exp(b*(z_range(j)-x_range(k)))*sin(z_range(j))-
sin(x_range(k));
    tan_theta_ru=(exp(b*(z_range(j)-
x_range(k)))*sin(z_range(j))-
(gamma/gamma_w)*ru*z0)/(exp(b*(z_range(j)-
x_range(k)))*cos(z_range(j)));
    theta_ru=atan(tan_theta_ru);
    int_z0=integral(@(theta_z0) ((exp(b*(z_range(j)-
x_range(k)))*cos(z_range(j)))*tan(theta_z0)-
sin(x_range(k)))*...
(exp(2*b*(z_range(j)-
x_range(k)))*cos(z_range(j))).^2*tan(theta_z0))./...
(cos(theta_z0)).^2),theta_ru,z_range(j));

    %work of pore pressure along the logspiral part
    %limit to calculate z1
    theta1=0;
    x01=(x_range(k)+y_range(1))/2;
    options=optimset('TolX',1e-18);
    [theta1 exitflag output] =
fzero(@(theta1) (exp(b*(theta1-x_range(k)))*cos(theta1)-
(cos(x_range(k)))+(L2_rx2-L1_rx1*rx1_rx2)),x01,options);

```

```

        if theta1 < z_range(j) | theta1 >
y_range(1)
            fw=5000000;
            funI(k,l,j)=50000;
        else
            %distance between the failure line from the
slope surface(depth for water pore pressure calculations)
            %z1 for distance from the horizontal part of
the slope(crest)and
            %z2 for distance from the inclined part
            int_z1=integral(@(theta_z1)
((exp(b*(theta_z1-x_range(k)))*sin(theta_z1)-
sin(x_range(k)))*...
(exp(2*b*(theta_z1-x_range(k)))*b),z_range(j),theta1);
            tan_beta1=(exp(b*(y1-x1))*sin(y1)-
sin(x1))/(cos(x1)-exp(b*(y1-x1))*cos(y1));
            int_z2 =
integral(@(theta_z2) (0.7*(exp(b*(theta_z2-
x_range(k)))*sin(theta_z2)-sin(y_range(1)))*...
exp(b*(y_range(1)-x_range(k)))+(exp(b*(theta_z2-
x_range(k)))*cos(theta_z2)-cos(y_range(1)))*...
exp(b*(y_range(1)-x_range(k)))*tan_beta1)*...
(exp(2*b*(theta_z2-x_range(k)))*b),theta1,y_range(1));
            %total energy dissipated along the failure
line due to the water pore pressure
            fw=int_z0+int_z1+int_z2;
        end

        end

        %-----
        -----
        -----

        if seismic==1
            %stability number without removing the
vertical mass from the new slope front
            if way==1
                funvalue(k,l,j)=(g+fcf)/((1+K_v)*(f1n-f2n-
f3n-f1o+f2o+f3o-f4n+f5n+f6n+f4o-f5o-f6o)+K_h*(f1n_h-f2n_h-
f3n_h-f1o_h+f2o_h+f3o_h-f4n_h+f5n_h+f6n_h+f4o_h-f5o_h-
f6o_h)+ru*fw);
                %stability number removing the trapezoid mass
from the new slope front
            elseif way==2
                funvalue(k,l,j)=(g+fcf)/((1+K_v)*(f1n-f2n-
f3n-f1o+f2o+f3o-f4n+f5n+f6n)+K_h*(f1n_h-f2n_h-f3n_h-
f1o_h+f2o_h+f3o_h-f4n_h+f5n_h+f6n_h)+ru*fw);
                %stability number using the whole logspiral as
the new slope face
            elseif way==3
                funvalue(k,l,j)=(g+fcf)/((1+K_v)*(f1n-f2n-
f3n-f1o+f2o+f3o-f4n+f5n+f6n+f4o-f5o-f6o-fp1)+K_h*(f1n_h-f2n_h-
f3n_h-f1o_h+f2o_h+f3o_h-f4n_h+f5n_h+f6n_h+f4o_h-f5o_h-f6o_h-
fp1)+ru*fw);
            end
            elseif seismic==2
                funvalue(k,l,j)=(cgH*g-(f1n-f2n-f3n-
f1o+f2o+f3o-f4n+f5n+f6n+f4o-f5o-f6o))/(lamda*(f1n-f2n-f3n-

```

```

f1o+f2o+f3o-f4n+f5n+f6n+f4o-f5o-f6o)+(f1n_h-f2n_h-f3n_h-
f1o_h+f2o_h+f3o_h-f4n_h+f5n_h+f6n_h+f4o_h-f5o_h-f6o_h)); %K_y
    end
    if seismic==1
        if (funvalue(k,l,j)< 1)
            funM(k,l,j)=Inf;
        elseif (funvalue(k,l,j) > 50000.0)
            funM(k,l,j)=Inf;
        else
            funM(k,l,j)=funvalue(k,l,j);
        end
    elseif seismic==2
        if (funvalue(k,l,j) < 0)
            funM(k,l,j)=Inf;
        elseif (funvalue(k,l,j)> 1)
            funM(k,l,j)=Inf;
        else
            funM(k,l,j)=funvalue(k,l,j);
        end
    end
end
end
end
end

M_=1000;
i=1;
for k=2:(n3-1)
    for l=2:(n4-1)
        for j=2:(n5-1)
            if funM(k,l,j)<M_;
                if seismic==1
                    M_=funM(k,l,j);
                    fK_y=K_h;
                    fval=M_;
                    X(1)=x_range(k);
                    X(2)=y_range(l);
                    X(3)=z_range(j);
                elseif seismic==2
                    M_=funM(k,l,j);
                    fK_y=M_;
                    X(1)=x_range(k);
                    X(2)=y_range(l);
                    X(3)=z_range(j);
                end
                i=i+1;
            end
        end
    end
end

if i==1 %no minimum found
    M_=-1;
    X(1)=NaN;
    X(2)=NaN;
    X(3)=NaN;
else
end

```



## Bibliography

---

- ABD, A. & UTILI, S. Geosynthetics layout optimization for reinforced soil slopes subject to cracks. *Landslides and Engineered Slopes. Experience, Theory and Practice: Proceedings of the 12th International Symposium on Landslides* (Napoli, Italy, 12-19 June 2016), 2016. CRC Press, 295.
- ARKIN, Y. & MICHAELI, L. 1985. Short-and long-term erosional processes affecting the stability of the Mediterranean coastal cliffs of Israel. *Engineering Geology*, 21, 153-174.
- ASKARINEJAD, A., LAUE, J., ITEN, M., ZWEIDLER, A., BLEIKER, E., BUSCHOR, H. & SPRINGMAN, S. Physical modelling of rainfall induced landslides under controlled climatic conditions. Eurofuge 2012, Delft, The Netherlands, April 23-24, 2012, 2012. Delft University of Technology and Deltares.
- BAKER, A., ALLMENDINGER, R., OWEN, L. & RECH, J. 2013. Permanent deformation caused by subduction earthquakes in northern Chile. *Nature Geoscience*, 6, 492-496.
- BAKER, R. 1981. Tensile strength, tension cracks, and stability of slopes. *Soils and foundations*, 21, 1-17.
- BARNES, G. E. 2010. *Soil mechanics: principles and practice*, Palgrave macmillan.
- BECK, S. L. & RUFF, L. J. 1989. Great earthquakes and subduction along the Peru trench. *Physics of the Earth and Planetary Interiors*, 57, 199-224.
- BENUMOF, B. T., STORLAZZI, C. D., SEYMOUR, R. J. & GRIGGS, G. B. 2000. The relationship between incident wave energy and seacliff erosion rates: San Diego County, California. *Journal of Coastal Research*, 1162-1178.
- BISHOP, A. & MORGENSTERN, N. 1960. Stability coefficients for earth slopes. *Geotechnique*, 10, 129-153.
- BISHOP, A. W. 1955. The use of the slip circle in the stability analysis of slopes. *Geotechnique*, 5, 7-17.
- BOLTON, M. & PANG, P. 1982. Collapse limit states of reinforced earth retaining walls. *Geotechnique*, 32, 349-367.
- BOON, C., HOULSBY, G. & UTILI, S. 2012. A new algorithm for contact detection between convex polygonal and polyhedral particles in the discrete element method. *Computers and Geotechnics*, 44, 73-82.
- BOON, C., HOULSBY, G. & UTILI, S. 2013. A new contact detection algorithm for three-dimensional non-spherical particles. *Powder Technology*, 248, 94-102.

- BOON, C., HOULSBY, G. & UTILI, S. 2014. New insights into the 1963 Vajont slide using 2D and 3D distinct-element method analyses. *Geotechnique*, 64, 800-816.
- BOON, C. W., HOULSBY, G. & UTILI, S. 2015. DEM modelling of a jointed rock beam with emphasis on interface properties. *Géotechnique Letters*, 5, 49-55.
- BOTTERO, A., NEGRE, R., PASTOR, J. & TURGEMAN, S. 1980. Finite element method and limit analysis theory for soil mechanics problems. *Computer Methods in Applied Mechanics and Engineering*, 22, 131-149.
- BRAY, M. J. & HOOKE, J. M. 1997. Prediction of soft-cliff retreat with accelerating sea-level rise. *Journal of Coastal Research*, 13, 453-467.
- BRIAUD, J.-L. 2008. Case histories in soil and rock erosion: woodrow wilson bridge, Brazos River Meander, Normandy Cliffs, and New Orleans Levees. *Journal of Geotechnical and Geoenvironmental Engineering*, 134, 1425-1447.
- BUCKY, P. B. 1931. *Use of models for the study of mining problems*, American Institute of Mining and Metallurgical Engineers, Incorporated.
- CAMONES, L. A. M., VARGAS JR, E. D. A., DE FIGUEIREDO, R. P. & VELLOSO, R. Q. 2013. Application of the discrete element method for modeling of rock crack propagation and coalescence in the step-path failure mechanism. *Engineering Geology*, 153, 80-94.
- CAMPONUOVO, G. ISMES experience on the model of St. Martino. Meeting on Rockfall dynamics and protective works effectiveness, 1977. 25-38.
- CAO, J. & ZAMAN, M. M. 1999. Analytical method for analysis of slope stability. *International journal for numerical and analytical methods in geomechanics*, 23, 439-449.
- CARSON, M. A. & KIRKBY, M. J. 1972. Hillslope form and process.
- CASTELLANZA, R., PARMA, M., PESCATORE, V. & SILVESTRO, G. 2009. Model footing load tests on soft rocks. *ASTM geotechnical testing journal*, 32, 262-272.
- CENGEL, Y. A. 2010. *Fluid mechanics*, Tata McGraw-Hill Education.
- CHANG, C.-J., CHEN, W. F. & YAO, J. T. 1984. Seismic displacements in slopes by limit analysis. *Journal of Geotechnical Engineering*, 110, 860-874.
- CHANG, Y. L. & HUANG, T. K. 2005. Slope stability analysis using strength reduction technique. *Journal of the Chinese Institute of Engineers*, 28, 231-240.
- CHEN, R.-H., KUO, K.-J. & CHIEN, W.-N. 2012. Failure Mechanism of Granular Soil Slopes under High Intensity Rainfalls. *Journal of GeoEngineering*, 7, 021-031.
- CHEN, W.-F., GIGER, M. & FANG, H.-Y. 1969. On the limit analysis of stability of slopes. *Soils and Foundations*, 9, 23-32.
- CHEN, W.-F. & LIU, X. 1990. *Limit analysis in soil mechanics*, Elsevier.
- CHEN, W.-F. & LIU, X. 2012. *Limit analysis in soil mechanics*, Elsevier.
- CHEN, W. 1975. *Limit analysis and soil plasticity*, 1975. Elsevier.

- CHEN, Z., MI, H., ZHANG, F. & WANG, X. 2003. A simplified method for 3D slope stability analysis. *Canadian Geotechnical Journal*, 40, 675-683.
- CHENG, Y., LANSIVAARA, T. & WEI, W. 2007. Two-dimensional slope stability analysis by limit equilibrium and strength reduction methods. *Computers and Geotechnics*, 34, 137-150.
- CIANTIA, M. O. & CASTELLANZA, R. 2015. Modelling weathering effects on the mechanical behaviour of rocks. *European Journal of Environmental and Civil Engineering*, 1-29.
- CIANTIA, M. O., CASTELLANZA, R., CROSTA, G. B. & HUECKEL, T. 2015a. Effects of mineral suspension and dissolution on strength and compressibility of soft carbonate rocks. *Engineering Geology*, 184, 1-18.
- CIANTIA, M. O., CASTELLANZA, R. & DI PRISCO, C. 2015b. Experimental Study on the Water-Induced Weakening of Calcarenes. *Rock Mechanics and Rock Engineering*, 1-21.
- CLEARY, P. W. & CAMPBELL, C. S. 1993. Self-lubrication for long runout landslides: examination by computer simulation. *JOURNAL OF GEOPHYSICAL RESEARCH-ALL SERIES*, 98, 21,911-21,911.
- COLLINS, B. D. & SITAR, N. 2010. Stability of steep slopes in cemented sands. *Journal of geotechnical and geoenvironmental engineering*, 137, 43-51.
- CONTE, E. & TRONCONE, A. 2012. A method for the analysis of soil slips triggered by rainfall. *Geotechnique*, 62, 187-192.
- COULOMB, C. A. 1776. *Essai sur une application des règles de maximis & minimis à quelques problèmes de statique, relatifs à l'architecture*, De l'Imprimerie Royale.
- CRESPELLANI, T., MADIAI, C. & VANNUCCHI, G. 1998. Earthquake destructiveness potential factor and slope stability. *Geotechnique*, 48.
- CROSTA, G., CASTELLANZA, R., DE BLASIO, F. & UTILI, S. Slope stability analysis for Valles Marineris, Mars: a numerical analysis of controlling conditions and failure types. EGU General Assembly Conference Abstracts, 2012a. 11667.
- CROSTA, G., HERMANN, R., VALBUZZI, E., DEHLS, J., YUGSI MOLINA, F. & SEPULVEDA, S. Slope instabilities along the Western Andean Escarpment and the main canyons in Northern Chile. EGU General Assembly Conference Abstracts, 2012b. 11343.
- CROSTA, G. B., HERMANN, R., DEHLS, J., LARI, S. & SEPULVEDA, S. in press. Rock avalanches clusters along the northern Chile coastal scarp: recurrence, environmental conditions, modelling.
- CROSTA, G. B., HERMANN, R., FRATTINI, P., VALBUZZI, E. & VALAGUSSA, A. 2014a. Large slope instabilities in Northern Chile: inventory, characterization and possible triggers. *Landslide Science for a Safer Geoenvironment*. Springer.
- CROSTA, G. B., UTILI, S., DE BLASIO, F. V. & CASTELLANZA, R. 2014b. Reassessing rock mass properties and slope instability triggering conditions in Valles Marineris, Mars. *Earth and Planetary Science Letters*, 388, 329-342.

- DAWSON, E., MOTAMED, F., NESARAJAH, S. & ROTH, W. 2000. Geotechnical stability analysis by strength reduction. *Geotechnical Special Publication*, 99-113.
- DE LANGE, W. P. & MOON, V. G. 2005. Estimating long-term cliff recession rates from shore platform widths. *Engineering Geology*, 80, 292-301.
- DRUCKER, D., PRAGER, W. & GREENBERG, H. 1952. Extended limit design theorems for continuous media. *Quarterly of Applied Mathematics*, 381-389.
- DRUCKER, D. C., GREENBERG, H. & PRAGER, W. 1950. *The safety factor of an elastic-plastic body in plane strain*, Division of Applied Mathematics, Brown University.
- DUNCAN, J. M. 1996. State of the art: limit equilibrium and finite-element analysis of slopes. *Journal of Geotechnical engineering*, 122, 577-596.
- DYER, M., UTILI, S. & ZIELINSKI, M. 2009. Field survey of desiccation fissuring of flood embankments. *Proceedings of the ICE-Water Management*, 162, 221-232.
- ESPINOZA, R., BOURDEAU, P. & MUHUNTHAN, B. 1994. Unified formulation for analysis of slopes with general slip surface. *Journal of geotechnical engineering*, 120, 1185-1204.
- FELLENIOUS, W. 1927. Erdstatische berechnungen mit reibung und kohesion und unter annahme kreiszylindrischer gleitflaechen (Statistical analysis of earth slopes and retaining walls considering both friction and cohesion and assuming cylindrical sliding surfaces). *W Ernst und Sohn, Berlin (in German)*.
- FOURIE, A. 1996. Predicting rainfall-induced slope instability. *Proceedings of the ICE-Geotechnical Engineering*, 119, 211-218.
- FRAYSSINES, M. & HANTZ, D. 2006. Failure mechanisms and triggering factors in calcareous cliffs of the Subalpine Ranges (French Alps). *Engineering Geology*, 86, 256-270.
- FREDLUND, D. Analytical methods for slope stability analysis. *Proceedings of the 4th International Symposium on Landslides*, 1984. s. I.:[sn], 229-250.
- FREDLUND, D., MORGENSTERN, N. & WIDGER, R. 1978. The shear strength of unsaturated soils. *Canadian Geotechnical Journal*, 15, 313-321.
- FREDLUND, M., LU, H. & FREDLUND, D. Three-Dimensional Limit Equilibrium Slope Stability Benchmarking. *Slope Stability 2011 Conference*, 2011.
- GAO, Y., SONG, W., ZHANG, F. & QIN, H. 2015. Limit analysis of slopes with cracks: Comparisons of results. *Engineering Geology*, 188, 97-100.
- GRAINGER, P. & HARRIS, J. 1986. Weathering and slope stability on Upper Carboniferous mudrocks in south-west England. *Quarterly Journal of Engineering Geology and Hydrogeology*, 19, 155-173.
- GRIFFITHS, D. & LANE, P. 1999. Slope stability analysis by finite elements. *Geotechnique*, 49, 387-403.
- GRIFFITHS, D. & LU, N. 2005. Unsaturated slope stability analysis with steady infiltration or evaporation using elasto-plastic finite elements.

- HACHINOHE, S., HIRAKI, N. & SUZUKI, T. 2000. Rates of weathering and temporal changes in strength of bedrock of marine terraces in Boso Peninsula, Japan. *Engineering Geology*, 55, 29-43.
- HALES, T. & ROERING, J. J. 2007. Climatic controls on frost cracking and implications for the evolution of bedrock landscapes. *Journal of Geophysical Research: Earth Surface (2003–2012)*, 112.
- HU, X.-W., TANG, H.-M. & LIU, Y.-R. 2005. Physical model studies on stability of Zhaoshuling landslide in area of Three Gorges Reservoir. *Yanshilixue Yu Gongcheng Xuebao/Chin. J. Rock Mech. Eng.*, 24, 2089-2095.
- HUANG, C.-C., LO, C.-L., JANG, J.-S. & HWU, L.-K. 2008. Internal soil moisture response to rainfall-induced slope failures and debris discharge. *Engineering Geology*, 101, 134-145.
- HUANG, M. & JIA, C.-Q. 2009. Strength reduction FEM in stability analysis of soil slopes subjected to transient unsaturated seepage. *Computers and Geotechnics*, 36, 93-101.
- HUGEMANN, W. 2010. Correcting lens distortions in digital photographs. *Ingenieurbüro Morawski+ Hugemann: Leverkusen, Germany*.
- HUTCHINSON, J. 1969. A reconsideration of the coastal landslides at Folkestone Warren, Kent. *Geotechnique*, 19, 6-38.
- HUTCHINSON, J. 2001. The Fourth Glossop Lecture Reading the Ground: Morphology and Geology in Site Appraisal. *Quarterly Journal of Engineering Geology and Hydrogeology*, 34, 7-50.
- HUTCHINSON, J. N. 1970. A coastal mudflow on the London Clay cliffs at Beltinge, North Kent. *Geotechnique*, 20, 412-438.
- HUTCHINSON, J. N. 1975. *The response of London Clay cliffs to differing rates of toe erosion*, Building Research Establishment, Department of the Environment.
- IVERSON, R. M., REID, M. E. & LAHUSEN, R. G. 1997. Debris-flow mobilization from landslides 1. *Annual Review of Earth and Planetary Sciences*, 25, 85-138.
- JANBU, N. Application of composite slip surfaces for stability analysis. Proc. European Conf. on Stability of Earth Slopes, Stockholm, 1954, 1954. 43-49.
- JANBU, N. Slope stability computations: In Embankment-dam Engineering. Textbook. Eds. RC Hirschfeld and SJ Poulos. JOHN WILEY AND SONS INC., PUB., NY, 1973, 40P. International Journal of Rock Mechanics and Mining Sciences & Geomechanics Abstracts, 1975. Pergamon, 67.
- JIA, G., ZHAN, T. L., CHEN, Y. & FREDLUND, D. 2009. Performance of a large-scale slope model subjected to rising and lowering water levels. *Engineering Geology*, 106, 92-103.
- KATZ, O. & AHARONOV, E. 2006. Landslides in vibrating sand box: What controls types of slope failure and frequency magnitude relations? *Earth and Planetary Science Letters*, 247, 280-294.

- KIMMANCE, G. 1988. *Computer aided risk analysis of open pit mine slopes in kaolin mined deposits*. Ph. D thesis, Imperial College London (University of London).
- KIMMANCE, J. P. 1998. *Computer aided risk analysis of open pit mine slopes in kaolin mineral deposits*. Imperial College London (University of London).
- KIMURA, T., TAKEMURA, J., SUEMASA, N. & HIRO-OKA, A. Failure of fills due to rainfall. *Centrifuge*, 1991. 509-516.
- KONRAD, J.-M. & AYAD, R. 1997. A idealized framework for the analysis of cohesive soils undergoing desiccation. *Canadian Geotechnical Journal*, 34, 477-488.
- LACAZE, L., PHILLIPS, J. C. & KERSWELL, R. R. 2008. Planar collapse of a granular column: Experiments and discrete element simulations. *Physics of Fluids (1994-present)*, 20, 063302.
- LE COSSEC, J., DUPERRÉ, A., VENDEVILLE, B. C. & TAIBI, S. 2011. Numerical and physical modelling of coastal cliff retreat processes between La Hève and Antifer capes, Normandy (NW France). *Tectonophysics*, 510, 104-123.
- LE ROUEIL, S. 2001. Natural slopes and cuts: movement and failure mechanisms. *Geotechnique*, 51, 197-243.
- LING, H. I. & LESHCHINSKY, D. 1995. Seismic Performance of Simple Slopes. *Soils and Foundations*, 35, 85-94.
- LING, H. I., WU, M.-H., LESHCHINSKY, D. & LESHCHINSKY, B. 2009. Centrifuge modeling of slope instability. *Journal of Geotechnical and Geoenvironmental Engineering*, 135, 758-767.
- LOMNITZ, C. 2004. Major earthquakes of Chile: a historical survey, 1535-1960. *Seismological Research Letters*, 75, 368-378.
- LOUKIDIS, D., BANDINI, P. & SALGADO, R. 2003. Stability of seismically loaded slopes using limit analysis. *Geotechnique*, 53, 463-479.
- LYAMIN, A. V. & SLOAN, S. 2002. Upper bound limit analysis using linear finite elements and non-linear programming. *International Journal for Numerical and Analytical Methods in Geomechanics*, 26, 181-216.
- LYSMER, J. 1970. Limit analysis of plane problems in soil mechanics. *Journal of Soil Mechanics & Foundations Div.*
- MAKRODIMOPOULOS, A. & MARTIN, C. 2006. Lower bound limit analysis of cohesive-frictional materials using second-order cone programming. *International Journal for Numerical Methods in Engineering*, 66, 604-634.
- MAKRODIMOPOULOS, A. & MARTIN, C. 2007. Upper bound limit analysis using simplex strain elements and second-order cone programming. *International journal for numerical and analytical methods in geomechanics*, 31, 835-865.
- MICHALOWSKI, R. 1995a. Slope stability analysis: a kinematical approach. *Geotechnique*, 45, 283-293.
- MICHALOWSKI, R. 2008. Limit analysis with anisotropic fibre-reinforced soil. *Geotechnique*, 58, 489-502.

- MICHALOWSKI, R. L. 1995b. Stability of slopes: limit analysis approach. *Reviews in Engineering Geology*, 10, 51-62.
- MICHALOWSKI, R. L. 1997. Stability of uniformly reinforced slopes. *Journal of Geotechnical and Geoenvironmental Engineering*, 123, 546-556.
- MICHALOWSKI, R. L. 1998. Limit analysis in stability calculations of reinforced soil structures. *Geotextiles and Geomembranes*, 16, 311-331.
- MICHALOWSKI, R. L. 2002. Stability charts for uniform slopes. *Journal of Geotechnical and Geoenvironmental Engineering*, 128, 351-355.
- MICHALOWSKI, R. L. 2013. Stability assessment of slopes with cracks using limit analysis. *Canadian Geotechnical Journal*, 50, 1011-1021.
- MORGENSTERN, N. & PRICE, V. E. 1965. The analysis of the stability of general slip surfaces. *Geotechnique*, 15, 79-93.
- MORIWAKI, H., INOKUCHI, T., HATTANJI, T., SASSA, K., OCHIAI, H. & WANG, G. 2004. Failure processes in a full-scale landslide experiment using a rainfall simulator. *Landslides*, 1, 277-288.
- OH, S. & LU, N. 2015. Slope stability analysis under unsaturated conditions: Case studies of rainfall-induced failure of cut slopes. *Engineering Geology*, 184, 96-103.
- OKURA, Y., KITAHARA, H., OCHIAI, H., SAMMORI, T. & KAWANAMI, A. 2002. Landslide fluidization process by flume experiments. *Engineering Geology*, 66, 65-78.
- ORENSE, R. P. 2004. Slope Failures Triggered by Heavy Rainfall. *Philippine Engineering Journal*, 25.
- PARSONS, A. J. 2002. *Hillslope form*, Routledge.
- PÉRON, H., HUECKEL, T., LALOU, L. & HU, L. 2009. Fundamentals of desiccation cracking of fine-grained soils: experimental characterisation and mechanisms identification. *Canadian Geotechnical Journal*, 46, 1177-1201.
- POTTS, D. M., ZDRAVKOVIC, L. & ZDRAVKOVIĆ, L. 2001. *Finite element analysis in geotechnical engineering: application*, Thomas Telford.
- RAHARDJO, H., LIM, T., CHANG, M. & FREDLUND, D. 1995. Shear-strength characteristics of a residual soil. *Canadian Geotechnical Journal*, 32, 60-77.
- RATHJE, E. M. & ANTONAKOS, G. 2011. A unified model for predicting earthquake-induced sliding displacements of rigid and flexible slopes. *Engineering Geology*, 122, 51-60.
- ROSCOE, K. 1968. Soils and model tests. *The Journal of Strain Analysis for Engineering Design*, 3, 57-64.
- SARMA, S. K. 1975. Seismic stability of earth dams and embankments. *Geotechnique*, 25, 743-761.
- SARMA, S. K. 1979. Stability analysis of embankments and slopes. *Journal of Geotechnical and Geoenvironmental Engineering*, 105.
- SCHOFIELD, A. N. 1978. Use of centrifugal model testing to assess slope stability. *Canadian Geotechnical Journal*, 15, 14-31.

- SELBY, M. J. 1982. Hillslope materials and processes. *Hillslope materials and processes*.
- SLOAN, S. 1988. Lower bound limit analysis using finite elements and linear programming. *International Journal for Numerical and Analytical Methods in Geomechanics*, 12, 61-77.
- SLOAN, S. 2013. Geotechnical stability analysis.
- SLOAN, S. & KLEEMAN, P. 1995. Upper bound limit analysis using discontinuous velocity fields. *Computer Methods in Applied Mechanics and Engineering*, 127, 293-314.
- SMITH, I. & HOBBS, R. 1974. Finite element analysis of centrifuged and built-up slopes. *Geotechnique*, 24, 531-559.
- SOULIÉ, F., EL YOUSOUFI, M. S., DELENNE, J.-Y., VOIVRET, C. & SAIX, C. 2007. Effect of the crystallization of a solute on the cohesion in granular materials. *Powder technology*, 175, 43-47.
- SPENCER, E. 1967. A method of analysis of the stability of embankments assuming parallel inter-slice forces. *Geotechnique*, 17, 11-26.
- SPENCER, E. 1968. Effect of tension on the stability of embankments. *Journal of Soil Mechanics & Foundations Div.*
- SPRINGMAN, S., THIELEN, A., KIENZLER, P. & FRIEDEL, S. 2013. A long-term field study for the investigation of rainfall-induced landslides. *Geotechnique*, 63, 1177.
- STARON, L. & HINCH, E. 2007. The spreading of a granular mass: role of grain properties and initial conditions. *Granular Matter*, 9, 205-217.
- TAKE, W. & BOLTON, M. 2011. Seasonal ratcheting and softening in clay slopes, leading to first-time failure. *Géotechnique*, 61, 757-769.
- TAKE, W., BOLTON, M., WONG, P. & YEUNG, F. 2004. Evaluation of landslide triggering mechanisms in model fill slopes. *Landslides*, 1, 173-184.
- TAYLOR, R. 1995. Centrifuges in modelling: principles and scale effects. *Geotechnical centrifuge technology*, 19-33.
- TERZAGHI, K. 1950. *Theoretical Soil Mechanics*, New York, USA, John Wiley & Sons.
- TOHARI, A., NISHIGAKI, M. & KOMATSU, M. 2007. Laboratory rainfall-induced slope failure with moisture content measurement. *Journal of Geotechnical and Geoenvironmental Engineering*, 133, 575-587.
- TSAI, C.-C. & CHIEN, Y.-C. 2016. A general model for predicting the earthquake-induced displacements of shallow and deep slope failures. *Engineering Geology*, 206, 50-59.
- UTILI, S. 2004. *Evolution of natural slopes subject to weathering: An analytical and numerical study*. Ph. D thesis, Politecnico di Milano, Milan, Italy.
- UTILI, S. 2013. Investigation by limit analysis on the stability of slopes with cracks. *Geotechnique*, 63, 140-154.
- UTILI, S. 2015. Discussion of "Limit analysis of slopes with cracks: Comparisons of results". *Engineering Geology*, 197, 306-307.



- UTILI, S. & ABD, A. H. 2016. On the stability of fissured slopes subject to seismic action. *International Journal for Numerical and Analytical Methods in Geomechanics*, 40, 785-806.
- UTILI, S. & CROSTA, G. 2011a. Modeling the evolution of natural cliffs subject to weathering: 1. Limit analysis approach. *Journal of Geophysical Research: Earth Surface* (2003–2012), 116, F01016.
- UTILI, S. & CROSTA, G. 2011b. Modeling the evolution of natural cliffs subject to weathering: 2. Discrete element approach. *Journal of Geophysical Research-Part F-Earth Surface*, 116, F01017.
- UTILI, S. & NOVA, R. 2007. On the optimal profile of a slope. *Soils and foundations*, 47, 717-729.
- UTILI, S. & NOVA, R. 2008. DEM analysis of bonded granular geomaterials. *International Journal for Numerical and Analytical Methods in Geomechanics*, 32, 1997-2031.
- UTILI, S., ZHAO, T. & HOULSBY, G. 2015. 3D DEM investigation of granular column collapse: evaluation of debris motion and its destructive power. *Engineering geology*, 186, 3-16.
- VANICEK, I. & VANICEK, M. 2008. *Earth structures: in transport, water and environmental engineering*, Springer Science & Business Media.
- VIRATJANDR, C. & MICHALOWSKI, R. L. 2006. Limit analysis of submerged slopes subjected to water drawdown. *Canadian Geotechnical Journal*, 43, 802-814.
- VOULGARI, C. & UTILI, S. 2017. A general analytical solution for the evolution of cliffs accounting for strength degradation, seismic action, formation of tension cracks and seepage. *Engineering Geology*, 219, 92-106.
- WANG, G. & SASSA, K. 2001. Factors affecting rainfall-induced flowslides in laboratory flume tests. *Geotechnique*, 51, 587-599.
- WANG, R., ZHANG, G. & ZHANG, J.-M. 2010. Centrifuge modelling of clay slope with montmorillonite weak layer under rainfall conditions. *Applied Clay Science*, 50, 386-394.
- WANG, Y. & LEUNG, S. 2008. Characterization of cemented sand by experimental and numerical investigations. *Journal of geotechnical and geoenvironmental engineering*, 134, 992-1004.
- WASOWSKI, J., KEEFER, D. K. & LEE, C.-T. 2011. Toward the next generation of research on earthquake-induced landslides: current issues and future challenges. *Engineering Geology*, 122, 1-8.
- WHITE, D., RANDOLPH, M. & THOMPSON, B. 2005. An image-based deformation measurement system for the geotechnical centrifuge. *International Journal of Physical Modelling in Geotechnics*, 5, 1-12.
- WHITE, D. & TAKE, W. 2002. GeoPIV: Particle Image Velocimetry (PIV) software for use in geotechnical testing.
- WHITE, D., TAKE, W. & BOLTON, M. 2003. Soil deformation measurement using particle image velocimetry (PIV) and photogrammetry. *Geotechnique*, 53, 619-631.
- WOOD, D. M. 2003. *Geotechnical modelling*, CRC Press.

- XU, G., ZHANG, L. & LIU, S. 2005. Preliminary study of instability behavior of levee on soft ground during sudden drawdown. *Geotechnical Special Publication*, 3009-3018.
- YANG, X.-G. & CHI, S.-C. 2014. Seismic stability of earth-rock dams using finite element limit analysis. *Soil Dynamics and Earthquake Engineering*, 64, 1-10.
- YERRO, A., ALONSO, E. & PINYOL, N. 2015. The material point method for unsaturated soils. *Geotechnique*, 65, 201-217.
- YOKOTA, S. & IWAMATSU, A. 2000. Weathering distribution in a steep slope of soft pyroclastic rocks as an indicator of slope instability. *Engineering Geology*, 55, 57-68.
- YOU, L. & MICHALOWSKI, R. L. 1999. Displacement charts for slopes subjected to seismic loads. *Computers and Geotechnics*, 25, 45-55.
- YU, H., SALGADO, R., SLOAN, S. & KIM, J. 1998. Limit analysis versus limit equilibrium for slope stability. *Journal of Geotechnical and Geoenvironmental Engineering*, 124, 1-11.
- ZHANG, G., QIAN, J., WANG, R. & ZHANG, J.-M. 2011. Centrifuge model test study of rainfall-induced deformation of cohesive soil slopes. *Soils and foundations*, 51, 297-305.
- ZHANG, G., WANG, R., QIAN, J., ZHANG, J.-M. & QIAN, J. 2012. Effect study of cracks on behavior of soil slope under rainfall conditions. *Soils and Foundations*, 52, 634-643.
- ZHANG, J., LI, Z. & QI, T. 2005. Q mechanism analysis of landslide of a layered slope induced by drawdown of water level. *Science in China Series E Engineering & Materials Science*, 48, 136-145.
- ZHENG, H., LIU, D. & LI, C. 2005. Slope stability analysis based on elasto-plastic finite element method. *International Journal for Numerical Methods in Engineering*, 64, 1871-1888.
- ZORNBERG, J. G., SITAR, N. & MITCHELL, J. K. 1998. Performance of geosynthetic reinforced slopes at failure. *Journal of Geotechnical and Geoenvironmental engineering*, 124, 670-683.

## **Online Sources**

<http://www.bgs.ac.uk>

<http://landslides.usgs.gov/learn/majorls.php>